



DISSERTATION

Slow Extraction Optimisation for the MedAustron Synchrotron

Ausgeführt zum Zwecke der Erlangung des akademischen Grades eines
Doktors der Naturwissenschaften

unter der Leitung von
Privatdoz. Dipl.-Ing. Dr.techn. Michael BENEDIKT
E141 - Atominstitut, Technische Universität Wien

und

Dale PROKOPOVICH, PhD
MedAustron, ABP

eingereicht an der Technischen Universität Wien
E130 - Fakultät für Physik

von

Florian Kühtheubl
Matrikelnummer 01226869

Wien, am 27. August 2024


Florian Kühtheubl

Kurzfassung der Dissertation

Das Ionentherapiezentrum MedAustron verwendet langsame Resonanzextraktion dritter Ordnung, um den Strahl aus dem Synchrotron mit Strahllängen zwischen einer und zehn Sekunden zu extrahieren. Im Rahmen des aktuellen klinischen Betriebes erfolgt diese Extraktion über die Beschleunigung der Teilchen durch einen Betatron Core. Alternative Extraktionsmethoden versprechen jedoch erweiterte Möglichkeiten, die Strahlparameter während der Extraktion zu verändern und die Behandlung zu optimieren.

Die vorliegende Dissertation liefert einen umfassenden Überblick über diese alternativen Extraktionsmethoden, deren potenzielle Implementierung bei MedAustron sowohl mit Simulationen als auch mit Messungen erforscht wurde. Im Fokus stehen dabei die Vorteile dieser Extraktionsmethoden zur Optimierung der Effizienz der Behandlung sowie die Kompatibilität mit komplexen Bestrahlungstechniken wie der dynamischen Intensitätsregulierung und der Extraktion von mehreren Energien innerhalb eines Spills.

Im Rahmen der Arbeit wird ein Überblick über den Beschleunigerkomplex von MedAustron unter besonderer Berücksichtigung der Extraktion, sowie eine Einführung in für diese Arbeit relevanten Aspekte der theoretischen Grundlagen der transversalen und longitudinalen Strahldynamik gegeben.

Eine der erforschten alternativen Extraktionsmethoden ist Radio Frequency Knock Out, bei der die Extraktion durch Anregung des Strahls mit einer hochfrequenten Wechselspannung erfolgt. Eine mehrdimensionale Optimierung der Strahl- und Beschleuniger-Parameter wird mithilfe von Simulationen durchgeführt, wofür ein detailliertes Verständnis der komplexen Strahldynamik während der Extraktion vorausgesetzt ist. Verschiedene Anregungssignale werden in der Praxis getestet und ihre Auswirkungen auf die Effizienz der Extraktion sowie die Schwankungen der Intensität des extrahierten Strahles untersucht.

Weitere Extraktionsmethoden wie Constant Optics Slow Extraction oder Phase Displacement Extraction werden untersucht und mögliche Vorteile, aber auch Limitierungen, aufgezeigt. Ein Vergleich der verfügbaren Extraktionsmethoden bezüglich Qualität des extrahierten Strahles wird durchgeführt. Besonderes Augenmerk liegt auf der Unterdrückung von Schwankungen in der Intensität des extrahierten Strahles durch Methoden wie Empty Bucket Channeling.

Alle genannten Extraktionsmethoden werden im Rahmen dieser Dissertation erfolgreich getestet und können durch die Ergebnisse dieser Arbeit mit der bestehenden Hardware- und Software-Infrastruktur bei MedAustron durchgeführt werden.

Abstract

The ion therapy facility MedAustron employs third-order resonant slow extraction to extract the beam from the synchrotron with beam lengths ranging from one to ten seconds. Currently, this extraction process relies on accelerating the particles via a betatron core. However, alternative extraction methods offer improved flexibility in adjusting the beam parameters during extraction, thus optimising the treatment.

This dissertation comprehensively examines these alternative extraction methods, utilising simulations and measurements to assess their potential implementation at MedAustron. The focus is on their capacity to enhance treatment efficiency and compatibility with advanced irradiation techniques, including dynamic intensity control and the extraction of multiple energies within a single spill.

The thesis offers an overview of the MedAustron accelerator complex, with a particular emphasis on the extraction, alongside with an introduction to the theoretical principles of transverse and longitudinal beam dynamics relevant to this work.

One such alternative extraction method explored is Radio Frequency Knock Out, wherein extraction is achieved by exciting the beam with a high-frequency alternating voltage. A multi-dimensional optimisation of the beam and lattice parameters is conducted through simulations, requiring a detailed understanding of the complex beam dynamics during extraction. Various excitation signals are examined, and their impact on extraction efficiency and beam intensity fluctuations is analysed.

Furthermore, other extraction methods such as Constant Optics Slow Extraction and Phase Displacement Extraction are investigated, highlighting their potential advantages and limitations. A comparative analysis of available extraction methods is conducted, considering the quality of the extracted beam. Special attention is given to the suppression of intensity ripples in the extracted beam through techniques such as Empty Bucket Channelling.

All alternative extraction methods discussed in this dissertation are successfully tested and can be implemented at MedAustron with the existing hardware and software infrastructure. This research furnishes the requisite findings to facilitate such implementation.

Contents

Kurzfassung der Dissertation	ii
Abstract	iii
Acronyms	vii
List of Symbols	x
1. Introduction	1
1.1. The MedAustron accelerator complex	3
1.1.1. Sources and Low Energy Beam Transfer Line (LEBT)	3
1.1.2. Linear Accelerator (LINAC) and Medium Energy Beam Transfer Line (MEBT)	4
1.1.3. Main Ring	5
1.1.4. High Energy Beam Transfer Line (HEBT) and treatment rooms . .	7
1.2. The MedAustron control system	9
1.3. Scope of the thesis	12
2. Selected topics of accelerator physics	14
2.1. Transverse beam dynamics	14
2.1.1. Motion of the reference particle	14
2.1.2. Equation of motion	16
2.1.3. Phase space concept and Twiss functions	20
2.1.4. Tune and chromaticity	22
2.2. Longitudinal beam dynamics	23
2.2.1. Stationary and moving buckets	24
2.2.2. Phase Jump	27
2.3. Slow extraction	30
2.3.1. Principles of slow extraction	30
2.3.2. Slow extraction techniques	37
2.3.3. Comparison of the slow extraction techniques	46
2.4. Ripple mitigation with Empty Bucket Channelling (EBC)	50

3. Methods	54
3.1. Simulation tools	54
3.1.1. MAD-X	54
3.1.2. Beam Longitudinal Dynamics (BLonD)	61
3.1.3. XSuite	63
3.1.4. Comparison of the simulation tools	65
3.2. Used detectors	66
4. Implementation of RFKO at MedAustron	69
4.1. RFKO setup	69
4.2. Parameter optimisation	72
4.2.1. Extraction	75
4.2.2. Transmission from the ESE to the MST	80
4.3. Beam stability measurements	86
4.3.1. Tune measurement	86
4.3.2. Beam stability for unbunched beam	87
4.3.3. Beam stability for bunched beam	88
4.4. Excitation patterns	93
4.4.1. Signal amplitude	93
4.4.2. Excitation frequency	100
4.5. Extraction measurements	105
5. Other extraction methods	110
5.1. Constant Optics Slow Extraction	110
5.1.1. Unbunched COSE	110
5.1.2. Bunched COSE	115
5.1.3. Multi Energy Extraction	119
5.1.4. Limitations of COSE	128
5.2. Phase Displacement Extraction (PDE)	130
5.2.1. Pulsed extraction	135
6. Intensity beam ripples	138
6.1. Quantification of intensity ripples	140
6.2. Intrinsic intensity beam ripples	144
6.3. Empty Bucket Channelling	147
6.3.1. Simulations	148
6.3.2. Measurements	150
6.4. Ripple transfer function	153
6.5. Ripples for alternative extraction methods	158

7. Conclusion and outlook	162
List of Figures	165
List of Tables	168
Bibliography	170
Acknowledgements	179
A. Example of a typical timing sequence	181
B. Flowchart of the GnuRadio script used for RFKO	182

Acronyms

AC	Alternating Current
AGS	Alternating Gradient Synchrotron
AM	Amplitude Modulation
BalUn	Balanced-Unbalanced
BLonD	Beam Longitudinal Dynamics
BNL	Brookhaven National Laboratory
BPSK	Binary Phase Shift Keying
CDP	Cycle-Dependent Property
CERN	European Organization for Nuclear Research
CNAO	Centro Nazionale di Adroterapia Oncologica
CoG	Center of Gravity
COSE	Constant Optics Slow Extraction
CPU	Central Processing Unit
CTS	Current Transformer System
DC	Direct Current
DDM	Dose Delivery Monitor
DDS	Dose Delivery System
DIC	Dynamic Intensity Control
EBC	Empty Bucket Channelling
ECR	Electron Cyclotron Resonance
EFE	Electric Field Fast Deflector
ESE	Electrostatic Extraction Septum
ESI	Electrostatic Injection Septum
FCR	Full COSE Ramp
FFT	Fast Fourier Transformation
FM	Frequency Modulation

FNAL	Fermi National Accelerator Laboratory
FPGA	Field Programmable Gate Array
FT	Flat-Top
FWHM	Full Width at Half Maximum
FX	Fast Extraction
GPU	Graphics Processing Unit
GSI	Helmholtzzentrum für Schwerionenforschung
HEBT	High Energy Beam Transfer Line
HEPHY	Institut für Hochenergiephysik
HIMAC	Heavy Ion Medical Accelerator in Chiba
HIT	Heidelberger Ionenstrahl-Therapiezentrum
ICFA	International Committee for Future Accelerators
ICM	Isocenter Monitor
IFAST-REX	Innovation Fostering in Accelerator Science and Technology - Resonant Extraction
IH-DTL	Interdigital H-mode Drift Tube Linac
IHEP	Institute for High Energy Physics
IMS	Intertank Matching Section
IR	Irradiation Room
J-PARC	Japan Proton Accelerator Research Complex
KOE	Knockout Candidate
LEBT	Low Energy Beam Transfer Line
LINAC	Linear Accelerator
MACS	MedAustron Control System
MAD	Methodical Accelerator Design
MAIPTA	MedAustron International Particle Therapy Accelerator
MEBT	Medium Energy Beam Transfer Line
MEE	Multi Energy Extraction
MIT	Marburger Ionenstrahl-Therapiezentrum
MKC	Magnetic Kicker Chopper
MR	Main Ring
MST	Magnetic Extraction Septum

MXR	Resonant Sextupole
NCR	Non-Clinical Research
PBS	Pencil Beam Scanning
PDE	Phase Displacement Extraction
PID	Proportional-Integral-Derivative
PIMMS	Proton-Ion Medical Machine Study
PS	Proton Synchrotron
PSK	Phase Shift Keying
PTC	Polymorphic Tracking Code
QIM	Quality Intensity Monitor
QPSK	Quadrature Phase Shift Keying
RF	Radio Frequency
RFKO	Radio Frequency Knock Out
RFQ	Radio Frequency Quadrupole
RMS	Root Mean Square
SDR	Software Defined Radio
SFX	Scintillating Fiber Hodoscope
SLC	Synchrotron Low-Level Controller
SOBP	Spread Out Bragg Peak
SPS	Super Proton Synchrotron
SSP	Single Setpoint
SSQ	Setpoint Sequence
SX	Slow Extraction
TSQ	Timing Sequence
USRP	Universal Software Radio Peripheral

List of Symbols

Sign	Description	Unit
A	Single-particle amplitude	m
A_0	Amplitude of the RFKO signal	V
α, β, γ	Twiss parameter	rad, m, m^{-1}
A_B	Bucket area	rad
α_c	Momentum compaction factor	-
\mathbf{B}	Magnetic field vector	T
$B\rho$	Magnetic rigidity	$T \cdot m$
β_r	Relativistic beta factor	-
c	Speed of light	$m \cdot s^{-1}$
$D_{x,y}$	Horizontal/vertical dispersion function	m
δ_B	Bucket height	-
$\Delta p/p = \delta$	Momentum offset to reference particle	-
$\Delta X'_3$	Spiral kick	rad
ΔX_3	Spiral step	m
ΔE_n	<i>MEE</i> : Energy step	eV
Δx_n	<i>MEE</i> : radial position change	m
df	<i>PDE</i> : frequency offset	Hz
DF	Duty factor	-
E_x	Electric field	$V \cdot m^{-1}$
e	Elementary charge	C
E	Kinetic energy of the particle	eV
E_{stable}	Area of the stable triangle	m^2
ϵ	Beam emittance	$\pi \cdot \text{mm} \cdot \text{mrad}$
ϵ_n	Normalised beam emittance	$\pi \cdot \text{mm} \cdot \text{mrad}$
ϵ_{ex}	Extraction efficiency	%
ϵ_{tr}	Transmission efficiency	%
η	Phase slip factor	-
f_0	Excitation frequency of the RFKO signal	Hz
\mathbf{F}	Force vector	$\text{kg} \cdot \text{m} \cdot \text{s}^{-2}$

Sign	Description	Unit
f	Frequency	Hz
f_{rev}	Revolution frequency	Hz
γ_r	Relativistic Lorentz factor	-
γ_{tr}	Transition energy	-
H	Hamiltonian	J
h	Harmonic number	-
I	Intensity	Hz
K_n	Integrated multipole strength	m^{-n}
k_n	Normalised multipole strength	$\text{m}^{-(n+1)}$
$\boldsymbol{\kappa}$	Local curvature vector	m^{-1}
L	Orbit length	m
l	Magnet length	m
$M(s \rightarrow s + l)$	Transfer matrix from s to $s + l$	-
m	Particle mass	kg
$\Delta\mu$	Phase advance	rad
N	Number of particles	-
ω_0	Angular cavity frequency	Hz
p	Particle momentum	$\text{kg} \cdot \text{m} \cdot \text{s}^{-1}$
P_{el}	Electric power	W
ϕ_x	Deflection angle	rad
ϕ_B	Bucket length	rad
ϕ	Longitudinal particle phase	rad
ϕ_s	Synchronous phase	rad
ψ	Transverse particle phase	rad
q	Particle charge	C
$Q_{x,y}$	Horizontal/vertical tune	-
$Q'_{x,y}$	Horizontal/vertical chromaticity	-
Q_{res}	Tune of the resonance	-
q_x	Fractional part of the horizontal tune	-
R_{el}	Electric impedance	Ω
R	Synchrotron radius	m
r	Peak to mean ratio	-
ρ	Radius of curvature	m
RF	Ripple factor	-
RTF	Ripple transfer function	-
s	Longitudinal particle position	m
$S(t)$	Time-dependent extraction rate	s^{-1}

Sign	Description	Unit
S	Modified sextupole strength	$\text{m}^{-1/2}$
σ	Standard deviation	a.u.
T	Period	s
t	Time	s
τ	Spill length in number of turns	-
\mathbf{v}	Velocity vector	$\text{m} \cdot \text{s}^{-1}$
V	Voltage	V
\hat{V}	Amplitude of the cavity voltage	V
x, y	Horizontal/vertical particle position	m
x', y'	Horizontal/vertical particle angle	rad
X, Y	Normalised horizontal/vertical particle position	$\text{m}^{1/2}$
z	Longitudinal particle position (reference particle)	m

1. Introduction

MedAustron is a synchrotron-based ion therapy centre, located in Wiener Neustadt, Austria. It is one of six facilities worldwide using both protons and carbon ions to irradiate the tumour with high precision.

Figure 1.1 shows the dose depth profile (deposited dose over depth) for an exemplary treatment with protons in comparison with conventional radiotherapy with photons or electrons.

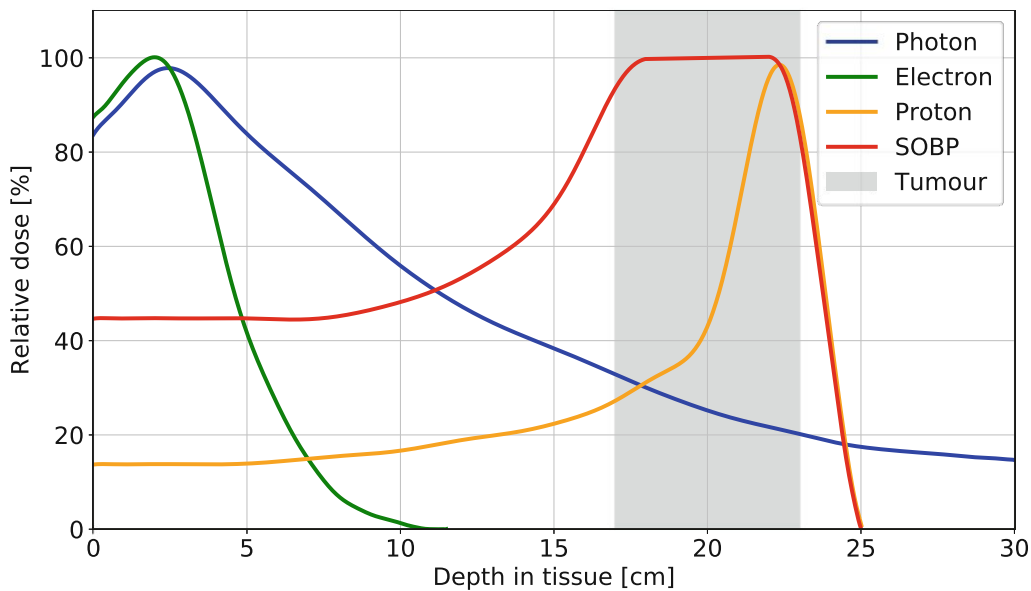


Figure 1.1.: Dose depth profile for a typical treatment with protons, photons and electrons (modified after [1]).

Compared to conventional radiotherapy with photons, particle therapy has the advantage that most energy is delivered at the so-called Bragg peak. The deposited dose before and after this Bragg peak is comparably low, which means that the healthy tissue surrounding the tumour can be conserved. The penetration depth is adjusted to the position of the tumour inside the body and can be precisely controlled with the energy of the beam. Particle therapy is therefore particularly important for the treatment of tumours

surrounded by radiation-sensitive tissue, such as tumours of the brain, the spinal cord, the prostate, or sarcomas. Additionally, radiation resistant tumours can be treated with heavy ions that are immune to conventional radiotherapy [2, 3].

As the tumour is a three-dimensional object with a given thickness, active energy variation is used to distribute the dose over the full tumour dimensions. Each energy is used to irradiate an iso-energy tissue slice of the tumour, subsequent irradiation with different energies leads to a superposition of the different Bragg peaks and a so-called Spread Out Bragg Peak (SOBP).

Additionally to the energy modulation, transverse scanning of the beam is necessary to cover each iso-energy slice of the tumour. This is done by Pencil Beam Scanning (PBS), where a focused beam with a small spot size is rastered over the tumour in a grid. The treatment planning calculates the required dose for each of the grid points, and the irradiation is guided by a fast scanning system and verified by online dosimetry.

The advantage of irradiation with heavy ions such as carbon is the improved relative biological effectiveness of the treatment, as more lesions can be created for the same energy. Additionally, both longitudinal and lateral scattering are reduced, resulting in a sharper Bragg peak and a reduced exit dose [4].

At MedAustron, proton and carbon ions are used for clinical treatment, with the energy ranges provided in Table 1.1. Additionally, the commissioning of a helium beam is currently being carried out¹.

Particle type	Energy range
proton H ⁺	62.4 - 252.7 MeV ²
carbon ions C ⁶⁺	120.0 - 402.8 MeV/u
helium ions He ²⁺	62.4 - 252.7 MeV/u ³

Table 1.1.: Particle types and clinical energy ranges at MedAustron.

¹For first results regarding the commissioning of the injector system for He²⁺ ions, see [5] and [6].

²Energies of up to 800 MeV are available for Non-Clinical Research (NCR) in IR1.

³For potential research applications of helium ions, energies between 40.0 and 402.8 MeV/u are available.

1.1. The MedAustron accelerator complex

This chapter provides an overview over the accelerator chain at MedAustron, from the ion source to the treatment room. The focus will be on the Main Ring, as it is the most relevant part of the accelerator complex for this thesis.

The structure of the MedAustron particle accelerator is based on the Proton-Ion Medical Machine Study (PIMMS) [7, 8] and is shown in Figure 1.2.

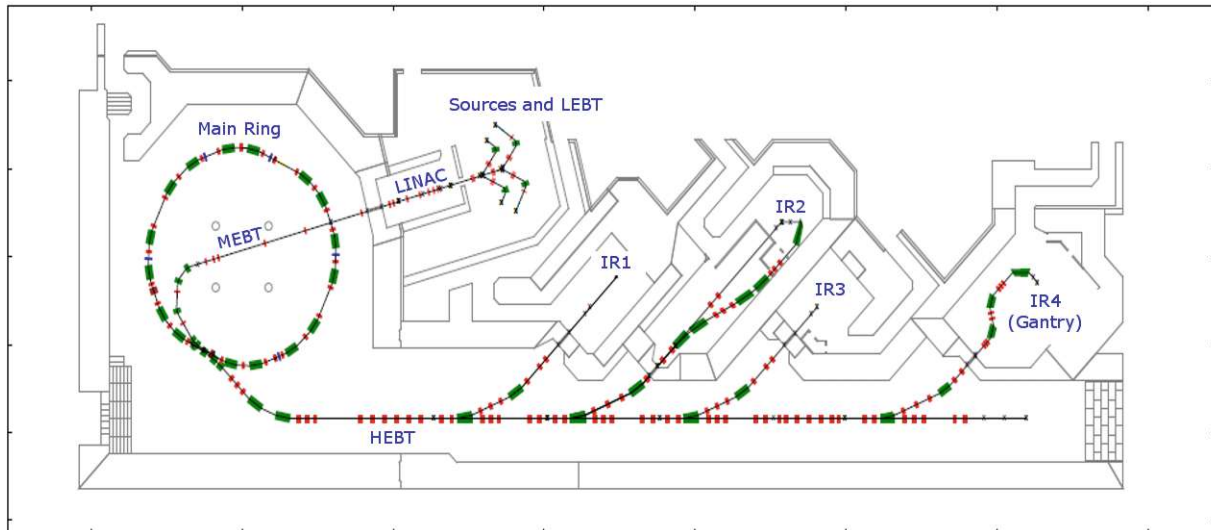


Figure 1.2.: The MedAustron accelerator complex (modified after [9]).

1.1.1. Sources and Low Energy Beam Transfer Line (LEBT)

The acceleration chain starts at the particle sources. Three identical Electron Cyclotron Resonance (ECR) ion sources are used to generate a hydrogen ($^1\text{H}_3^+$ in S1), carbon ($^{12}\text{C}^{4+}$ in S2) or helium ($^4\text{He}^{2+}$ in S3) ion beam of 8 keV/u. Note that while the charge-to-mass ratio is 1/3 for protons and carbon ions, it is 1/2 for helium ions.

After leaving the plasma chamber of the source, the particles reach the Low Energy Beam Transfer Line (LEBT). A 90 degree spectrometer dipole magnet is used to purify the beam by removing by-products of the particle generation in the sources, such as unwanted charge states. Dipole magnets are used to switch between the different ions beams. The beam is steered by horizontal and vertical steering magnets and focused by quadrupole triplets. The LEBT is equipped with various beam diagnostic devices to analyse beam parameters like current, intensity, position and profile [10].

1.1.2. Linear Accelerator (LINAC) and Medium Energy Beam Transfer Line (MEBT)

After the LEBT, the beam enters the Linear Accelerator (LINAC) section, where the particles are pre-accelerated before they are injected in the Main Ring. The whole structure is embedded in a bunker to allow for access of the source area during operation. The LINAC is composed of a four-rod type Radio Frequency Quadrupole (RFQ) to accelerate the beam to 400 keV/u and an Interdigital H-mode Drift Tube Linac (IH-DTL) for further acceleration to the injection energy of 7 MeV/u. Between the RFQ and the IH-DTL, the Intertank Matching Section (IMS) is used for matching the beam to the IH-DTL [10].

Before exiting the LINAC bunker and after focussing the beam with a quadrupole triplet, a carbon stripping foil is used to ionise the particles further by stripping H_3^+ to three protons (H^+) and $^{12}\text{C}^{4+}$ to $^{12}\text{C}^{6+}$ [10]. Helium ions are not affected by the stripping foil as they are already fully ionised, which enables simultaneous acceleration of carbon and helium ions with an almost identical charge to mass ratio of $q/m \approx 1/2$ [5].

The beam is delivered to the Main Ring via the Medium Energy Beam Transfer Line (MEBT). A debunching cavity is used to rotate the beam in the longitudinal phase space to optimise the energy spread of the micro-bunched beam. A degrader can be used to reduce the injected beam current if necessary. The MEBT also contains multiple beam diagnostics devices to ensure the beam parameters are as expected before injection [11].

1.1.3. Main Ring

The Main Ring of the MedAustron accelerator complex is realised as synchrotron with a circumference of 77.65 m. Figure 1.3 provides an overview of the general structure of the Main Ring.

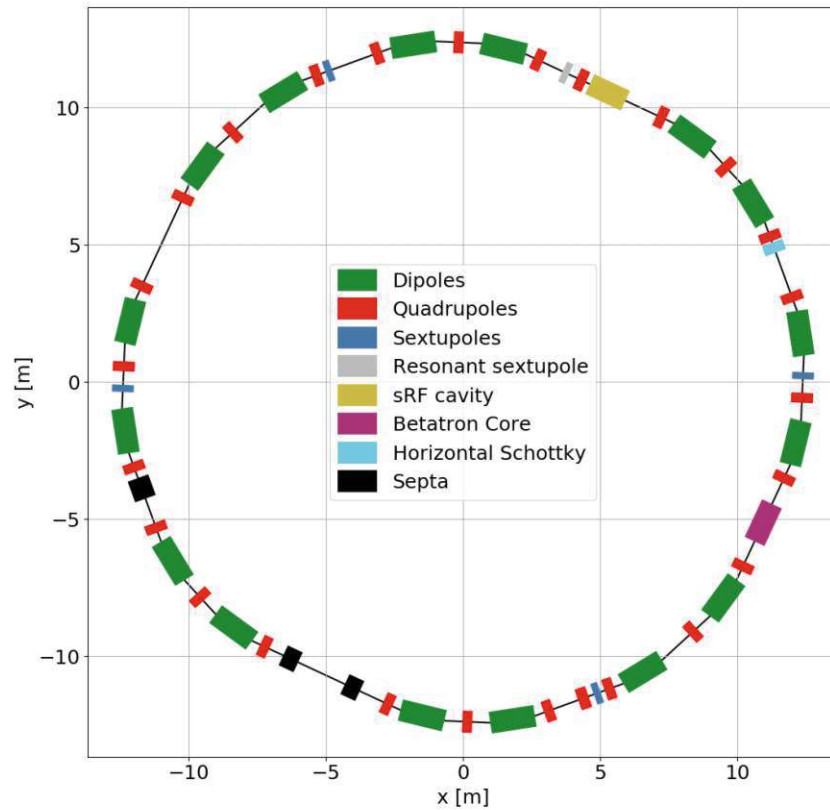


Figure 1.3.: The Main Ring of the MedAustron accelerator complex.

The ring is divided in 16 sections, each equipped with one dipole (green) to guide the beam on a circular trajectory. 24 quadrupole magnets (red), divided in two focusing and one defocusing family, as well as four chromatic sextupoles (blue) (two pairs for horizontal and vertical chromaticity correction, respectively) are installed to control the trajectory of the beam and its properties. An additional resonant sextupole (grey) is used to excite the resonance for extraction and is placed next to the Synchrotron Radio Frequency (RF) cavity (yellow) in one of the two dispersion-free sections of the ring. The betatron core (purple) is used in current operation to accelerate the beam into resonance for extraction, while the horizontal Schottky plates (cyan) are used for beam excitation for Radio

Frequency Knock Out (RFKO) extraction (see chapter 4). Three septa (black) are used for injection and extraction of the beam, namely (from left to right) the Electrostatic Extraction Septum (ESE), the Electrostatic Injection Septum (ESI) and the Magnetic Extraction Septum (MST). Additionally, ten horizontal and eight vertical corrector magnets (not drawn) can be used to correct the beam position in both planes to steer the beam [12].

Injection, capturing and acceleration

The beam is injected from the MEBT at 7 MeV/u into the Main Ring by using horizontal multi-turn injection. For this, the beam is injected in multiple turns by a collapse of the injection bump. This technique ensures that at each turn, a different part of the Main Ring acceptance is filled with particles and the available phase space is slowly 'painted' with particles [7].

After the injection, the beam is circulating as coasting beam and fills the whole synchrotron circumference. Prior to acceleration, the beam needs to be captured by the RF cavity by quasi-adiabatically ramping the cavity voltage. The beam is trapped in the RF bucket and therefore bunched. The longitudinal beam stability is ensured by the radial and phase correction loops of the Low Level RF system, which uses the signal of a shoebox pickup to correct for position or phase deviations of the beam by adjusting the frequency and phase of the RF cavity.

The bunched beam can now be accelerated from flatbottom to flattop with the frequency programme of the RF cavity. Characteristically for a synchrotron, the strengths of all magnet components must be ramped in synchronisation with the RF frequency to follow the changing kinetic energy of the particles. The optics of the Main Ring are changed from injection to extraction optics during the acceleration by changing the normalised strengths of the quadrupole and sextupole magnets. The acceleration is finished as soon as the particles have reached the energy requested by the user [12].

Extraction

As the main topic of this thesis is the slow extraction, the following provides a closer look on the details of the extraction process itself. The theoretical aspects of the extraction are discussed in section 2.3.

The preparation for the extraction starts at flattop, when the particles have already been accelerated to the target energy requested by the user. The horizontal lattice tune is set to the resonant tune of $Q_x = 5/3$. The circulating beam is kept off-momentum (the momentum offset with respect to the reference particle is between 2.3×10^{-3} for high-energy proton beams and all carbon beams, and 3.5×10^{-3} for the low-energy proton beams), so

that the tune shift originating from the non-zero chromaticity keeps the beam on a stable trajectory and no particles are prematurely extracted.

As first step, the radial and phase correction loops are turned off, resulting in the beam not being actively controlled anymore. A phase jump is performed to increase the momentum spread of the beam. The theory behind a phase jump is discussed in section 2.2.2.

After the phase jump, the RF cavity is turned off, leading to a de-bunching of the particles and after a few milliseconds, a coasting beam fills the whole synchrotron circumference⁴. The resonant sextupole is then ramped to its extraction setpoint to configure the resonance by opening up the V-shape in the Steinbach diagram (see section 2.3.1).

After the preparations are finished and the beam has stabilised with the desired configuration, the extraction process itself starts. The betatron core is ramped and accelerates the particles to slowly push the beam into the resonance by reducing the momentum offset of the beam. As soon as the particles hit the resonance, their oscillation amplitude increases, until they transit to the outside of the wire of the ESE. A strong electric field then deflects the particle into the extraction channel.

After a phase advance $\Delta\mu_x$ of approximately 51° ⁵, the extracted particle reaches the magnetic septum (MST), where the particle is further deflected by a magnetic field and leaves the Main Ring [12].

1.1.4. High Energy Beam Transfer Line (HEBT) and treatment rooms

The High Energy Beam Transfer Line (HEBT) connects the Main Ring to the treatment rooms. After the deflection from the MST, the extracted beam is guided through a dispersion suppressor where the dispersion is closed. A chopper (horizontal closed-orbit bump as magnetic chicane, created by four fast kicker magnets MKC) is used to cut away the head and the tail of the beam at the start and the end of the extraction, where the average extracted energy differs from the core of the beam, especially for betatron core extraction [13]. The chopper is also an important part of the safety system as it stops beam delivery in case of an interlock with a latency of below $100\ \mu\text{s}$ [14]. The system is designed to be fail-safe, as the power-off state is also the beam-off state [13]. The principle of the beam chopper is shown in Figure 1.4.

⁴For extraction with Empty Bucket Channelling (EBC) active, the RF cavity remains active during the whole extraction phase. However, the voltage is set to zero after phase jump, before it is ramped up again to create the empty bucket. This short time with $V_{\text{RF}} = 0$ still allows the de-bunching of the beam. More details about the theory of EBC can be found in section 2.4

⁵The ideal phase advance between the two septa would be 90° , which could not be reached during the commissioning of the Main Ring. The deviation of the phase advance from the ideal setpoint results in a reduction of the effective ESE kick strength by 22% [12].

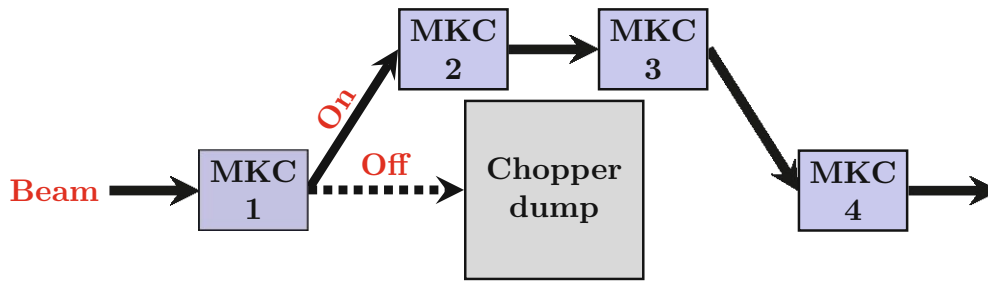


Figure 1.4.: Principle of the beam chopper (modified after [15]).

A phase shifter stepper is used to control the beam size in the treatment room in both planes by rotating the beam in the horizontal phase space and setting the vertical beta function to the desired value with a series of six quadrupoles [7, 13].

The beam is then guided to one of four irradiation rooms:

- **IR1** is the irradiation room dedicated to non-clinical research and is equipped with a fixed horizontal beam line.
- **IR2** is a clinical treatment room with both a horizontal (IR2H) and vertical (IR2V) fixed beam line, both focussing the beam at the same isocentre.
- **IR3** is also dedicated to clinical treatment, containing a fixed horizontal beam line only.
- **IR4** is proton gantry, allowing irradiation angles between -30° and $+180^\circ$. To properly transform the beam properties in the reference frame of the gantry, a rotator system is used to pre-rotate the beam in phase space to match the gantry rotation angle. This system is the first of a kind to be commissioned for particle therapy [16].

The beam is directed to the selected treatment room via one of the four switching dipoles. The treatment delivery itself is controlled by the Dose Delivery System (DDS), which uses magnetic PBS and active energy selection to irradiate the tumour based on the doses calculated by the treatment planning system, while closely monitoring the beam parameters [17].

1.2. The MedAustron control system

The components of the Main Ring are controlled by the MedAustron Control System (MACS). Each combination of relevant parameters, including particle type, beam energy, spill length, treatment room, and others, is uniquely characterised by a 16-bit hexadecimal number, which is called the cycle code. If a spill with a certain cycle code is requested by the user, the Cycle-Dependent Property (CDP) data associated with this cycle code is executed on the relevant system components.

The CDP data contains a general Timing Sequence (TSQ) as well as Setpoint Sequence (SSQ) or Single Setpoint (SSP) data for each component in the accelerator complex. For testing purposes in non-clinical use, a modified configuration can be loaded. For clinical use, the validated configuration is released onto the system and any modified data is removed.

The TSQ defines the timing of all events during the cycle. An example TSQ for a 10 seconds proton beam with 252.7 MeV is provided in Appendix A. The timing events most relevant for this thesis are:

- The whole spill is contained between *StartCycle* and *EndCycle*.
- The beam is injected in the Main Ring between *StartMultiturn* and *StopMultiturn*. The timing between the two events defines the opening time of the Electric Field Fast Deflector (EFE) and controls how many particles are injected into the Main Ring, as well as the emittance of the beam. Increasing the EFE opening timing increases the beam current in the Main Ring, but also blows up the horizontal emittance.
- The beginning of the acceleration of the beam in the Main Ring is defined by the timing event *StartAcceleration*. The acceleration to the final energy is finished at *PrepareExtraction*.
- *RFJump* marks the timing of the phase jump to increase the momentum spread of the beam.
- As part of the preparation for the extraction, the resonant sextupole needs to be ramped. This happens between *StartMXR* and *StopMXR*.
- After the circulating beam has been set up properly, the extraction itself starts at *StartExtraction*, which is the timing event that activates the betatron core, that pushes the beam in momentum space until *StopExtraction*.
- Although particles are extracted for the whole extraction period, the chopper at the beginning of the HEBT prohibits particles at the start and the end of the spill to

reach the treatment room. This is done to avoid irradiation with the head and the tail of the beam, which are extracted with slightly lower and higher average energies, respectively. The chopper opening in non-clinical workflow is controlled with the *StartChopper* and *StopChopper* timing events.

- *StopRFSynchrotron* marks the deactivation of the RF system of the Main Ring. For unbunched operation, the RF system can be turned off after the phase jump so that the beam can de-bunch. For bunched operation (or unbunched extraction with enabled empty bucket channelling), the RF system needs to stay active during the whole extraction phase, so the timing event needs to be moved after *StopExtraction*.
- Lastly, *StartHysteresis* starts the hysteresis curve, which prepares all magnets for the next cycle.

While the TSQ is globally valid for all components of the accelerator complex, there is an individual configuration for each component, where the magnet currents are defined for a specific event from the timing sequence or from the control system itself. If the current is constant for the whole cycle and does not need to be changed mid-spill, a SSP file is used. This is the case for only a few components of the Main Ring, for example the injection and extraction electrostatic septa.

For most components of the Main Ring, the current needs to change over time during the acceleration, which can be done via SSQ file. A SSQ file contains the magnet current at different points in time, relative to certain timing events. A typical SSQ time-current curve for a Main Ring quadrupole⁶ is plotted in Figure 1.5.

⁶The curve would look similar for most Main Ring magnets. One exception is the resonant sextupole, which stays at a current of 0 A until it is ramped to the final current between *StartMXR* and *StopMXR*.

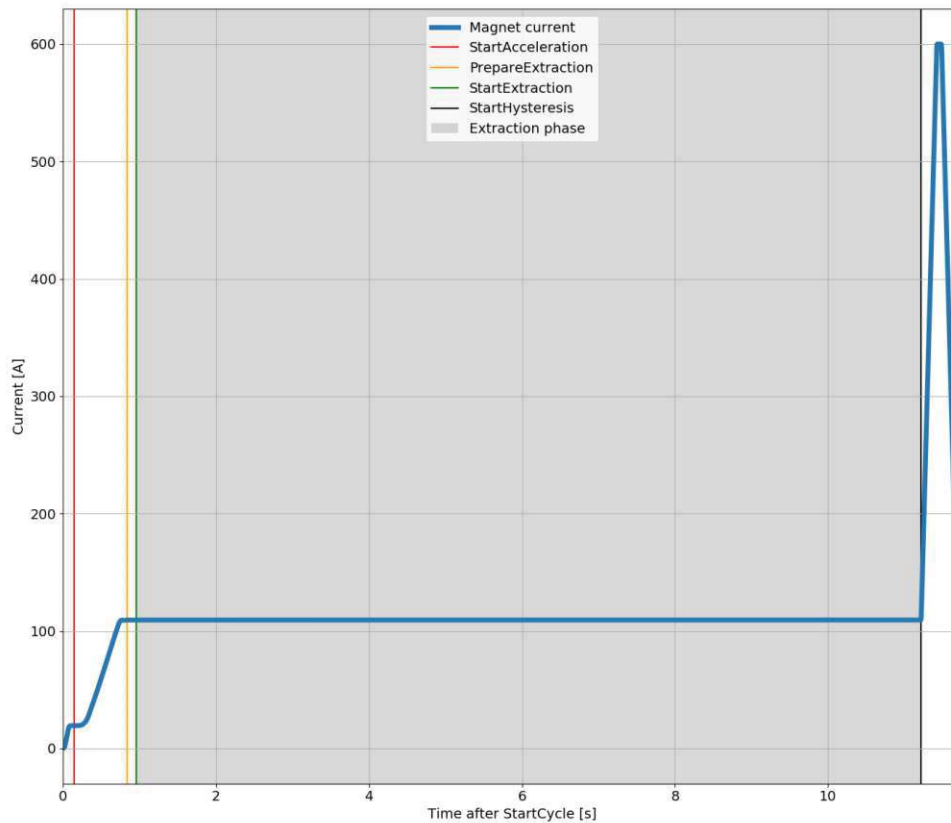


Figure 1.5.: A typical SSQ time-current curve for a Main Ring quadrupole magnet (proton beam, 252.7 MeV).

After the start of the cycle, the magnet current is ramped up to the flatbottom value for the injection and capture of the particles. At *StartAcceleration* (red line), the acceleration of the particles starts and the magnet current follows the momentum of the beam, until it reaches the flattop current when the acceleration is finished at *PrepareExtraction* (orange line). After the phase jump is performed and the resonant sextupole is activated, the extraction phase starts at *StartExtraction* (green). After a default extraction length of ten seconds, the extraction phase is stopped and the magnet hysteresis cycle is started at *StartHysteresis* (black). The magnet current is ramped up to the maximum value, followed by a ramp down to zero, at which point the magnet is ready for the next cycle⁷.

⁷This only applies to this example quadrupole. For other magnets, the hysteresis cycle may have other configurable minimum and maximum currents.

1.3. Scope of the thesis

While the current extraction method via betatron core is reliable, it has serious downsides, compared with alternative extraction techniques. The main disadvantages of betatron core extraction are evident in its limited compatibility or incompatibility with the following techniques or methods:

- **Multi Energy Extraction:** As extraction with the betatron core requires a coasting beam, the beam needs to be unbunched before the extraction starts by turning off the RF cavity. However, to change the energy of the beam via correction loops, an active RF cavity and a bunched beam is required. Therefore, it is impossible to change the beam energy during the spill⁸. If a different energy is requested, the beam has to be dumped and a new acceleration cycle has to be started.

The treatment plan for a typical tumour demands a variety of different energies, and the required dose for each energy layer is comparably low. That means that often only a fraction of the accelerated particles are needed for a certain energy layer, before the next energy is requested. As there are no possibilities to change the energy of the already accelerated beam mid-spill, most of the accelerated particles are not needed and are dumped. This 'waste' of particles also prolongs the treatment duration, as the preparation of a new cycle and the injection, capture and acceleration of a new beam takes up to several seconds of unnecessary 'dead time', in which the patient cannot be irradiated.

The possibility of modifying the beam energy during the spill enables the utilisation of a technique known as Multi Energy Extraction (MEE), which permits the extraction of multiple energies within a single spill. This results in a reduction in particle waste, consequently minimising the 'dead time'. While betatron core extraction is not compatible with MEE, there are alternative extraction methods which operate with a bunched beam and are thus capable of being used for MEE.

- **Fast intensity adaptation:** Another disadvantage of the present extraction method is that the reaction time of the betatron core is relatively long. Due to the high impedance of the component, fast current changes are not possible without significant delays. High particle doses extracted in a short time cannot be delivered via betatron core extraction.
- **Dynamic intensity control:** Due to the slow reaction of the betatron core, no feedback system can be implemented that adjusts the extracted intensity in a sub-

⁸In theory, it is possible to re-capture the beam after the first energy is extracted and change the beam energy. However, this re-capturing has proven to be prone to significant beam losses, which in reality makes this re-capturing process unpractical and uneconomical.

millisecond time scale based on the measured intensity in the treatment room via Dynamic Intensity Control (DIC).

- **Gated irradiation:** As switching the betatron core on or off is also relatively slow, the extraction cannot be started/stopped immediately. Therefore, gated irradiation of moving organs with betatron core extraction can only be realised using the chopper, which would throw away extracted particles, as the extraction is not stopped when the chopper is closed.

The implementation of alternative extraction techniques such as RFKO makes it possible to overcome these limitations [18–20] and could enhance the flexibility of the treatment process and extend the possible field of use of the accelerator [21].

The scope of this thesis is to investigate these alternative extraction methods and their potential advantages in tailoring beam parameters for NCR applications or for reducing treatment time. The study involves both simulations and measurements, which contribute to deepen the understanding of the complex beam dynamics in play and illustrate the potential feasibility of implementation at MedAustron and other clinical facilities.

The focus of this thesis is predominantly on RFKO as a promising extraction technique for future development at MedAustron. The simulation work to understand the principles of RFKO and to optimise the parameter settings in order to maximise the quality of the extraction is discussed as well as the measurement setup and results at MedAustron, including considerations about the excitation of the beam.

In addition to RFKO, the extraction techniques Constant Optics Slow Extraction (COSE) and Phase Displacement Extraction (PDE) were studied and their limitations and opportunities are discussed.

A crucial quality feature for clinical accelerators are low intensity ripples of the extracted particle flux. This thesis discusses the origin of these ripples and possible mitigation methods as well as the impact of the different extraction techniques.

Finally, this thesis aims to compare the different extraction methods and highlight their respective advantages and disadvantages. Their compatibility with advanced irradiation techniques to maximise the effectivity and the performance of the treatment process is discussed as well as the possibilities to further improve the quality of the treatment by delivering the required dose rate with as few fluctuations as possible.

While the mentioned extraction techniques have been studied previously, this thesis presents, for the first time, a comprehensive analysis of RFKO, PDE, and COSE at a single accelerator, enabling a direct comparison through both simulation and measurement in a clinical facility. The connection of these extraction techniques with a detailed analysis of the ripple structure of the extracted beam offers new insights into the complex beam dynamics during slow extraction.

2. Selected topics of accelerator physics

This chapter discusses the theoretical aspects of accelerator physics that are relevant for this work. A comprehensive study of accelerator physics can be found in [22], [23] or [24].

2.1. Transverse beam dynamics

This section provides an introduction to the transverse dynamics of a beam in a synchrotron, taking into account the different magnetic components of the lattice and the properties of the beam.

2.1.1. Motion of the reference particle

The circular movement of a relativistic particle with charge q , mass m , velocity \mathbf{v} and relativistic Lorentz factor γ_r in a magnetic dipole field \mathbf{B} is defined by the equilibrium of the centrifugal force and the Lorentz force.

$$\begin{aligned}
 \mathbf{F}_{\text{centrifugal}} + \mathbf{F}_{\text{Lorentz}} &= 0 \\
 m\gamma_r v^2 \boldsymbol{\kappa} + q[\mathbf{v} \times \mathbf{B}] &= 0
 \end{aligned} \tag{2.1}$$

$\boldsymbol{\kappa} = (\kappa_x, \kappa_y, \kappa_z)$ is the local vector of curvature, which is the inverse of the radius of the local radius of curvature in the three planes.

Assuming negligible transverse components of the particle velocity $\mathbf{v} = (v_x, v_y, v_z) \approx (0, 0, v)$ and purely transverse magnetic fields $\mathbf{B} = (B_x, B_y, 0)$, equation 2.1 can be further simplified.

$$\begin{aligned}
 m\gamma_r v^2 \kappa_{x,y} + qv \cdot (\mp B_{y,x}) &= 0 \\
 p\kappa_{x,y} &= \pm qB_{y,x},
 \end{aligned} \tag{2.2}$$

where $p = m\gamma_r v$ is the relativistic momentum of the particle.

Substituting the radius of curvature $\rho_0 = 1/\kappa$, equation 2.2 can be written as follows:

$$|B\rho_0| = \frac{p}{q} = \frac{\beta_r E}{cq}, \tag{2.3}$$

In 2.3, $E = \gamma_r mc^2$ denotes the energy of the particle, while c is the speed of light and $\beta_r = v/c$ is the relativistic beta function.

As for a synchrotron, the radius of curvature is constant and defined by the geometry of the lattice, the magnetic dipole field B needs to be ramped synchronously with the particle momentum p and energy E , so that the particles remain on a circular path with the radius ρ_0 .

In an ideal accelerator lattice, an on-momentum particle 2.3 passing through the magnets on the optical axis is termed the *reference particle*, and its path is referred to as the *reference trajectory*. This reference particle remains unaffected by higher-order magnetic field components, as the magnetic centre of each magnet is aligned with the trajectory of the particle through the magnet.

To analyse the motion of a particle that deviates from the reference trajectory, it is beneficial to use an orthogonal coordinate system that follows along the reference trajectory. The *Frenet-Serret* coordinate system, which is shown in Figure 2.1, directly measures the displacement with respect to the reference particle in horizontal, vertical and longitudinal plane.

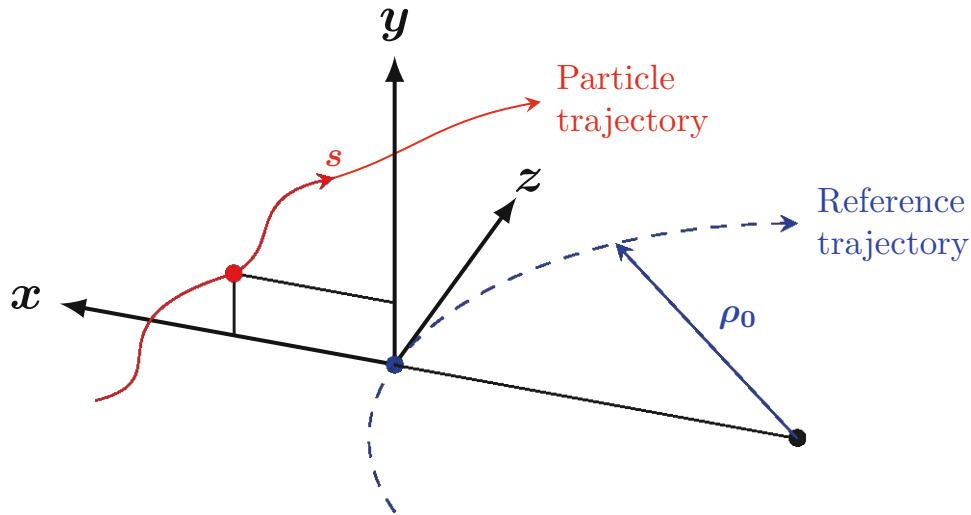


Figure 2.1.: The Frenet-Serret coordinate system (modified after [22]).

2.1.2. Equation of motion

If a particle deviates from the reference trajectory defined by equation 2.3 in either horizontal or vertical plane, the particle will start to oscillate. The equation of motion of these betatron oscillations in the Frenet-Serret coordinate system will be derived in this section. Based on the definition of the curvature, the equation of motion 2.4 can be derived.

$$u'' = -(1 + \kappa_0 u)\kappa + \kappa_0, \quad (2.4)$$

with $u = x$ or y being the deviation of the particle from the reference trajectory in the horizontal or vertical plane, respectively. κ_0 is the local curvature of the trajectory of the reference particle defined by the dipole field, while κ describes the curvature of the trajectory of an arbitrary particle.

In the horizontal plane, we set $u = x$, $\kappa_0 = \kappa_{0,x}$ and $\kappa = \kappa_x$. For the curvature κ_x , the multipole field expansion 2.5 can be used, taking into account only the terms up to quadratic order.

$$\kappa_x = \frac{1}{1 + \delta} \left(\underbrace{\kappa_{0,x}}_{\text{dipole}} + \underbrace{k_1 x}_{\text{quadrupole}} + \underbrace{\frac{1}{2} k_2 x^2}_{\text{sextupole}} + \mathcal{O}(x^3) \right) \quad (2.5)$$

k_1 and k_2 are the normalised strengths of the quadrupole and the sextupole, respectively. $\delta = \Delta p/p_0$ denotes the momentum deviation from the momentum p_0 of the reference particle, as $p = p_0 + \Delta p = p_0(1 + \delta)$.

Including the Taylor expansion of $1/(1 + \delta)$ and combining equations 2.4 and 2.5, an inhomogeneous differential equation of second order for the horizontal deviation x from the reference trajectory 2.6 can be found. All terms above second order in x or δ are neglected.

$$x'' + (k_1 + \kappa_{0,x}^2)x = \kappa_{0,x}(\delta - \delta^2) + (k_1 + \kappa_{0,x}^2)x\delta - \frac{1}{2}k_2x^2 - \kappa_0k_1x^2 + \mathcal{O}(x^3) \quad (2.6)$$

In the vertical plane, the equation of motion can be derived analogously by using the multipole field expansion 2.7 in vertical plane. As no bending in the vertical plane (i.e. no vertical dipoles) are present at the MedAustron synchrotron, the dipole term $\kappa_{0,y}$ is zero for the vertical plane.

$$\kappa_y = \left(\underbrace{0}_{\text{dipole}} + \underbrace{k_1 y}_{\text{quadrupole}} + \underbrace{k_2 xy}_{\text{sextupole}} + \mathcal{O}(x^3) \right) \quad (2.7)$$

Using equations 2.4 and 2.7 for $u = y$ yields in a differential equation for the motion in the vertical plane.

$$y'' - k_1 y = -k_1 y \delta + k_2 xy + \mathcal{O}(x^3) \quad (2.8)$$

The equations of motion can also be derived from the Lagrangian and the Hamiltonian of the system, as shown in [22].

Homogeneous equation

To solve the homogeneous equation for both the horizontal and the vertical plane in first order, the right-hand sides of equations 2.6 and 2.8 are set to zero, resulting in equations 2.9, which describe the motion of an on-momentum particle in both planes.

$$\begin{aligned} x'' + (k_1 + \kappa_{0,x}^2)x &= 0 \\ y'' - k_1y &= 0 \end{aligned} \quad (2.9)$$

Under the assumption of a hard edge model, both k and κ_0 are piece-wise constant (i.e. edge effects and position-dependent fields at the start and the end of the magnets are ignored or assumed to be piece-wise constant), both equations can be summarised into one general equation of motion 2.10.

$$u'' + Ku = 0 \text{ with } K = \begin{cases} (k_1 + \kappa_{0,x}^2) & \text{for horizontal plane } (u = x) \\ -k_1 & \text{for vertical plane } (u = y) \end{cases} \quad (2.10)$$

The solution of the differential equation 2.10 is any arbitrary linear combination of the two principal solutions $C(z)$ and $S(z)$ given in equation 2.11.

$$\begin{aligned} C(z) &= \begin{cases} \cos(\sqrt{K}z) & \text{for } K > 0 \\ \cosh(\sqrt{|K|}z) & \text{for } K < 0 \end{cases} \\ S(z) &= \begin{cases} \frac{1}{\sqrt{K}} \sin(\sqrt{K}z) & \text{for } K > 0 \\ \frac{1}{\sqrt{|K|}} \sinh(\sqrt{|K|}z) & \text{for } K < 0 \end{cases} \end{aligned} \quad (2.11)$$

Therefore, the general solution of the differential equation 2.10 can be written with the principal solutions 2.11.

$$\begin{aligned} u(z) &= C(z)u_0 + S(z)u'_0 \\ u'(z) &= C'(z)u_0 + S'(z)u'_0 \end{aligned} \quad (2.12)$$

u_0 and u'_0 are arbitrary initial parameters of the particle trajectory. Equations 2.12 can also be written in a compact way as matrix equation 2.13.

$$\begin{bmatrix} u(z) \\ u'(z) \end{bmatrix} = \begin{bmatrix} C(z) & S(z) \\ C'(z) & S'(z) \end{bmatrix} \begin{bmatrix} u_0 \\ u'_0 \end{bmatrix} = M(z) \cdot \begin{bmatrix} u_0 \\ u'_0 \end{bmatrix} \quad (2.13)$$

$M(z)$ is the transfer matrix for the given magnet setup with the magnetic field components defined in equation 2.10. The final coordinates of the particles with the initial parameters (u_0, u'_0) after being affected by a magnetic field with constant dipole and quadrupole field components over a distance l_0 can be computed by multiplying the initial conditions with the transfer matrix $M(l_0)$.

If n elements with lengths Δs_n and piece-wise constant field components are combined, the corresponding transfer matrices M_n can be multiplied to calculate the total transfer matrix M_{total} from the starting point s_0 to the position $s_0 + l$, with $l = \sum_n \Delta s_n$.

$$M_{\text{total}}(s_0 \rightarrow s_0 + l) = M_n(\Delta s_n) \cdot M_{n-1}(\Delta s_{n-1}) \cdot \dots \cdot M_2(\Delta s_2) \cdot M_1(\Delta s_1) \quad (2.14)$$

Equation 2.14 allows the tracking of particles through a lattice of magnetic components and is the base for the tracking tools discussed in chapter 3.1.

The general form of the transfer matrix 2.13 can be simplified for special magnetic components of length l with given values for $K = (k_1 + \kappa_{0,x}^2)$. Table 2.1 summarises the transfer matrices for the different magnets.

Component	Field components	Transfer matrix $M(s_0 \rightarrow s_0 + l)$
Drift space	$K = 0$	$\begin{bmatrix} 1 & l \\ 0 & 1 \end{bmatrix}$
Dipole (sector magnet)	$\kappa_{0,x} \neq 0$ $k_1 = 0$	$\begin{bmatrix} \cos(l\kappa_{0,x}) & \rho_0 \sin(l\kappa_{0,x}) \\ -\kappa_{0,x} \sin(l\kappa_{0,x}) & \cos(l\kappa_{0,x}) \end{bmatrix}$
Focusing quadrupole	$\kappa_{0,x} = 0$ $k_1 > 0$	$\begin{bmatrix} \cos(l\sqrt{k_1}) & \frac{1}{\sqrt{k_1}} \sin(l\sqrt{k_1}) \\ -\sqrt{k_1} \sin(l\sqrt{k_1}) & \cos(l\sqrt{k_1}) \end{bmatrix}$
Defocusing quadrupole	$\kappa_{0,x} = 0$ $k_1 < 0$	$\begin{bmatrix} \cosh(l\sqrt{ k_1 }) & \frac{1}{\sqrt{ k_1 }} \sinh(l\sqrt{ k_1 }) \\ \sqrt{ k_1 } \sinh(l\sqrt{ k_1 }) & \cosh(l\sqrt{ k_1 }) \end{bmatrix}$
Quadrupole (thin lens)	$\kappa_{0,x} = 0, k_1 \neq 0$ $l \rightarrow 0$	$\begin{bmatrix} 1 & l \\ -k_1 l & 1 \end{bmatrix}$

Table 2.1.: Transfer matrices for special magnets.

Inhomogeneous equation

A general solution for the equations of motion 2.6 and 2.8 needs to consider the inhomogeneous right hand side of the equation. Neglecting all terms of equation 2.6 that are higher than linear order in x and δ , the horizontal equation of motion can be simplified to equation 2.15.

$$x'' + (k_1 + \kappa_{0,x}^2)x = \kappa_{0,x}\delta \quad (2.15)$$

The right hand side of equation 2.15 describes the deviation from the reference trajectory for a particle with a relative momentum offset δ . The deviation originates in the lattice dipoles, which induce a chromatic error for off-momentum particles.

The solution of equation 2.15 can be found by using the Green's function method and is a linear combination of the general solution of the homogeneous equation (as derived in the last section) and a particular solution of the inhomogeneous equation.

$$\begin{aligned} x(z) &= aC_x(z) + bS_x(z) + \delta D_x(z) \\ x'(z) &= aC'_x(z) + bS'_x(z) + \delta D'_x(z) \end{aligned} \quad (2.16)$$

a and b are arbitrary constants that can be determined via the initial conditions. The *dispersion function* $D(z)$ can be determined using the Green's function method.

$$D_x(z) = \int_0^z \kappa_{0,x} [S_x(z)C_x(\tilde{z}) - C_x(z)S_x(\tilde{z})] d\tilde{z} \quad (2.17)$$

With this solution 2.16 for the inhomogeneous equation of motion, which takes into account the trajectory change for off-momentum particles in dipoles in first-order approximation, the 2D matrix formalism 2.13 can be extended to a 3D matrix by adding the relative energy offset δ to the coordinate vector, assuming it remains constant throughout the lattice.

$$\begin{bmatrix} u(z) \\ u'(z) \\ \delta \end{bmatrix} = \begin{bmatrix} C(z) & S(z) & D(z) \\ C'(z) & S'(z) & D'(z) \\ 0 & 0 & 1 \end{bmatrix} \begin{bmatrix} u_0 \\ u'_0 \\ \delta \end{bmatrix} \quad (2.18)$$

2.1.3. Phase space concept and Twiss functions

The formalism developed in the previous section describes the trajectory of a single particle through an arbitrary beam line. Another rational approach is to establish a representation of the whole beam in the six-dimensional phase space $(x, x', y, y', s, \delta)$. s represents the longitudinal coordinate along the individual particle trajectory, while $\delta = \Delta p/p_0$ is the relative momentum offset from the ideal momentum of the reference particle p_0 .

With this phase space concept, the general homogeneous equation of motion 2.10 can be solved by using equation 2.19 with an z -depending amplitude $\beta(z)$ and phase $\psi(z)$, which resembles the solution of a harmonic oscillator.

$$u(z) = \sqrt{\epsilon} \sqrt{\beta(z)} \cos(\psi(z) - \psi_0) \quad (2.19)$$

By inserting 2.19 in the differential equation 2.10, two conditions can be derived.

$$\beta' \psi' + \beta \psi'' = 0 \quad (2.20)$$

$$\frac{1}{2} \left(\beta \beta'' - \frac{1}{2} \beta'^2 \right) - \beta^2 \psi'^2 + \beta^2 K = 0 \quad (2.21)$$

The first condition 2.20 can be fulfilled by setting $\beta \psi'$ to a constant value, which can be set to 1. This results in an equation for the phase $\psi(z)$.

$$\psi(z) = \int_0^z \frac{1}{\beta(\tilde{z})} d\tilde{z} + \psi_0 \quad (2.22)$$

The phase ψ of the oscillation at a given position z is therefore defined by the integral of the inverse beta functions from the start of the beam line until z .

The second condition 2.21 can be re-written as

$$\beta'' + 2K\beta - 2\gamma = 0, \quad (2.23)$$

with introducing the new functions $\alpha := -\frac{1}{2}\beta'$ and $\gamma := \frac{1+\alpha^2}{\beta}$.

Combining this definition with the equation 2.19, the *Courant-Snyder invariant* can be derived.

$$\gamma u^2 + 2\alpha u u' + \beta u'^2 = \epsilon \quad (2.24)$$

Equation 2.24 describes an ellipse in phase space (u, u') with the area $\pi\epsilon$ and size, shape and orientation defined by the functions α , β and γ , which are called the *Twiss* or *betatron functions*. The *emittance* ϵ is therefore a measure for the area occupied by the beam particles in phase space, divided by π .

An exemplary phase space ellipse defined by the Twiss functions is shown in Figure 2.2.

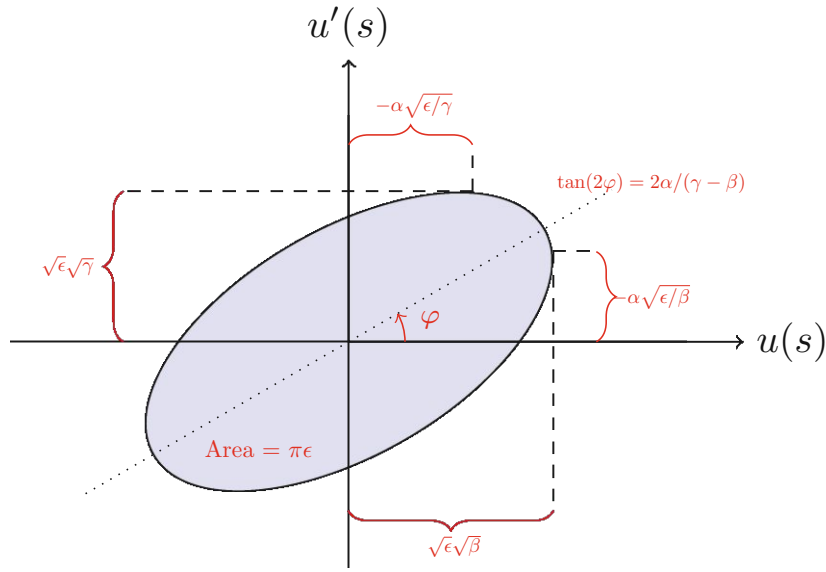


Figure 2.2.: Phase space ellipse defined by the Twiss functions.

It can be beneficial for some calculations to replace the real particle coordinates u and u' with normalised coordinates U and U' , according to equation 2.25.

$$\begin{aligned} U &= \frac{1}{\sqrt{\beta}}u \\ U' &= \sqrt{\beta}u' + \frac{\alpha}{\sqrt{\beta}}u \end{aligned} \quad (2.25)$$

Both U and U' are in units of $[m^{1/2}]$ and the phase space ellipse is reduced to a circle with area ϵ when plotted in normalised phase space, as the Courant Snyder invariant 2.24 can be written as $U^2 + U'^2 = \epsilon$.

The shape of the ellipse defined in equation 2.24 changes throughout the beam line, as the Twiss functions vary. However, the area $\pi\epsilon$ remains always constant, as the beam emittance is an invariant of the particle motion as a consequence of Liouville's theorem. More precisely, the normalised emittance $\epsilon_n = \beta_r\gamma_r\epsilon$ with the relativistic beta and gamma functions is an invariant of the particle motion, as acceleration of the particles leads to a shrinking of the emittance due to adiabatic damping.

2.1.4. Tune and chromaticity

Two important accelerator lattice parameters that play an important role during the extraction process are the tune and the chromaticity.

The *betatron tune* (or *lattice tune*) Q describes the number of betatron oscillations per one revolution in the synchrotron and can be computed for the horizontal and vertical plane using equation 2.26.

$$Q_{x,y} = \frac{1}{2\pi} \oint \frac{1}{\beta_{x,y}(s)} ds \quad (2.26)$$

By comparing equation 2.26 with equation 2.22, the tune is the accumulated particle phase after one full revolution, divided by 2π . The beta function and thus (in first approximation) the quadrupoles determine the tune.

For instance, a horizontal tune of $Q_x = 1.666$ indicates that a particle performs 1.666 horizontal betatron oscillations for every revolution in the synchrotron. After three revolutions, the particles have completed five full oscillations and have returned to their original phase space position.

The *chromaticity* Q' describes how the tune changes with the momentum of the particles and is the ratio of the tune shift ΔQ and the relative momentum offset $\Delta p/p$.

$$\Delta Q_{x,y} = Q'_{x,y} \frac{\Delta p}{p} \quad (2.27)$$

The tune shift ΔQ originates from the momentum-dependence of the focal length of the quadrupoles (equivalent to the chromatic aberration in optical lenses) and can be mathematically derived by including higher-order perturbation terms in the equation of motion. The chromaticity can be controlled by sextupoles in the dispersive regions of the synchrotron.

For an off-momentum particle, a particle tune Q_{particle} can be defined in equation 2.28 by adding the lattice tune (tune for an on-momentum particle) and the tune shift resulting from non-zero chromaticity. For particles with non-zero amplitudes, amplitude-dependent detuning occurs due to non-linear effects, introducing another tune shift term $\Delta Q_{\text{amplitude}}$ [24, 25]. This term is of particular significance in the context of RFKO extraction, where high particle amplitudes can be attained.

$$Q_{\text{particle}} = Q_{\text{lattice}} + \Delta Q + \Delta Q_{\text{amplitude}} = Q_{\text{lattice}} + Q' \frac{\Delta p}{p} + \Delta Q_{\text{amplitude}} \quad (2.28)$$

2.2. Longitudinal beam dynamics

As the details of the acceleration process and related concepts are not critical for this thesis, only very few relevant topics are discussed in this chapter. For a detailed discussion, the reader is referred to accelerator physics books such as [22] and [24].

In a synchrotron, the acceleration or deceleration of the beam requires an electric field in the direction of motion. This longitudinal kick is given by an RF cavity, powered with a voltage that follows $V_{\text{RF}} = \hat{V} \sin(t\omega_0 + \phi_s)$. \hat{V} is the amplitude of the voltage, ϕ_s the synchronous phase and ω_0 the angular cavity frequency. ω_0 needs to be tuned to a harmonic h of the angular revolution frequency ω_{rev} of the particles with $\omega_0 = h\omega_{\text{rev}}$.

If a particle with the charge e passes through the cavity in synchronisation with the RF voltage at a certain phase ϕ_s , its kinetic energy is increased every turn by $\Delta E = e\hat{V} \sin \phi_s$. Similar to the transverse plane, the particle motion can also be viewed in phase space, which is constructed by the phase ϕ and the relative momentum offset $\delta = \Delta p/p_0$. While an ideal synchronous particle with $\phi = \phi_s$ and $\delta = 0$ is per design accelerated by the RF voltage, any particles with small deviations in momentum or phase oscillate around the synchronous reference particle.

A non-zero momentum offset $\delta \neq 0$ results also in the change of other beam trajectory parameters [26]:

- The orbit length L changes due to dispersive effects in the dipoles, is quantified with the **momentum compaction factor** $\alpha_c = \frac{dL}{L} \left(\frac{dp}{p} \right)^{-1}$.
At MedAustron, $\alpha_c = 0.2521$, which means that a relative momentum change of 1×10^{-3} results in an orbit length change of 2.5×10^{-4} or 19.6 mm.
- As the orbit length and the speed of the particle change, also the revolution frequency f_{rev} is altered, resulting in the definition of the **phase slip factor** $\eta = \frac{df_{\text{rev}}}{f_{\text{rev}}} \left(\frac{dp}{p} \right)^{-1}$.
The phase slip factor can be calculated from the momentum compaction factor α_c and the relativistic Lorentz factor γ_r , according to equation 2.29.

$$\eta = \frac{1}{\gamma_r^2} - \alpha_c \quad (2.29)$$

η can be positive (below transition with $\gamma_r^{-2} > \alpha_c$) when the increase in speed for higher momenta dominates or negative (above transition with $\gamma_r^{-2} < \alpha_c$) when the prolonged orbit for higher momenta dominates.

The transition energy is defined as $\gamma_{\text{tr}} = \alpha_c^{-1/2}$, resulting in $\eta = 0$, so a momentum change does not impact the revolution frequency as the speed increase and the orbit length difference cancel out each other.

At MedAustron, $\gamma_{\text{tr}} = 1.9915$, which means that the synchrotron is operated below

transition for all available energies, as γ_r is between 1.0665 and 1.269 for protons and between 1.1289 and 1.4325 for carbon ions.

2.2.1. Stationary and moving buckets

The oscillations of the asynchronous particles around the reference particle are illustrated in Figure 2.3a.

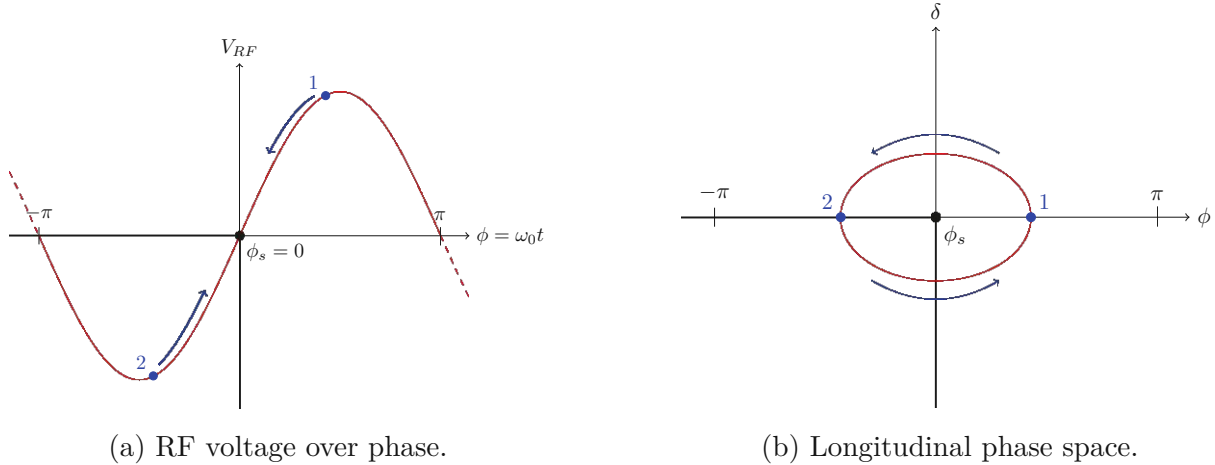


Figure 2.3.: Phase oscillations without acceleration ($\phi_s = 0$).

For $\phi_s = 0$, there is no net acceleration, as the voltage is always negligible when the synchronous reference particle reaches the cavity. The synchronous particle is thus located at the zero crossing of the voltage, i.e. $\phi_s = 0$. If a particle arrives at the cavity later than the synchronous particle ($\phi > \phi_s$, point 1), it is affected by a positive voltage, resulting in an acceleration of the particle, moving it towards ϕ_s . Eventually, the particle arrives earlier than the reference particle ($\phi < \phi_s$, point 2) and is slowed down by the negative cavity voltage. Therefore all asynchronous particles are starting to oscillate around the synchronous particle in a motion called **synchrotron oscillation**.

Viewing these synchrotron oscillations in phase space (ϕ, δ), as shown in Figure 2.3b, reveals that the particles move around the synchronous particle in closed anti-clockwise ellipses, as a delayed particle ($\phi > 0$) is accelerated ($\delta > 0$), thus arrives earlier ($\phi < 0$) and is decelerated ($\delta < 0$).

It is shown in [24] that the longitudinal motion of such an asynchronous particle with charge e , velocity $c\beta_r$ and energy E in an electric RF field of amplitude V , harmonic

number h and frequency ω_0 can be described with the Hamiltonian 2.30.

$$H = \frac{1}{2}h\omega_0\eta\delta^2 + \frac{\omega_0 eV}{2\pi\beta_r^2 E} [\cos\phi - \cos\phi_s + (\phi - \phi_s)\sin\phi_s] \quad (2.30)$$

The contour plot of the Hamiltonian 2.30 for $\phi_s = 0$ is shown in Figure 2.4.

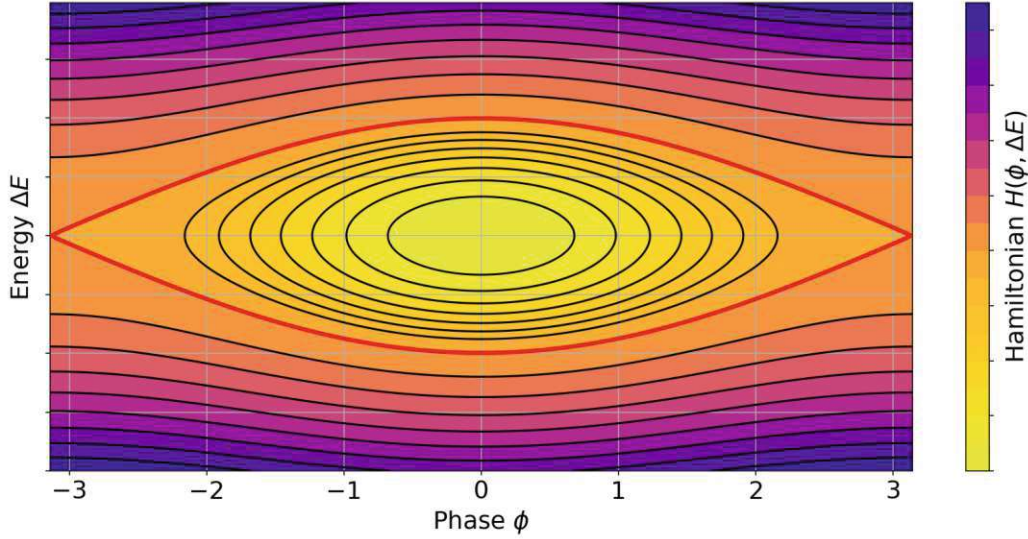


Figure 2.4.: Contour plot of the longitudinal Hamiltonian 2.30 at $\phi_s = 0$ (stationary bucket).

For $\phi_s \neq 0$, the symmetry of the Hamiltonian 2.30 with respect to the phase ϕ is lost. This can be understood by considering that by setting a non-zero synchronous phase, the working point is moved from the zero crossing of the voltage in Figure 2.3a, leading to asymmetries of the resulting oscillations. For synchrotrons, the synchronous phase for the accelerating bucket needs to be proportional to the change of the magnetic field \dot{B} during the acceleration process [26].

$$\phi_s = \arcsin\left(2\pi\rho R\frac{\dot{B}}{V}\right) \quad (2.31)$$

The contour plot of the Hamiltonian 2.30 for an exemplary accelerating bucket with a synchronous phase of 20° is shown in Figure 2.5.

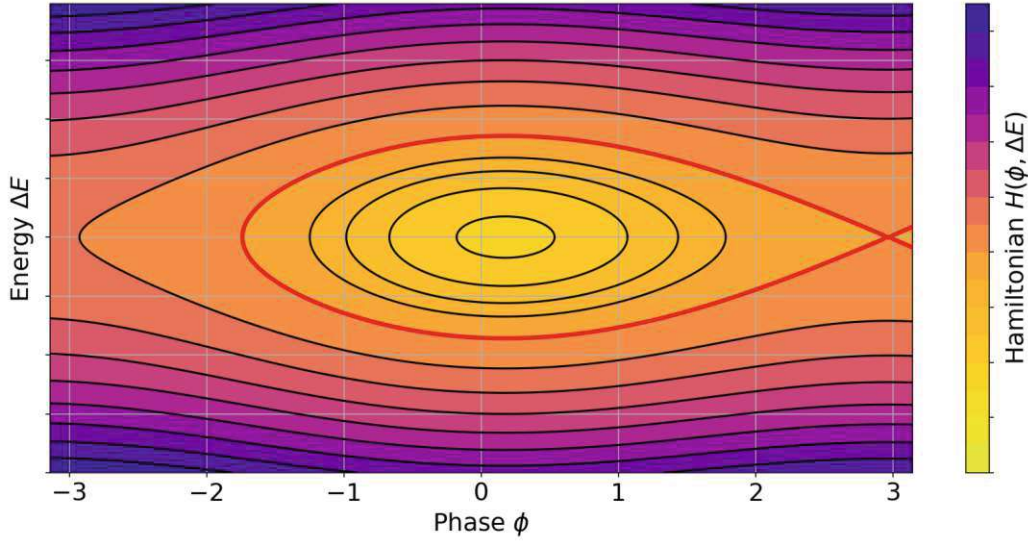


Figure 2.5.: Contour plot of the longitudinal Hamiltonian 2.30 at $\phi_s = 10^\circ$ (accelerating bucket).

Contour plot 2.5 shows that the longitudinal phase space is divided in a stable and an unstable region. For low momentum offsets, the particles oscillate around the synchronous particle in elliptical trajectories. This stable region with bound oscillations forms a bucket, which can be populated by particles during capturing and subsequent acceleration and extraction. As these particles are contained inside the bucket, this setup of the RF cavity results in a bunched beam. For $\phi_s = 0$, the bucket is stationary and the particle momentum remains unchanged. $\phi_s \neq 0$ results in a moving bucket, which can be either accelerating ($\phi_s > 0$) or decelerating ($\phi_s < 0$)¹ [7].

For higher momentum offsets, these ellipses break open into hyperbolas and the oscillations become unbound. The separatrix (red line in Figure 2.4) that separates the regions with bound and unbound oscillations can be mathematically described with equation 2.32.

$$\delta^2 + \frac{eV}{\pi\beta_r^2 E h \eta} [\cos \phi + \cos \phi_s - (\pi - \phi - \phi_s) \sin \phi_s] = 0 \quad (2.32)$$

The proportions of the stationary bucket can be quantified with the bucket area A_B 2.33, height δ_B 2.34 (which is equivalent to the momentum acceptance of the bucket) and length

¹This is true only for operation below transition. For energies above the transition energy, a bucket with $\phi_s > 0$ is decelerating and with $\phi_s < 0$ accelerating.

ϕ_B 2.35.

$$\text{Bucket area} = A_B = 16 \left(\frac{eV}{2\pi\beta_r^2 E h |\eta|} \right)^{\frac{1}{2}} \quad (2.33)$$

$$\text{Bucket height} = \delta_B = 2 \left(\frac{eV}{2\pi\beta_r^2 E h |\eta|} \right)^{\frac{1}{2}} \quad (2.34)$$

$$\text{Bucket length} = \phi_B = 2\pi \quad (2.35)$$

The size of moving buckets is reduced compared to the stationary case. Mathematically, the area and the height need to be multiplied with a dedicated factor that depends on the synchronous phase and can be found in tables [27]. The bucket length is also reduced to $|\pi - \phi_s - \phi_u|$, with ϕ_u satisfying equation 2.36.

$$\cos \phi_u + \phi_u \sin \phi_s = -\cos \phi_s + (\pi - \phi_s) \sin \phi_s \quad (2.36)$$

If the RF cavity remains operating during extraction, the beam is extracted in bunched mode. If on the other hand the RF voltage is turned off after acceleration, the particles start to de-bunch and fill the whole circumference of the synchrotron. This results in a coasting beam and unbunched extraction.

2.2.2. Phase Jump

Another relevant longitudinal beam manipulation performed in the MedAustron synchrotron is referred to as phase jump, which is used to increase the momentum spread of the beam prior to extraction. This enables a faster driving of the particles into resonance for momentum-based extraction techniques like betatron core extraction. Additionally, the momentum distribution can be smoothed by performing a phase jump, turning an initially Gaussian into a approximately uniform distribution.

The typical process of a phase jump is outlined in Figure 2.6.

After acceleration, the bunch is matched to a stationary bucket with $\phi_s = 0$ (subplot a). When the phase jump is performed, the synchronous phase is quickly changed to $\phi_s = \pi^2$, displacing the stationary bucket. The bunch is now no longer centred at the stable fixed point, but located on the unstable fixed point of the separatrix (subplot b). The particles are following the separatrix, stretching out the bunch ellipse (subplot c). After a few hundreds of nanoseconds, the phase of the RF voltage is set back to $\phi_s = 0$, returning to the initial stationary bucket (subplot d). The beam is now no longer matched to the bucket and starts rotating and filamenting. The RF voltage is then turned off as soon as

²In practice, this is done by inverting the voltage of the RF cavity.

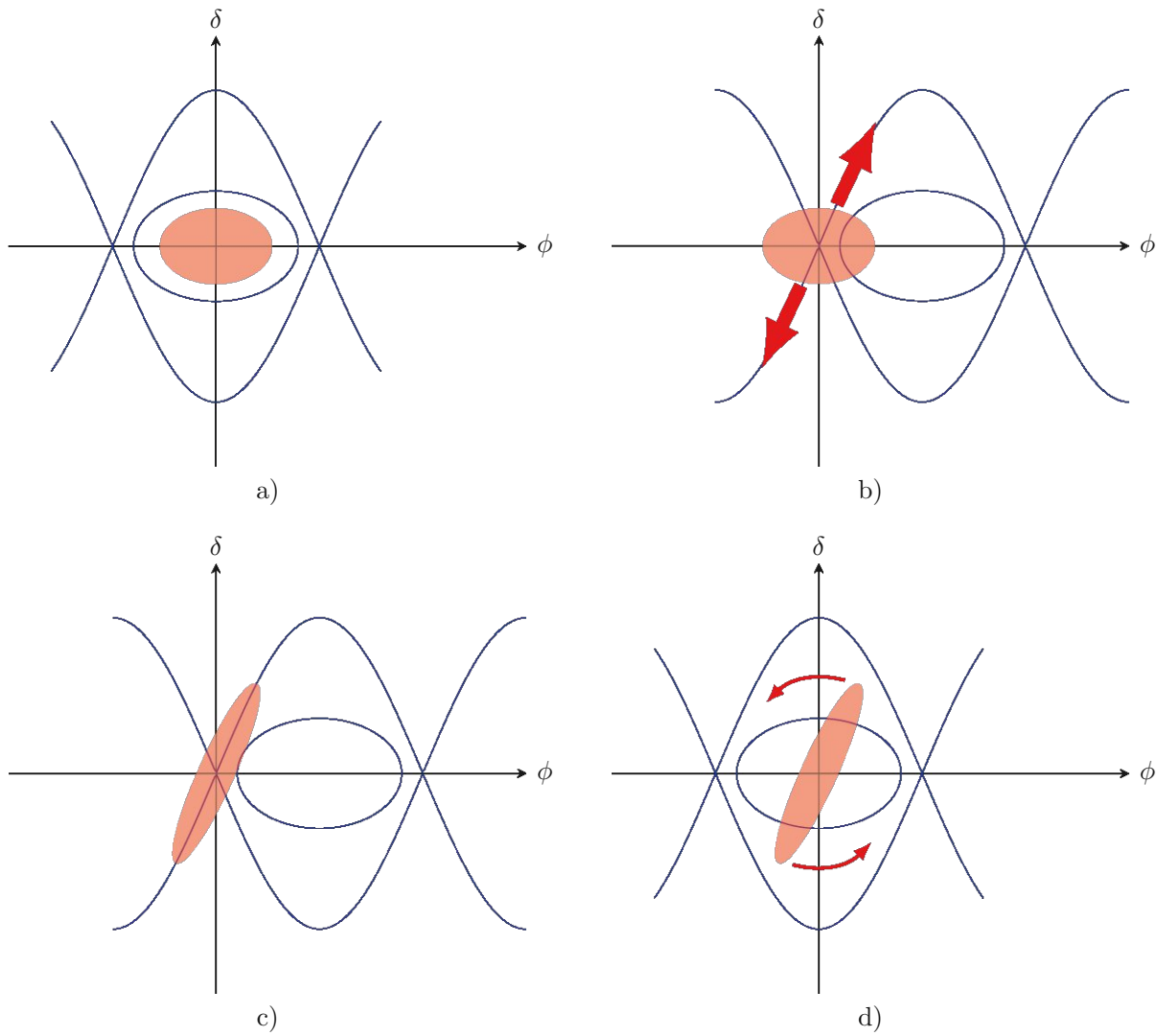


Figure 2.6.: Typical phase jump process (modified after [12]).

the bunch ellipse reaches an upright position, resulting in the highest possible momentum spread (i.e. projection of the distribution on the δ axis).

The Schottky measurement [28–30] of the momentum distribution with and without phase jump and especially the increase in momentum spread are compared in Figure 2.7.

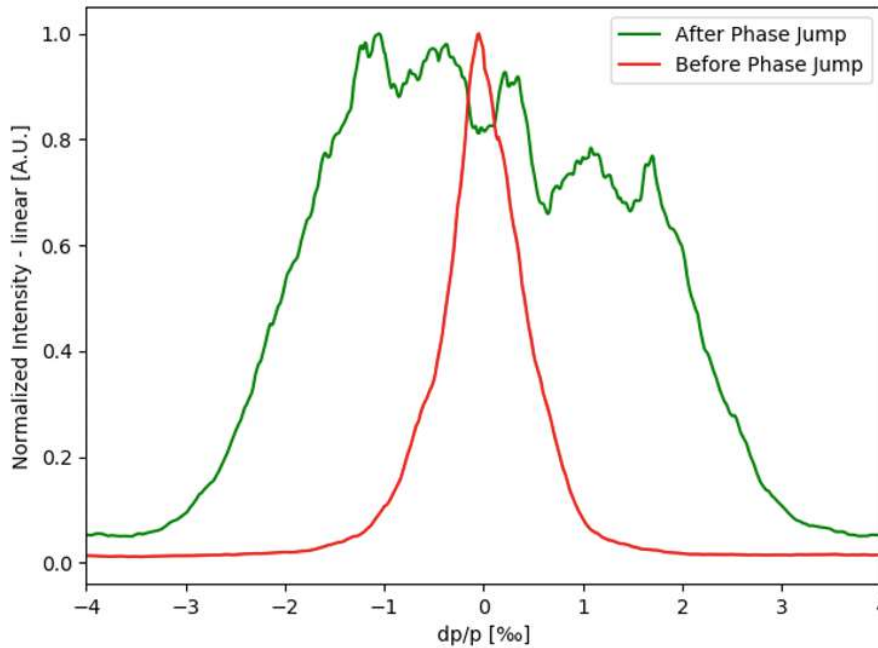


Figure 2.7.: Comparison of the momentum distribution with and without phase jump for a proton beam with 252.7 MeV.

The phase jump increases the FWHM of the momentum spread from 0.86×10^{-3} to 3.70×10^{-3} . While the momentum distribution resembles a Gaussian curve before phase jump, the peak is spread out to a more uniform distribution after the phase jump, although there are obviously some asymmetries and fluctuations, which are smoothed out once the RF cavity is turned off. The final momentum distribution before extraction is close to a uniform distribution.

2.3. Slow extraction

To deliver the beam from the synchrotron to the patients in a controlled and reproducible manner, third-order slow extraction is used in most facilities. This section discusses the theoretical principles of slow extraction and its visualisation as separatrices in phase space or with a Steinbach diagram. Furthermore, the most important slow extraction techniques are discussed and compared.

2.3.1. Principles of slow extraction

The need for slow extraction arises from the requirements for clinical treatment. The treatment plan defines a certain dose rate for each point of the tumour, which is requested from the control system. These requested dose rates require a constant particle intensity over a prolonged spill duration of up to ten seconds, which explains the necessity to extract the beam slowly and in a controlled manner.

These prolonged spill lengths are also necessary for the DDS to be able to scan the beam over the 2D slices of the tumour. The extraction process needs to be slow enough that the scanning system can react to unexpected dose rates. Additionally, it is important to consider risk mitigation requirements and safety aspects. In the event of an issue, the irradiation must be stopped with minimal excess dose hitting the patient in error. If the full beam were extracted in a short pulse, the excess dose would be unacceptably high. This is because non-zero reaction times, due to the time needed to detect the issue and propagate the signal to the beam termination system, would allow too many particles to be transmitted to the treatment room.

Due to these limitations, the beam cannot be extracted by simply turning on a dipole kicker magnet. This Fast Extraction (FX) would cause the entire beam to be extracted in one turn, resulting in spill lengths of only a few microseconds. To prolong the spill to an acceptable duration, Slow Extraction (SX) techniques must be employed.

Resonances

In first approximation, each magnetic component applies a kick to the particle coordinate x' , defining the reference trajectory. For a circulating beam within a periodic lattice of a circular accelerator, field imperfections accumulate over many turns and excite resonances. This leads to an amplitude increase and particle losses.

Field imperfections in different magnets excite resonances of varying orders, with each resonance requiring a specific tune condition to be met in order to increase the particle amplitude resonantly. The tune condition for a resonance of order $(|m| + |n|)$, where

$m, n \in \mathbb{Z}$ and $p \in \mathbb{N}$, is described by equation 2.37.

$$mQ_x + nQ_y = p \quad (2.37)$$

Resonances of orders $(|m| + |n|) = 1, 2$ and 3 are excited by the magnetic fields of dipoles, quadrupoles and sextupoles, respectively.

As these field imperfections cannot be completely avoided for a real accelerator, the lattice tune needs to be set in a way to avoid the main resonance conditions, as the particles would else be lost. Figure 2.8 show the tune footprint with all resonance lines up to fourth order, with the line colour denoting the resonance order. Figure 2.8a shows the tune footprint for horizontal and vertical tunes between 1 and 2, while Figure 2.8b focuses on the tune region relevant for betatron core extraction with the ramp from the injection optics ($Q_x/Q_y = 1.739/1.779$) to the extraction optics ($Q_x/Q_y = 1.666/1.789$) [12]. The third-order horizontal resonance $Q_x = 5/3$ is used for extraction. A fourth-order resonance $2Q_x + 2Q_y = 7$ is crossed during the ramp, but as the resonance is not strongly excited by the optics and the crossing is fast, the perturbation is negligible.

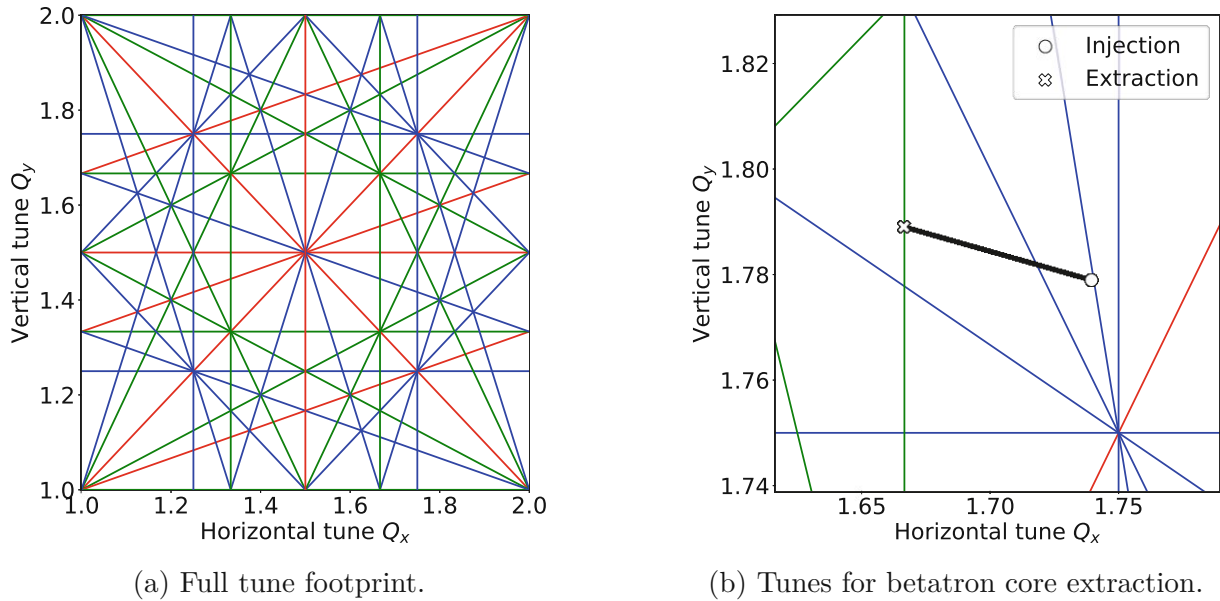


Figure 2.8.: Tune footprint with resonances up to fourth order.

Second order: red; Third order: green; Fourth order: blue

Third-order resonant slow extraction

Although the previously discussed resonances need to be avoided during acceleration and circulation, they can be utilised for slow extraction. If the particle tune is gradually adjusted until it meets a resonance condition that is excited by an adequate magnetic field, the particles become gradually unstable and their amplitude is increased until they get lost or are extracted. For this thesis, third-order resonant extraction is of main interest and will be discussed in this section. A detailed analysis of particle motion near a third-integer resonance can be found in various publications, such as [31] and [32].

For a horizontal particle tune near a third-integer resonance $Q_x = n \pm 1/3 + \Delta Q_x$ with $n \in \mathbb{N}$ and $\Delta Q_x \ll 1/3$, the particle motion with three turns as fundamental time unit can be described in first approximation with the *Kobayashi Hamiltonian* 2.38 [31].

$$H = \frac{\epsilon}{2} (X^2 + X'^2) + \frac{S}{4} (3XX'^2 - X^3), \quad (2.38)$$

where $\epsilon = 6\pi\Delta Q_x$ is the tune difference from the third-integer resonance, X and X' are the normalised phase space coordinates of the particle, and $S = (1/2)\beta_x^{3/2}K_2$ the modified sextupole strength³. The first term describes the unperturbed circular motion, while the second term introduces the perturbations by the sextupole, which distorts the circular phase-space trajectory into a triangular shape.

The change of the particle position and angle after three turns ΔX_3 and $\Delta X'_3$ can be calculated by differentiating the three-turn Kobayashi Hamiltonian 2.38.

$$\Delta X_3 = \frac{\partial H}{\partial X'} = \epsilon X' + \frac{3S}{2} XX' \quad (2.39)$$

$$\Delta X'_3 = -\frac{\partial H}{\partial X} = -\epsilon X + \frac{3S}{4} (X^2 - X'^2) \quad (2.40)$$

ΔX_3 and $\Delta X'_3$ are called *spiral step* and *spiral kick* and are used to characterise the motion of the particle in the last three turns before extraction.

A contour plot of the Hamiltonian 2.38 in phase space (X, X') is shown in Figure 2.9. For small values of the Hamiltonian (and thus small absolute values of X and X'), the particle trajectories are closed, which means that particles in this area are stable and are not extracted. For higher absolute position and angle values (i.e. larger Hamiltonian values), the trajectories open up and particles in this area are unstable and will be extracted. The boundary between the stable and the unstable areas are three lines called *separatrices*, which form a triangle at a value of $H_{\text{separatrix}} = (2\epsilon/3)^3 S^{-2}$. At this value, the Kobayashi

³In [7], S is referred to as the normalised sextupole strength. However, in this thesis, the term 'modified' is used to distinguish it clearly from k_2 and to avoid potential confusion.

Hamiltonian 2.38 can be factorised into three terms, which are the mathematical representation of the three separatrices.

The separatrices form the stable triangle, which contains all particles with a stable trajectory. Particles outside of this triangle are in the unstable region and will be extracted in a few turns, following a trajectory converging to the closest separatrix.

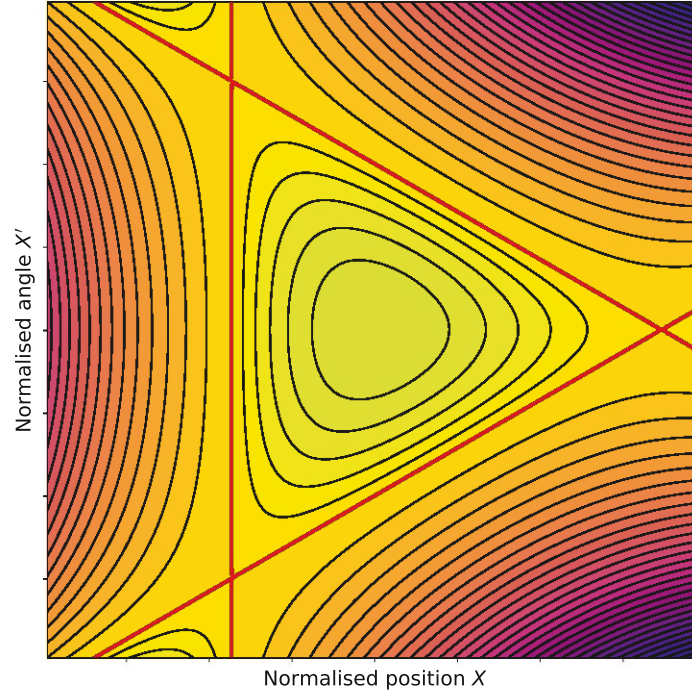


Figure 2.9.: Contour plot of the Kobayashi Hamiltonian.

The area of the stable triangle 2.41 can be calculated by using the equation of the separatrices and depends on the distance to the resonance tune ΔQ_x and the modified sextupole strength S .

$$E_{\text{stable}} = \frac{48\sqrt{3}\pi^2}{S^2} \Delta Q_x^2 \quad (2.41)$$

The closer the particle tune is to the resonance and the stronger the sextupole strength is, the smaller is the area of the stable triangle. For on-resonance particles, the stable area becomes zero and all particles are extracted, independently of their positions and angles. The shown orientation of the stable triangle is only valid at the location of the resonant sextupole. For other components, the phase advance between the component of interest and the resonant sextupole needs to be applied to the stable triangle as a rotation around the centre point, which changes the angle of the outgoing separatrices.

Steinbach diagram

Another possible visualisation of the stable and unstable regions is the so-called *Steinbach diagram*, where the abscissa is the tune offset ΔQ_x and the vertical axis is the normalised amplitude $A = \sqrt{E_{\text{stable}}/\pi}$. As E_{stable} is proportional to ΔQ_x^2 , A is proportional to $|\Delta Q_x|$, which means that the area of the stable triangle in the phase-space representation corresponds to a V-shaped structure in the Steinbach diagram, as shown in Figure 2.10.

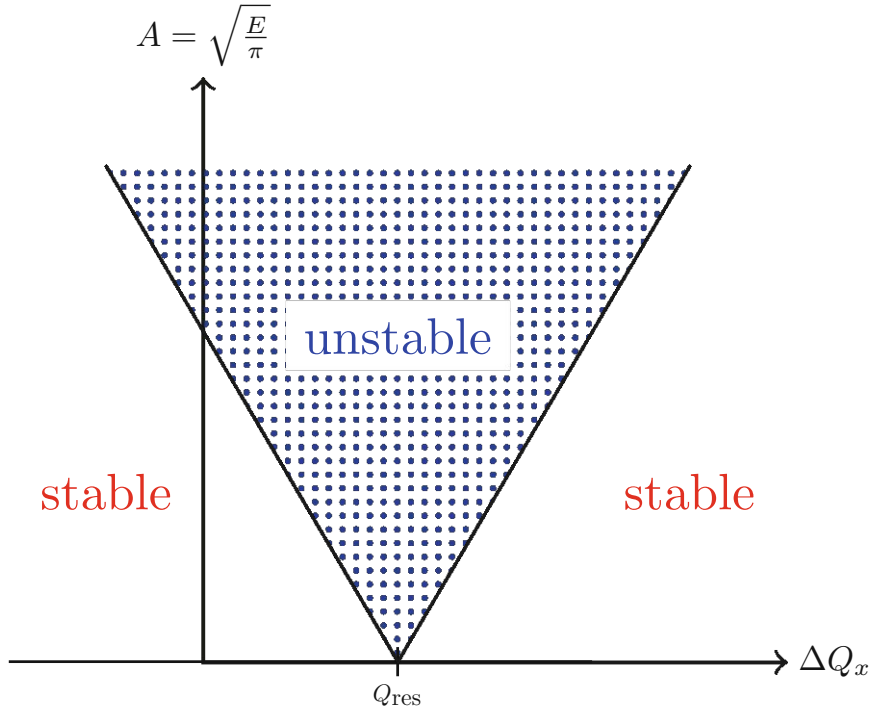


Figure 2.10.: Steinbach diagram near a resonance Q_{res} .

The edge of the Steinbach diagram, that separates the stable from the unstable region, can be mathematically expressed by equation 2.42⁴.

$$A = \sqrt{\frac{E_{\text{stable}}}{\pi}} = \sqrt{48\sqrt{3}\pi} \frac{|\Delta Q_x|}{|S|} = \sqrt{48\sqrt{3}\pi} \frac{|Q_x - Q_{\text{res}} + Q'_x \frac{\Delta p}{p}|}{|S|} \quad (2.42)$$

⁴As equation 2.41 was derived from a first-order approximation of the Hamiltonian, the linear equation of the Steinbach edge is only valid in first approximation. If higher-order effects are included, a deviation from linearity is to be expected.

Increasing the strength of the resonant sextupole decreases the slope of the Steinbach edge, which opens up the V-shape and leads to particles becoming unstable at lower amplitudes, corresponding to a smaller area of the stable triangle in the phase space representation. Increasing the tune offset from resonance, either by directly matching the optics or by enlarging the chromatic tune shift while operating off-momentum, leads to a higher amplitude acceptance before reaching the unstable area. The properties of the extraction can be tempered by adjusting these parameters in order to shape the stable and unstable area.

Hardt condition

According to equation 2.41, the area of the stable triangle depends on the square of the tune distance to the resonance and thus on the momentum offset. Particles with different momenta thus in general follow different separatrices and reach the electrostatic septum with slightly different angles, as shown in Figure 2.11a. The resulting angular spread $\Delta X'$ at the septum results in additional losses, as particles with a small angle deviation might hit the septum wire while traversing the 0.8 m long ESE. These losses due to the increased effective thickness of the ESE wire can grow quite substantial, as small angular mismatches at the septum entry can lead to significant position offsets at the septum exit. Additionally, an increased angular spread might lead to an unfavourable beam distribution in the HEBT.

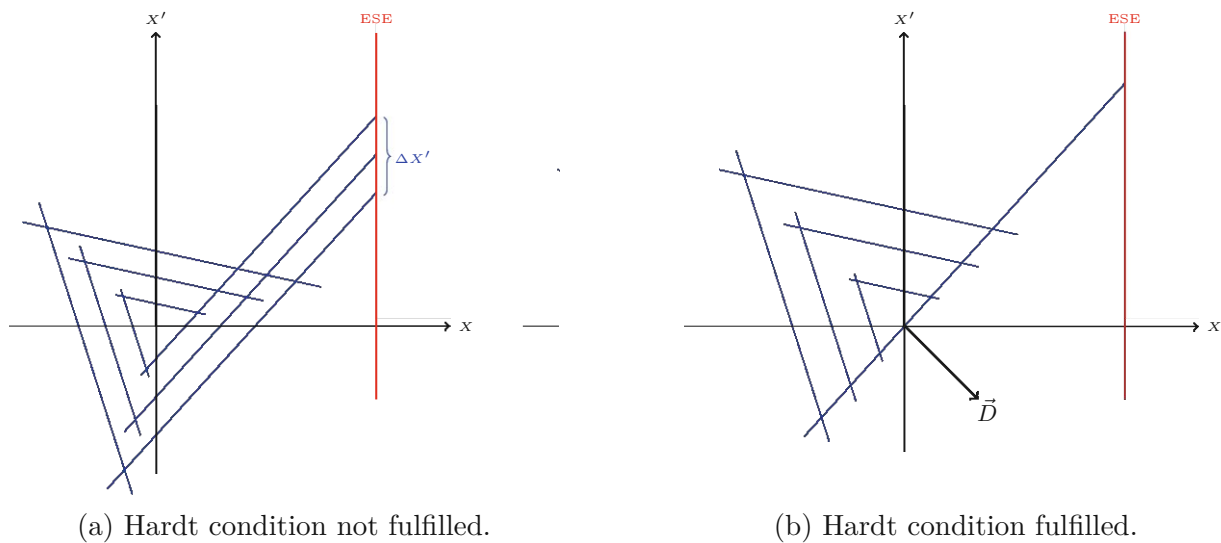


Figure 2.11.: Phase space at the ESE for three particles with different momentum offsets.

To minimise these losses, the separatrices for particles with different momenta need to be superimposed, as shown in Figure 2.11b. It can be shown that this can be achieved by balancing the lattice parameters to fulfil the *Hardt condition* 2.43 [33].

$$D_n \cos(\alpha - \Delta\mu) + D'_n \sin(\alpha - \Delta\mu) = -\frac{4\pi}{S} Q'_x \quad (2.43)$$

The left-hand side of equation 2.43 represents the scalar product of the normalised dispersion vector (D_n, D'_n) and the vector $(\cos(\alpha - \Delta\mu), \sin(\alpha - \Delta\mu))$, which describes the orientation of the separatrix at the electrostatic septum, as α denotes the orientation of the separatrix at the resonant sextupole and $\Delta\mu$ is the phase advance between the resonant sextupole and the ESE. Both vectors are determined by the lattice design and the extraction geometry [7].

The modified sextupole strength S and the horizontal chromaticity Q'_x on the right-hand side of equation 2.43 are used to match the value of the scalar product. In practice, only the chromaticity can be varied with reasonable effort in order to fulfil equation 2.43.

For the MedAustron synchrotron, the Hardt condition is satisfied for a chromaticity of $Q'_x = -4.041$ [12].

2.3.2. Slow extraction techniques

To slowly extract the beam, the particles need to get from the stable to the unstable region. Based on the Steinbach diagram, different techniques can be identified to extract the beam, as shown in Figure 2.12.

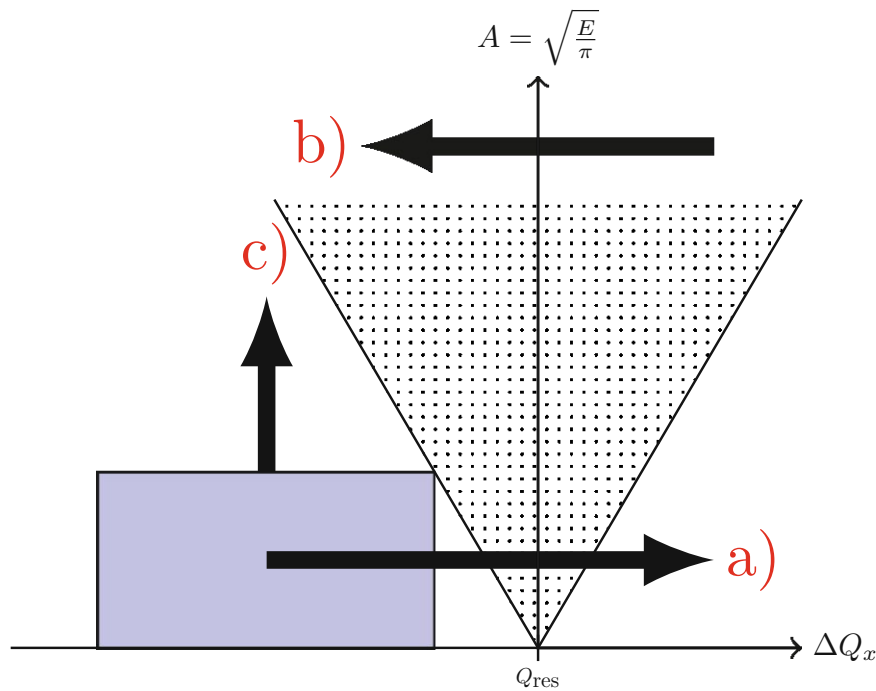


Figure 2.12.: Overview of the principal methods for slow extraction.

Three principal methods can be distinguished:

- (a) Moving the beam via acceleration into the resonance (Betatron Core extraction, longitudinal techniques such as Phase Displacement extraction and Stochastic RF Noise extraction⁵)
- (b) Moving the resonance into the beam (Tune Sweep/Constant Optics Slow Extraction)
- (c) Increasing the amplitude of the beam (Radio Frequency Knockout)

The following pages contain a summary of the mentioned extraction methods.

⁵Not under consideration for this thesis due to technical limitations. Details can be found in [7, 34, 35].

Betatron Core extraction

The default extraction technique for MedAustron is extraction with a betatron core. The particles are kept at an off-momentum orbit during acceleration and circulation, while the on-momentum lattice tune is set to a third-order resonance (in the case of MedAustron, $Q_x = 5/3$). The particles are then moved into resonance by inductive acceleration via a betatron core, which results in a tune shift due to the non-zero chromaticity. The lattice remains unchanged during extraction, and the betatron core pushes the beam stack into the stationary resonance. When the stopband of the Steinbach edge is reached, the particle enters the unstable area, causing an increase in oscillation amplitude and extraction of the particle when it jumps over the wire of the electrostatic septum. The betatron core extraction process is illustrated schematically in Figure 2.13.

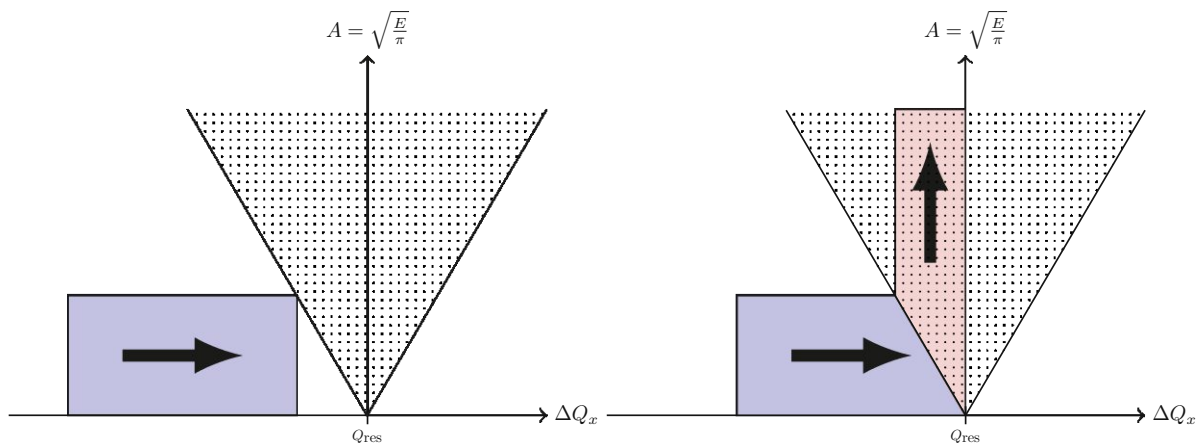


Figure 2.13.: Schematic view of betatron core extraction in the Steinbach diagram [36].

The extraction rate for betatron core extraction is determined by the acceleration rate introduced by the betatron core. To suppress ripples, it is advantageous to quickly bring the particles into resonance (see section 2.4). To achieve extraction lengths of up to ten seconds, a phase jump must be performed, which increases the momentum spread of the beam. Because of this, betatron core extraction is a momentum selection technique that requires a low-emittance beam with a high momentum spread.

As the momentum of the extracted particles remains constant throughout the core of the spill, no momentum drifts are observed during the spill, as the head and the tail of the beam are chopped. To prevent that different amplitudes are extracted at significantly different momenta, the V-shape of the Steinbach diagram needs to be steep.

Tune Sweep

Tune sweep extraction is a widely used extraction technique in research facilities due to its relative simplicity of implementation [37–40].

Similar to betatron core extraction, the beam is kept at a distance from the resonance by off-momentum operation during acceleration and circulation. However, with tune sweep extraction, the beam remains stationary while the resonance is swept through it by changing the horizontal tune Q_x and thus ΔQ_x . The Steinbach diagram for tune sweep extraction is shown in Figure 2.14.

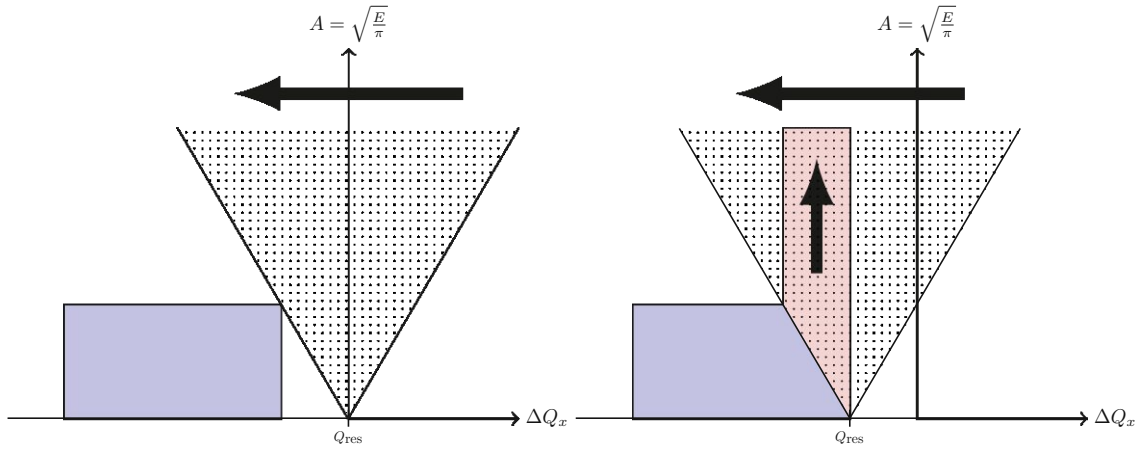


Figure 2.14.: Schematic view of tune sweep extraction in the Steinbach diagram.

As the tune is in first approximation defined by the quadrupole strengths, the tune can be changed by ramping all synchrotron quadrupoles. As shown in [41], the relative tune change $\Delta Q_x/Q_x$ is at first order identical to the relative change of the quadrupole strength $\Delta k_i/k_i$ for each quadrupole family i . The tune change needs to cover the entire chromatic tune spread for a momentum spread of $\Delta p/p \approx 4 \times 10^{-3}$ for an unbunched beam after phase jump. The corresponding relative tune change can be calculated with equation 2.44, using the nominal flattop tune $Q_x = 5/3$ and chromaticity $Q'_x = -4$.

$$\frac{\Delta Q_x}{Q_x} = \frac{1}{Q_x} Q'_x \frac{\Delta p}{p} \approx -1\% \quad (2.44)$$

For this relative tune change of -1%, all quadrupoles need to be scaled by the same factor, as shown in equation 2.45.

$$\frac{\Delta Q_x}{Q_x} = -1\% \iff \frac{\Delta k_i}{k_i} \approx -1\% \iff k_{i, \text{end}} \approx k_{i, \text{start}} \cdot \left(1 - \frac{1}{100}\right) \quad (2.45)$$

Tune sweep requires a low-emittance beam with a high momentum spread, resulting in extraction by momentum selection. As the RF system is no longer needed to accelerate the beam, the technique is compatible with both bunched and unbunched operation. Analogue to betatron core extraction, a phase jump is needed to enhance the momentum spread of the waiting beam prior to extraction to be able to achieve extended extraction times with higher quadrupole sweep rates.

Contrary to betatron core extraction, the extracted particle momentum differs between the start and the end of the spill for tune sweep extraction, as the resonance traverses through the stationary beam in momentum space. This leads to an intraspill momentum drift, which results in an intraspill movement of the beam for non-zero dispersion. For this reason, tune sweep is not ideal for medical applications where a constant energy during the spill is required.

An additional disadvantage of extracting via tune sweep is that the separatrices for particles with different momenta are not superimposed, but shifted in the direction of the dispersion vector [41]. Due to this shifting, the Hardt condition cannot be fulfilled, which changes the angle of particles at the electrostatic septum over the extraction, leading to an enlarged angular spread, an angular momentum-sorting and increased losses. As the beam rigidity $B\rho$ changes during the course of the extraction due to the changing momentum of the extracted particles, also the optics affecting the particles just before extraction differ over time [42].

Constant Optics Slow Extraction

Constant Optics Slow Extraction (COSE) was developed by Kain et al. [43], advancing the tune sweep extraction.

With COSE, the aforementioned disadvantages of tune sweep originating in the changing optics are met by keeping the separatrix constant during the whole extraction process. This can be realised by ramping not only the quadrupoles, but scaling $B\rho$ and thus synchronously ramping all synchrotron magnets, according to equation 2.46 [43].

$$\frac{\partial^n B(t)}{\partial x^n} = k_n \cdot (B\rho)(t) \quad (2.46)$$

where k_n are the normalised multipole strengths.

The scaling factor of magnets is equivalent to the relative momentum change from start to end of the extraction. As the momentum change is equal to the momentum spread $\Delta p/p$ of the unbunched beam after phase jump, the required magnet scaling factor for COSE is different to the value 2.45 for tune sweep extraction.

$$\frac{\Delta p}{p} = 4 \times 10^{-3} \iff \frac{\Delta k_i}{k_i} \approx -4 \times 10^{-3} \iff k_{i, \text{end}} \approx k_{i, \text{start}} \cdot \left(1 - \frac{4}{1000}\right) \quad (2.47)$$

Radio Frequency Knockout

With RFKO, the amplitude of the circulating particles is gradually increased by applying a horizontal kick on the particles via a horizontal RF electric field application. The beam with a small momentum spread is kept near a third-order resonance, when the RF kicker is turned on for extraction. The amplitude is resonantly increased until the particles hit the separatrix and are extracted. For RFKO, no acceleration is needed and the lattice parameters and magnet currents are constant during the whole spill. The RFKO extraction process is depicted in Figure 2.15.

The RFKO extraction process is depicted in Figure 2.15.

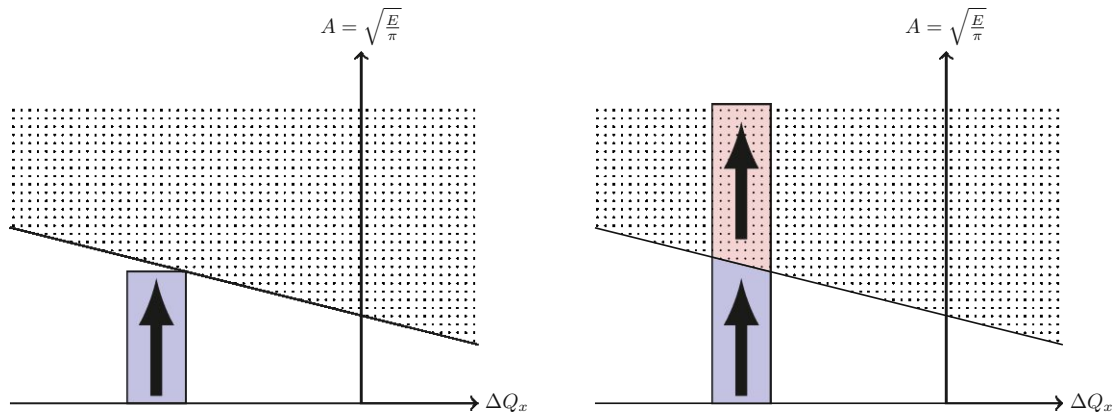


Figure 2.15.: Schematic view of RFKO extraction in the Steinbach diagram [36].

The excitation frequency f_0 required to excite the particles needs to be tuned to the revolution frequency and the tune of the betatron oscillations of the particles, according to equation 2.48.

$$f_0 = (n \pm q_x) f_{\text{rev}} \quad (2.48)$$

In equation 2.48, q_x is the fractional part of the horizontal particle tune, n is an integer and f_{rev} is the revolution frequency of the beam. Different values of n define different excitation modes and higher-harmonic excitation.

Excitation with a single-frequency sinusoidal signal is possible in theory, but requires high signal amplitudes and fails to reach acceptable extraction efficiencies, as not all particles are excited evenly. In reality, the beam with a non-zero momentum spread and $Q' \neq 0$ spreads over a frequency range that needs to be covered by the excitation signal. In addition, the required frequency also changes for high-amplitude particles due to amplitude-dependent detuning. As a result, the excitation frequency must be extended over a certain bandwidth for effective extraction.

Two techniques for this signal modulation are discussed in this thesis:

1. **Frequency modulation:** The frequency of the excitation signal is modulated over time, leading to a signal that can be described with equation 2.49.

$$V(t) = A_0 \cos \left(2\pi \int_0^t f(\tau) d\tau + \phi \right) \quad (2.49)$$

A_0 is the amplitude of the signal that defines the extraction rate. $f(\tau)$ is the time-dependent instantaneous frequency, while ϕ is the stationary phase.

Most facilities use a sawtooth modulation of the frequency, where the frequency is ramped linearly from f_{start} to f_{end} and then jumps back to f_{start} . The bandwidth of the modulation needs to correspond to the frequency spread of the beam, which can be computed by the momentum spread and the phase slip factor, as derived in section 2.2.

The duration of the modulation (i.e. the period of the sawtooth wave) can be adjusted in order to optimise the quality of the extracted beam. However, the modulation frequency is the main contributor to the intensity ripples of the extracted beam.

To improve the intensity ripples and improve the uniformity of the extracted intensity, additional excitation signals can be added to the main signal. For dual frequency modulation, a second signal with a phase difference of π to the main signal can be used to smoothen out the extraction [44].

Frequency modulation is discussed in detail in section 4.4.2.

2. **Phase modulation:** While the excitation frequency remains constant, the phase of the signal is varied over time, resulting in the excitation signal 2.50.

$$V(t) = V_0 \cos (2\pi f_0 t + \phi(t)) \quad (2.50)$$

f_0 is the now constant frequency, while the phase $\phi(t)$ is modulated over time. The resulting effective frequency can be calculated with equation 2.51.

$$f(t) = f_0 + \frac{1}{2\pi} \frac{d\phi(t)}{dt} = f_0 + G(t) \quad (2.51)$$

$G(t)$ has to be chosen in a way to cover the whole frequency span of the beam.

The most prominent example for a phase modulation is a technique called Phase Shift Keying (PSK).

For Binary Phase Shift Keying (BPSK), the phase is shifted by π with a probability of 50%. To achieve this, a random number n_{random} between 0 and 1 is chosen with a

frequency of f_{shift} . If n_{random} is less than 0.5, the signal remains unchanged, while a phase shift of π is added for $n_{\text{random}} \geq 0.5$.

$$\phi = \phi + \begin{cases} 0 & \text{for } n_{\text{random}} < 0.5 \\ \pi & \text{for } n_{\text{random}} \geq 0.5 \end{cases} \quad \text{for } n_{\text{random}} \in [0, 1) \text{ with } f_{\text{shift}} \quad (2.52)$$

For Quadrature Phase Shift Keying (QPSK), the phase shift can be $\pi/4$, $3\pi/4$, $5\pi/4$ or $7\pi/4$, each with a probability of 25%.

$$\phi = \phi + \begin{cases} \pi/4 & \text{for } n_{\text{random}} \in [0, 0.25) \\ 3\pi/4 & \text{for } n_{\text{random}} \in [0.25, 0.5) \\ 5\pi/4 & \text{for } n_{\text{random}} \in [0.5, 0.75) \\ 7\pi/4 & \text{for } n_{\text{random}} \in [0.75, 1) \end{cases} \quad \text{for } n_{\text{random}} \in [0, 1) \text{ with } f_{\text{shift}} \quad (2.53)$$

A detailed analysis of PSK can be found in section 4.4.2.

Other excitation signals (and combinations of techniques) are proposed in current research to further improve the spill quality, such as a combination of noise and sinusoidal excitation [45].

Additionally to the modulation of the excitation frequency, the signal amplitude A_0 also possibly needs to be adjusted during the spill in order to obtain a constant intensity of the extracted beam. It is shown in [46] that the excitation amplitude required for a constant extraction rate follows a bathtub curve with a higher amplitude needed at the start and the end of the spill. Amplitude modulation is discussed in section 4.4.1.

For RFKO, the momentum spread of the extracted beam is equal to the momentum spread of the circulating beam prior to extraction. Therefore, it is necessary to keep the momentum spread as small as possible by not performing a phase jump, limiting the energy spread for irradiation. If the beam is kept off-momentum during extraction, the momentum offset is entrained to the HEBT and further to the treatment room, which must be taken into account for treatment planning.

For a simultaneous extraction of the full momentum spread of the beam, the separatrix of the Steinbach diagram needs to be as flat as possible, which can be achieved by setting a low absolute chromaticity value and increasing the strength of the resonant sextupole. On the other hand, a relatively high chromaticity of $Q'_x \approx -4$ is needed to fulfil the Hardt condition 2.43. However, it is shown in [47] that the overall extraction efficiency can benefit from breaking the Hardt condition. Additionally, the angular spread can be reduced by adjusting the dispersion between the ESE and the MST, meaning that it is acceptable to not fulfil the Hardt condition by using a lower chromaticity.

RFKO is compatible with both bunched and unbunched operation and allows very fast shutdown times, which is important for safety concerns. Multi energy extraction is possible if a front-end acceleration mechanism is implemented. The intensity of the extracted beam can be easily adjusted in a short time scale by changing the signal amplitude, allowing sub-millisecond intensity adaptations as needed for DIC schemes. High particle kick voltages lead to high extraction rates and very short spill lengths.

Phase Displacement Extraction

Phase Displacement Extraction (PDE) is a longitudinal extraction technique that was used at the European Organization for Nuclear Research (CERN) in the 1960s [48]. PDE was proposed in [7] as alternative to betatron core extraction. It is similar to Empty Bucket Channelling (see section 2.4), but instead of a stationary empty bucket, the bucket is moved through the waiting beam to accelerate the particles into resonance.

The beam is positioned near the resonance and an empty bucket is established by the RF cavity at a given frequency offset from the beam, so that the beam is initially not disturbed by the bucket.

The bucket frequency is then ramped down, until the bucket interacts with the beam. Due to Liouville's theorem, the particles behave like an incompressible fluid and are therefore displaced by the approaching bucket. They move through the bucket gap and are accelerated into extraction when crossing the resonance.

As the phase space density is conserved, the area of the displacement $A_d = \Delta E \cdot 2\pi$ is equal to the bucket area A_B , which is given by equation 2.33. The resulting energy change due to the acceleration for a single sweep is given in equation 2.54 [7].

$$\Delta E = \frac{A_B}{2\pi} = 8 \left(\frac{eV}{2\pi^3 \beta_r^2 E h |\eta|} \right)^{\frac{1}{2}} \quad (2.54)$$

For a proper configuration of PDE, the bucket voltage has to be set in a way that the induced acceleration ΔE of the particles corresponds to the energy offset between the resonance and the beam.

The initial bucket frequency is chosen in a way that the lower part of the bucket is just above the high-momentum part of the beam. This configuration avoids unnecessary dead times when the bucket is moving through frequency ranges that are not containing any particles. In reality, a higher initial frequency is chosen to avoid premature extraction of the high-momentum tail of the beam by increasing the distance between the bucket and the beam.

The required bucket frequency change Δf_B to sweep the bucket through the whole beam

corresponds to the energy spread $\Delta E/E$ of the beam [7].

$$\Delta f_B = \eta f_{\text{rev}} \left(\frac{\Delta p}{p} \right)_{\text{spread}} = \frac{\eta}{\beta_r^2} f_{\text{rev}} \left(\frac{\Delta E}{E} \right)_{\text{spread}} \quad (2.55)$$

The advantage of PDE is that the bucket sweep can be repeated multiple times for a pulsed extraction [49–51]. For this burst extraction, the bucket voltage (and thus according to equation 2.34 the bucket height) is set to zero after every completed sweep, before the bucket frequency is ramped again to the starting point. This bucket collapse makes sure that the beam is not disturbed during the reset of the bucket configuration.

In addition, the bucket can be moved through the beam very quickly, allowing short pulse lengths of down to 8 ms for PIMMS-based facilities [49].

In pulsed operation, consistent extraction intensity for each sweep is desired. However, the extraction intensity depends on the energy distribution of the beam and the properties of the bucket. To achieve homogeneous extraction, the bucket voltage needs to be adjusted for each sweep, thereby varying the energy change ΔE per sweep and controlling the number of extracted particles. The necessary voltage modulation can be determined using a feedback loop based on intensity measurements [49, 50].

As one RF cavity is installed at the MedAustron synchrotron, only one bucket can be generated in first-harmonic operation. This means that for PDE, as the bucket is needed for sweeping through the beam, it cannot be used to keep the beam bunched. Therefore, PDE is not compatible with extractions requiring other use of the synchrotron RF system such as bunched beam operation and MEE. Additionally, EBC cannot be used together with PDE to suppress the beam ripples.

Another disadvantage of PDE is that particles are extracted in a burst during the bucket sweep, but no extraction occurs when the bucket configuration is reset to the starting point. This leads to a strong modulation of the extracted intensity with the sweep frequency and thus a strong contribution to the intensity ripples. Continuous extraction would require to simultaneously generate multiple buckets, which are swept through the beam one after another with a short delay. However, the current RF cavity at MedAustron is not capable of this multi-bucket operation mode.

2.3.3. Comparison of the slow extraction techniques

Table 2.2 compares the discussed extraction techniques and summarises their respective advantages and disadvantages.

Extraction technique	Advantages	Disadvantages
Betatron Core	<ul style="list-style-type: none"> • Easy to implement • Compatible with EBC as ripple mitigation technique • Lattice is constant during extraction • Hardt condition can be fulfilled 	<ul style="list-style-type: none"> • Not compatible with bunched beams and MEE • Slow responses and long shut-off times • No fast intensity control possible
Tune Sweep	<ul style="list-style-type: none"> • Requires no additional components • Compatible with bunched beams and easy implementation of MEE • Only quadrupoles need to be ramped and limit the extraction rate 	<ul style="list-style-type: none"> • Lattice is not constant during extraction • Particle momentum of the extracted beam changes during extraction • Enlarged angular spread at the ESE leads to increased losses

Extraction technique	Advantages	Disadvantages
Constant Optics Slow Extraction	<ul style="list-style-type: none"> • Requires no additional components • Compatible with bunched beams and easy implementation of MEE • Minimised losses due to reduced angular spread 	<ul style="list-style-type: none"> • Lattice is not constant during extraction • Particle momentum of the extracted beam changes over time • Extraction rate is limited by the dipole ramping
Radio-frequency Knockout	<ul style="list-style-type: none"> • Compatible with bunched beams and MEE • Short response time allows sub-millisecond intensity adaption • Ripples can be reduced by advanced excitation signals and closed-loop feedback regulation 	<ul style="list-style-type: none"> • Additional equipment needed at MedAustron • Intensity ripples can be introduced by the excitation signal • Not compatible with EBC • Hardt condition cannot be fulfilled at MedAustron
Phase Displacement Extraction	<ul style="list-style-type: none"> • Constant lattice during extraction • Short spill lengths with high extraction rates are possible • Beam quality improved by fast resonance crossing 	<ul style="list-style-type: none"> • Not compatible with bunched beams and MEE • No ripple mitigation with EBC possible • Strong modulation of the extracted intensity at the sweep frequency

Table 2.2.: Comparison of the extraction techniques.

As part of the ICFA Mini-Workshop on Slow Extraction 2022⁶, a survey was conducted by the author of this thesis to query the most important extraction parameters of the participating facilities [52]. As part of this survey, the used particle types and extraction methods were collected, which are listed in Table 2.3. The medical-focused facilities are highlighted in grey. An additional survey was conducted as part of the IFAST-REX collaboration⁷ [53].

The participants of the survey are:

- Brookhaven National Laboratory (BNL) - United States of America
- European Organization for Nuclear Research (CERN) - Switzerland/France
 - ◊ Proton Synchrotron (PS)
 - ◊ Super Proton Synchrotron (SPS)
- Centro Nazionale di Adroterapia Oncologica (CNAO) - Italy
- Fermi National Accelerator Laboratory (FNAL) - United States of America
- Helmholtzzentrum für Schwerionenforschung (GSI) - Germany
- Heavy Ion Medical Accelerator in Chiba (HIMAC) - Japan
- Heidelberger Ionenstrahl-Therapiezentrum (HIT) - Germany
- Institute for High Energy Physics (IHEP) - Russia
- Japan Proton Accelerator Research Complex (J-PARC) - Japan
- MedAustron - Austria
- Marburger Ionenstrahl-Therapiezentrum (MIT) - Germany

As part of the survey, the main extraction method of the facilities were collected. The results are summarised for both medical-focused (grey) and research-focused (white) facilities in Table 2.3.

⁶see <https://conference-indico.kek.jp/event/163/overview>.

⁷see <https://indico.gsi.de/event/14171/>.

Facility	Particle type(s)	Extraction method(s)
BNL Booster	Proton all ions until Uranium	Tune Sweep
CERN PS and SPS	Proton	COSE
CNAO Synchrotron	Proton Carbon	Betatron Core RFKO
FNAL Delivery Ring (Mu2e)	Proton	Tune Sweep
GSI SIS-18	Proton all ions until Uranium	Tune Sweep RFKO
HIMAC Synchrotron	Carbon	RFKO
HIT Accelerator	Proton Carbon Helium	RFKO
IHEP-Synchrotron U-70	Proton	Longitudinal RF phase noise
J-PARC Synchrotron	Proton	Tune Sweep
MedAustron Synchrotron	Proton Carbon Helium (experimentally)	Betatron Core RFKO (in development)
MIT Synchrotron	Proton Carbon	RFKO

Table 2.3.: Extraction method used by selected accelerator facilities (as of January 2024).
The medical-focused facilities are highlighted in grey.

The medical facilities are primarily using RFKO as extraction method, which can be explained by flexibility of this technique. Only the PIMMS-based institutions MedAustron and CNAO are still facilitating extraction with a betatron core [54], but both facilities have either already implemented or are currently developing RFKO as secondary extraction technique [36, 51, 55–57].

The main extraction method for research-focused facilities is tune sweep, while CERN has recently moved to COSE for extraction particles from the PS and the SPS. GSI also uses RFKO to extract ions, while IHEP is the only centre to facilitate a longitudinal extraction technique, namely RF phase noise, which is explained in [58] and is out of scope of this thesis.

2.4. Ripple mitigation with Empty Bucket Channelling (EBC)

In an ideal setting, the beam would be extracted with a perfectly uniform intensity profile, thereby enabling the irradiation with a constant dose rate. However, in practice, fluctuations of the intensity over time are inevitable. The mitigation of these intensity ripples is an important topic for all medical facilities (see section 6 for a detailed discussion) and a good understanding of the ripple structure as well as mitigation methods is mandatory to optimise the performance of the accelerator and the efficiency of the treatment.

Multiple techniques are available to reduce the intensity ripples in the extracted beam. This thesis focuses on Empty Bucket Channelling (EBC), as this is the ripple mitigation used at MedAustron as well as at the facilities of BNL AGS [59], CNAO [60] and CERN (PS [61] and SPS [62, 63]). The theory of EBC, originally proposed by Cappi and Steinbach [64] and adapted for a medical facility in the PIMMS [7], is discussed in this chapter.

The time-dependent extraction rate $S(t)$, which is equivalent to the particle rate reaching the treatment room when losses in the HEBT are neglected, is defined in equation 2.56

$$S(t) = \frac{dN}{dt} = \frac{dN}{dQ} \frac{dQ}{dt}, \quad (2.56)$$

where N is the number of extracted particles and Q is the horizontal particle tune. For a uniform intensity, $S(t)$ needs to be constant to extract particles at a constant rate.

dN/dQ is defined by the momentum distribution of the waiting beam, which correlates to the tune distribution via the chromaticity. $dQ/dt = \dot{Q}_0 + \dot{Q}_r$ is the tune change over time, which is composed of two parts:

1. \dot{Q}_0 is induced by the betatron core when the beam is pushed into resonance. For normal operation, this value remains unchanged for the whole spill, as the acceleration induced by betatron core is constant.
2. Current ripples in the quadrupole magnets induce tune ripples \dot{Q}_r at various frequencies. This unwanted ripples cannot be completely avoided in reality and results in the need for ripple suppression.

The tune change over time can be written as

$$\frac{dQ}{dt} = \dot{Q}_0 \left(1 + \frac{\dot{Q}_r}{\dot{Q}_0} \right) \quad (2.57)$$

To minimise the impact of the tune ripples, the speed of the particles crossing the resonance \dot{Q}_0 should be as high as possible. However, the speed cannot be increased for the whole

stack, as it would lead to faster extraction and shorter spill lengths, which are restricted by safety regulations. Therefore, \dot{Q}_0 is increased locally only for particles close to the resonance, which maximises the speed of the resonance crossing while conserving the spill length. To keep $S(t)$ constant while increasing dQ/dt , the density of the particles dN/dQ in this area close to the resonance has to be reduced, resulting in a desired configuration of the extraction process as shown in Figure 2.16.

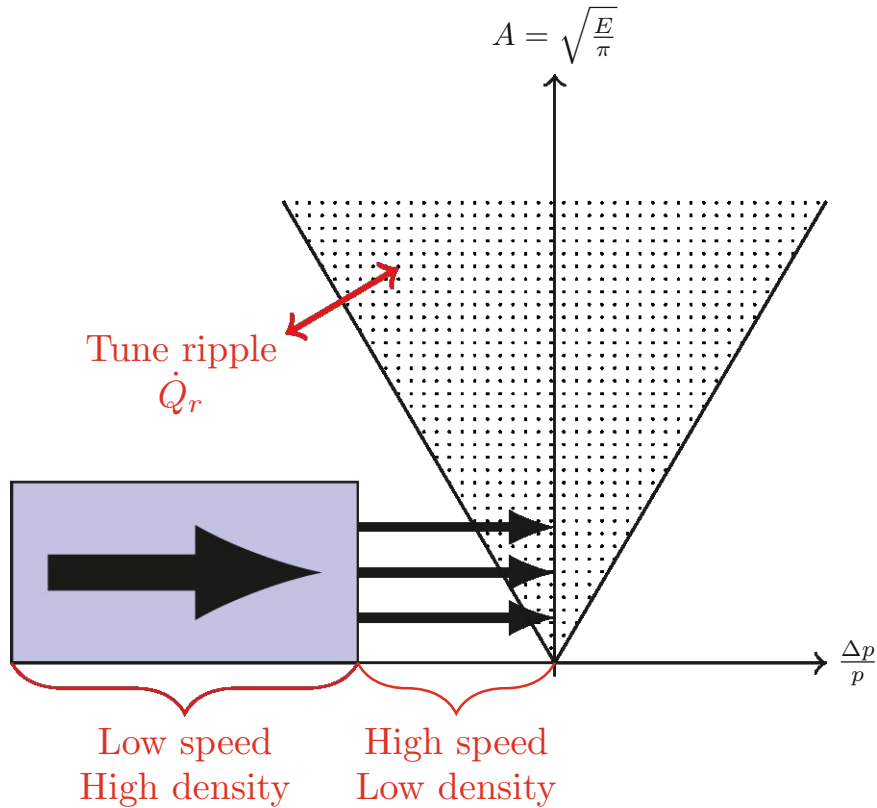


Figure 2.16.: Configuration for ripple mitigation (modified after [7]).

To realise a configuration as shown in Figure 2.16, empty RF buckets can be used for Empty Bucket Channelling (EBC). The buckets are placed so that they overlap with the resonance band. The beam is accelerated to the resonance via betatron core and is channelled through the gap between the bucket separatrices. As it moves through this 'bottle neck', the speed of the particles is increased and they cross the resonance with higher dQ/dt , as the particles behave like an incompressible fluid due to Liouville's theorem. A typical bucket configuration for EBC is shown in Figure 2.17.

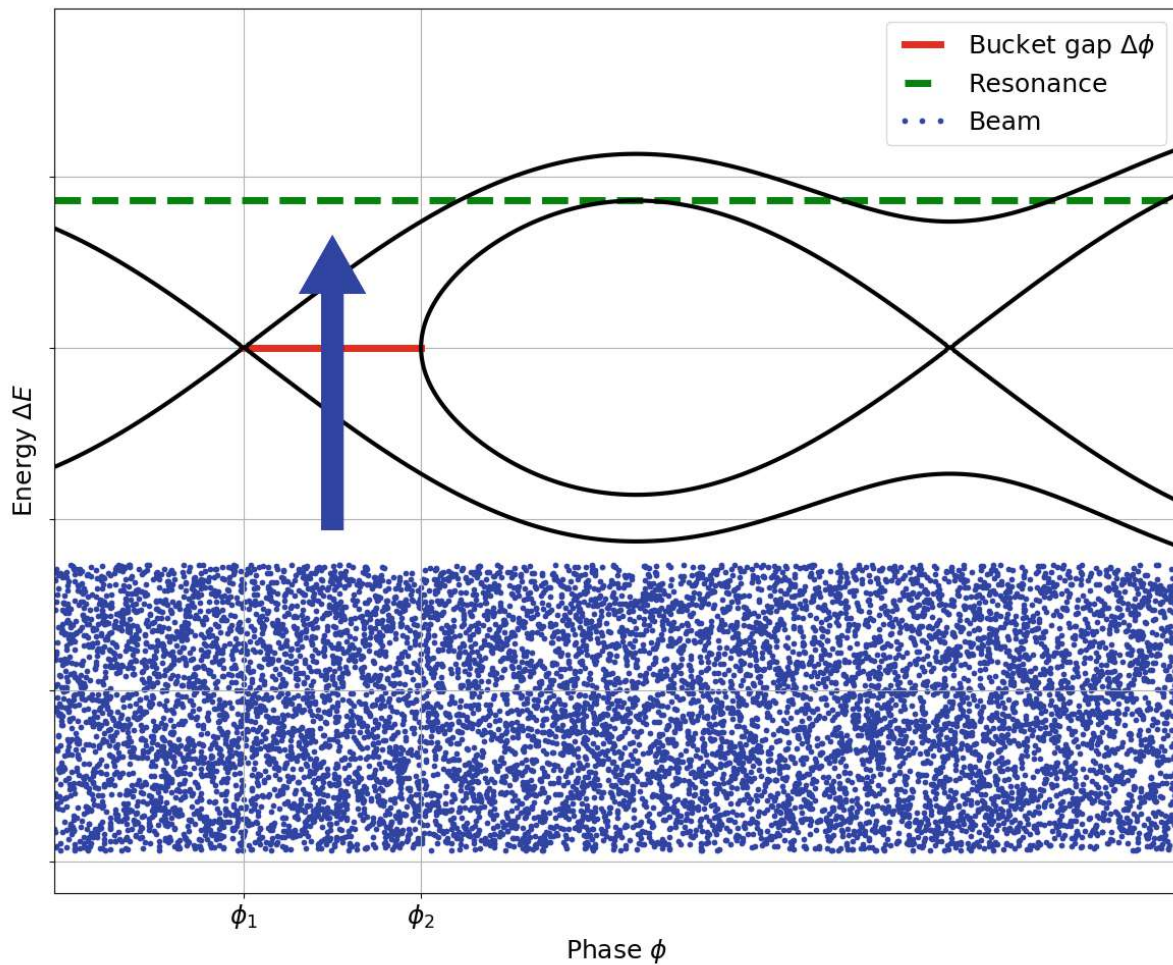


Figure 2.17.: Typical bucket configuration for EBC (modified after [7]).

The empty bucket is positioned above the waiting beam, which is then accelerated via betatron core. The particles are channelled through the bucket gap $\Delta\phi = \phi_2 - \phi_1$ and cross the resonance at high speed. The resonance should ideally align with the bucket separatrix, touching the high-momentum part of the bucket at $\phi = \phi_s$. Particles with non-zero amplitudes are extracted at energies below the resonance, according to the stopband defined by the separatrix in the Steinbach diagram. In theory, the ripple reduction is optimised when the extraction energy of the particles with the highest amplitude is aligned with the centre of the bucket. The relation between the bucket and the resonance region for low- and high-amplitude particles can be controlled by the bucket frequency and voltage.

The speed increase induced by EBC depends on the betatron amplitude and phase of the particles. The mean acceleration $(dE/dt)_{\text{mean}}$ can be derived as

$$\left(\frac{dE}{dt}\right)_{\text{mean}} = -\frac{qV}{2\pi}\omega_0 \frac{2\pi \sin(\phi_s)}{\Delta\phi}. \quad (2.58)$$

Equation 2.58 shows that the particle speed is increased for heavier ions, leading to a better ripple reduction for carbon ions than for protons. A higher bucket voltage V as well as a lower gap width $\Delta\phi$ between the bucket also increases the effect of EBC. The channelling width $\Delta\phi$ can be approximated for small synchronous phases by

$$\Delta\phi \approx 2\sqrt{\pi \sin(\phi_s)} = 2\sqrt{\pi\Gamma} \quad \text{for } \phi_s \ll 2\pi, \quad (2.59)$$

where $\Gamma = \sin(\phi_s)$. Therefore, EBC typically employs a quasi-stationary bucket ($\phi_s \rightarrow 0$) with a high bucket voltage (limited by the hardware restrictions of the RF cavity).

As described above, the bucket frequency and voltage must be selected in a way that the particles are channelled for all betatron amplitudes, so the resonance stopband has to be positioned entirely in the upper half of the bucket, aligning the resonance line for high-amplitude particles with the centre of the bucket. However, experimental evidence (see section 6.3) demonstrates that other bucket configurations, even those without overlapping with the resonance region, can still significantly reduce the ripples [62, 63].

EBC is compatible with all unbunched extraction techniques, provided that the RF cavity is not required for extraction. As the particles cross the resonance in a narrow window of the longitudinal phase, the intensity of the extracted beam is strongly modulated with the RF frequency of the bucket (and harmonics). However, these ripples induced by EBC are at frequencies of a few MHz and are not relevant for clinical treatment, as ripples at such high frequencies are averaged out during the integration time of the dose delivery system.

3. Methods

As part of this thesis, the processes during the extraction are analysed both in simulation and measurement. This section provides an overview over both the tools used for simulating the extraction and the detectors to measure the beam parameters.

3.1. Simulation tools

Simulating the extraction is critical to understand the physics behind the extraction process and to optimise the parameters to improve the quality of the extraction. The simulation tools relevant to this thesis are outlined in this section.

3.1.1. MAD-X

Methodical Accelerator Design (MAD)-X [65] is a versatile tool for studying particle accelerators and beam lines that was developed by CERN and was first released in 2002. It is based on the code MAD-8 and is written in C, C++, Fortran77 and Fortran90. Tool-kits to use MAD-X in a Python framework are available.

MAD-X can be used for a great variety of tasks in designing, studying and optimising a particle accelerator. For this study, it is mainly used to modify the particle optics and for particle tracking during the extraction process with betatron core extraction and RFKO. The general structure of a typical MAD-X script is shown in Figure 3.1. Initially, the sequence is built by loading the defining files. In the element definition file, the properties of the element classes such as the type of the class (e.g. drift space, monitor, dipole, quadrupole, ...), the length of the component or the rotation angles of the entry and exit pole faces are defined. The default starting values for calculating the twiss functions are loaded via the default settings file. The definition file contains the information that maps all components to their respective element classes. The sequence file puts then together the elements with the correct spacing to build the sequence. The aperture file applies the dimensions of the vacuum chamber as physical apertures to all elements, while the strength files provide the initial strengths for all components.

After the sequence is successfully built by loading the aforementioned files, the *TWISS*

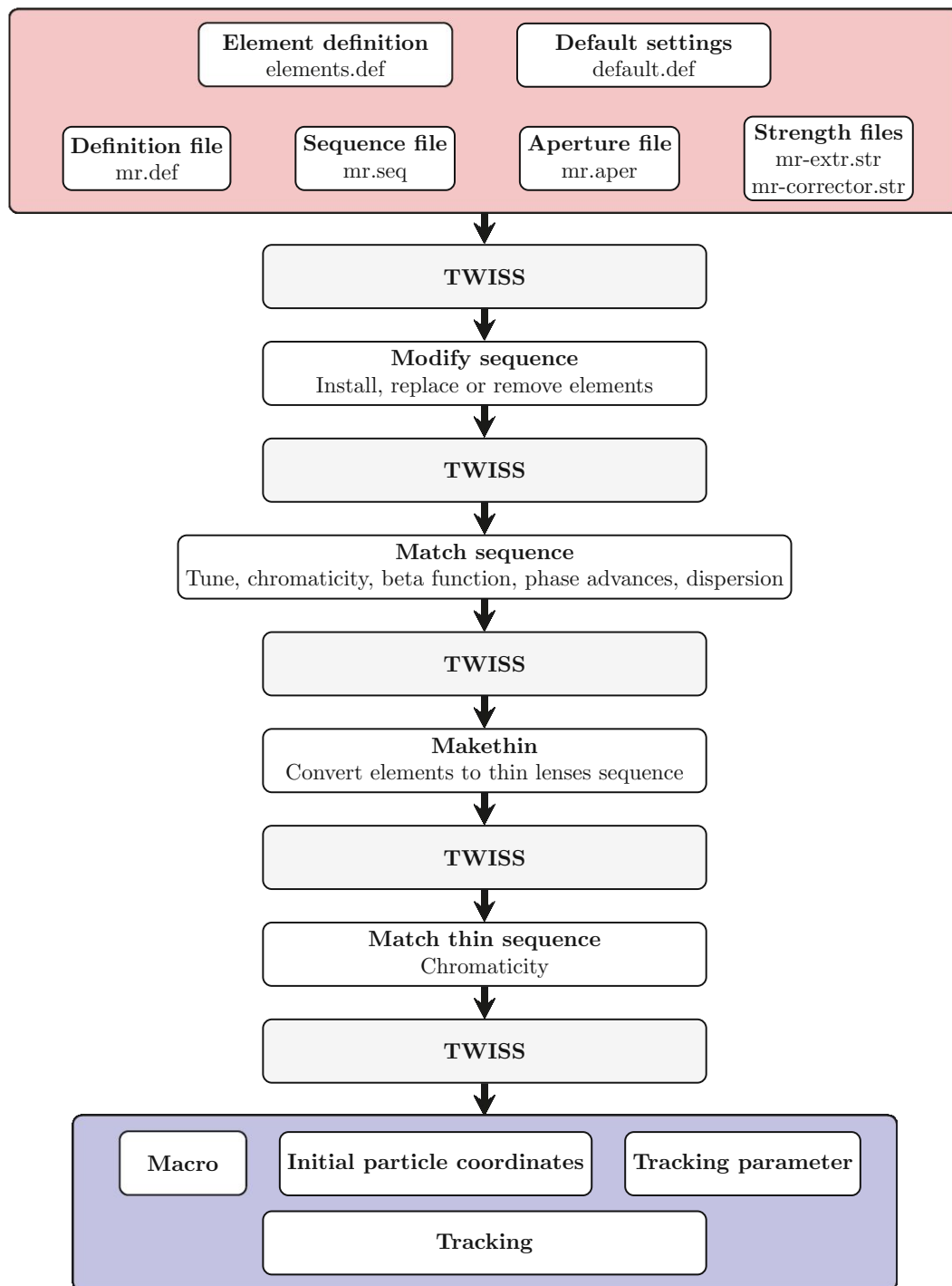


Figure 3.1.: Structure of a typical MAD-X script.

command is executed to apply the changes on the lattice by executing the *USE* command and to calculate the lattice functions.

As a next step, the sequence can be modified by adding, removing or replacing elements. For this thesis, two major modifications were necessary:

1. The betatron core or the RFKO exciter module need to be installed. Both elements were modelled by using the *MATRIX* element class of MAD-X, which allows to apply a kick on any of the particle coordinates.
For betatron core extraction, the *KICK6* property was used, which applies a kick on the particle momentum to simulate the acceleration by betatron core.
For RFKO, this property was changed to *KICK2*, which modifies the horizontal angle x' of the particles, corresponding to a kick in the horizontal plane.¹
2. To identify if a particle is extracted, a marker with an asymmetric aperture was installed on both the start and the end of the electrostatic septum. If a particle exceeds the aperture defined by this markers on the side of the ESE wire, it can be considered as extracted. This speeds up the simulation process, as the tracking is stopped for particles which jump on the other side of the ESE wire and are thus extracted.

After these modifications, the sequence can be matched to the requirements. For this, the strength of the three quadrupole and two sextupole magnet families are varied. It was ensured that the polarity of the magnets is conserved by constraining the allowed variation range. The matching was done for the following parameter:

- Matching the horizontal and vertical tune Q_x and Q_y to the set value.
- Matching the horizontal and vertical chromaticity Q'_x and Q'_y to the set value. As the vertical plane is of minor importance for the extraction process, Q'_y was not matched to an exact value, but rather an acceptable range of $[-4; -1]$ was set to avoid extreme values.
- Limiting the maximum horizontal beta function to 16.6 m in order to avoid a blow-up of the beam size.
- Setting the horizontal dispersion D_x and D'_x to zero at the RF cavity and the injection septum to provide straight sections with zero dispersion, in accordance with [7].

¹For simulating a purely sinusoidal horizontal kick, also the *HACDIPOLE* element class can be used for RFKO simulations.

- The phase advance between the resonant sextupole and the electrostatic septum as well as between the electrostatic septum and the magnetic septum are matched to their design values specified in [12], which are $\Delta\mu_x^{\text{MXR-ESE}} = 229^\circ = 0.64 \cdot 2\pi$ and $\Delta\mu_x^{\text{ESE-MST}} = 51^\circ = 0.14 \cdot 2\pi$, respectively.

After performing the matching and another *TWISS* command, the sequence is converted into thin lenses using the *MAKETHIN* command to allow thin-lens tracking. The sextupoles are sliced in three parts for more accurate tracking results. Dipole edge elements are generated at the start and the end of each dipole to conserve the edge focusing effect from pole face angles.

After the slicing of the magnets, another matching has to be performed to re-match the chromaticity, which might have changed due to the slicing of the sextupoles.

After a final *TWISS* command, the tracking process itself can start. To simulate the extraction, a macro needs to be used to change the lattice parameters during tracking. The following general approach is used:

1. Initially, the strength of the resonant sextupole was set to zero. The ramping of the resonant sextupole is simulated by linearly increasing the magnet strength from 0 to the final value for the first 3,000 turns.
2. To make sure that the configuration has stabilised after the ramping of the resonant sextupole, a waiting time of 500 turns is added before the excitation starts. In this waiting time, the resonant sextupole has reached the final strength, but the strength of the matrix element that is used to excite the beam is still set to zero.
3. After 3,500 turns, the excitation process starts.

For betatron core extraction, the *KICK6* strength is set to a constant value to simulate the momentum push of the betatron core. Simulations showed that a kick per per turn of $(\Delta p/p)_{\text{turn}} = 4 \times 10^{-8}$ is sufficient to extract the beam in $N = 110,000$ turns, resulting in reasonable computation times of 1.3 s per particle for the entire extraction process with the setup used.

The total momentum push 3.1 agrees well with the expected value 3.2 from the momentum distribution of the circulating unbunched beam.

$$\left(\frac{\Delta p}{p}\right)_{\text{total}} = \sum_n \left(\frac{\Delta p}{p}\right)_n = N \cdot \left(\frac{\Delta p}{p}\right)_{\text{turn}} = 4.4 \times 10^{-3} \quad (3.1)$$

$$\stackrel{!}{=} \left| \left(\frac{\Delta p}{p}\right)_{\text{off}} \right| + \frac{1}{2} \left(\frac{\Delta p}{p}\right)_{\text{spread}} = 4.3 \times 10^{-3} \quad (3.2)$$

For RFKO, the kick strength needs to be changed over time to excite the entire momentum distribution, as described in section 2.3.2. This means that it is not sufficient to set the kick to a constant value, as done for betatron core extraction. Due to constraints of tracking with MAD-X, not a sinusoidal excitation with a frequency matched to the beam was utilised, but white noise was used as horizontal kick strength $KICK2$ of the RFKO exciter to simulate the extraction. The Fourier spectrum of white noise contains all frequencies, so it can also be used for beam excitation. Note that as the power is distributed over a broad frequency range, the effective power used to excite the beam is reduced when compared to excitation with a sinusoidal signal. This has to be considered when comparing MAD-X simulation with measurement. However, this difference only affects the temporal evolution of the extraction, but not the characteristics of the extracted beam, which is the main focus of the MAD-X simulations.

The kick amplitude needs to be set to extract the whole beam in the number of turns of the simulation. For 150,000 turns, a kick amplitude of 5×10^{-5} per turn proved to be effective.

The initial particle distribution is generated in Python, saved in a file and loaded into the MAD-X script to access the particle coordinates. An exemplary particle distribution used for RFKO tracking is shown in Figure 3.2

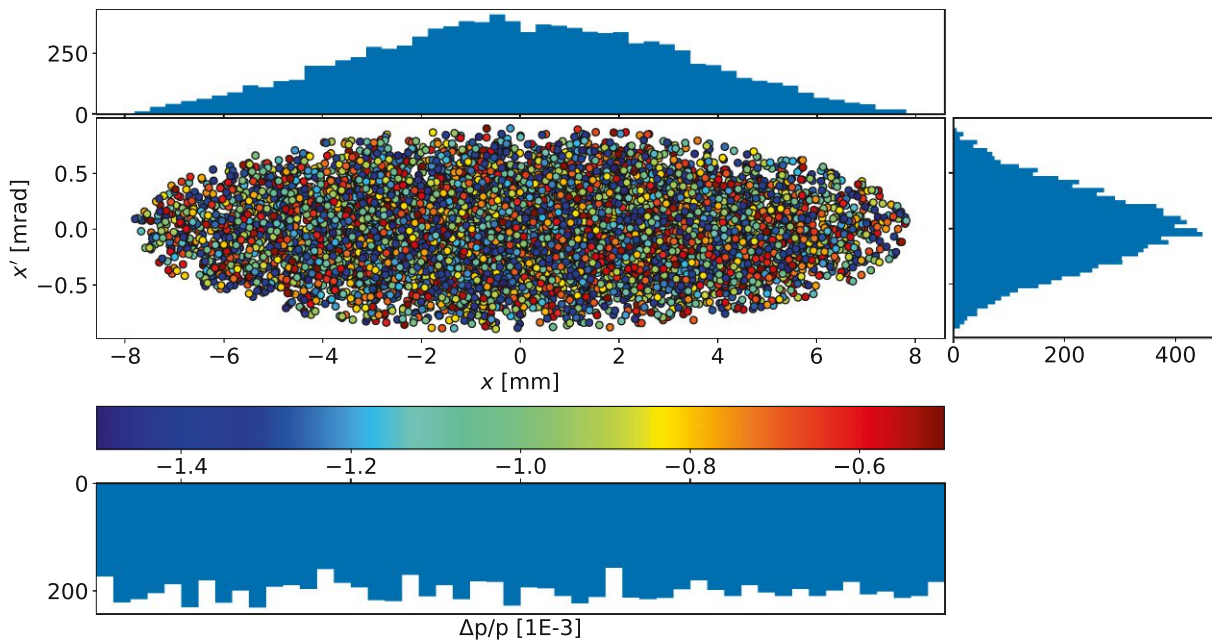


Figure 3.2.: Exemplary initial particle distribution for simulating RFKO.

A centred Gaussian distribution is used for the horizontal position x and angle x' . The standard deviation of the Gaussian distributions were calculated from the design Root Mean Square (RMS) value of the geometric emittance of $\epsilon_{\text{RMS}} = 1.4 \pi \cdot \text{mm} \cdot \text{mrad}$ (for a proton beam with 62.4 MeV) and the horizontal beta function at the injection septum $\beta_x = 8.6 \text{ m}$ [12, 66], using equations 3.3² from [24]. The beam distribution was cut off at 5σ to consider 96.3% of all particles.

$$\begin{aligned}\sigma_x &= \sqrt{\epsilon_{\text{RMS}} \cdot \beta_x} \\ \sigma_{x'} &= \sqrt{\frac{\epsilon_{\text{RMS}}}{\beta_x}}\end{aligned}\tag{3.3}$$

The distribution of the particle momentum ($\Delta p/p$) is implemented as uniform distribution³, centred around the momentum offset $(\Delta p/p)_{\text{off}}$ with a total momentum spread $(\Delta p/p)_{\text{spread}}$ (i.e. the FWHM of the approximated uniform distribution).

Table 3.1 summarises the measured parameter of the longitudinal distribution for a 252.7 MeV proton beam with and without phase jump, which were used to generate the initial momentum distribution for MAD-X tracking.

	$\frac{\Delta p}{p}$ [10^{-3}]	$\frac{\Delta E}{E}$ [10^{-3}]	ΔE [MeV]	Δf [Hz]
Offset w.r.t. resonance	-2.33^4	-4.2	-1.05	-2040
Spread (FWHM, without phase jump)	0.86	1.5	0.39	750
Spread (FWHM, with phase jump)	3.70	6.6	1.67	3240

Table 3.1.: Parameters of the longitudinal distribution of the circulating proton beam with 252.7 MeV before extraction.

After the tracking parameters (e.g. number of turns and observation points) are defined, the MAD-X tracking itself is started. The output contains the 6D particle coordinates of all lost particles (note that due to the asymmetric aperture definition of the ESE, also the extracted particles are treated as lost particles) as well as the turn-by-turn coordinates of all circulating particles. The output files can be accessed via a Python script to plot the particle distribution and to perform further analysis.

²Equations 3.3 are only valid for $\alpha_x = 0$, which is true for the injection septum.

³Without phase jump, the momentum distribution is more Gaussian than uniform. However, for simplicity, a uniform momentum distribution was assumed also for simulating a beam without phase jump.

⁴For RFKO, this parameter was varied during the optimisation process. For the exemplary particle distribution shown in Figure 3.2, a value of -1×10^{-3} was used.

Limitations

While the extraction process is easy to model with MAD-X, there are some serious limitations about what can be simulated with the tool.

Firstly, MAD-X mainly focuses on processes in the transverse phase space, the longitudinal plane cannot be modelled properly. Therefore, techniques taking place in the longitudinal plane like bunched beam extraction and EBC cannot be simulated with MAD-X.

Secondly, MAD-X internally generates an array to store the coordinates for all particles turn by turn. In case many particles are simulated for a high number of turns, the array grows too big to be handled by MAD-X, resulting in a memory overflow error and the abortion of the tracking. MAD-X tracking is therefore limited to approximately 1×10^9 particles \times turns. To exceed this limit, batched processing can be used to split the initial distribution in multiple parts and tracking each sub-distribution one after to other, before finally merging the results to obtain the full picture for the whole distribution.

Thirdly, the expression defined in the macro are called and evaluated every turn, but cannot be changed mid-turn. This means that all particles within one turn receive the same kick, independent of their longitudinal position in the ring. For RFKO, the kick changes with a frequency in the order of magnitude of the revolution frequency of the particles, the kick strength varies significantly for particles with different longitudinal positions, especially for a coasting beam that fills large portions of the ring. This kick variation in sub-turn timescales cannot be reproduced with MAD-X tracking.

Finally, time-dependent kicks cannot be implemented with MAD-X tracking, as only the turn number is available for the expressions in the macro. Because of this, white noise is used to excite the beam instead of a proper sinusoidal signal with frequency or phase modulation⁵. A sinusoidal kick can be set up, but the resulting function would be an approximation of the sine wave with a step function. Additionally, no advanced modulations are possible with the limited options of MAD-X tracking.

These limited flexibility of MAD-X tracking made it necessary to use other tracking codes for a proper simulation of the extraction processes relevant for this thesis. These alternative tools are discussed in the following sections.

⁵Alternatively, *HACDIPOLE* elements can be used to apply sinusoidal kicks. A frequency modulation could be realised by changing the frequency of these elements with a macro.

3.1.2. Beam Longitudinal Dynamics (BLonD)

Beam Longitudinal Dynamics (BLonD) [67] is a 2D tracking code to study longitudinal dynamics and has been developed by CERN since 2014. It can model complex longitudinal processes, such as RF manipulations, the interaction of the bunched beam with the components of the accelerator and corrections of the beam with feedback loops. The 2D phase space evolution can be tracked accurately during capturing, acceleration and extraction, considering collective effects in the frequency and time domain. BLonD allows 2D tracking of the particles in the longitudinal phase space, while the transverse phase space is not considered. For this thesis, BLonD was used to simulate the evolution of the longitudinal phase space distribution during phase jump, EBC and PDE, as all of the mentioned methods require longitudinal manipulation with an RF cavity [68].

BLonD is used within a Python user environment with pre-defined elements to model the RF components of the accelerator. For an RF cavity, the class *RFStation* is used.

```
RFcavity = RFStation(Ring, [h], [V], [dphi], [omega])
```

Ring is a class instance that contains information about the accelerator and the beam, such as length of the ring, bending radius of the dipoles, number of turns, particle type, momentum compaction factor and time-dependent magnetic field to model the acceleration program. *h*, *V*, *dphi* and *omega* are the harmonic number, the voltage, the phase and the frequency (in case the frequency program does not follow the condition $f_{RF} = hf_{rev}$) of the cavity, respectively. The parameters can be given as array to perform tracking with time-dependent settings of the RF cavity, which can be used to simulate moving buckets or bucket voltage changes.

To track the particles in the longitudinal phase space, the class *RingAndRFTracker* can be used.

```
tracker = RingAndRFTracker(RFcavity, beam, periodicity = True)
```

This element uses the RF cavity defined above and a beam distribution in momentum (offset and spread) and phase (bunched or unbunched beam) to track the beam in the ring, as periodicity is forced via the corresponding flag. The longitudinal particle coordinates can be obtained turn-by-turn and plotted together with the separatrix of the bucket to analyse the longitudinal phase space.

BLonD can also simulate the difference between bunched and unbunched beams, as the debunching of the particles can be simulated by setting the cavity voltage to zero.

Limitations

BLonD is only capable of simulating the longitudinal plane, it does not include any effects in transverse phase space. The extraction process can only be modelled indirectly by as-

suming a particle is extracted as soon as its momentum exceeds the momentum defined by the resonance in the transverse plane. By tracking the momentum distribution and checking if the resonance momentum is exceeded turn-by-turn, the extracted particles can be identified and removed from the tracking routine.

The simulation toolkit does not have any information about the lattice of the accelerator, apart from the circumference, the bending radius and the properties of the RF cavity. As BLoND does not 'know' the location and the strength of the magnets, it cannot include these elements and processes like the ramping of the resonant sextupole in the tracking. Additionally, particle losses are not taken into account as no apertures can be defined.

Only certain extraction techniques can be simulated with BLoND. Apart from the longitudinal extraction with Phase Displacement, betatron core extraction can be simulated with the help of the magnetic field, which can be used as surrogate for the acceleration programme. RFKO, Tune Sweep and COSE cannot be simulated as they don't impact the momentum of the particles and are purely transverse extraction techniques.

3.1.3. XSuite

XSuite [69] was developed at CERN since 2021 and is a modern Python simulation toolkit. It combines features from different simulation codes to simulate a broad spectrum of phenomena and applications with great flexibility. A variety of other tools can be introduced to XSuite by dedicated interfaces.

The toolkit is designed in a modular way so that each functional block is isolated from the other components and interaction between the blocks happens through clearly defined interfaces. This 'orthogonal' design ensures that contributors can improve specific components of the code without the a full knowledge of other parts, minimising the complexity of the codebase [70].

The main physics modules of XSuite are summarised in Figure 3.3.

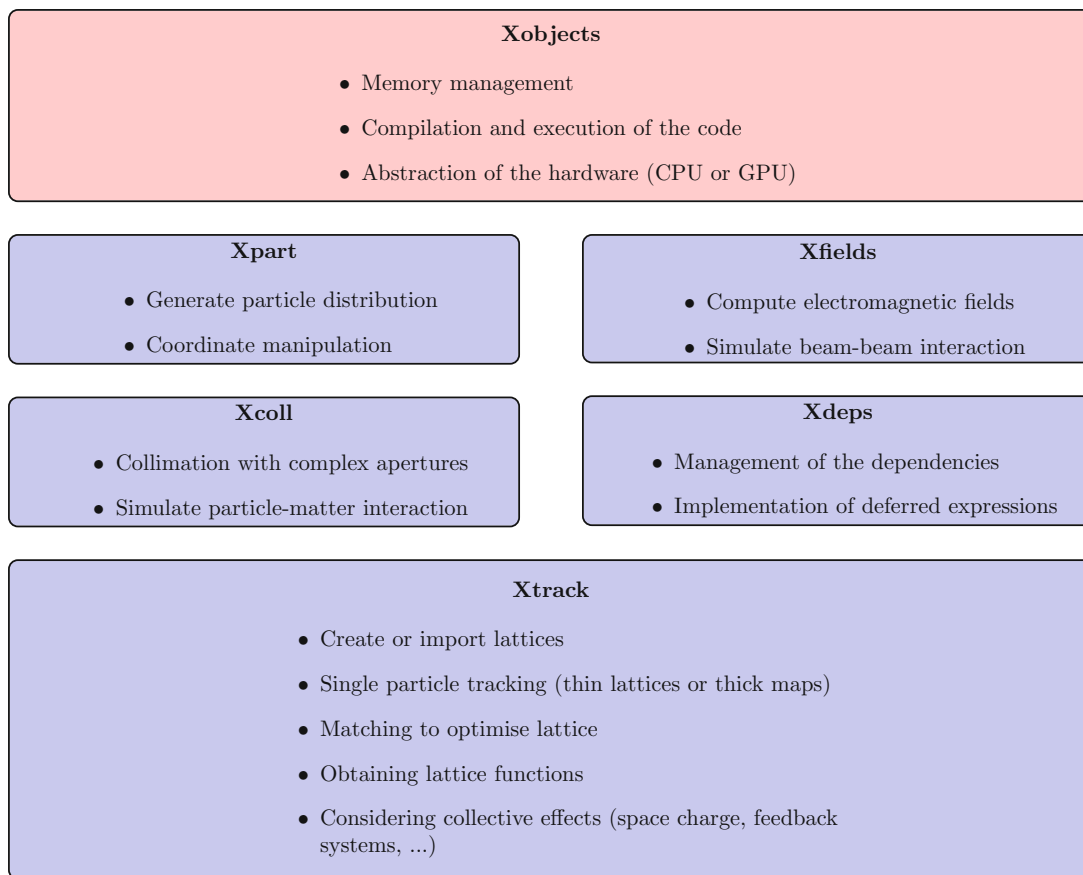


Figure 3.3.: Physics modules of XSuite.

For running XSuite simulations, either a (multi-core) Central Processing Unit (CPU)

or a Graphics Processing Unit (GPU) can be used, allowing a significant reduction of the computation time.

The simulation toolkit runs in a Python user interface and the beam line is represented as a sequence of Python modules, which represents either an accelerator element or a physical process. This setup allows a combination of particle tracking with the possibility to implement custom functions using Python libraries. This is especially important for RFKO, as arbitrary excitation signals can be modelled with Python and used for tracking the extraction process. Full 6D tracking for both transverse and longitudinal plane is possible by including BLoND in the simulation process [70].

3.1.4. Comparison of the simulation tools

Table 3.2 shows a comparison of the capabilities of the mentioned simulation tools.

Can it simulate...	MAD-X	BLonD	XSuite
Betatron Core Extraction	✓	(✓)	✓
RFKO	(✓)	✗	✓
COSE	✓	✗	✓
PDE	✗	(✓)	✓
EBC	✗	(✓)	✓
Ripple transfer	(✓)	✗	✓

Legend:
 ✓: Tool can be used for simulation.
 (✓): Tool can be used for simulations with limitations (see below).
 ✗: Tool cannot be used for simulation.

Table 3.2.: Capabilities of the simulation tools.

MAD-X enables basic simulation of betatron core extraction and COSE. RFKO can only be simulated for certain trivial excitation signals (noise and sinusoidal), and ripple transfer functions can only be computed for dipoles. BLonD is designed to simulate processes in the longitudinal plane, such as PDE and EBC. Given that the extraction takes place in the transverse plane, BLonD does not permit an explicit examination of the extraction process itself. Betatron core extraction can also only be implemented indirectly via a dipole strength ramp. XSuite is the most versatile tool due to its interfaces for including external modules, allowing for the simulation of all processes relevant for this thesis.

MAD-X serves as the primary simulation tool for this thesis, as it is easy to set up and provides a comprehensive framework for simulating most processes relevant for this thesis. BLonD was mainly used to simulate EBC with varying cavity voltages and frequencies, where transverse tracking is not needed. XSuite was initially not available and was only used in the final research phase to study advanced RFKO extraction including frequency, phase, and amplitude modulation.

3.2. Used detectors

At the MedAustron accelerator complex, various detector systems are used to monitor important beam parameters such as beam current, intensity, beam position or beam size. Especially the detectors in the Main Ring and the HEBT up until the treatment rooms are of importance for this study, as they are used to quantify the quality of the extracted beam for the different extraction techniques. This section provides a short overview over the relevant detectors.

The properties of the detectors relevant for this thesis are summarised in Table 3.3. In addition to the listed detectors, additional special detectors and measurement routines were used:

- The MedAustron synchrotron is equipped with one pair of Schottky plates in both planes. As shown in [29] and [30], the Fourier transform of the Schottky signal can be used to measure the momentum distribution as well as the tune and the chromaticity of the beam. For RFKO, the horizontal Schottky plates are used to excite the particles, but the vertical Schottky can still be used for tune and chromaticity measurements. Due to a strong plane coupling, the horizontal tune is visible even on the vertical Schottky, which allows a measurement of both tunes in a single non-destructive measurement.

Figure 3.4 shows a typical tune measurement with the vertical Schottky. The peaks with the largest amplitude (marked with a black line) are the first three harmonics of the revolution frequency at $n \cdot f_{\text{rev}}$, while the sidebands ($n \cdot f_{\text{rev}} \pm q_x$) marked with a red line indicate the horizontal tune. The sidebands ($n \cdot f_{\text{rev}} \pm q_y$) marked in green originate from the vertical tune.

- Tune and chromaticity can not only be measured with the Schottky, but also with an alternative measurement setup with a kicker and a pickup. A dedicated kicker magnet perturbs the beam into oscillations, which are measured by the pickup and analysed via a Fast Fourier Transformation (FFT) to obtain the tune. With this measurement, only the particle tune at the momentum offset of the beam can be acquired. To calculate the lattice tune at $\Delta p/p = 0$, the measurement has to be repeated for different momentum settings by changing the radial position of the beam. An interpolation of the data points and an extrapolation to $\Delta p/p = 0$ results in the lattice tune, while the slope of the linear fit corresponds to the chromaticity. In contrary to the tune measurement via Schottky, an external kick needs to be applied that affects the beam, which means that this method is invasive and cannot be performed parasitically while taking other measurements. However, the precision

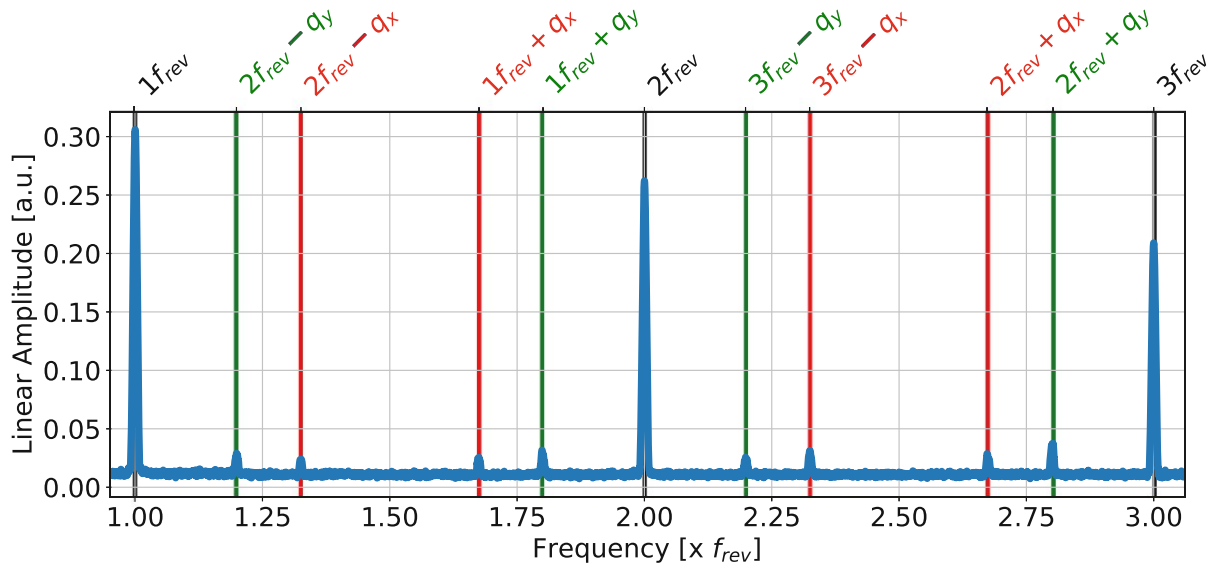


Figure 3.4.: Tune measurement with the vertical Schottky.

and resolution of the Schottky tune measurement is worse compared with the pickup measurement.

- A Synchrotron Low-Level Controller (SLC) measurement is used to record the parameters of the RF cavity and control loop signals. For this thesis, mainly the cavity voltage, the beam frequency as well as the radial position and phase of the beam are of interest. The measurement is non-destructive and can be performed in parallel to other activities. The radial and phase loop signal can only be measured when the beam is bunched, as the pickups only record noise for an unbunched beam.

	Current Transformer System (CTS)	Pick-up coils	Quality Intensity Monitor (QIM)	Scintillating Fiber Hodoscope (SFX)	Dose Delivery Monitor (DDM)	Isocenter Monitor (ICM)	CIVIDEC [®] detector
Location	Main Ring	Main Ring	HEBT	HEBT	Nozzle in irradiation room	Isocenter	Isocenter
Measured quantity	Circulating current in the MR	Beam position	Beam intensity	Beam position, width and intensity	Beam position, width and intensity	Beam position, width and intensity	Intensity
Used for (in this thesis)	Losses, extraction efficiency	Trajectory of the beam in the ring	Extracted intensity, ripple studies	Trajectory of the beam in the HEBT	Beam parameters at nozzle	Beam parameters at isocenter	Ripple studies
Destructive measurement?	No	No	Yes	Yes	No	n.a.	n.a.
Maximum sampling rate	1 kHz	1 kHz	50 kHz	4 Hz	50 Hz	10 Hz	78 MHz

Table 3.3.: Properties of detectors relevant for this thesis.

4. Implementation of RFKO at MedAustron

This chapter describes the testing and implementation of Radio Frequency Knock Out at MedAustron as main part of this thesis. The hardware and software setup as well as the simulations and measurements carried out to find optimised settings for RFKO are also presented.

The advantages of RFKO and the reason why clinical treatment benefits from using this extraction method are discussed in section 2.3.3.

The implementation of RFKO in other facilities has been detailed in several studies, including [71–76].

4.1. RFKO setup

This section describes the system design for RFKO. A multi-staged approach was used to generate a signal suitable for RFKO. On the software side, a remotely controllable GnuRadio script [77] is used to generate the excitation signal. The script contains the building blocks to generate both FM and PSK excitation, with the ability to add multiple bands to extend the excitation spectrum. Attachment B contains a schematic view of the GnuRadio script used in this thesis. Calculation of the base frequency requires the revolution frequency and the horizontal particle tune, which can be obtained from measurement.¹ Additionally, the parameters required to produce the excitation waveform, such as the bandwidth and sweep frequency for FM and the shift frequency for PSK (refer to section 4.4) as well as the gain of the signal can be set and adjusted as input in the script.

The digital signal set up by the GnuRadio script is then generated using an *Ettus USRP X310* Software Defined Radio (SDR), connected to the GnuRadio laptop via Ethernet cable. The SDR is equipped with a *Kintex 7-410T* FPGA with 406,000 logic cells and a streaming bandwidth of 200 MS/s. Additional daughterboards operating between DC and 30 MHz are used to receive and transmit high-frequency signals required for the RFKO signal generation.

¹In future it might be possible to automatically read in the revolution frequency via a direct connection to the MedAustron measurement devices and control system infrastructure.

The SDR output is fed through a 1 kW amplifier. An RF switch between the SDR and the amplifier receives a toggling signal from the control system, which opens the connection at `StartExtraction` and closes it at `StopExtraction` to prevent beam excitation during acceleration or capture of the beam.²

After amplification, the signal is transmitted to the synchrotron hall via an RF cable. Prior to application on the exciter planes, an impedance matching network in the form of an RF BalUn is utilised, which was built as part of a project thesis [78]. As the $50\ \Omega$ impedance of the amplifier is connected to the excitation plates with an estimated impedance of $1\ \text{k}\Omega$, this impedance matching network is necessary in order to minimise transmission losses and potential signal reflections. Additionally, the BalUn also splits the original RF signal in two signals with a phase difference of 180° , which are applied on the inner and the outer plate of the exciter module.

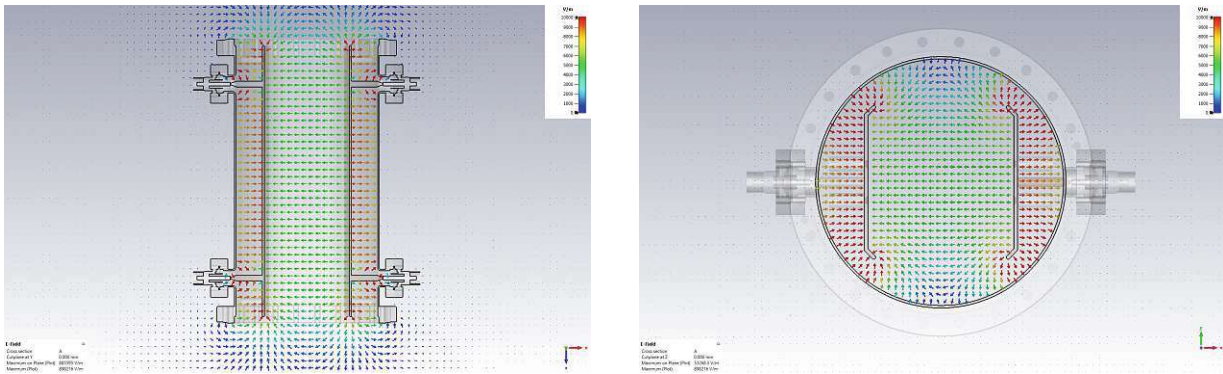
In the absence of a dedicated RFKO exciter at the existing MedAustron lattice, the horizontal Schottky plates ($l_{\text{eff}} = 0.95\ \text{m}$) are currently being used to apply RF kicks on the beam. However, it is not an ideal solution for RFKO due to the C-shaped structure of the electrodes, as shown in Figure 4.1, which may result in field inhomogeneities affecting the RFKO kick. Figure 4.1b shows these minor inhomogeneities near the curved part of the electrodes in the simulated static electric field using CST Studio Suite³. However, the beam is close to centred when passing through the Schottky monitor and its size is smaller than the dimensions of the device. Therefore, the particles are not getting close to the non-homogeneous parts of the electric field and the device remains suitable for RFKO excitation.

An additional problem with using the Schottky monitor as RFKO exciter is that the plates cannot be used as a monitor if they are facilitated to apply a kick, so an important measurement device in the ring is not available during RFKO operation. In order to implement RFKO as the standard extraction method for the MedAustron International Particle Therapy Accelerator (MAIPTA), a dedicated exciter is foreseen that can be utilised for RFKO, without having to use the Schottky plates.

To read out the kick applied by the plates, the signal is measured via a 65 dB attenuator and visualised with an oscilloscope, which can be accessed remotely to confirm in real time that a correct RFKO is being applied and to allow post-processing of the stored kick data.

²In future, it would be beneficial to feed the trigger signal directly into to SDR, which allows a direct control of the extraction without the need of an external RF switch. This is crucial for any implementation of amplitude modulation of the signal during the spill.

³<https://www.3ds.com/products/simulia/cst-studio-suite>.



(a) View from the top.

(b) View from the front.

Figure 4.1.: View from the top and the front of the horizontal Schottky device and the simulated static electric field. (courtesy of Dale Prokopovich)

Figure 4.2 shows a schematic representation of the current RFKO setup at MedAustron. The setup is under continuous development and will be further improved for future use.

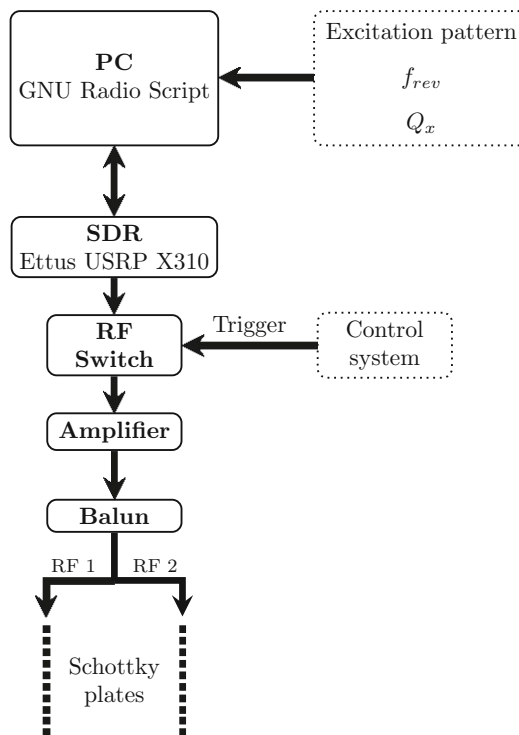


Figure 4.2.: Schematic RFKO setup at MedAustron.

4.2. Parameter optimisation

The quality of the beam extracted with RFKO is highly dependent on the parameter setpoint of the machine. The main machine parameters affecting the extraction are:⁴

- Horizontal tune Q_x
- Horizontal chromaticity Q'_x
- Momentum offset of the beam $(\Delta p/p)_{\text{off}}$
- Integrated strength of the resonant sextupole $K_{2,\text{res}}$
- Transverse emittance of the beam ϵ
- Vertical tune Q_y and chromaticity Q'_y
- For bunched RFKO: bucket height
- Strengths of the electrostatic septum (ESE) and the magnetostatic septum (MST)

The position of the beam in momentum space can be controlled by the momentum offset, while the position of the resonance in momentum space is defined by the horizontal tune. The strength of the resonant sextupole and the horizontal chromaticity Q'_x define the slope of the edge of the Steinbach diagram in $(\Delta p/p, A)$ space and thus the distance of the beam to the resonance. The transverse emittance is proportional to the maximum amplitude of the beam and therefore defines the distance in amplitude from the Steinbach edge.

The vertical tune and chromaticity do not affect the extraction itself as much as their counterparts in the horizontal plane, but they are important to avoid any additional resonances and to keep the beam in a stable state at flattop.

The bucket height affects longitudinal effects that are only relevant for bunched RFKO, such as the synchrotron motion of the particles in the bucket. Finally, the ESE and MST settings are important to compensate for angle mismatch and to properly transmit the extracted beam to the room.

The impact of the machine parameters on the extraction setup is visualised in Figure 4.3.

⁴Also the excitation parameters affect the extraction, but they can be treated independently of the machine parameters. For the optimisation of the RFKO excitation see section 4.4.

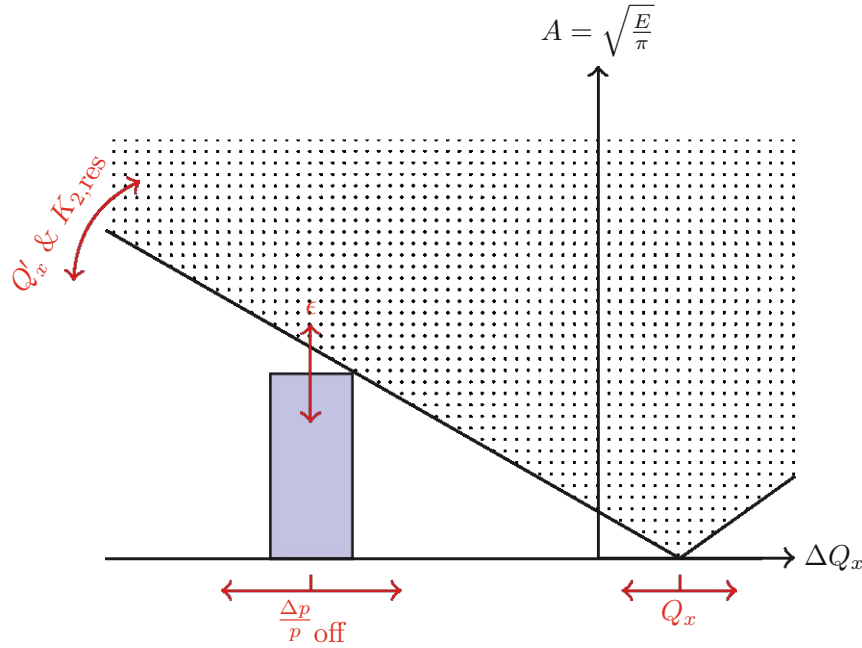


Figure 4.3.: The impact of the machine parameters on the extraction setup.

To identify the best machine parameters for RFKO, the objectives of the optimisation must be defined. A detailed discussion of the parameter optimisation for RFKO at MedAustron can be found in [36].

- The **extraction efficiency** η_{ex} should be reasonably high, ideally well above 90%. η_{ex} is defined as the number of particles extracted from the Main Ring during the spill divided by the number of particles at flattop, as defined in equation 4.1.

$$\eta_{\text{ex}} = \frac{N_{\text{extracted}}}{N_{\text{flattop}}} \quad (4.1)$$

- The **spiral step** ΔX_3 is defined as the change in particle position between the third-to-last turn before extraction and the turn where it is extracted. It quantifies how far the particles jump over the septum wire. As a first approximation, it can be assumed that the particle was already very close to the septum wire three turns before extraction. Therefore, the spiral step is the particle position at extraction minus the position of the ESE wire.

If the spiral step is insufficient, the losses due to particles hitting the septum wire will increase. Conversely, if the spiral step is too large, the particles will hit the vacuum

chamber wall on the outer side of the ESE. A spiral step of 10 mm is considered ideal, which is close to the theoretical value of 9.2 mm for betatron core extraction [12].

- The **beam distribution at the electrostatic septum** is chosen to closely resemble the beam distribution obtained by default betatron core extraction. This minimises the probability of unexpected beam behaviour during commissioning reduces the need for significant changes to the machine configuration, particularly in the HEBT. Note that as the Hardt condition cannot be fulfilled for the low-chromaticity configuration for RFKO, the angular spread of the beam at the ESE is always larger than for betatron core extraction, where the Hardt condition is at least partially met. The centre of gravity of the angle does not have to be considered as optimisation goal, as any offset can be easily corrected by changing the strength of the kick applied by the ESE.
- Small fluctuations in the currents of the synchrotron components can cause changes in parameters, particularly the tune and chromaticity. During the commissioning of RFKO, it may be necessary to make slight adjustments to certain parameters to ensure a reproducible configuration of the synchrotron. Therefore, it is crucial to set the working point at the centre of a plateau where the key parameters, such as extraction efficiency and beam distribution, are not affected by minor changes in the machine configuration.

If we consider not only the extraction process itself, but also the propagation of the beam further downstream from the ESE, we can define more optimisation objectives:

- It is important to avoid beam losses not only for extraction, but also for the **transmission of the beam from the ESE to the MST**. Therefore, the transmission efficiency η_{tr} , which is defined as the ratio of particles reaching the MST to the particles extracted at the ESE, should be maximised.
- As shown before, the beam distribution parameters at the ESE should be as similar as possible to the betatron core case. This also applies to the **beam distribution at the MST**. Minimising the differences reduces the effort required for re-commissioning the HEBT and propagating the beam to the treatment room.
- Finally, the **horizontal beam dispersion D_x at the MST** should be negative. This allows for a matching process similar to the one used for betatron core extraction and prevents any dispersion flips in the HEBT.

4.2.1. Extraction

To determine the optimal configuration for RFKO extraction with regard to the optimisation objectives listed above, a multi-dimensional scan of the horizontal tune, the horizontal chromaticity and the momentum offset of the beam was performed. The extraction was simulated with MAD-X for 100 particles and 1.5×10^5 turns for each parameter combination, using RFKO excitation with random noise with an amplitude of 5×10^{-5} . Figure 4.4 displays the results of the scan.

The plots of extraction efficiency (first row) confirm the existence of areas with high η_{ex} for all momentum offsets. The 'high-efficiency region' becomes steeper as the momentum offset increases, and the chromaticity acceptance for a given tune becomes smaller. For on-momentum RFKO, the region with high extraction efficiency is almost flat with acceptable horizontal tunes ranging from 1.6707 to 1.6747, as the chromatic tune shift disappears.

The second and third rows display the centre of gravity and the spread (i.e. the spiral step) of the horizontal position of the extracted beam of the ESE. Since one side of the extracted distribution is fixed by the position of the ESE wire at -35 mm, the spiral step also determines the centre of gravity of the position, making the latter a redundant optimisation parameter. The higher the horizontal tune offset $\Delta Q = Q_x - Q_{res} + Q'_x \cdot (\Delta p/p)$ is, the smaller becomes the spiral step. Similar to the extraction efficiency plots, the area (marked with solid lines) where the spiral step is within ± 1 mm from 9.8 mm, which is the value for betatron core extraction, gets steeper for higher momentum offsets, which means that the chromaticity acceptance benefits from lower absolute values of the momentum offset. For all momentum offsets, regions can be identified where the 'high-efficiency region' overlaps with the area with acceptable spiral steps.

The final row shows the angle spread of the extracted beam at the ESE. As previously stated, the angle spread is generally larger than for betatron core extraction due to the inability to meet the Hardt condition with RFKO settings. Only a few regions can be identified where the angular spread is comparable to betatron core extraction, and these occur at low momentum offsets and high absolute values of the chromaticity. This is because the Hardt condition is closer to being fulfilled for a chromaticity similar to the betatron core setting of $Q'_x = -4$. The closer the configuration is to on-momentum operation, the smaller the angular spread becomes.

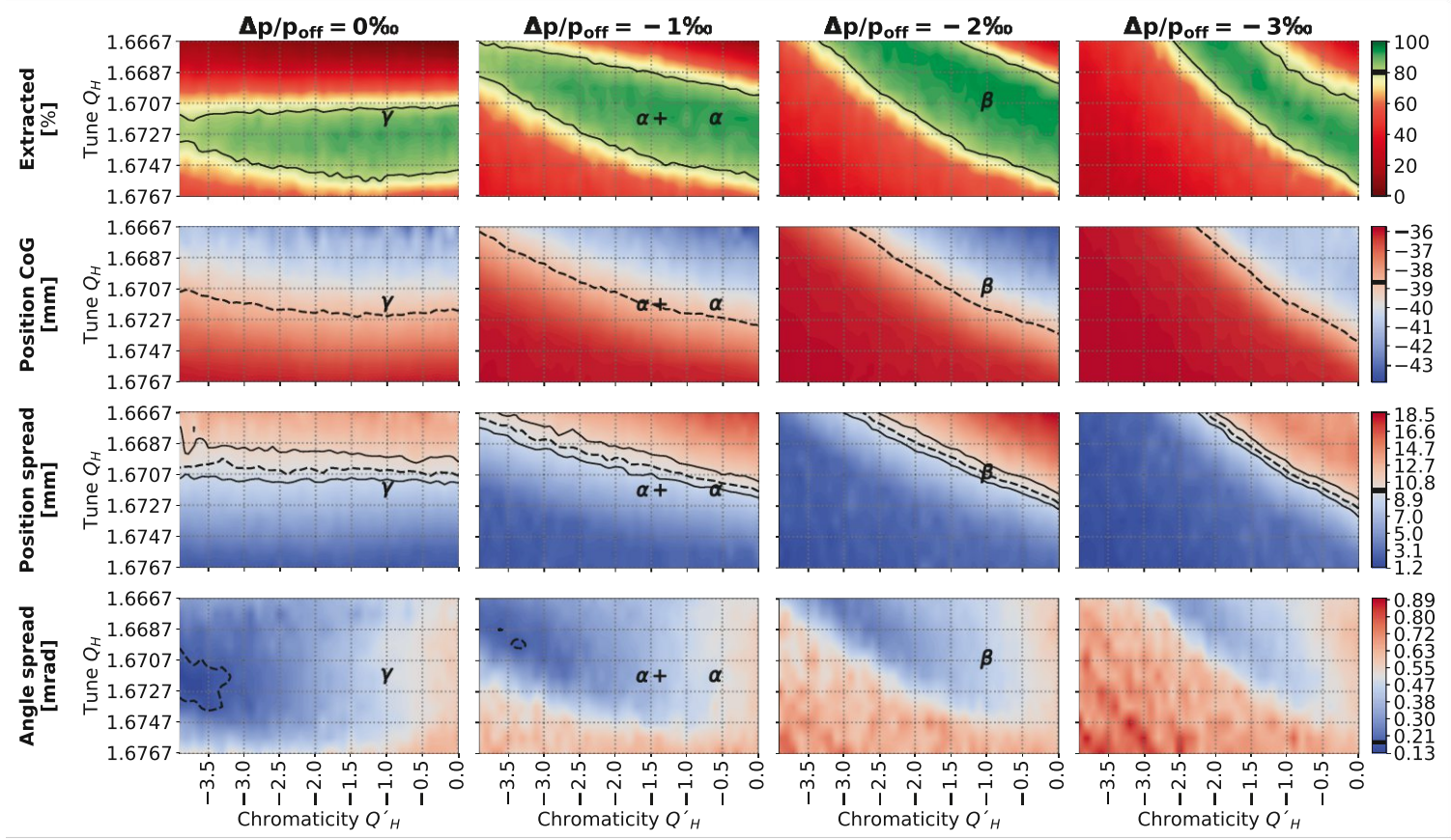


Figure 4.4.: Tune-chromaticity scans with different momentum offsets for RFKO optimisation at the ESE. The columns show the results for momentum offsets of 0 , -1×10^{-3} , -2×10^{-3} and -3×10^{-3} , respectively. For the extraction efficiency (first row), the areas with $\eta_{\text{ex}} > 90\%$ are highlighted. For the beam distribution parameter, the values for betatron core extraction are marked with a dashed line. The promising candidates for RFKO listed in Table 4.1 are marked with the corresponding Greek letter.

The resonant sextupole strength is a crucial parameter for extraction optimisation as it affects both the spiral step and the slope of the unstable area in the Steinbach diagram. Figure 4.5 shows the extraction efficiencies and spiral steps resulting from a scan of the resonant sextupole strength for the settings ($Q_x = 1.6717$, $Q'_x = -0.6$, $(\Delta p/p)_{\text{off}} = -1 \times 10^{-3}$)⁵.

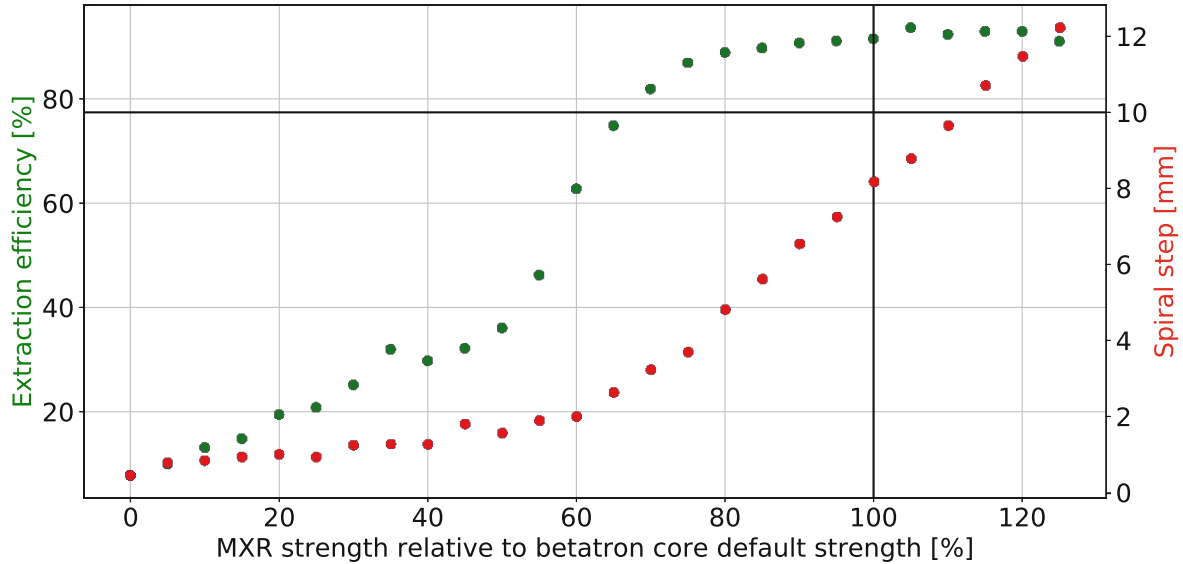


Figure 4.5.: Extraction efficiency and spiral step for $\text{KOE}\alpha$ for different strengths of the resonance sextupole.

The extraction efficiency plateaus at over 90% efficiency for sextupole strengths above 85% of the nominal strength for betatron core extraction. An analysis of the losses reveals that for lower MXR strengths, the reduced spiral step is the primary cause of losses, as it causes particles to hit the ESE wire. Losses due to insufficient particle excitation and incomplete extraction (resulting from insufficient resonance opening) are additional factors contributing to ultra-low strengths below 30% of the nominal value. On the other hand, increasing the strength of the resonant sextupole to more than 115% of the default value leads to losses due to particles being too close to resonance, as the Steinbach edge becomes so flat that it starts to hit the high-amplitude particles in the waiting beam before extrac-

⁵This setting was chosen as it is a promising candidate with a high extraction efficiency and acceptable beam distribution parameters at the ESE. As discussed in section 4.2.2, this candidate also performs well when considering the transmission from the ESE to the MST. This setting is abbreviated with $\text{KOE}\alpha$ for a clear nomenclature (see Table 4.1).

tion. Furthermore, it is not possible to achieve ultra-high sextupole strengths in practice due to limitations imposed by the existing magnet hardware and its current capacity.

The spiral step increases linearly in the plateau region of the extraction efficiency, ranging from 5.6 mm for 85 % sextupole strength to 12.2 mm for 125 %. The target value of 10 mm is reached at 110 % of the nominal strength. Furthermore, the spiral step can be adjusted within a wide range of 5.6 to 12.2 mm without impacting the extraction efficiency or other relevant beam parameters, which might be relevant for future commissioning work.

It should be noted that the presented findings in this section are only applicable for a geometric beam emittance of $1.4 \pi \cdot \text{mm} \cdot \text{mrad}$ ⁶. The resulting extraction efficiencies are highly dependent on the emittance of the beam, as a higher-than-nominal emittance decreases the distance to the unstable area in the Steinbach diagram. This could result in losses at flattop before the excitation begins, as some high-amplitude particles are too close to resonance. Figure 4.6 shows the simulation results for the dependence of the beam distribution parameters on the emittance for $\text{KOE}\alpha$.

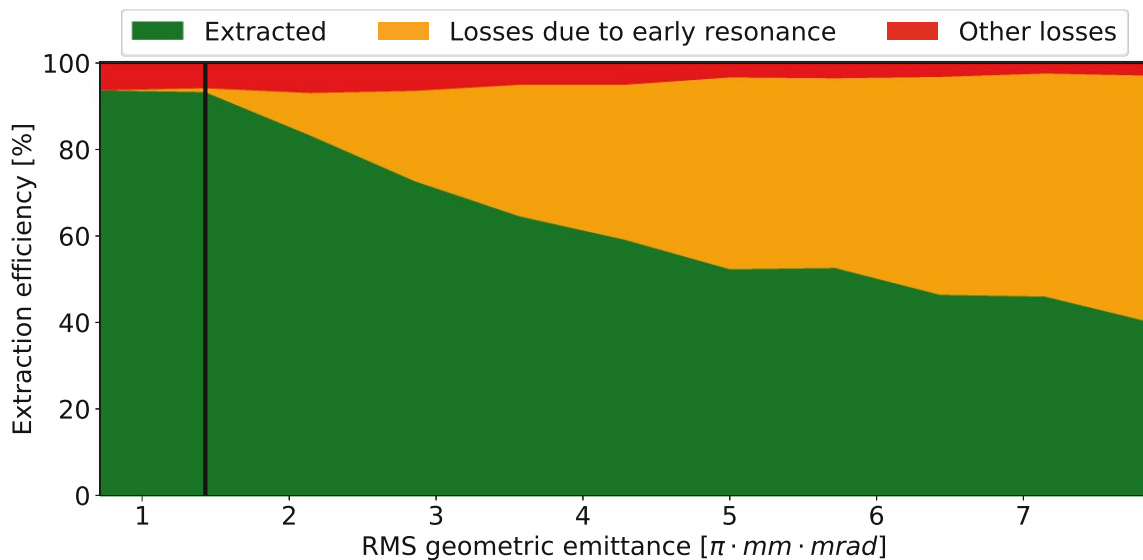


Figure 4.6.: Extraction efficiency for $\text{KOE}\alpha$ for different beam emittances.

Figure 4.6 displays the extraction efficiency in green, while losses due to particles being too close to resonance and being extracted before excitation are shown in yellow. The remaining losses (shown in red) are primarily due to particles hitting the ESE wire (an

⁶This is the value of the 1σ -emittance. The beam distribution was cut off at 5σ .

effective ESE width of 0.5 mm was used for this simulation) because of insufficient spiral step, and are not significantly impacted by the beam emittance. The efficiency of extraction decreases significantly as the beam emittance increases, while the losses of particles too close to resonance increase. At the nominal geometric emittance of $1.4 \pi \cdot \text{mm} \cdot \text{mrad}$ (marked with a black vertical line), the extraction efficiency is over 93 %, with less than 1 % of particles lost due to being too close to resonance. However, for a doubled emittance, the extraction efficiency drops to below 73 %, and the losses due to early resonance crossing increase to 21 %.

These results are not surprising, as the entire parameter optimisation process was based on the assumption of a beam distribution with nominal emittance. The size of the stable triangle was optimised to precisely encompass the beam with nominal emittance, which explains the losses observed for higher-than-nominal emittances. Figure 4.6 highlights the importance of precise measurement of the Main Ring emittance for an effective implementation of RFKO. For the MedAustron synchrotron, it was demonstrated in [66] that the actual Main Ring emittance is in good agreement with the design value.

At this point, possible setpoints for RFKO extraction can be identified by balancing the requirements defined above. The settings for the four most promising candidates are listed in Table 4.1 and are also marked with the corresponding Greek letter in Figure 4.4. The best candidate was identified for momentum offsets of 0, -1 and -2×10^{-3} , respectively. For $(\Delta p/p)_{\text{off}} = -1 \times 10^{-3}$, two candidates $\text{KOE}\alpha$ and $\text{KOE}\alpha+$ were chosen for reasons explained in section 4.2.2.

Candidate	Hor. tune Q_x	Hor. chromaticity Q'_x	Momentum offset $\left(\frac{\Delta p}{p}\right)_{\text{off}}$
$\text{KOE}\alpha$	1.6717	-0.6	-1×10^{-3}
$\text{KOE}\alpha+$	1.6717	-1.5	-1×10^{-3}
$\text{KOE}\beta$	1.6706	-1	-2×10^{-3}
$\text{KOE}\gamma$	1.6717	-1	0

Table 4.1.: Promising candidates for RFKO extraction.

All four candidates are situated in an area with a high extraction efficiency and the properties of the particle distribution at the electrostatic septum are similar to those of the betatron core extraction. The centre of gravity of the particle position is closest to the betatron core extraction for $\text{KOE}\alpha$, while the spiral step is optimised best for $\text{KOE}\beta$. The spiral steps for the other candidates are slightly reduced to values between 7.3 and 8.8 mm. The angle spread is the smallest for $\text{KOE}\alpha+$, but still more than twice as high as for betatron core extraction.

Table 4.2 summarises the relevant beam distribution parameters⁷ at the ESE for all four promising RFKO candidates and compares them to the distribution parameters for betatron core extraction.

Candidate	Extraction efficiency [%]	Position CoG [mm]	Spiral step [mm]	Angle spread [mrad]
KOE α	92.0	-38.9	8.8	0.59
KOE α +	89.2	-37.9	7.3	0.49
KOE β	91.9	-38.9	9.3	0.56
KOE γ	86.8	-38.8	8.3	0.53
Betatron Core	92.0	-38.7	9.8	0.18

Table 4.2.: Horizontal distribution parameters for RFKO candidates at the ESE in comparison with betatron core extraction.

4.2.2. Transmission from the ESE to the MST

When considering the transmission from the ESE to the MST, the tune-chromaticity scans for different momentum offsets can be repeated with the MST as the observation point. For this, the extracted particle distribution at the ESE for each combination of momentum offset, tune and chromaticity is tracked via simulation from the ESE to the MST using MAD-X. The combined efficiency (which is the extraction efficiency multiplied by the transmission efficiency) as well as the beam parameters at the MST are plotted in Figure 4.7. The ESE kick strength was adjusted for each combination to compensate for the offset of the mean angle at the ESE. This was achieved by changing the applied kick so that the total angle change $\Delta x'_{\text{total}} = k_{\text{ESE kick}} + x'_{\text{mean, ESE}}$ for all combinations is identical to the total angle change for betatron core extraction. Only combinations with a combined efficiency greater than 5% were plotted. This is because combinations where only a few particles reach the MST can result in significant statistical fluctuations of the beam parameter, which would distort the overall trends.

⁷The following sections discuss only the distribution in the horizontal plane, as the extraction takes place in this plane. The vertical beam distribution remains unaffected during extraction and does not impact the parameter optimisation.

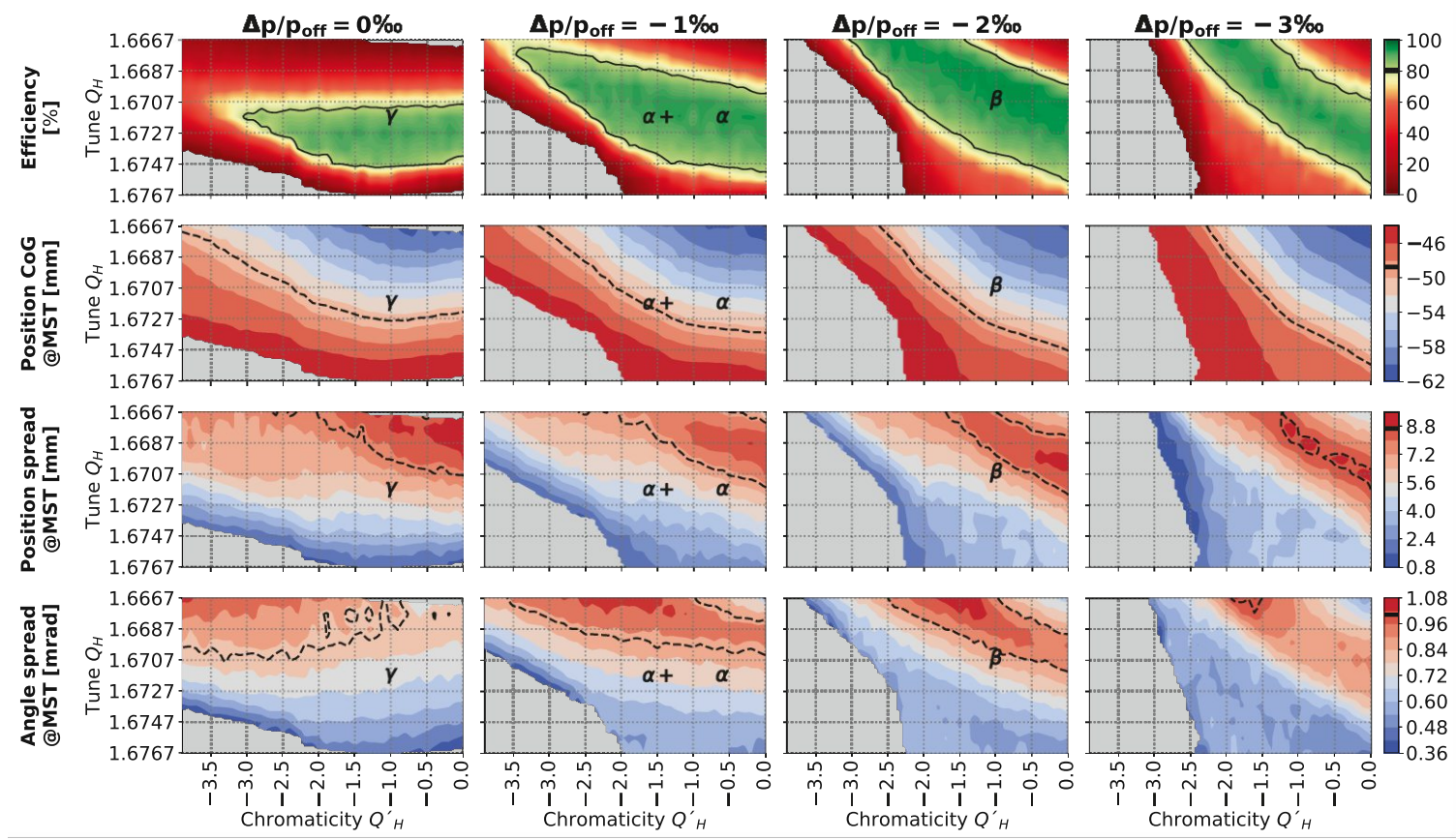


Figure 4.7.: Tune-chromaticity scans with different momentum offsets for RFKO optimisation at the MST. The columns show the results for momentum offsets of 0 , -1×10^{-3} , -2×10^{-3} and -3×10^{-3} , respectively. For the beam distribution parameter, the values for betatron core extraction are marked with a dashed line. Areas with less than 5% efficiency are masked in grey. The promising candidates for RFKO listed in Table 4.1 are marked with the corresponding Greek letter.

When considering transmission to the MST, the part of Figure 4.4 with high absolute values of chromaticity is removed. This is because particles are lost between the ESE and the MST for these tune-chromaticity combinations. However, for small absolute values of the chromaticity, almost all extracted particles reach the MST, resulting in a combined efficiency equal to the extraction efficiency. The trend observed in the extraction simulation, where the region with good extraction efficiency becomes steeper for higher momentum offsets, is also evident when considering the combined efficiency.

The plot of the mean position and position spread reveals that settings with similar values regarding the position distribution at the MST to those for the betatron core extraction can be identified within the area of high combined efficiency. The mean position increases for higher tunes, while the position spread decreases. For on-momentum operation, the position distribution shows almost no dependency on the chromaticity. Non-zero momentum offsets result in an increase of the mean position and a decrease of the position spread for higher absolute values of the chromaticity. Similar to the combined efficiency, the dependence on the chromaticity becomes stronger for higher momentum offsets, resulting in a steeper pattern.

Table 4.3 summarises the parameters of the beam distribution at the MST for the four RFKO candidates and betatron core extraction.

Candidate	Combined efficiency [%]	Position CoG [mm]	Position spread [mm]	Angle CoG [mrad]	Angle spread [mrad]
KOE α	92.0	-49.3	7.3	1.18	0.89
KOE α +	89.2	-47.7	5.9	1.30	0.82
KOE β	91.9	-46.1	6.5	1.79	0.93
KOE γ	86.7	-52.4	6.5	0.55	0.86
Betatron	92.0	-48.9	8.7	1.03	1.00

Table 4.3.: Horizontal distribution parameters for RFKO candidates at the MST in comparison with betatron core extraction.

Dispersion at the MST

The beam distribution at the magnetostatic septum also shows the impact of the tune-chromaticity combinations on the dispersion at the MST. The dispersion was evaluated by dividing the vector from the phase space centre of gravity for the high-momentum particles to the one for the low-momentum particles by the momentum difference.

$$\begin{bmatrix} D_x \\ D'_x \end{bmatrix} = \frac{1}{\max(\Delta p/p) - \min(\Delta p/p)} \left(\begin{bmatrix} x_{\text{CoG}} \\ x'_{\text{CoG}} \end{bmatrix}_{\text{high } \Delta p/p} - \begin{bmatrix} x_{\text{CoG}} \\ x'_{\text{CoG}} \end{bmatrix}_{\text{low } \Delta p/p} \right) \quad (4.2)$$

The beam distribution at the MST and the resulting dispersion vector for $\text{KOE}\alpha$ and $\text{KOE}\alpha+$ is shown in Figure 4.8.

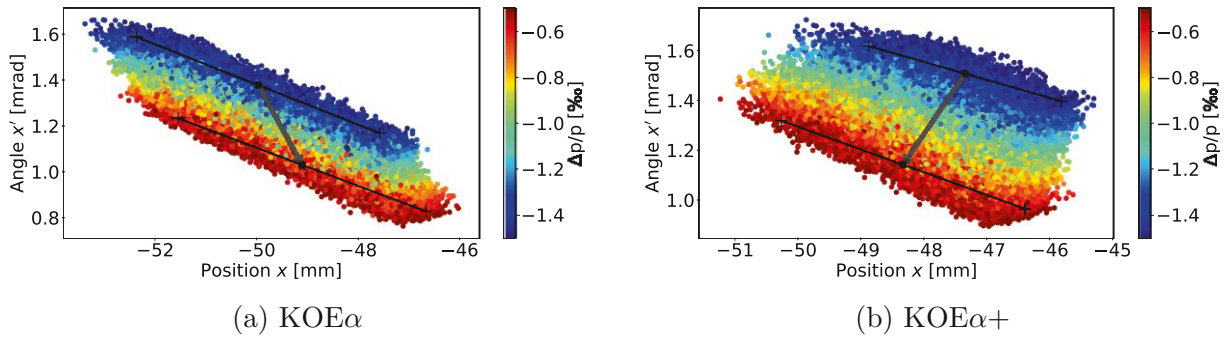


Figure 4.8.: Horizontal dispersion at the MST entry.

While D_x is positive for $\text{KOE}\alpha$, its sign is flipped for $\text{KOE}\alpha+$. This difference in the beam distributions originates in the different spiral steps for high- and low-momentum particles for different chromaticities. Simulations showed that a negative dispersion at the MST is favourable for commissioning, as it allows matching with reasonable Twiss parameters. Table 4.4 summarises the dispersion at the MST for the RFKO candidates.

Candidate	D_x [m]	D'_x [rad]
$\text{KOE}\alpha$	0.91	-0.36
$\text{KOE}\alpha+$	-1.04	-0.38
$\text{KOE}\beta$	-0.41	-0.37
$\text{KOE}\gamma$	0.38	-0.38
Betatron Core	-5.48	-0.50

Table 4.4.: Dispersion at the MST for RFKO candidates.

ESE kick strength

As mentioned above, the optimised ESE kick strength is obtained by comparing the mean horizontal angle x' at the ESE with the default value from betatron core extraction and compensating the ESE kick accordingly. The resulting compensated kick strengths for the four RFKO candidates are shown in Table 4.5

Candidate	ESE kick [mrad]
KOE α	-2.34
KOE $\alpha+$	-2.55
KOE β	-1.97
KOE γ	-2.81
Betatron Core	-2.50

Table 4.5.: Compensated ESE kick for RFKO candidates.

The required ESE kick strengths show that only small adaptations of the default kick of -2.50 mrad are needed to compensate for the angle offset for RFKO. The kick has to be reduced by 6.4 % for KOE α , as for this candidate, the particles are extracted with a lower mean angle than for betatron core extraction. For KOE $\alpha+$, the mean angle is higher, requiring an kick strength increased by 2 %. KOE β requires the lowest kick strength of 79% of the nominal value, while the kick needs to be increased by 12% for KOE γ .

As the ESE kick strength affects the trajectory of the beam after extraction, it also impacts the transmission efficiency from the ESE to the MST and further to the treatment room. A scan of the ESE kick was performed to identify the limits for acceptable efficiency. The beam intensity at the first SFX after the MST was measured for different ESE kicks for KOE $\alpha+$ settings and a proton beam with 252.7 MeV. The results of the scan are shown in Figure 4.9. For other RFKO candidates, the scan results vary slightly due to differences in particle distribution at the ESE. However, these discrepancies are marginal, and the main conclusions from the measurement remain valid for all candidates. The nominal kick strength for betatron core extraction $\Delta x' = -2.5$ mrad is denoted as vertical line.

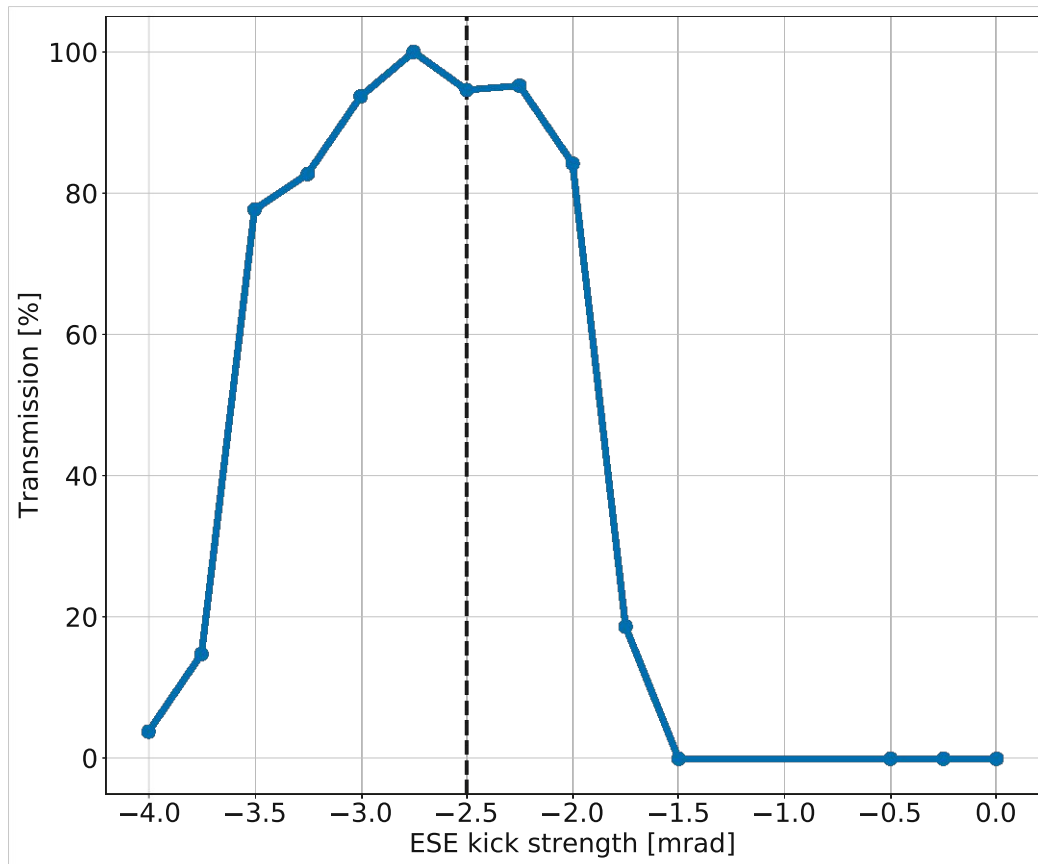


Figure 4.9.: Measured transmission from the ESE to the MST for different ESE kick strengths (KOE α +, proton beam, 252.7 MeV).

The kick strength scan confirms that nearly the entire beam is transmitted from the ESE to the MST for ESE strengths ranging from -3.5 to -2 mrad. Beyond this range, losses increase as particles hit the aperture of the elements between the septa. All of the optimised ESE kicks for the four RFKO candidates listed in Table 4.5 are within this high-transmission region. The value for KOE β is already at the threshold where transmission efficiency decreases, resulting in increased losses and necessitating an adjustment of the ESE kick.

4.3. Beam stability measurements

To compare the results of the optimisation simulations in practice at the MedAustron synchrotron, the settings obtained from simulation have to be tested and measured in the real synchrotron. Especially the stability of the beam is of importance to ensure that the extraction is solely guided by the RFKO excitation signal, and other instabilities or beam losses do not affect the beam.

4.3.1. Tune measurement

As the tune scans showed that the extraction is sensitive to changes of the horizontal tune, a tune measurement was performed to ensure that the working point of the machine is at the correct tune. Both horizontal and vertical tune and chromaticity were measured using both the Schottky monitor and the tune kicker, as described in section 3.2. There is no significant difference between the values obtained from the two measurement methods.

The tune measurements showed that there is an offset between the matched tune in MAD-X and the real tune in the machine, which might come from effects in the synchrotron that cannot be modelled in simulation, such as quadrupole strengths errors or slightly incorrect calibration curves. This offset is energy-dependent and needs to be considered during the MAD-X matching, in order to obtain the correct tune settings in reality.

With this offset corrected, the tune measurements showed that real machine tune and chromaticity are very close to the simulated values for $\text{KOE}\alpha$, as shown in Table 4.6 for a proton beam with 252.7 MeV.

	Q_x	Q'_x	Q_y	Q'_y
Simulation	1.6716	-0.60	1.7900	-3.00
Measurement	1.6717	-1.36	1.7931	-3.31

Table 4.6.: Comparison of simulated and measured values for tune and chromaticity for a proton beam with 252.7 MeV with $\text{KOE}\alpha$ settings.

While the measured tunes agree really well with the simulated values, the chromaticity is not matched as well and is closer to $\text{KOE}\alpha+$. However, it is still very much in the acceptable range. A higher absolute value of the horizontal chromaticity leads even to a more favourable dispersion at the MST, so the measured values are within acceptance and the setting can be used for further studies.

4.3.2. Beam stability for unbunched beam

The first tests with the optimised machine settings summarised in Table 4.6 were performed with a coasting beam. To ensure that the amplifiers are still powered during the whole extraction and thus the signal from the SDR is correctly amplified, the accelerator is set up as for bunched beam extraction. However, the cavity voltage is ramped down to zero just before extraction, so that the beam is debunched and can spread over the whole synchrotron. To avoid any remaining effects from small cavity voltage noise, the cavity frequency is set to an offset of 15 kHz with regard to the waiting beam, making sure that a remaining bucket cannot interfere with the beam. To minimise the momentum spread of the beam, no phase jump is applied.

Figure 4.10 shows the temporal evolution of the particle current in the Main Ring without any excitation for the $\text{KOE}\alpha$ settings. It shows that only marginal losses occur when the resonant sextupole is ramped (marked with a dashed green line at StartMXR) and the beam can be kept at flattop for the whole extraction period. This shows that the distance of the beam to the resonance is big enough so that no unwanted uncontrollable early extraction takes place when particles getting into resonance without any excitation. The overall particle losses during flattop and extraction phase are below 5%.

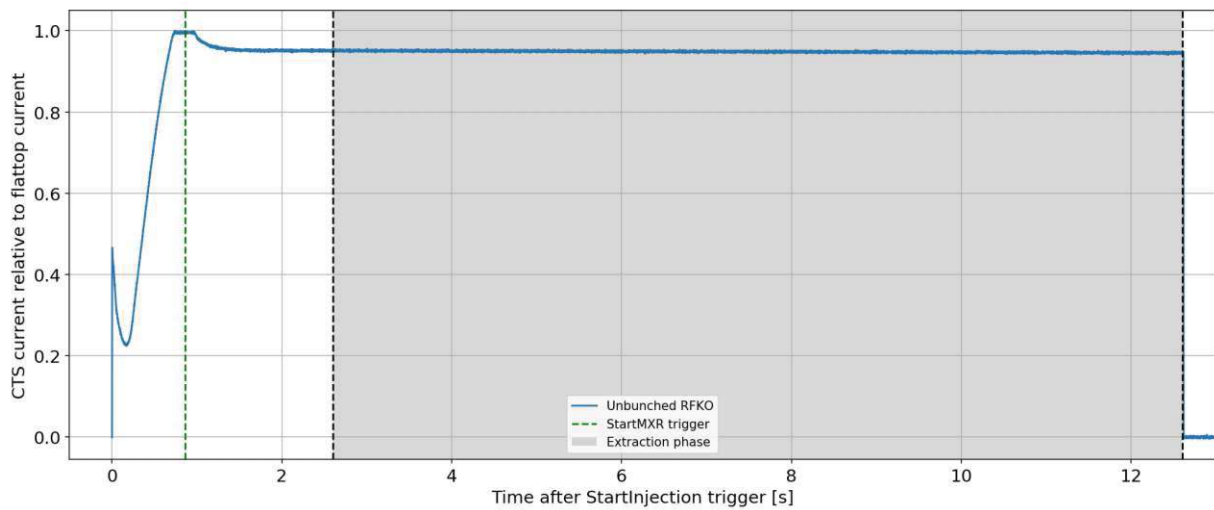


Figure 4.10.: Particle current in the Main Ring for unbunched RFKO without any excitation ($\text{KOE}\alpha$, proton beam with 252.7 MeV).

4.3.3. Beam stability for bunched beam

One of the main advantages of RFKO is its compatibility with bunched beam extraction, which allows for multi energy extraction. To keep the beam inside the bucket during extraction, the bucket voltage must not be ramped down to zero.

If the CTS measurement without excitation for unbunched beam with $KOE\alpha$ settings shown in Figure 4.10 is repeated for bunched beam, the current data shows significant immediate losses when the resonant sextupole is ramped, but also during the extraction phase, where the particles are slowly getting lost. As the transverse settings are identical for unbunched and bunched RFKO, it suggests that the losses originate in an effect in the longitudinal plane, which also explains why these losses cannot be reproduced in MAD-X simulations with 4D tracking in the transverse plane only. Figure 4.11 compares the losses for bunched and unbunched RFKO.

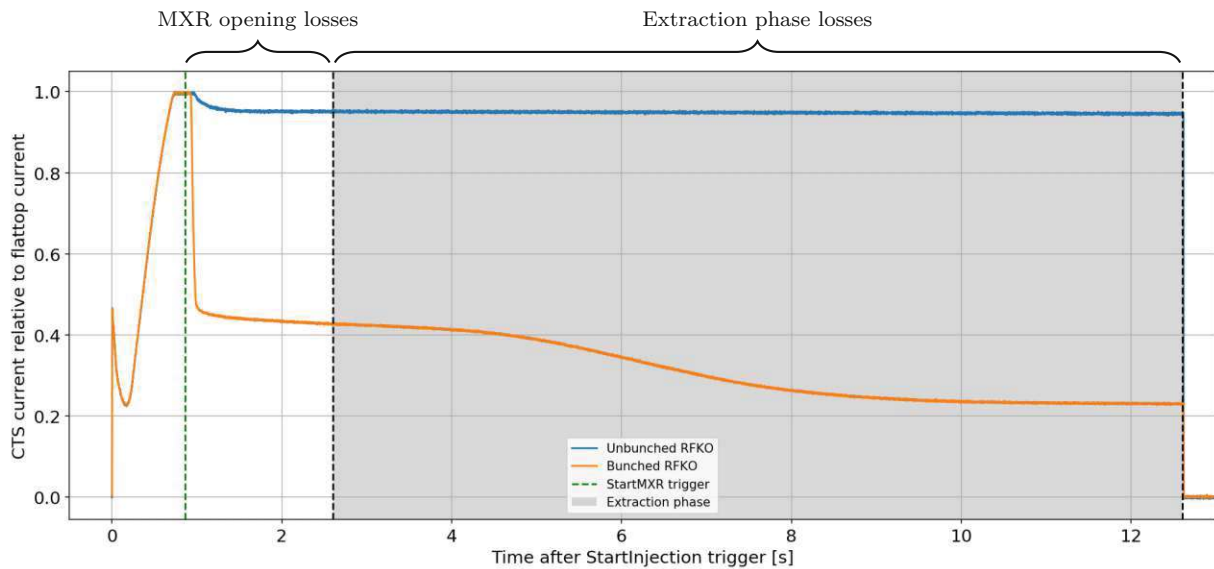


Figure 4.11.: Comparison of the CTS particle current in the Main Ring for bunched and unbunched RFKO with a momentum offset of -1×10^{-3} without any excitation ($KOE\alpha$, proton beam with 252.7 MeV).

The total losses are 77% of the number of particles at flattop. More than 50% of the particles at flattop are lost while the resonant sextupole is ramped, further 27% are slowly lost in the extraction phase. An additional problem is that these slow losses during the extraction phase cannot be controlled, so particles might reach the patient without a possibility to control, which is obviously not acceptable for clinical usage. Because of this, it is necessary to investigate measures to mitigate these losses.

The origin of the losses for bunched beam operation can be found in a frequency mismatch between the beam and the bucket, occurring when the RF loops are turned off, as demonstrated in [79]. This mismatch leads to an offset of the beam in the bucket and oscillations with the synchrotron frequency. These oscillations can also be observed in the Schottky spectrum, as multiple sidebands appear, separated by the synchrotron frequency. Figure 4.12 shows the Schottky spectrum for a typical bunched beam with clearly visible sidebands due to the bucket oscillations. The mean separation between the six highest peaks (shown as vertical red lines) is 740 Hz, which is close to the synchrotron frequency of 700 Hz.

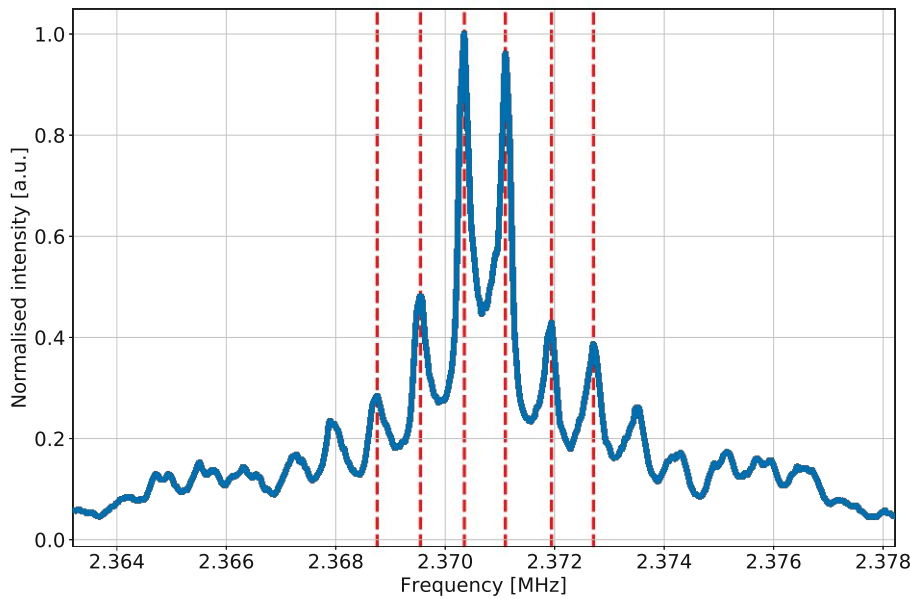


Figure 4.12.: Schottky spectrum for bunched beams (KOE α , proton beam, 252.7 MeV).

The oscillations in longitudinal phase space lead to a variation of the particle momentum and thus the particle tune, which can be enough to extract the particles in close proximity to the resonance.

As the frequency mismatch could not be easily corrected at the time of the measurement, two approaches are available to mitigate the losses for bunched RFKO:

- Increasing the momentum offset to move the beam further away from resonance. This can be done by changing the radial loop position to a higher value. However, it is important to note that changing the momentum offset of the beam also affects the distribution of the extracted beam, as demonstrated in section 4.2. It is crucial

to consider the decrease in the spiral step when going to higher momentum offsets, as this may result in increased losses if the spiral step becomes too small.

- Limiting the amplitude of the oscillations by decreasing the cavity voltage to reduce the bucket size. For the nominal bucket voltage of 660 V, the bucket size δ_B is 3.46×10^{-3} , which is approximately four times larger than the momentum spread of the bunched beam. This large bucket size permits high-amplitude oscillations of the beam within the bucket, contributing to the loss mechanism previously described. However, if the cavity voltage is reduced to 100 V, the bucket size decreases to 1.34×10^{-3} , bringing it much closer to the momentum spread of the beam and thereby limiting these oscillations.

The measurement for bunched RFKO with $\text{KOE}\alpha$ settings was repeated with lower voltage settings of 100 V, resulting in a current measurement showed in Figure 4.13. The losses are compared with unbunched RFKO and the baseline bunched RFKO with nominal RF voltage.

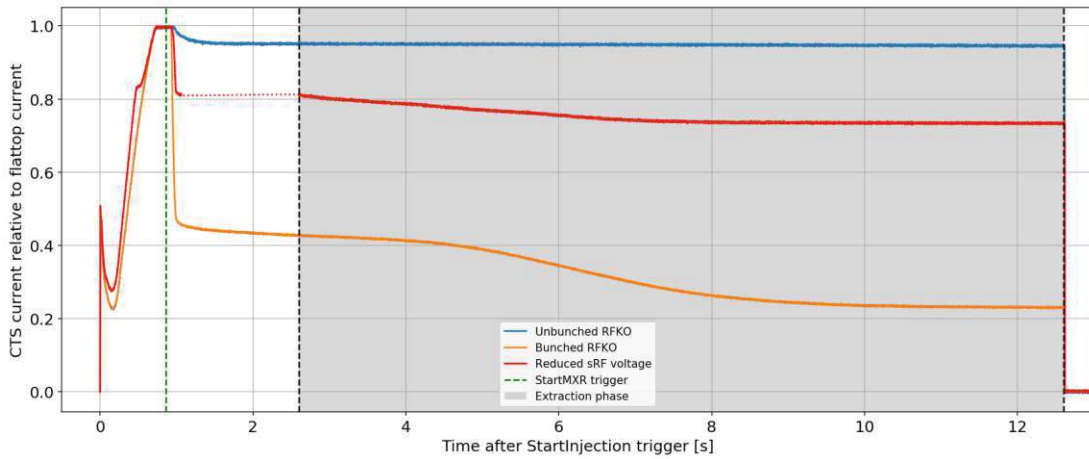


Figure 4.13.: Beam stability for bunched RFKO with reduced RF voltage ($\text{KOE}\alpha$, proton beam with 252.7 MeV).

Reducing the RF voltage clearly helps limiting the losses for bunched beam operation. The losses incurred during the ramping of the resonant sextupole are reduced by more than half to 19%, while only an additional 7% is lost during the extraction phase.

Although the reduced RF voltage improves the situation, the overall losses of 26% are still unacceptably high for clinical operation. Therefore, a combination of both approaches is needed. It was found that reducing the RF voltage and additionally moving to a higher radial loop position of 20 mm (corresponding to a momentum offset of -2.3×10^{-3}) achieves

the goal of almost no losses for a proton beam with 252.7 MeV. Additional measurements showed that the RF voltage can be further reduced to 70 V to improve the beam stability even more. Any bucket voltages below 70 V would result in a bucket height smaller than the momentum spread of the beam and would thus lead to increased losses.

The resulting CTS plot for the hereby optimised settings for bunched RFKO with $KOE\alpha$ settings is shown in Figure 4.14. The total losses are below 5% and thus comparable with

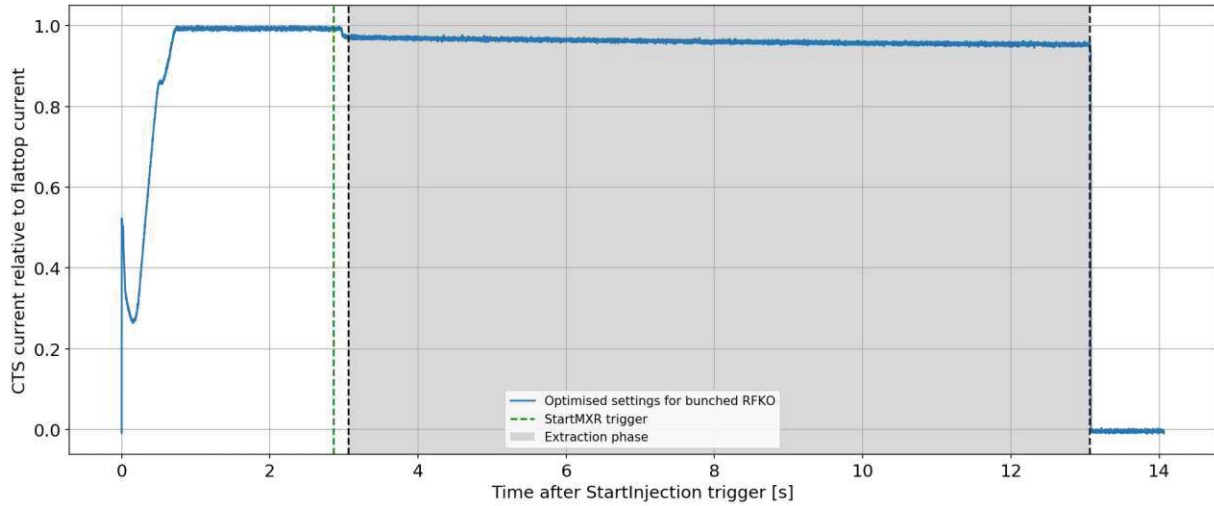


Figure 4.14.: Beam stability for optimised settings for bunched RFKO (radial loop position at 20 mm, RF voltage at 100 V) without any excitation ($KOE\alpha$, proton beam with 252.7 MeV).

unbunched RFKO. To quantify the changes in the beam distribution parameters when moving the momentum offset from -1×10^{-3} to -2.3×10^{-3} , a dedicated simulation of the extraction for both momentum offsets was performed. As the beam is further away from the resonance, the spiral step is reduced by 0.5 mm to 7.5 mm for the higher absolute value of the momentum offset. The simulation of the extraction efficiency confirms that this small change in the spiral step should not increase the losses and can be accepted. Related to the reduction of the spiral step, the centre of gravity of the position of the extracted beam is also shifted by 0.5 mm. Due to the dispersion vector at the ESE, the centre of gravity of the angle is also affected by the changed momentum offset and varies from -0.5 to -1 mrad. As mentioned before, this angle offset can easily be corrected via adjusting the kick strength of the ESE. The angle spread as well as the momentum distribution of the extracted beam is not affected by the change in the momentum offset.

This means that the $KOE\alpha$ settings with the RF voltage reduced to 70 V and an in-

creased radial loop position of 20 mm are a proper configuration for RFKO with bunched beam⁸. For unbunched RFKO, the modification of the radial loop is not necessary, as the beam stability is already acceptable for the nominal radial loop position of 8.6 mm. However, it would be advisable to also use the increased radial loop position of 20 mm for unbunched RFKO, to ensure a proper comparability between bunched and unbunched operation.

⁸The optimisation was focused on a proton beam with 252.7 MeV. Other energies and particles types may require a different optimisation, which is beyond the scope of this thesis. However, singular measurements for a proton beam with 62.4 MeV as well as for a carbon beam with various energies confirmed that the optimised settings might be similar to the studied case of a proton beam with 252.7 MeV.

4.4. Excitation patterns

In this section, the optimisation of the excitation signal itself is shown. Especially the amplitude of the signal and the excitation frequency and its modulation is important to increase the extraction linearity and efficiency.

4.4.1. Signal amplitude

The amplitude of the excitation signal controls the extraction rate and thus the spill length of the extracted beam. It can be directly controlled via the gain setting of the GnuRadio script [77].

The maximum kick that can be applied on the circulating beam depends on the maximum effective kick voltage, the kicker geometry and the momentum of the beam, and can be calculated with equation 4.3 [74].

$$\phi_x = \tan^{-1} \left(\frac{|E_x| \cdot q \cdot l_{\text{eff}}}{p \cdot \beta_r} \right) \quad (4.3)$$

ϕ_x is the deflection angle, q the charge of the particles in units of the elementary charge, l_{eff} the effective length of the kicker, p the momentum of the beam in eV/c and β_r the relativistic Lorentz factor. E_x is the electric field of the kicker, that can be calculated by dividing the effective peak-to-peak voltage by the distance between the plates.

At MedAustron, the effective length of the Schottky plates that are used as the kicker is 0.95 m. The plates are at a distance of 6 cm.⁹ The maximum power P_{el} of the amplifier is 1 kW, the impedance R_{el} of the electric line is 50 Ω . This electronic setup results in an peak-to-peak voltage given in equation 4.4.

$$V_{\text{p-p}} = 2 \cdot \sqrt{2 \cdot P_{\text{el}} \cdot R_{\text{el}}} = 2 \cdot \sqrt{2 \cdot 1000 \text{ W} \cdot 50 \Omega} = 632.45 \text{ V} \quad (4.4)$$

Thus, the maximum electric field of the kicker plates is $E_x = V_{\text{p-p}}/d = 10\,533 \text{ V/m}$.

The maximum deflection angles that can be achieved with the kicker setup at MedAustron for different particle types and beam energies are summarised in Table 4.7 and plotted for the clinical energy ranges for both proton and carbon beams in Figure 4.15¹⁰.

⁹As discussed in section 4.1, the electrode plates of the Schottky are C-shaped, which means that the equations for parallel plates are not valid. However, they can still be used as a good approximation for the more complex geometry of the kicker. The distance of 6 cm is measured at the closest point of the C-shape.

¹⁰These calculations are only valid for a perfect impedance matching, so that the signal is fully transmitted to the Schottky plates and no losses or reflections occur.

Particle type	Beam energy [MeV/u]	Maximum deflection angle [μrad]
Proton	252.7	22.15
Proton	62.4	82.76
Carbon	402.8	7.32
Carbon	120.0	22.11

Table 4.7.: Maximum deflection angles with the MedAustron kicker for different particle types and beam energies. Calculation based on equation 4.3.

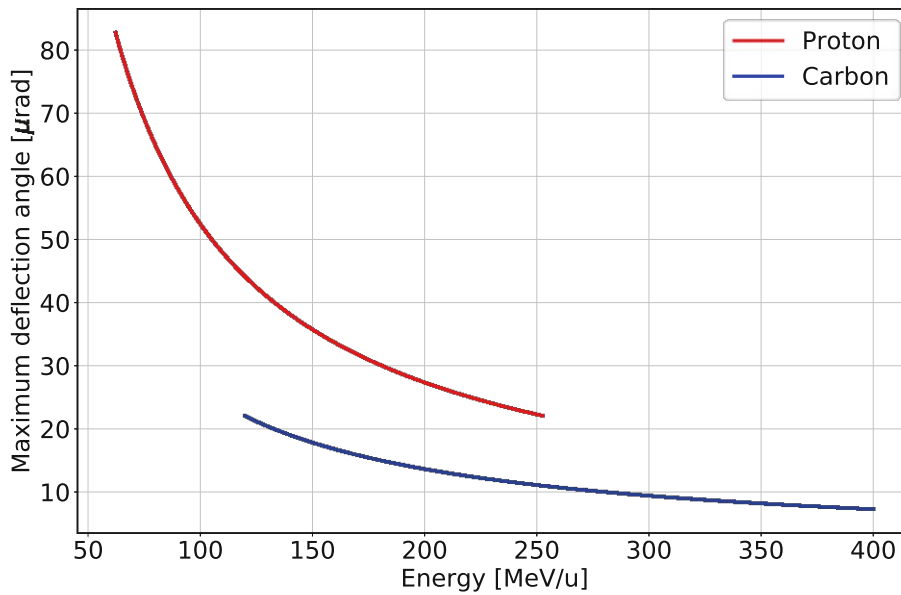


Figure 4.15.: Maximum deflection angles for the clinical energy ranges for proton and carbon beams.

Spill length calculations

The deflection angle corresponds to the extraction speed and thus to the resulting spill length of the extracted beam. Lower excitation amplitudes excite the beam slower and lead to an decreased particle flux and longer spills. The correlation between kick strength of the exciter and the spill length was studied via MAD-X simulation, as shown in Figure 4.16. The RFKO excitation was simulated for different exciter strengths and the number of turns after which 10%, 50% and 90% of the particles are extracted was recorded. Because of limitations of the computation time, only kick strengths above $5 \mu\text{rad}$ were simulated.

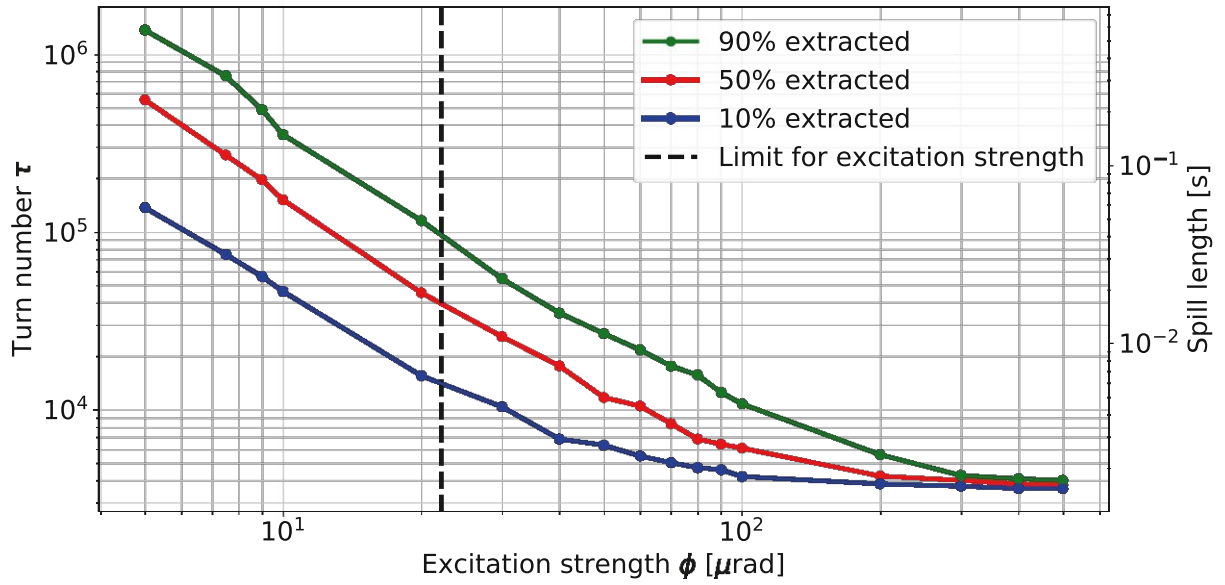


Figure 4.16.: Simulated spill lengths for different excitation amplitudes. The spill length is calculated for a proton beam with 252.7 MeV.

Figure 4.16 shows that for excitation strengths below 50 μrad the relation between excitation strength and spill length appears linear in a double logarithmic scale, which indicates that the relation can be described with a power law $y(x) = k \cdot x^a$. Fitting a power function to the simulated spill lengths for excitation strengths below 50 μrad results in equation 4.5.

$$\tau(\phi) = 2.54 \times 10^7 \cdot \phi^{-1.7949} \quad (4.5)$$

τ is the spill length in number of turns and ϕ is the excitation strength in μrad .

The vertical line denotes the maximum excitation strength with the setup at MedAustron for a proton beam with 252.7 MeV, as listed in Table 4.7. As the upper limit is still in the region where equation 4.5 is valid, the power law can be applied for all excitation strengths achievable with the current setup.

It is also worth mentioning that the lines for 90%, 50% and 10% extraction are in first approximation parallel to each other for low excitation strengths, which indicates that the temporal shape of the extraction does not change for different gains and the particles are extracted with a constant flux.

For excitation strengths above 50 μrad , equation 4.5 is no longer valid and the relation between strength and spill length can not be described with a power law. The extraction takes place slower than the power law would predict, which might come from limitation due to the transit time of the particles, that cannot be controlled with the excitation strength.

However, these ultra-high kick strengths are not relevant for the setup at MedAustron, as they are on the edge of the achievable kick strengths for the existing hardware, as shown in Table 4.7.

Equation 4.5 is based on a simplified model for a rough estimation of the spill length. Important effects that would affect the extraction speed, such as arrival time differences, are not considered. For the simulation shown in Figure 4.16 is based on excitation with white noise instead of a proper excitation signal like FM or PSK. Therefore, the model is limited and in reality, the spill lengths might differ from the predictions based on equation 4.5.

By inverting equation 4.5, the excitation strength that is necessary for certain spill lengths can be predicted. The extraction strengths needed for a 10s extraction as well as the peak-to-peak kicker voltages required to achieve these extraction strengths (obtained by inverting equation 4.3) are summarised in Table 4.8.

Beam	Excitation strength [μrad]	Kicker voltage [V]
Proton, 252.7 MeV	1.04	30
Proton, 62.4 MeV	1.43	11
Carbon, 402.8 MeV/u	0.95	82
Carbon, 120.0 MeV/u	1.21	35

Table 4.8.: Excitation strengths and kicker voltages required for a 10 s extraction.

Amplitude modulation

While the micro-spill structure can be enhanced by optimising the excitation signal as discussed in section 6.5, improving the macro-spill structure requires modulating the excitation amplitude to achieve a constant particle flux in the extracted beam and thus a linear extraction. For this Amplitude Modulation (AM), a bathtub curve proves to be suitable, where the amplitude of the excitation signal is increased at the start and the end of the extraction.¹¹ The parameters of the bathtub curve can be obtained by analysing the intensity measurement for a constant excitation amplitude and correcting it in an iterative process to obtain constant intensity.

At MedAustron, the existing setup for RFKO does not allow for amplitude modulation by pre-programmed bathtub curve. This is because the timing signal of the control system to start and stop the extraction is not directly fed into the SDR, but into an external switch between the SDR and the amplifier. Therefore, any amplitude modulation cannot be synchronised with the extraction phase, as the timing events are unknown to the SDR. A future upgrade is planned to include direct triggering within the SDR to allow the implementation of amplitude modulation.

At other facilities, a feedback correction loop was established for an automatic amplitude modulation for RFKO [46, 81]. The dose delivery system measures the extracted dose rate and compares it to the requested value. Any deviations are immediately compensated for by a Proportional-Integral-Derivative (PID) controller, which adjusts the excitation amplitude accordingly. The development of such a closed-loop feedback system is also possible at MedAustron and can be implemented in a future development.

In simulation, amplitude modulation can be modelled by adjusting the RFKO kick strength turn by turn. The macroscopic spill structure with and without amplitude modulation is shown in Figure 4.17 for a MAD-X simulation of 5,000 particles for 100,000 turns. The top plot shows the amplitude of the RFKO kick, while the profile of the extracted intensity over time is plotted in the middle with an integration interval of 110 turns. The bottom plot presents the simulated MR current over time, with the orange line denoting an ideal extraction with constant intensity.

¹¹For RFKO amplitude modulation at other facilities, see [80] (GSI), [19, 46] (HIMAC), [81] (HIT) and [57] (CNAO).

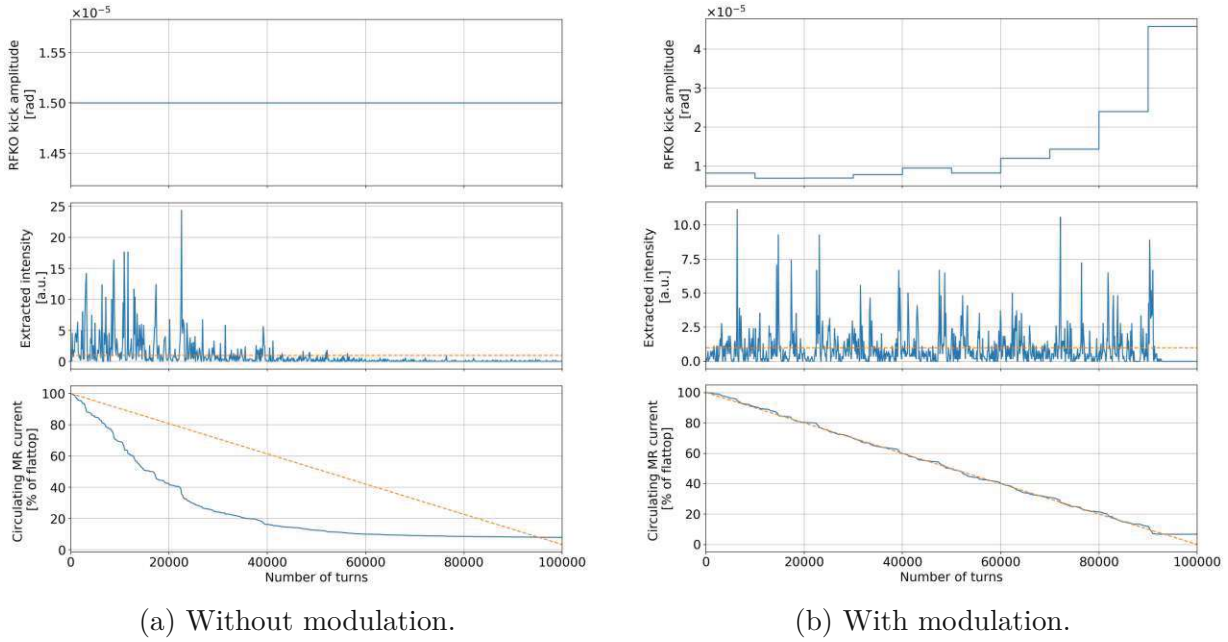


Figure 4.17.: Simulation of amplitude modulation for RFKO.

Figure 4.17a displays the extraction profile with a constant kick amplitude of $15 \mu\text{rad}$ without any modulation. The majority of the particles are extracted during the first half of the extraction, while almost none are extracted during the second half. This results in a highly non-linear extraction, which can be improved with amplitude modulation. To determine the necessary modulation of the kick amplitude, the entire spill is divided into ten intervals i of 10,000 turns each. The cumulative intensity extracted in each interval $I_{\text{meas}, i}$ is divided by the ideal cumulative intensity I_{ideal} for a linear extraction, which is given as

$$I_{\text{ideal}} = \frac{\text{number of particles} \cdot \text{interval length}}{\text{total number of turns}} = \frac{5,000 \cdot 10,000}{100,000} = 500. \quad (4.6)$$

The previous kick strength $k_{\text{new}, i}$ in each window i is then divided by this quotient to obtain the new kick strength.

$$k_{\text{new}, i} = k_{\text{old}, i} \cdot \left(\frac{I_{\text{meas}, i}}{I_{\text{ideal}}} \right)^{-1} \quad (4.7)$$

This method ensures that a higher-than-nominal intensity in a given window results in a ratio greater than one, and thus a reduced kick amplitude, and vice versa. To ensure that the amplitude modulation does not diverge for close-to-zero intensities, it is necessary

to limit the maximum kick strength. Furthermore, a global correction factor for the kick strength can be implemented to prevent fast extraction. To avoid over-correction, damping factor can be introduced to reduce the magnitude of the corrections.

This produces a modulated kick amplitude in steps of 10,000 turns, which can be implemented into MAD-X to simulate RFKO extraction with amplitude modulation. The algorithm can be repeated multiple times to iteratively converge to a linear extraction.

Figure 4.17b shows the extraction profile after 20 iterations of amplitude modulation. The MR current follows the ideal linear decrease closely and the extracted intensity is much more homogeneous than for the spill without modulation of the amplitude. The linearity of the extraction could be further improved by using more intervals with less turns.

The optimised kick amplitude profile for a linear extraction follows an asymmetric bathtub curve with a stronger kick required at the start and the end of the spill and a lower in the middle. This result agrees well with the empirical results at other facilities [46, 57, 81]. The kick strength at the start of the spill is determined by the distance of the waiting beam to the resonance and might require even stronger kicks in reality, leading to a more symmetric bathtub curve.

4.4.2. Excitation frequency

The excitation parameters must be selected to cover the entire momentum spread of the waiting beam, which is $(\Delta p/p)_{\text{spread}} = 0.86 \times 10^{-3}$, according to Table 3.1. It should be noted that for RFKO, minimising the momentum spread is crucial to reducing the energy spread in the treatment room. Consequently, the phase jump is deactivated even for unbunched operation.

Two main approaches to excite the beam were investigated and are discussed in the next sections.

Frequency modulation

For frequency modulation (FM), the frequency is changed over time to cover the entire momentum distribution of the waiting beam. This is achieved through a sawtooth-like modulation of the excitation frequency.

There are three main parameters relevant to FM:

- The lowest frequency and starting point of the sawtooth carrier function to periodically ramp the frequency is known as the **base frequency** f_0 . It can be calculated using equation 2.48, which takes into account the revolution frequency and the horizontal particle tune.¹² For the tests described in this thesis, we used the first harmonic of the fractional part of the tune. For a proton beam with 252.7 MeV and the primary RFKO setup, the base frequency is 1.597 MHz.
- The **bandwidth** Δf of the excitation controls the amplitude of the sawtooth carrier function and thus the excited frequency region of the beam. It is important to match the bandwidth to the momentum spread of the beam. If the bandwidth is too small, only a portion of the beam will be excited, resulting in reduced extraction efficiency. Using a Δf value that is too high, regions of the momentum spectrum without any particles in it are excited, resulting in a waste of excitation power and unwanted effects on the intensity ripples structure.

The Full Width at Half Maximum (FWHM) of the momentum spread for a beam without phase jump is 0.86×10^{-3} , corresponding to a standard deviation σ of 0.36×10^{-3} . To make sure almost all particles are considered, a 5σ range for the excitation was used, corresponding to a bandwidth of 3.17 kHz.

¹²The particle tune is different to the lattice tune if the momentum offset of the beam is non-zero: $Q_{x,\text{part}} = Q_{x,\text{lattice}} + Q'_x \cdot (\Delta p/p)$. As f_0 is the lowest and not the central frequency, the maximum momentum offset (and not the central momentum offset) needs to be used.

Figure 4.18 shows the measured extraction efficiency for different bandwidths for a proton beam with 252.7 MeV. The bandwidth scan shows that the extraction efficiency increases even further to 89.5% for bandwidths up to 5 kHz, before it reaches saturation. Because of this, 5 kHz was used as default bandwidth for RFKO with FM.

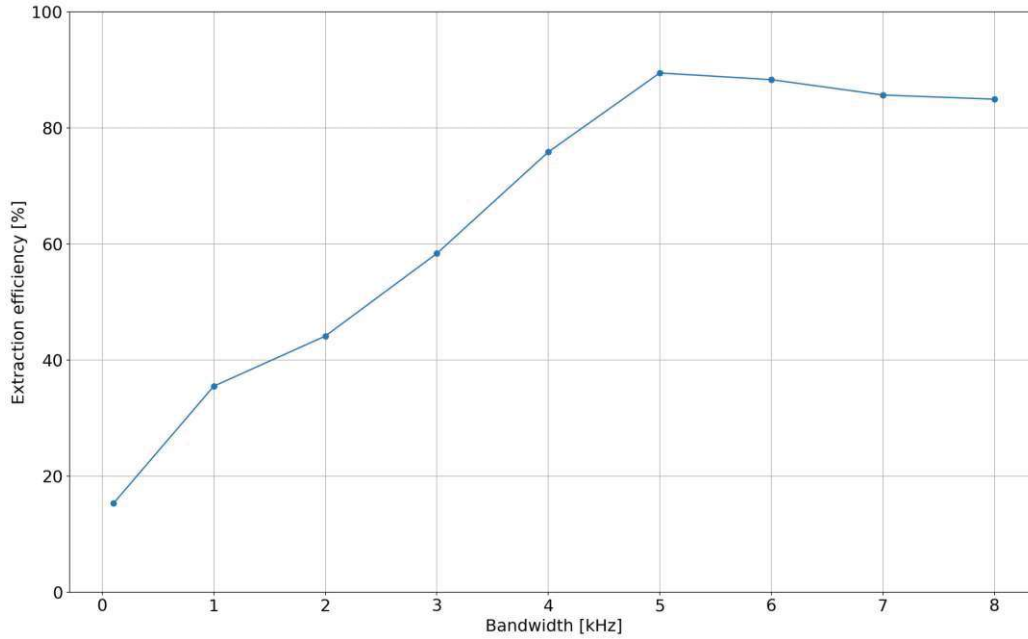


Figure 4.18.: RFKO extraction efficiency for different FM bandwidths for a bunched proton beam with 252.7 MeV.

- The **sweep frequency** f_{sweep} describes the frequency of the sawtooth carrier function and therefore the periodicity of the frequency modulation. The sweep frequency does not have a significant impact on the extraction efficiency, but on the intensity ripple structure of the extracted beam, as it is the main ripple contributor for RFKO with FM. Using a high sweep frequency is favourable, as it moves the ripples in a high-frequency region with a reduced relevance for clinical treatment.

The frequency over time for an exemplary FM signal, the resulting signal and the Fourier spectrum of the signal is shown in Figure 4.19 with $f_0 = 1.597$ MHz, a bandwidth of 5 kHz and a sweep frequency of 100 Hz, corresponding to a sweep period of $T_{\text{sweep}} = 10$ ms. As the base frequency is much larger than the sweep frequency, the frequency change cannot be properly visualised in the signal.

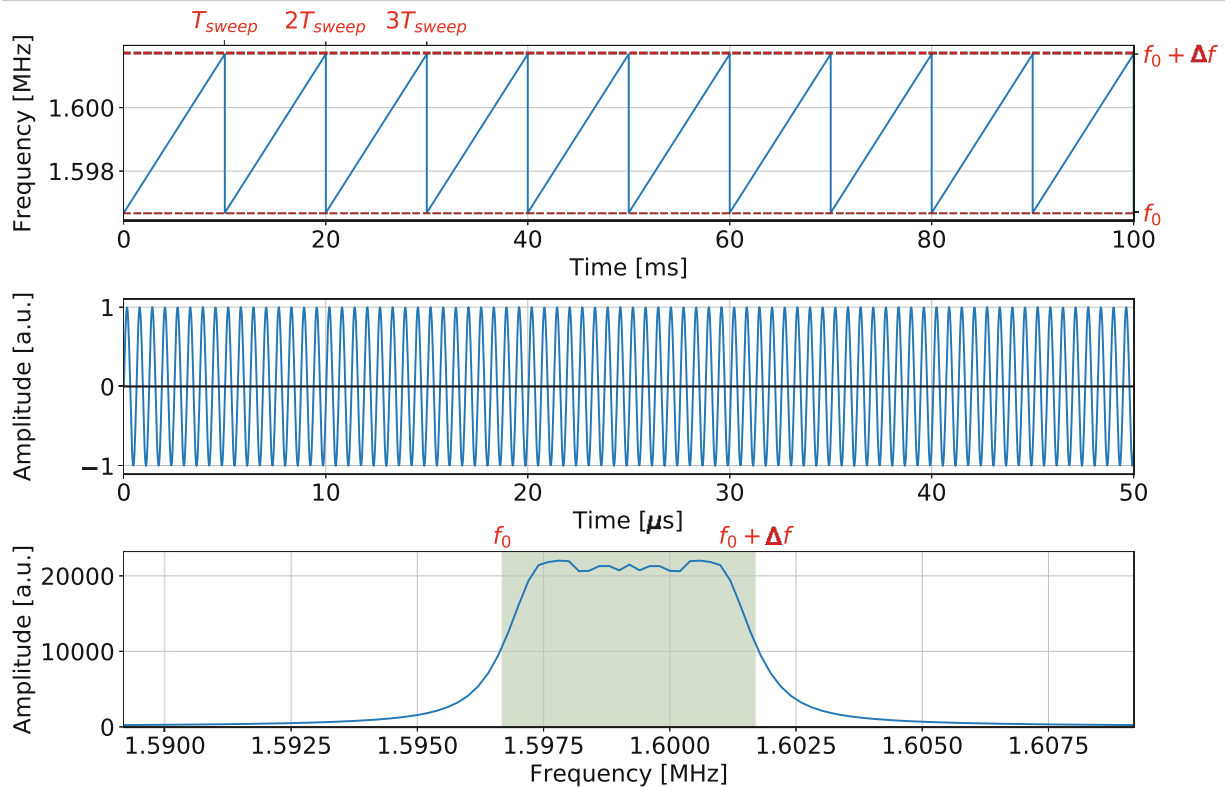


Figure 4.19.: Exemplary FM signal.

Top: Frequency over time.

Middle: Signal over time. The amplitude of the signal was set to 1.

Bottom: Fourier spectrum of the signal.

Phase shift keying

Another possibility to broaden the excitation spectrum is to change the phase of the signal by applying a phase shift, which is done for the phase shift keying (PSK) method. The phase shifts are taking place at a fixed interval, but with a random chance.

For phase shift keying, two parameters are of importance:

- The **base frequency** f_0 is (as for FM) the main frequency of the excitation without any phase shifts. It is identical to the base frequency for FM and needs to correspond to the revolution frequency and the horizontal tune of the beam, as described above.
- The **shift frequency** f_{shift} describes how often a possible phase shift can occur. If a phase shift is realised is determined randomly, but f_{shift} sets the maximum frequency

at which the shifts can take place. A higher shift frequency leads to a broader excitation spectrum, as the primary nodes of the main band are at $f_0 \pm f_{\text{shift}}$.

Compared to FM, shifting the phase has the advantage that fewer intensity ripples are induced into the extracted beam by the excitation. This is because the frequency is not directly modulated through a periodic function, which would otherwise lead to a periodic modulation of the extraction at the same frequency. This benefits the beam quality, as shown in section 6.5. Additionally, the sidebands in the excitation spectrum allow that frequencies outside the main band of $[f_0 - f_{\text{shift}}, f_0 + f_{\text{shift}}]$ can be excited. Small frequency errors are therefore compensated and particles with a frequency mismatch due to amplitude-dependent detuning are still extracted. The sidebands can also be used to excite different frequency regions at one, which can be useful for extracted a multi-ion beam.

An exemplary BPSK signal with $f_0 = 1.597\text{ MHz}$ and $f_{\text{shift}} = 500\text{ Hz}$ together with its Fourier spectrum is shown in Figure 4.20.

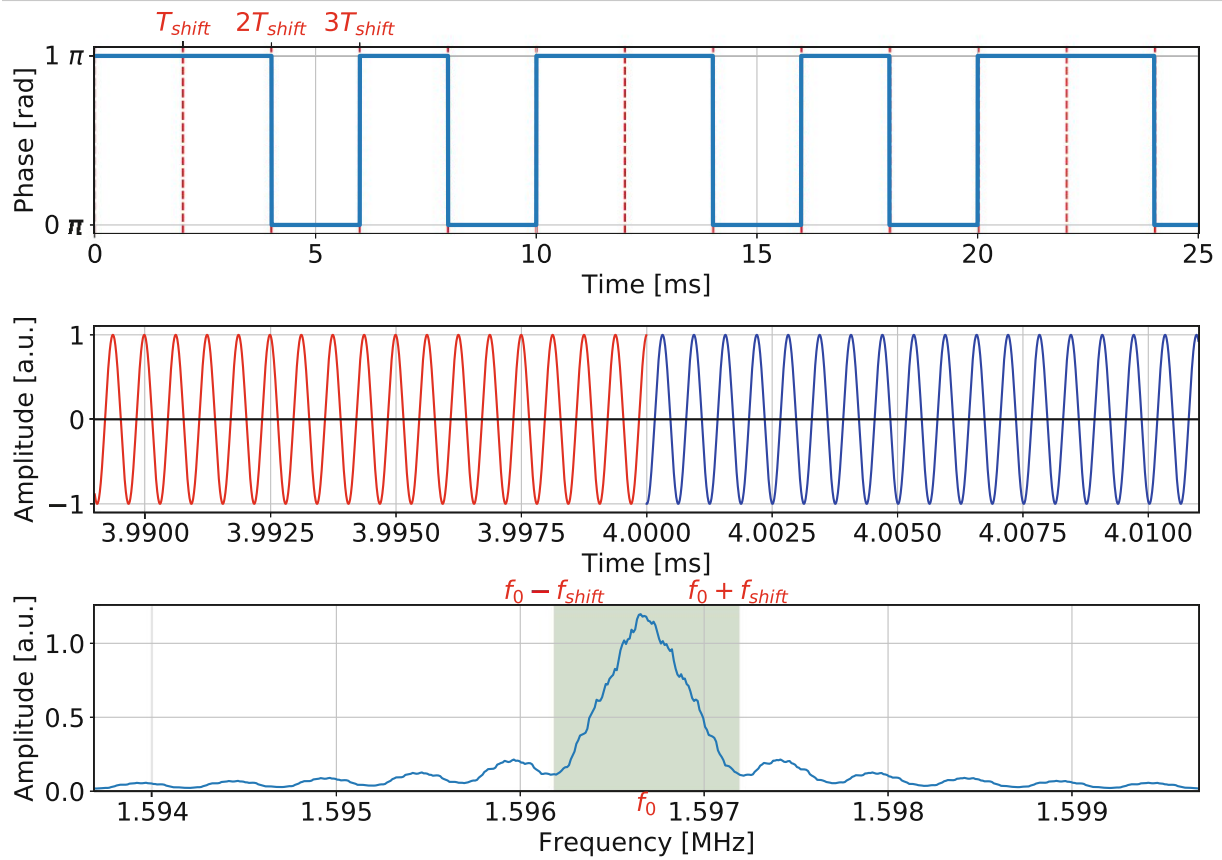


Figure 4.20.: Exemplary BPSK signal.

Top: Phase over time. f_{shift} was set to 500 Hz.

Middle: Signal over time. The amplitude of the signal was set to 1. The different colours were used to highlight the phase shift.

Bottom: Fourier spectrum of the signal.

4.5. Extraction measurements

RFKO was successfully implemented as experimental extraction technique at MedAustron, using the setup described above. The beam can be extracted from the Main Ring in a reproducible manner with a constant dose rate. The optimised $KOE\alpha$ setpoint is used to ensure a high extraction efficiency with favourable beam parameters. Both FM and PSK can be employed to excite the beam with optimised parameter settings. Throughout the extraction process, the beam remains bunched without significant losses, thus enabling the potential for future energy modulation.

Figure 4.21 displays a typical RFKO extraction with FM (red) and PSK (orange) as a plot of the measured circulating current in the Main Ring over time, in comparison to the default extraction via betatron core (blue).

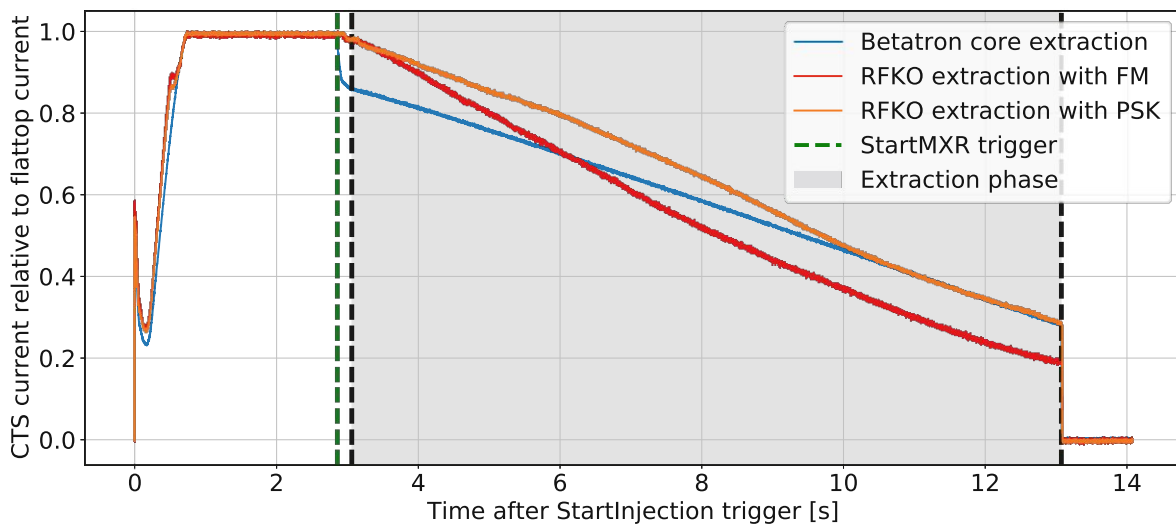


Figure 4.21.: Measured circulating MR current for RFKO extraction.

The extraction efficiency reaches values of up to 80% (FM) and 70% (PSK) with RFKO, which are even higher than for betatron core extraction¹³. Due to the optimised optics for RFKO, there are only minimal losses when the resonant sextupole is ramped. It is evident that both RFKO techniques show non-linear extractions. In contrast, extraction using a betatron core results in a very linear extraction and a constant spill rate.

¹³However, the beam is chopped for betatron core extraction to cut off the non-linear head and tail of the spill. In particular, the end of the spill is heavily cut, chopping away up to 30% of the particles at flattop. The chopper timings need to be re-evaluated for RFKO in the future.

To improve the linearity of RFKO extraction, amplitude modulation of the excitation is necessary, as discussed in section 4.4.1.

This thesis primarily addresses the extraction process with RFKO from the Main Ring over the ESE up to the MST. The transmission from the MST to the treatment room was beyond the scope of this thesis and was therefore not optimised. Nonetheless, overview measurements with the DDM detector in the treatment room were conducted to estimate the beam parameters and intensity at the isocentre. Figure 4.22 presents the 2D intensity plot (horizontal position over time with colour-coded intensity) for a proton beam at 252.7 MeV in IR1 for both RFKO extraction with FM and betatron core extraction.

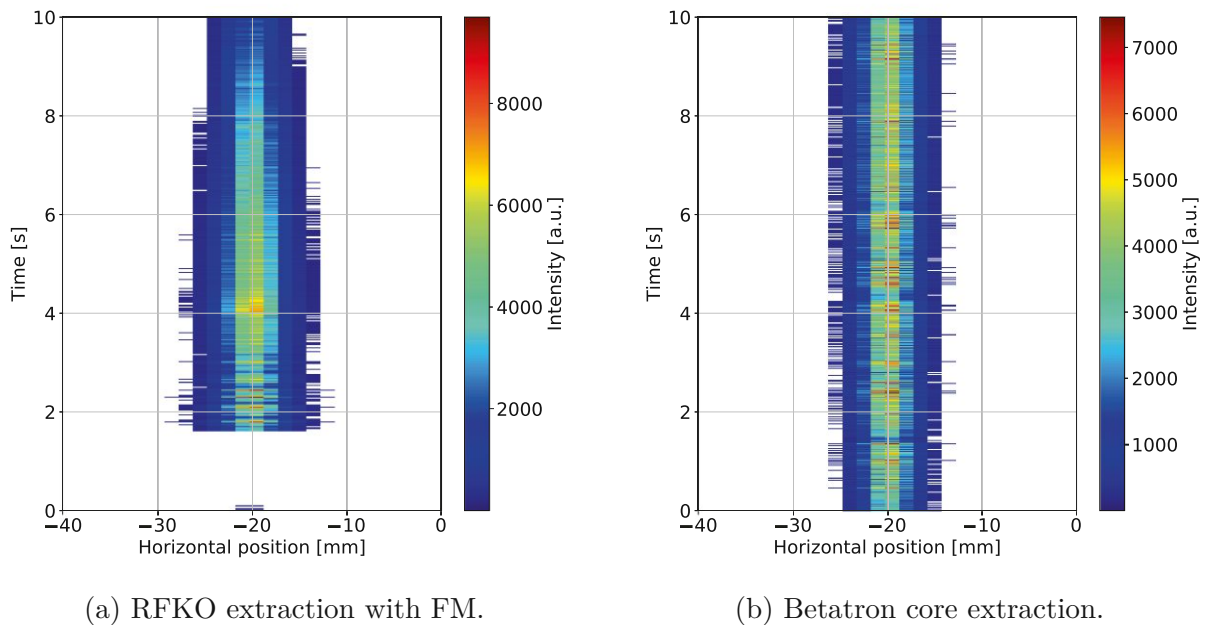


Figure 4.22.: DDM beam intensity measurement for RFKO in IR1.

As anticipated from the CTS plot 4.21, the dose rate for RFKO extraction 4.22a without AM is not constant, but varies significantly over time. Most particles are delivered during the first half of the spill, with the second half exhibiting a tail-like structure characterised by exponentially decreasing intensity. This behaviour contrasts markedly with the betatron core extraction 4.22b, where the intensity is evenly distributed throughout the entire spill, ensuring a constant dose rate. In both cases, the horizontal position change over time is minimal, as no intra-spill beam movement is observed. The horizontal beam width is comparable for both extraction techniques, although the beam size decreases towards the tail of the RFKO extraction as fewer particles are reaching the detector.

The DDM measurement also enables the calculation of the integrated intensity of the entire spill, quantifying the total number of particles reaching the treatment room. This value can be compared with the number of extracted particles obtained from the CTS measurement to determine the transmission efficiency from the Main Ring to the treatment room, using equation 4.8.

$$\eta_{\text{tr}} = I_{\text{DDM}}/I_{\text{CTS}} \quad (4.8)$$

The values of both measured intensities as well as η_{tr} are presented for a proton beam at 252.7 MeV in Table 4.9.

	Extracted particles (CTS)	Particles at IR1 (DDM)	Transmission efficiency η_{tr}
RFKO with FM	1.12×10^{10}	8.3×10^9	74%
Betatron core extraction	8.5×10^9	8.1×10^9	95%

Table 4.9.: Measured number of particles and calculated transmission efficiency.

As discussed above, more particles are extracted with RFKO than with betatron core due to the extensive beam chopping applied for the latter. Consequently, the CTS records a higher number of extracted particles for RFKO.

However, the number of particles reaching the DDM detector in the treatment room is nearly identical for both extraction techniques. This leads to the conclusion that while almost all extracted particles reach the treatment room for betatron core extraction, the transmission efficiency from the Main Ring to the treatment room is only 74% for RFKO extraction. This reduced efficiency can be attributed to the scraping of the RFKO-extracted beam at some point in the HEBT due to two possible reasons:

1. For RFKO, the beam is extracted with a momentum offset that is not present for betatron core extraction. Since the amplitude of the off-momentum beam is increased without any acceleration, the momentum offset of the circulating beam in the Main Ring is transferred to the extracted beam in the HEBT. For betatron core extraction, the beam is accelerated into resonance, reducing the momentum offset to a value close to zero.

Figure 4.23 shows the simulated energy distribution of a proton beam at 252.7 MeV at the isocentre for both RFKO and betatron core extraction. The significant energy offset between the two extraction techniques is clearly visible. For betatron core extraction (orange), the energy of the extracted beam is close to the design energy of 252.7 MeV (vertical black line), with an average energy offset of $\Delta E = -0.2$ MeV. The high-energy part of the distribution aligns with the resonance energy. The small

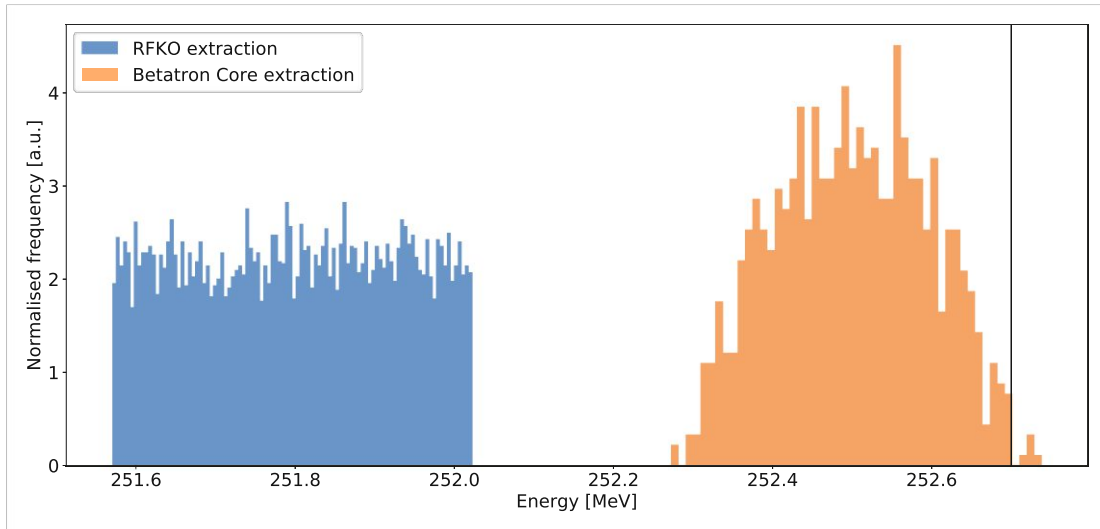


Figure 4.23.: Simulated energy distribution at the isocentre of a proton beam at 252.7 MeV.

shift to lower energies originates from the earlier extraction of high-amplitude particles due to the slope of the separatrix in the Steinbach diagram. Thus, the energy distribution represents the amplitude distribution of the beam.

For RFKO extraction (blue), all particles are extracted with a significantly larger energy offset of $\Delta E = -0.9$ MeV due to the off-momentum extraction at a mean radial loop position of 20 mm. Since RFKO is an extraction based on momentum selection, the energy distribution represents the momentum distribution of the circulating beam¹⁴.

As the nominal setpoint of the HEBT is used for RFKO extraction, this momentum offset is not compensated. The beam follows the local dispersion vector of the HEBT lattice, leading to a significant beam offset in high-dispersive regions.

2. Although the beam parameters for RFKO at the ESE and MST are adapted to match those for betatron core extraction, the beam distributions at the septa may differ slightly. Since the default kick strength of the MST remained unchanged for RFKO, the particle positions and angles through the HEBT might not match those of betatron core extraction. This again leads to a deviation from the default trajectory and results in losses due to aperture scraping.

Additionally, during the extraction tests shown in Figure 4.22, the default ESE kick

¹⁴In reality, the momentum distribution for a bunched beam is rather Gaussian than uniform, given that no phase jump was performed. However, a uniform initial momentum distribution was used for the simulation, resulting in the energy distribution for RFKO shown in Figure 4.23.

strength of $\Delta x' = -2.5$ mrad was still used. This unoptimised setpoint further reduces the transmission efficiency into the treatment room.

Both discussed effects contribute to an increased horizontal beam offset in the HEBT for RFKO, leading to increased particle losses due to scraping at the vacuum chamber walls and reduced transmission efficiency.

Optimising the HEBT is required for the potential clinical implementation of RFKO as an alternative extraction technique.

5. Other extraction methods

In addition to the RFKO extraction method discussed in the previous chapter, alternative slow extraction methods were also investigated. Specifically, Constant Optics Slow Extraction (COSE) and Phase Displacement Extraction (PDE) are of interest as they could potentially allow for future improvements of the accelerator, opening up possibilities to enhance the performance of clinical treatment. Additionally, COSE and PDE can be used as comparison to the RFKO extraction and the current betatron core extraction with respect to beam quality and intensity ripples. This chapter provides a brief overview of the simulations and measurements conducted on COSE and PDE.

5.1. Constant Optics Slow Extraction

Chapter 2.3.2 describes the process for COSE, where all magnets are ramped synchronously to sweep the resonance through the stationary waiting beam. The beam can be either unbunched (as for default operation with betatron core extraction) or bunched, which enables the possibility of performing Multi Energy Extraction (MEE).

5.1.1. Unbunched COSE

For unbunched COSE, the RF cavity is turned off after acceleration and phase jump, allowing the beam to de-bunch into a coasting beam with an increased momentum spread. This method can be seen as the inverse of betatron core extraction, as the machine settings are identical. In betatron core extraction, the beam is moved into a stationary resonance, whereas in COSE, the resonance is moved into a stationary beam.

The spill length of the extracted beam is determined by the ramp rate of the synchrotron magnets. The FWHM momentum spread of the waiting beam after the phase jump was measured as $(\Delta p/p)_{\text{spread}} = 3.7 \times 10^{-3}$. As shown by Kain et al. [43], the magnetic field must be scaled by the same relative change as the momentum spread that needs to be covered. However, the radial loop position of 20 mm corresponds to a momentum offset of $(\Delta p/p)_{\text{off}} = -2.3 \times 10^{-3}$, resulting in a configuration that is shown true to scale in Figure 5.1.

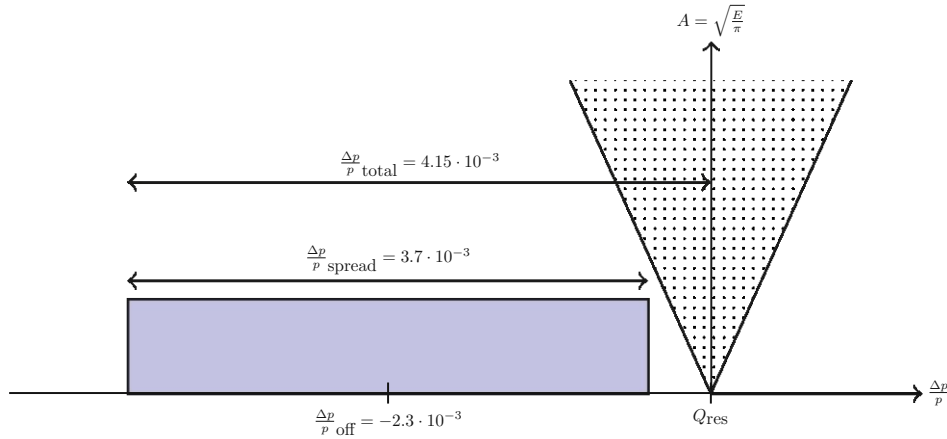


Figure 5.1.: Beam configuration for unbunched COSE before the start of the extraction, drawn to scale.

Based on Figure 5.1, the total momentum spread that needs to be covered in order to extract the entire beam (and therefore the scaling factor of the magnetic strengths) can be calculated with equation 5.1.

$$\frac{\Delta k_n}{k_{n,0}} = \left(\frac{\Delta p}{p} \right)_{\text{total}} = \left(\frac{\Delta p}{p} \right)_{\text{off}} - \frac{1}{2} \left(\frac{\Delta p}{p} \right)_{\text{spread}} = -4.15 \times 10^{-3} \quad (5.1)$$

This implies that all magnet strengths must be gradually reduced by 0.415% over a period of 10s in order to extract the entire beam within that time. However, since there are no particles within the momentum slice between on-momentum and the high-momentum edge of the momentum distribution, there is a significant dead time at the start of the spill, which reduces the effective spill length to less than ten seconds. In order to achieve effective spill lengths of 10s, this dead time must be compensated by reducing the scaling factor of the magnet ramp to -0.35%. This ensures that the spill length is long enough, but it also means in return that not the full momentum spread of the spill is extracted and the resulting intensity is reduced.

Measurements performed for a coasting proton beam with an energy of 252.7 MeV confirm this ramp rate calculation. Figure 5.2 displays the extracted intensity (relative to the extracted intensity with a very high magnet ramp of -2%, which extracts the full beam in less than two seconds) at the top, and the effective spill length for different COSE magnet ramps at the bottom.

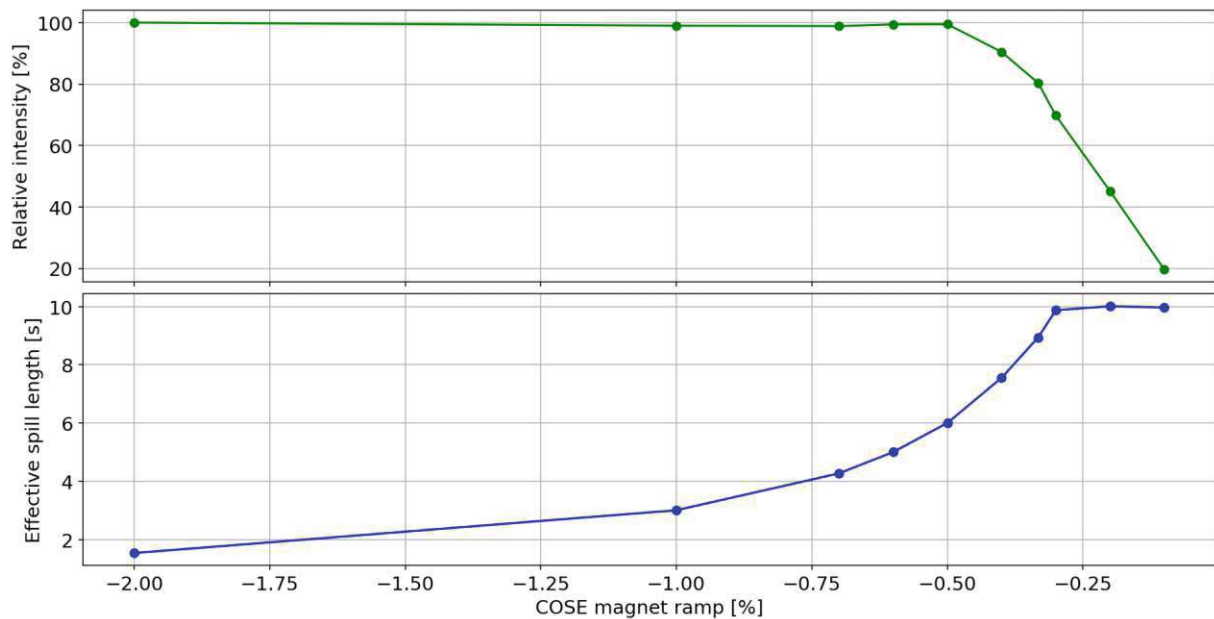


Figure 5.2.: Extracted intensity and effective spill length for different COSE magnet ramps with unbunched proton beam (252.7 MeV).

Figure 5.2 confirms that the full beam is extracted for ramps below -0.5% , which agrees well with the theoretical value calculated in equation 5.1. However, at this scaling factor, the effective spill length is only six seconds due to the aforementioned dead time. To achieve the nominal spill length of ten seconds, a magnet ramp of -0.3% is required, which is again very close to the theoretical value. Magnet ramps above this threshold would result in spill lengths longer than ten seconds. As the chopper opening time was set to 10 s for this measurement, the last few data points for the spill length are at exactly at this value, as this is the longest possible spill length for the measurement setup.

For further investigations, a magnet ramp of -0.4% was chosen as a compromise between spill length and extracted intensity. This scaling factor allows for the extraction of over 90% of the momentum distribution while maintaining a reasonably high effective spill length of 8.9 s.

Figure 5.3 summarises the COSE tests with an unbunched proton beam of 252.7 MeV and a magnet ramp of -0.4% . The upper left plot displays the strength of the dipole magnets over time, which is representative of all synchrotron magnets as they are ramped by the same scaling factor. The extraction period is highlighted in grey. The lower left plot shows the particle current in the Main Ring. The plot on the right displays the horizontal position of the beam in the room, with beam intensity represented by colour-coding.

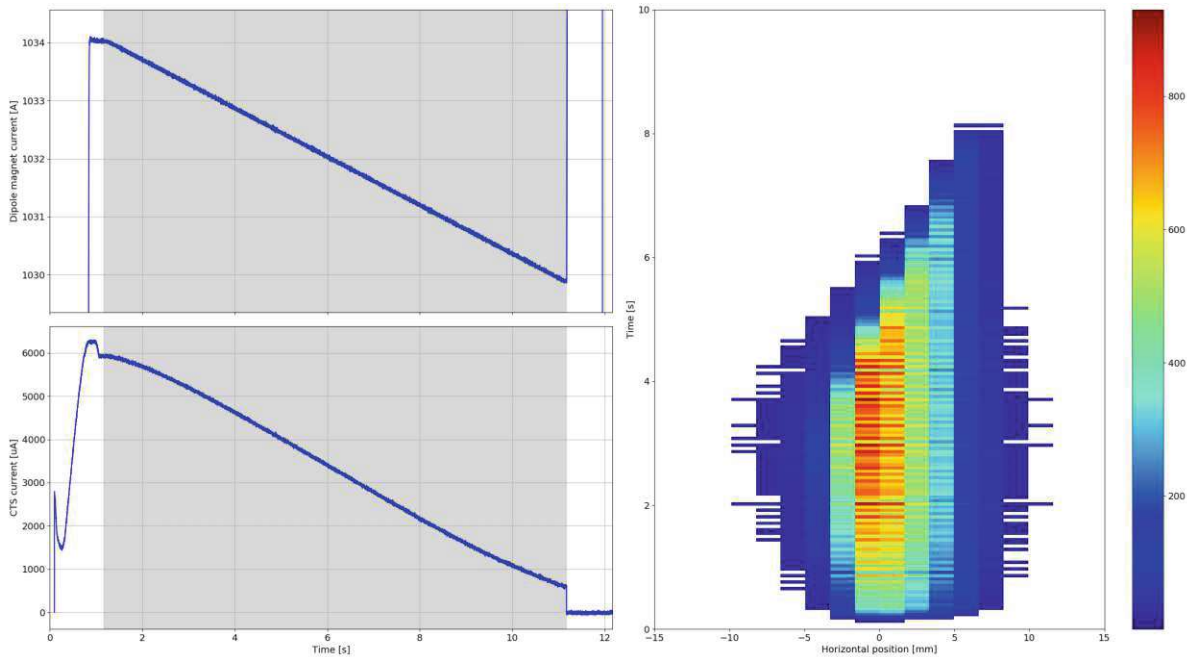


Figure 5.3.: Unbunched COSE measurement with a magnet ramp of -0.4% , using a proton beam (252.7 MeV).

Top left: Measured current of the dipole magnet over time.

Bottom left: CTS particle current in the Main Ring over time.

Right: 2D intensity plot in the treatment room over horizontal position and time, measured with the DDM.

The magnet current measurement confirms that the dipole strength follows a linear ramp by -0.4% . The Main Ring current shows a mostly linear extraction with good efficiency, although a minor S-shape is visible as the head and the tail of the beam are not chopped. The DDM measurement validates that the beam reaches the treatment room with high intensity and a spill length of over eight seconds. No intra-spill position change is observed in the middle part of the beam.

However, there is a quite distinct tail at the end of the beam, where the centre of gravity of the beam shifts to more positive values, while the intensity and the beam size decrease, causing a triangular shape in the 2D plot. This effect arises from the last part of the extraction process, where the resonance has already been moved almost entirely through the momentum distribution of the beam. A similar pattern can be observed for unchopped extraction with betatron core. To remove this tail, the chopper settings need to be adjusted in order to cut away the last part of the beam. Additionally, the head of the beam can also be cut with the chopper to ensure a constant intensity without the ramp-up at

the start of the spill.

The optimisation of chopper settings and the adjustment of the scaling factor to extend the middle part of the beam was not performed in this thesis and can be carried out in future studies.

The benefits of COSE, as opposed to 'normal' tune sweep extraction (where only the quadrupole magnets are ramped, as discussed in section 2.3.2), are illustrated in Figure 5.4.

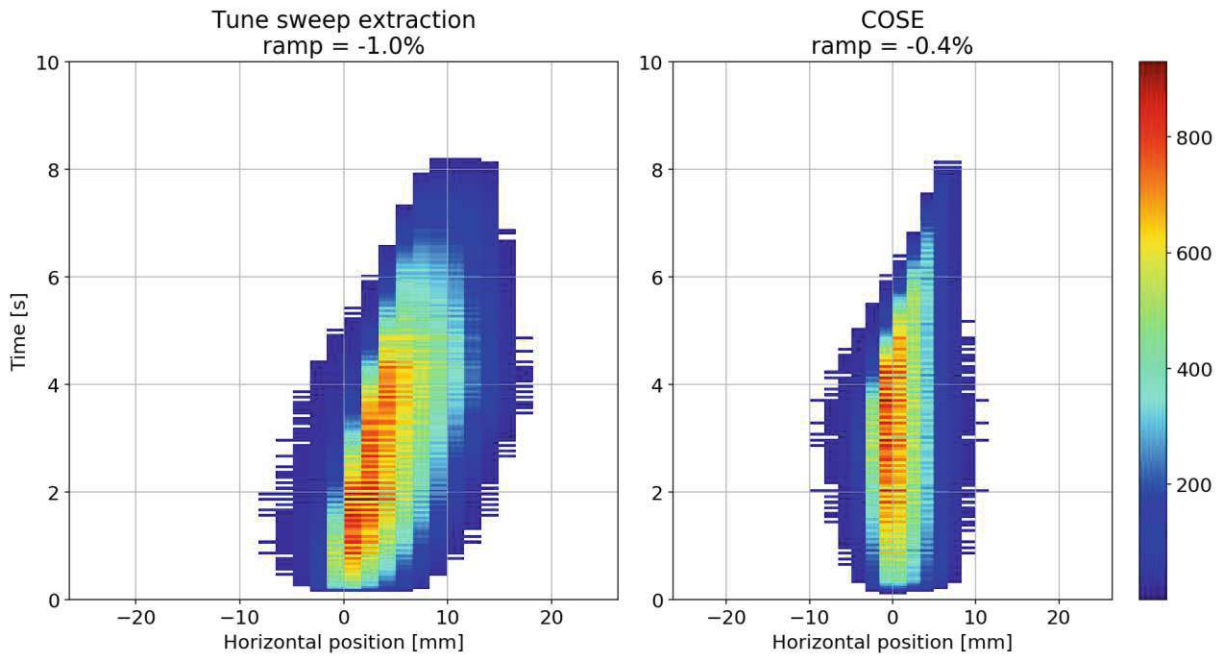


Figure 5.4.: Comparison of unbunched COSE with unbunched tune sweep extraction, using a proton beam (252.7 MeV). 2D intensity plot in the treatment room over horizontal position and time, measured with the DDM.

To achieve extraction rates similar to COSE with a ramp of -0.4% during tune sweep extraction, the scaling factor must be adjusted to -1 as the total momentum spread is multiplied with the absolute value of the horizontal chromaticity Q'_x to calculate the scaling factor for the quadrupole magnets for tune sweep extraction [41].

While there is almost no intra-spill movement (apart from the already discussed tail) for COSE, the horizontal centre of gravity shifts from 1.2 mm to 11.4 mm over the whole spill for tune sweep extraction. This observation can be explained by the fact that the

separatrices are not superimposed for tune sweep extraction, which leads to a momentum sorting of the position of the extracted beam at the electrostatic septum. Due to the resonance sweep, particles with a lower absolute momentum offset are extracted earlier. This transforms the momentum sorting into a temporal sorting, which is then transferred to the treatment room, causing the intra-spill movement over the duration of the spill. For COSE, the separatrices for different momenta overlap, causing the position of the full momentum distribution to be mixed at the septum. This leads to a negligible position drift during the core part of the spill.

5.1.2. Bunched COSE

COSE with a bunched beam differs to unbunched COSE in two aspects:

- If the RF cavity remains active during extraction, it is impossible to perform a phase jump because the phase loop correction needs to be turned off for a proper phase jump, which is incompatible with bunched beam operation. As a result, the momentum spread of the bunched beam is significantly smaller than that of the coasting beam, with a FWHM value of $(\Delta p/p)_{\text{spread}} = 0.86 \times 10^{-3}$. As the magnet ramp for COSE needs to be matched to the momentum spread of the beam, the magnet ramp must be adjusted accordingly in order to extract with the required extraction rate for an equivalent spill length of ten seconds.
- During bunched beam operation, the radial correction loop is active throughout the extraction process to enable radial steering and control of the beam. If the mean radial position, which is controlled via the correction loop, is maintained at a fixed value, the beam would be steered away from the approaching resonance. This beam movement occurs as the radial offset is defined in relation to the on-momentum reference trajectory, which changes when the dipole strengths are scaled, causing it to move together with the resonance during the COSE ramp.

To ensure a controlled extraction of the beam and avoid changes in beam properties during extraction, the mean radial position must be ramped down in synchronisation with the magnet ramp. As shown in equation 5.2, the change in radial position Δx can be calculated using the relative magnetic strength scaling $\Delta k_n/k_{n,0}$ and the horizontal dispersion D_x at the location of the pickup coils that are used for the radial correction loop, which is $D_x = -8.6$ m for the MedAustron synchrotron.

$$\Delta x = D_x \cdot \frac{\Delta k_n}{k_{n,0}} \quad (5.2)$$

Apart from the two changes mentioned, the COSE process for bunched beams is identical to that for coasting beams. Figure 5.5 shows a measurement for bunched COSE with a

proton beam at 198.0 MeV. The mean radial position is ramped down from the initial value of 20 to 10 mm at the end of the spill, using the correction loop. This radial position ramp corresponds to a magnet scaling factor of -1.2×10^{-3} , as per equation 5.2.

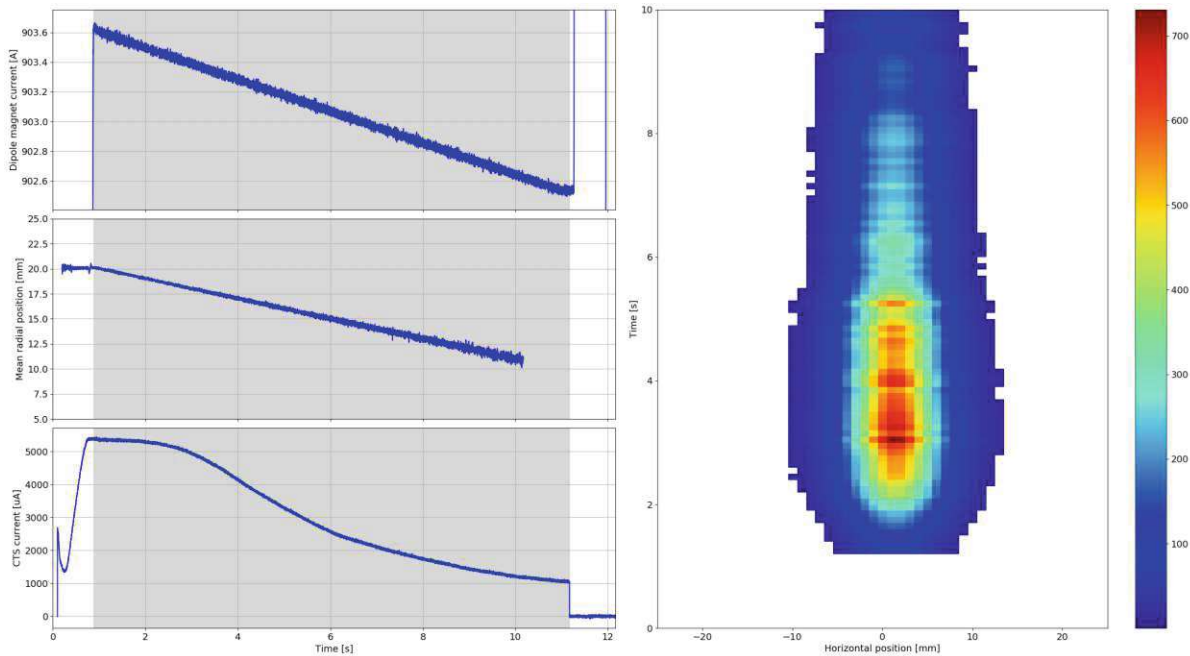


Figure 5.5.: Bunched COSE measurement with a radial position ramp from 20 to 10 mm, using a proton beam (198.0 MeV).

Top left: Measured current of the dipole magnet over time.

Middle left: Measured mean radial position of the beam over time.

Bottom left: CTS particle current in the Main Ring over time.

Right: 2D intensity plot in the treatment room over horizontal position and time, measured with the ICM.

Figure 5.5 confirms that the dipole magnets and the mean radial position of the beam are ramped down synchronously during the extraction phase.¹ The Main Ring CTS shows that the extraction is highly non-linear, particularly when compared with the CTS plot for unbunched COSE in Figure 5.3. This can be explained by the fact that, as previously described, the momentum distribution is Gaussian-shaped instead of uniform due to the absence of a phase jump. As the resonance approaches the beam at a constant speed, the

¹The measurement of the radial position of the beam stops shortly before StopExtraction due to an issue with the measurement setup. An additional measurement confirmed that the ramp is continued down to 10 mm.

extracted intensity varies over time, following the momentum distribution. The Gaussian extraction profile can be compensated by adapting the profile of the magnet ramping accordingly. The absence of the phase jump is also the reason for the delayed start of the extraction, with almost no extraction in the first second of the ramp. This is because the smaller momentum spread of the beam causes the resonance to initially approach the beam without exciting any particles, as the corresponding momentum slices are almost empty. This dead time could be avoided by increasing the strength of the resonant sextupole or by reducing the momentum offset of the beam. However, it was decided to keep the default settings for betatron core extraction for the COSE studies in this thesis, accepting the delayed extraction start.

The ICM measurement indicates minimal intra-spill movement of the position over time. However, a distinct trailing edge is visible, extending even beyond the chopper opening time of 10 s. This suggests that not all particles are extracted during the extraction phase, which is confirmed by the slightly lower extraction efficiency visible on the CTS plot.

The reduced efficiency originates from the chosen final radial position at the end of the ramp. To quantify this correlation, a scan of the endpoint of the radial position ramp was performed for a bunched proton beam with 252.7 MeV, resulting in the plot shown in Figure 5.6. The initial radial position was kept at 20 mm for all measurements. The extraction efficiency was measured using the CTS for radial loop ramps with different Δx . The efficiency of extraction increases significantly with increasing Δx of the radial loop ramp for position changes below 8 mm, which corresponds to endpoints of the radial position above 12 mm. For position changes larger than 8 mm, the curve flattens out and the extraction efficiency increases more slowly, until it reaches almost 100% for a full radial loop ramp by 20 mm, going from 20 to 0 mm.

For $\Delta x = 10$ mm, 80% of the beam is extracted. Increasing Δx by an additional 10 mm only results in a further 20% increase in efficiency. This can be explained by the fact that most particles occupy momentum slices corresponding to radial loop positions below 10 mm, while only a few particles populate momentum slices with a higher absolute value of the momentum offset.

If a full ramp by $\Delta x = 20$ mm from 20 to 0 mm is used, the intensity extracted in the second half of the radial loop ramp is one fourth of the intensity in the first half, as 80% of the particles are extracted when the radial loop moves from 20 to 10 mm.

The lower intensity in the second half of the spill could pose a problem for multi energy extraction, as the energies extracted during this second part of the ramp would contain significantly fewer particles, making it challenging to apply corrections to achieve the same intensity for all sub-spills. Furthermore, as the number of particles in the ring decreases, the pick-up measurement for the radial loop becomes noisier, which sets a lower limit on the application of the radial correction. Because of this, it was decided to use 10 mm as

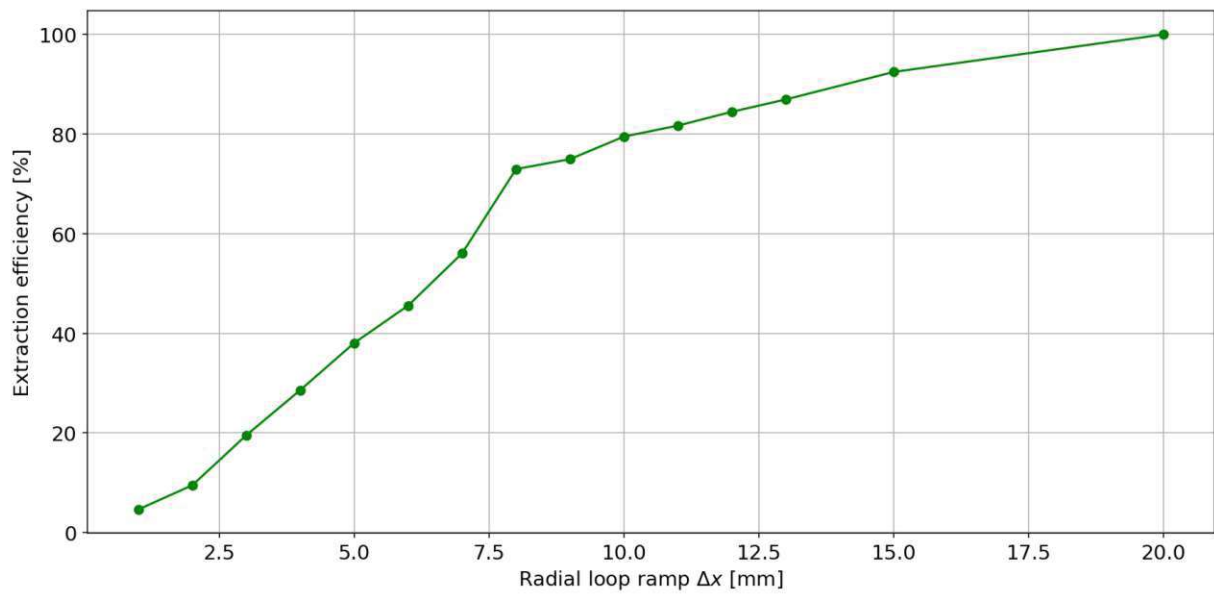


Figure 5.6.: Extraction efficiency for different radial loop ramps for bunched COSE with a proton beam (252.7 MeV). The initial radial position was kept at 20 mm for all measurements.

the endpoint of the radial position ramp for future measurements and to accept that 20% of the particles are not extracted.

5.1.3. Multi Energy Extraction

Bunched COSE can be used to extract different energies within one spill. To achieve multi energy extraction (MEE), multiple COSE ramps have to be combined with energy change phases in between. For MEE of n energies, the spill can be divided into n extraction phases with bunched COSE ramps, combined with synchronised ramps of the radial position by Δx_n , to extract energy E_n , and $(n - 1)$ energy change phases. During the energy change phase, the radial position remains constant, while the dipole strengths and thus $B\rho$ change. The feedback correction loop corrects the radial offset from the set position that originates from the $B\rho$ change by accelerating or decelerating the circulating particles, resulting in an energy change. The size of the energy step ΔE_n can be controlled by adjusting the amount of change in dipole strengths.

A schematic summary of the configuration for MEE is presented in Figure 5.7.

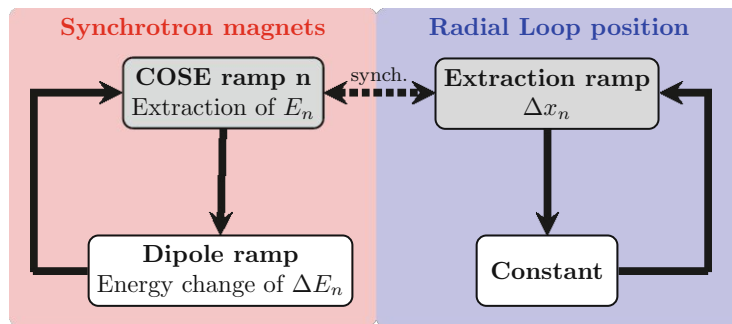


Figure 5.7.: Schematic configuration for MEE with bunched COSE. The extraction phase is depicted with grey nodes, the energy change phase with white nodes.

The given configuration depicted in Figure 5.7 was used to perform extraction tests for MEE with 10 energies using a proton beam with a base energy of 252.7 MeV. The total radial position ramp was set up from 20 to 10 mm, resulting in a radial position change per energy Δx_n of 1 mm. The energy change between two subsequent energies ΔE_n was set to 52 keV, resulting in a total energy change over the whole spill ΔE of 0.52 MeV. The extraction resulting from this setup is shown in Figure 5.8.

While the radial loop follows the position ramps closely, the beam is kept too close to resonance during the energy change phase and some particles are extracted due to longitudinal mismatches occurring during the energy change phase, consequent coherent longitudinal beam oscillations and resulting proximity to the resonance. This results in a 'smearing out' of the beam as the particles are extracted without clear pauses. The extraction ramps are not clearly distinguishable in the CTS plot and the SFX data shows that particles are reaching the detector in the periods between the COSE ramps.

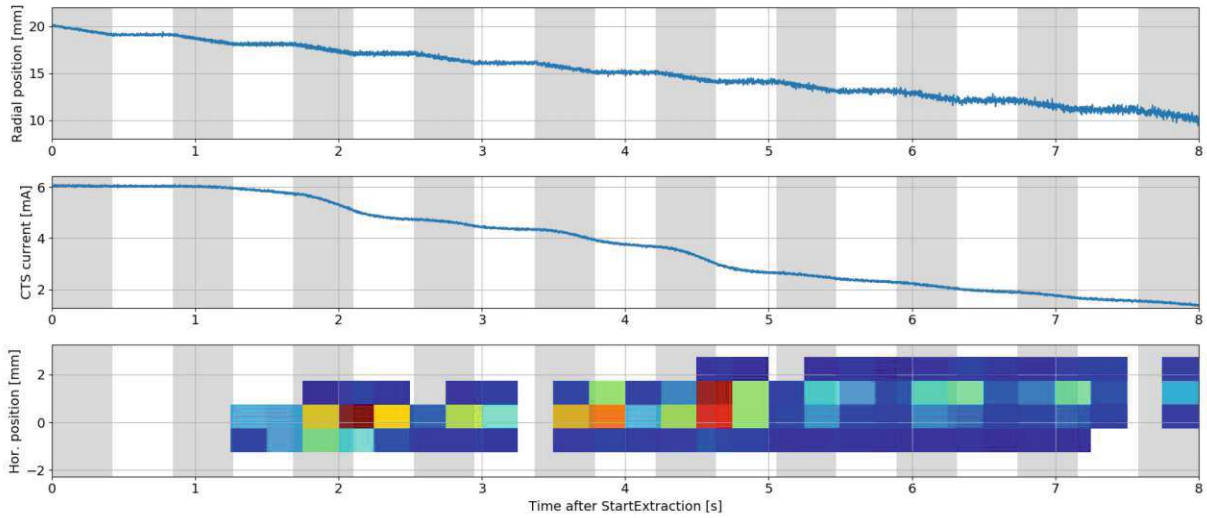


Figure 5.8.: Extraction test for ten energy MEE with bunched COSE. The extraction phase is depicted in grey.

Top: Radial position of the beam over time.

Middle: CTS particle current in the Main Ring over time.

Bottom: 2D intensity plot over horizontal position and time, measured with an SFX in the HEBT.

Two possible solutions were tested to prevent that extraction occurs during the energy change phase:

1. **The 'full jump back' approach:** The radial position is set back to the original value of 20 mm during the energy change phase and jumps back to the last value of the COSE ramp in $10 \mu\text{s}$ at the start of the next extraction phase. This ensures that the beam remains far enough from the resonance, preventing extraction between the COSE ramps.

The schematic configuration of this approach is summarised in Figure 5.9. The results of the test with $\Delta x_n = 1 \text{ mm}$ and $\Delta E_n = 52 \text{ keV}$ are shown in Figure 5.10.

As anticipated, the SFX measurement shows eight distinct extractions with clear pauses in between². Note that the extraction times do not align perfectly with the grey extraction phases due to the frame rate of the SFX monitor of only 4 Hz, resulting in an integration time of 0.25 s. This explains why some intensity data

²No particles are extracted for the first two COSE ramps, as the corresponding momentum slice seems to be unpopulated. This is related to the dead time observed for bunched COSE, as seen in Figure 5.5.

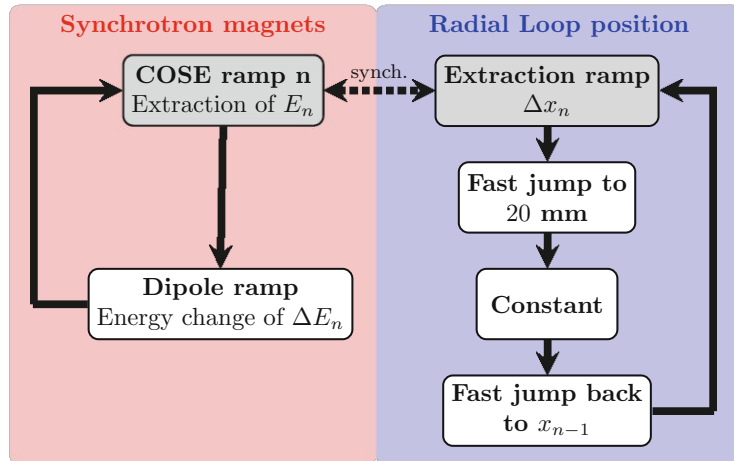


Figure 5.9.: Schematic configuration for MEE with the 'full jump back' approach. The extraction phase is depicted with grey nodes, the energy change phase with white nodes.

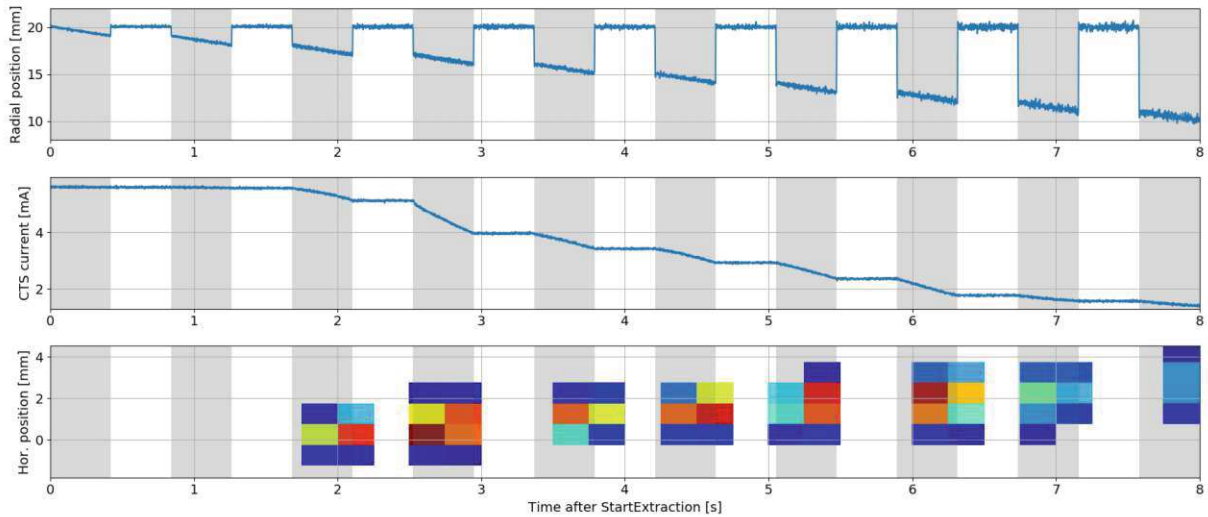


Figure 5.10.: Extraction test for ten energy MEE with bunched COSE with the 'full jump back' approach. The extraction phase is depicted in grey.

Top: Radial position of the beam over time.

Middle: CTS particle current in the Main Ring over time.

Bottom: 2D intensity plot over horizontal position and time, measured with an SFX in the HEBT.

points appear with a delay after the start of the ramp or remain visible after the end of the ramp, as the detector integrates the intensity within these 0.25 s. The CTS measurement confirms the extraction in eight of the ten extraction phases, with no extraction visible during the energy change phase, as the intensity of the circulating beam in the Main Ring remains constant during these phases.

However, an issue arises when measuring the extraction with the 'full jump back' approach using a detector with a high frame rate. For this study, the QIM is used, as it is the fastest detector installed in the synchrotron with a sampling rate of 50 kHz. The results of the QIM intensity measurement for ten energy MEE using the 'full jump back' approach is shown in Figure 5.11.

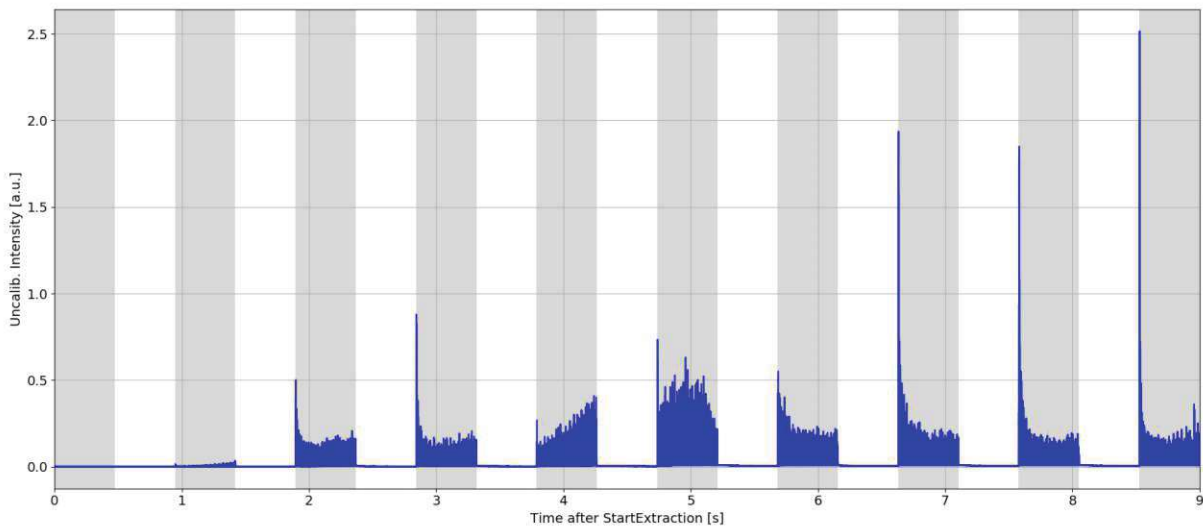


Figure 5.11.: QIM intensity measurement for ten energy MEE with bunched COSE with the 'full jump back' approach. The extraction phase is depicted in grey.

While the temporal structure again indicates clear pauses between each extraction phase and confirms that no particles are extracted during the energy change phase, a significant intensity peak can be observed at the beginning of most extraction phases, when the radial position of the beam is rapidly ramped back down from 20 mm. The amplitude of the spikes increases for the last three extraction phases, where the radial loop jumps from 20 mm to 12, 11 and 10 mm, respectively.

The spikes can be explained by the fact that when the radial loop is rapidly ramped down to x_n mm in $10 \mu\text{s}$, all particles that are within the momentum slice corresponding to radial loop positions between 20 mm and x_n mm are immediately extracted, resulting in an intensity spike.

This intensity spike is not acceptable for clinical use as it would deliver a high dose rate to the patient in a short amount of time. Since synchrotron oscillations cannot be completely suppressed and some refilling will always occur, the 'full jump back' approach had to be discarded.

2. **The 'draw back' approach:** Another method to minimise the extraction during the energy change phase while avoiding intensity spikes caused by the fast jump down of the radial loop, is to adjust the radial position to a slightly higher value before ramping the dipoles. This was realised by a radial position jump of 1 mm immediately after the COSE ramp and before the energy change phase, which moves the beam further away from the resonance³. In contrast to the 'full jump back' approach, the radial position is not moved down again before the next extraction phase. Instead, it remains at a distance of 1 mm above the last point x_{n-1}^{end} of the previous extraction ramp, as defined in equation 5.3.

$$x_n^{\text{start}} = x_{n-1}^{\text{end}} + 1 \text{ mm} \quad (5.3)$$

Each consecutive radial loop ramp covers a distance of $\Delta x_n = 2 \text{ mm}$ from $x_{n-1}^{\text{end}} + 1 \text{ mm}$ to $x_{n-1}^{\text{end}} - 1 \text{ mm}$ ⁴. The first millimetre of the ramp covers a momentum slice that has already been emptied, while the second millimetre of the ramp extracts particles from a previously unaffected momentum slice. Therefore, the effective radial loop ramp Δx_n^{eff} remains at 1 mm. During the safety jump by 1 mm, the beam energy is slightly increased, resulting in a reduction of the effective energy change between consecutive sub-spills to $\Delta E_n^{\text{eff}} = 52 \text{ keV}$, which is the same as for the 'full jump back' approach.

To ensure synchronisation with the radial loop ramp, the magnet scaling factor must correspond to a radial position change of 2 mm for this approach.

Figure 5.12 presents the schematic configuration, while Figure 5.13 visualises the measurement data for $\Delta x_n^{\text{eff}} = 1 \text{ mm}$ and $\Delta E_n^{\text{eff}} = 52 \text{ keV}$ obtained using this approach.

³Other radial position jumps are also possible. Smaller jumps lead to more extraction during the extraction phase, larger jumps might decrease the efficiency of the extraction ramps and reduces the effective length of the sub-spills.

⁴This is true for all but the first radial loop ramp, where the radial position is still ramped from 20 to 19 mm. As this first momentum slice is anyway unpopulated and no particles are extracted with this first ramp, the different ramp rates of the first and all other ramps are not relevant.

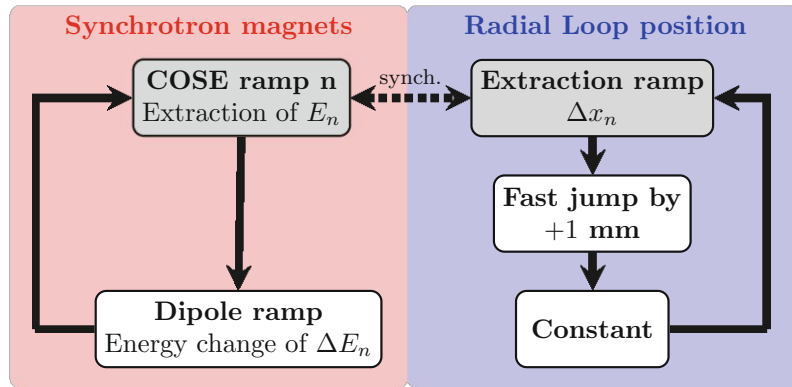


Figure 5.12.: Schematic configuration for MEE with the 'draw back' approach. The extraction phase is depicted with grey nodes, the energy change phase with white nodes.

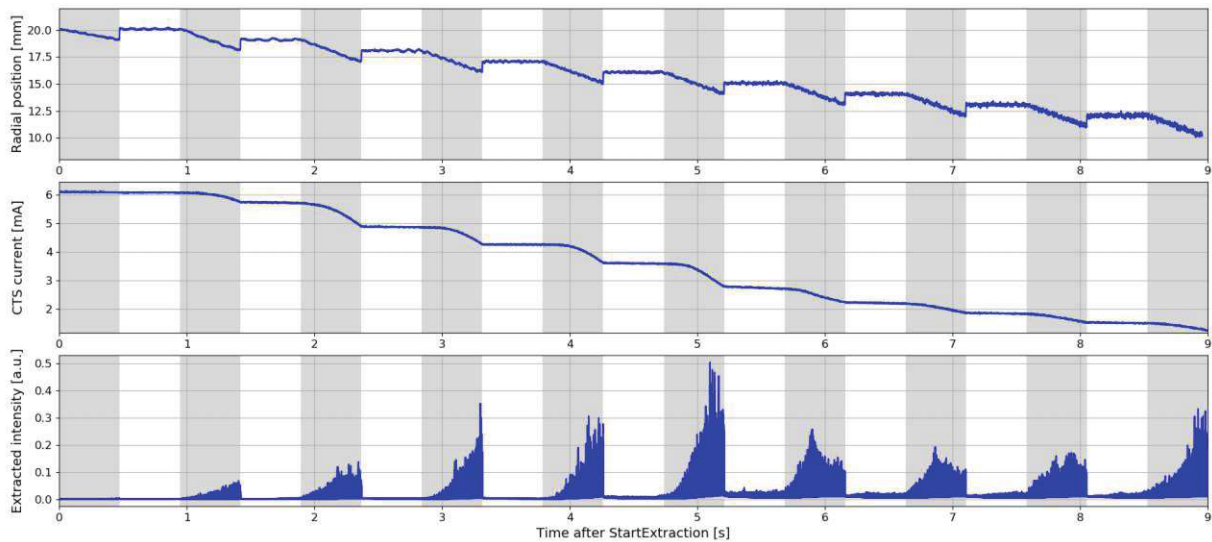


Figure 5.13.: Extraction test for ten energy MEE with bunched COSE with the 'draw back' approach. The extraction phase is depicted in grey.

Top: Radial position of the beam over time.

Middle: CTS particle current in the Main Ring over time.

Bottom: Intensity of the extracted beam, measured with the QIM.

Nine out of the ten sub-spills are visible on both the QIM data and the CTS current. Although the pauses between the extraction phases are less distinct than in the 'full jump back' approach, the intensity extracted during the energy change phases is significantly lower than that extracted during the extraction phase. The extraction phases experience a delay due to the first half of each sub-spill extracting a momentum slice that was already emptied in the previous sub-spill. Due to synchrotron motion of the particles, the momentum slices corresponding to the first half of each sub-spill are refilled during the energy change phase and are therefore not completely empty. The extracted intensity is gradually increased during each sub-spill, as the closer the ramp is to the previously unaffected momentum slice, the higher is the refilled particle density.

The QIM intensity measurements confirm that, unlike the 'full jump back' approach, there are no intensity spikes at the beginning of each sub-spill for the 'draw back' approach, as sudden jumps of the radial position are avoided. The temporal structure of the intensity is more uniform and suitable for clinical treatment.

The 'draw back' approach was employed for further testing and optimisation of MEE with bunched COSE.

Energy acceptance

The maximum total energy change $\Delta E = \sum_n \Delta E_n$ achievable with the proposed method for MEE with bunched COSE is limited by the energy acceptance of the HEBT. While the Main Ring magnet strengths are scaled and therefore follow the changing energy of the beam, the setpoints of the HEBT magnets are fixed at a certain energy and cannot be changed during the spill⁵. Due to dispersive effects, the trajectory of the beam in the HEBT changes for different energies. If this energy-related offset is large enough to cause the beam to hit the vacuum chamber wall at any point in the HEBT, the sub-spill with that particular energy offset will be lost.

To determine the acceptance, a scan of the magnet ramp during the energy change phase, which proportional to ΔE_n , is performed for MEE with two energies. The HEBT magnets are set to a setpoint corresponding to the first energy. When the energy offset of the second sub-spill exceeds the energy acceptance of the HEBT, only the first sub-spill will reach the room anymore. By measuring the intensity of the second sub-spill at the DDM, the energy acceptance can be estimated, as demonstrated in Figure 5.14.

⁵This restriction is present as most HEBT dipoles are in single setpoint (SSP) mode and changing them to follow a setpoint sequence (SSQ) is not straightforward.

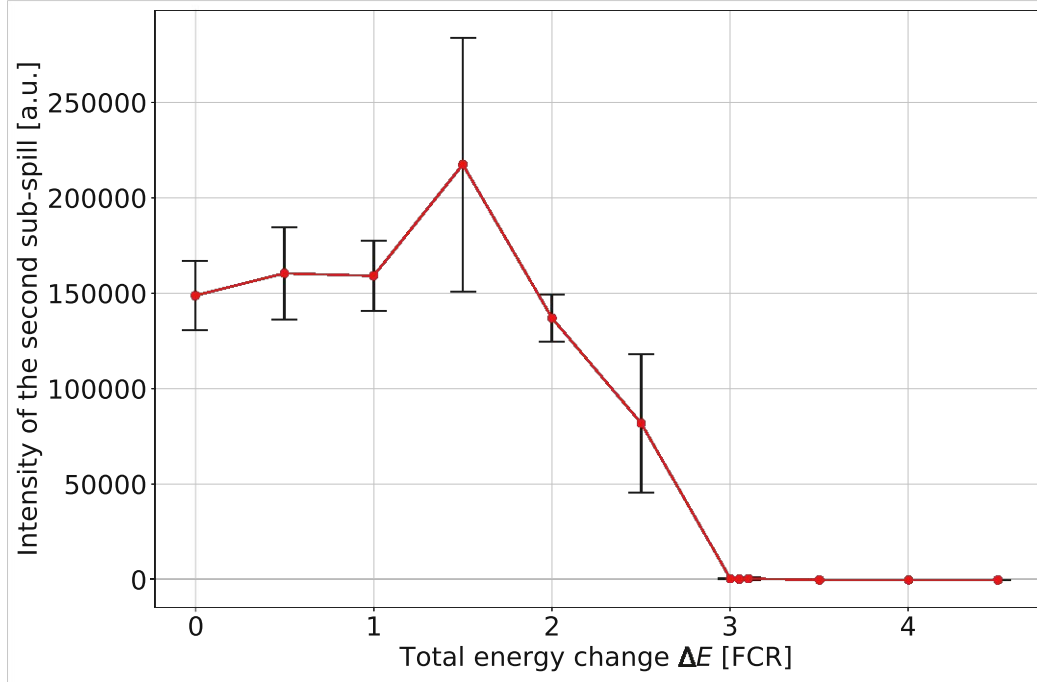


Figure 5.14.: Intensity of the second sub-spill at the DDM for two energy MEE (proton, 252.7 MeV).

The total energy change ΔE is measured in Full COSE Ramp (FCR) units. One FCR is defined as the energy change due to one bunched COSE ramp, synchronised with a radial position ramp from 20 to 10 mm. According to equations 5.1 and 5.2, this ramp corresponds to a relative momentum change of $\Delta p/p = -1.2 \times 10^{-3}$, which is equivalent to an absolute energy change of $\Delta E = 525 \text{ keV}$ for a proton beam with an energy of 252.7 MeV.

For MEE with bunched COSE, it is important to consider that the energy of the beam is affected not only by the dipole ramp during the energy change phase, but also by the COSE ramp during the extraction phase. This results in particles extracted at the beginning of the sub-spill having slightly higher energy compared to those at the end of the sub-spill. The cumulative energy change due to all COSE ramps in the n extraction phases of the MEE spill is, by definition, exactly 1 FCR. To obtain the total energy change from the first extracted particles in the first sub-spill to the last extracted particle in the last sub-spill, one FCR needs to be added to the energy change due to the dipole ramps in the energy change phase, resulting in equation 5.4.

$$\Delta E_{\text{total}} = \Delta E + \Delta E_{\text{COSE}} = \Delta E + 1 \text{ FCR} \quad (5.4)$$

Equation 5.4 is valid regardless of the number of extracted energies within the MEE, as long as the total radial position change is equal to 10 mm.

Figure 5.14 shows that the intensity of the second sub-spill remains constant until an energy change of just below 2 FCR, which indicates that the entire second sub-spill is transmitted through the HEBT and reaches the treatment room. However, when the energy change exceeds 2 FCR, the second sub-spill reaches the treatment room only partially, resulting in a decrease of the measured intensity. At 3 FCR, the energy change has increased to a level where the entire second sub-spill falls outside the energy acceptance range of the HEBT and almost no particles from the second sub-spill reach the detector.

The total energy acceptance range, where all particles from the second sub-spill still reach the room, is therefore $\Delta E_{\text{total}} = 2 \text{ FCR} + 1 \text{ FCR} = 3 \text{ FCR} \hat{=} 1.575 \text{ MeV}$. If ten energies are extracted, the energy difference between two consecutive spills can be calculated as 158 keV. This energy change is too small to be used for clinical application of MEE, since the position of the Bragg peak does not significantly differ for such small energy deviations.

To increase the energy acceptance, the setpoint of the HEBT magnets can be adjusted to the centre of the expected energy range. This doubles the acceptance as both the higher-energy and lower-energy sides of the reference trajectory are used to transmit particles. Figure 5.15 shows this increase of the energy acceptance in the treatment room by scaling the magnet setpoint of the HEBT to the middle of the energy range.

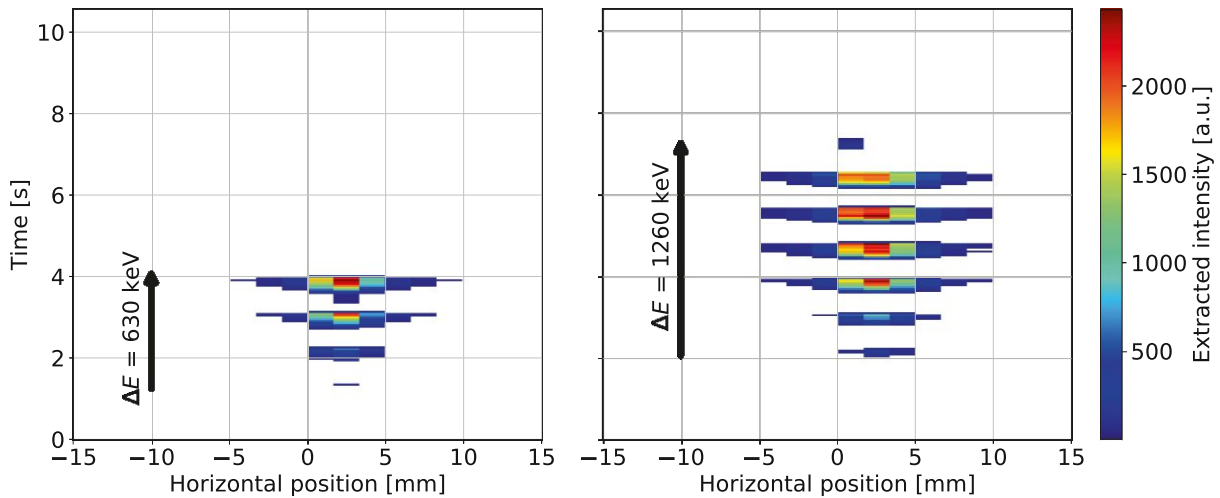


Figure 5.15.: Energy acceptance magnification by scaling the setpoint of the HEBT magnets for ten energy MEE with $\Delta E = 3 \text{ FCR}$ (proton, 252.7 MeV).

Left: Unscaled HEBT magnet setpoint.

Right: HEBT magnet setpoint scaled to middle of energy range.

For both scaled and unscaled HEBT, a energy change ΔE of 3 FCR was used, which corresponds to a total energy change of $\Delta E_{\text{total}} = 4 \text{ FCR} \cong 2.1 \text{ MeV}$. The energy difference between each consecutive sub-spill is therefore 210 keV.

In case of an unscaled HEBT magnet setpoint corresponding to a beam energy of 252.7 MeV, only four energies reach the room, with the first energy having a very low intensity. If the HEBT magnets are set to an energy of 252.0 MeV (which is half of the energy acceptance lower than the highest energy), seven sub-spills are visible on the DDM. This indicates that seven energies are transmitted through the HEBT and reach the room. This result is consistent with the expected doubling of the energy acceptance due to the scaling of the HEBT.

5.1.4. Limitations of COSE

As demonstrated previously, bunched COSE exhibits strong compatibility with MEE. However, the extraction speed for all types of COSE extractions is primarily constrained by the rate of the magnet ramps. If the ramp rate is too high, the power converters are unable to follow the current curve specified in the SSQ data, resulting in a loss of synchronisation between the magnets. To evaluate the speed limitation, SSQ data for ultra-fast COSE with a magnet current scaling factor of -5% in 1 ms was applied to a proton beam with 252.7 MeV. The current of the Main Ring dipoles was measured and compared with the pre-programmed current curve of the SSQ data, as shown in Figure 5.16.

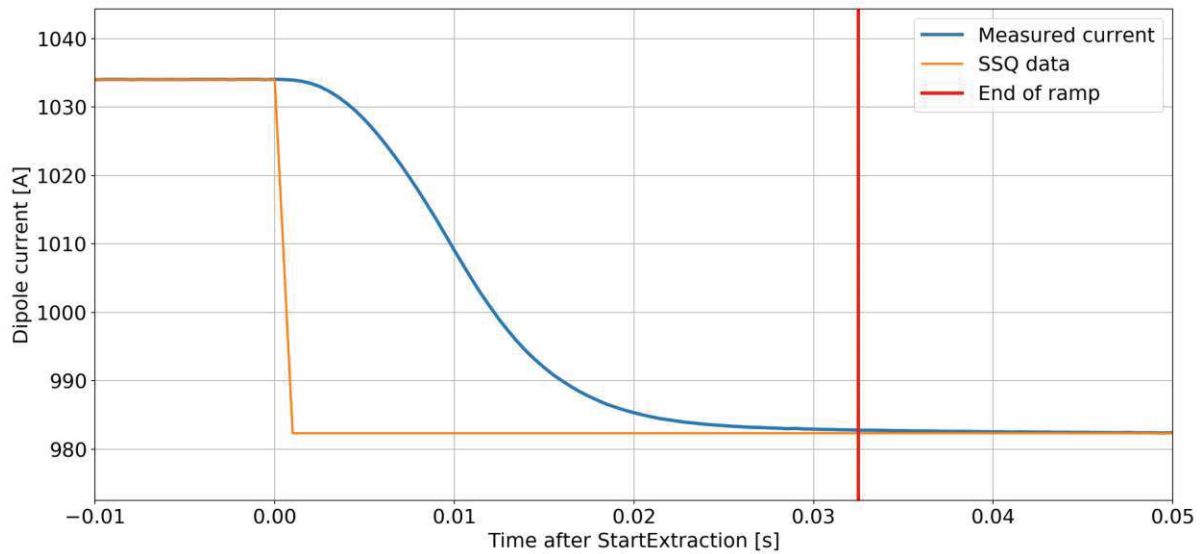


Figure 5.16.: Comparison of the measured and set current for ultra-fast COSE (proton, 252.7 MeV).

While the SSQ data follows the fast current ramp in 1 ms, the measured magnet current shows that in reality, the power converter does not react fast enough to reach the requested ramp rate. As a result, the dipole current ramp takes approximately 33 ms until the current is reduced by 5%⁶. This corresponds to a maximum ramp rate of 1.59 A or -0.15% per millisecond for a proton beam with 252.7 MeV. According to section 5.1.2, the total ramp required to extract the entire beam is -0.12%. Therefore, the minimum spill length achievable with bunched COSE is 0.8 ms⁷. An analogous calculation yields a limit of 2.7 ms for unbunched COSE with a phase jump. However, these ultra-high ramp rates may result in significant rounding effects for the current (as also visible in Figure 5.16,) which could cause a desynchronisation between the ramps of the different magnets and result in an insufficient COSE setup.

The maximum ramp speed was also measured for the Main Ring quadrupole and sextupole magnets to confirm that the dipole magnets are indeed the limiting components. For all three quadrupole and two sextupole families, the real ramp duration for a 1 ms ramp was measured as 20 ms, which corresponds to a maximum ramp rate of -0.25% per millisecond. The quadrupole and sextupole magnets react therefore 40% faster than the dipole magnets and can be neglected when estimating the minimum spill length. Furthermore, the current setpoint at flattop is significantly higher for dipoles than for all other magnet components. This means that a higher absolute current difference ΔI must be achieved for the same relative scaling factor $\Delta I/I$, which further confirms that the dipoles impose the most critical speed limitation.

An additional limitation of COSE in general is that as the resonance is moved through the beam, there is a significant intra-spill energy drift (and thus also a position movement in regions with $D_x \neq 0$), as particles with different momentum offsets are extracted at different points in time. The energy difference is given by the momentum spread of the circulating beam. According to Table 3.1, this spread is 1.67 MeV for unbunched and 0.39 MeV for bunched COSE⁸, both for a proton beam with 252.7 MeV. However, scattering effects inside the patient may limit the clinical relevance of this intra-spill energy drift.

⁶The end point of the ramp is defined by the time when relative error between the set and measured current $\Delta I/I$ gets smaller than 5×10^{-4} .

⁷This is a rough estimation of the spill length limit, as the rounding at the beginning and end of the ramp might not allow a direct extrapolation.

⁸The energy drift for bunched COSE with the configuration previously described is mainly defined by the radial loop ramp and not by the momentum spread of the beam.

5.2. Phase Displacement Extraction (PDE)

Phase Displacement Extraction (PDE) involves sweeping a properly configured empty bucket through the stationary beam, as theoretically described in section 2.3.2.

The equations 5.5, 5.6 and 5.7 for the PDE bucket parameter derived in this section represent theoretical predictions based on a simplified model of the longitudinal phase space. While these predictions provide a useful starting point, implementing PDE in a real accelerator requires further parameter optimisation to maximise extraction efficiency. To implement PDE, three parameters must be set:

- The **bucket voltage** controls the bucket height and must be set in a way that the bucket overlaps with both the resonance and the beam throughout the entire sweep. For single-sweep PDE, it also needs to cover the distance from the low-momentum particles to the resonance at the end of the sweep to ensure that all particles can be extracted. The required bucket height can be calculated using equation 5.5.

$$(\Delta p/p)_{\text{bucket height}} > |(\Delta p/p)_{\text{beam offset}}| + \frac{1}{2}(\Delta p/p)_{\text{beam spread}} \quad (5.5)$$

For MedAustron, the lower limit of the bucket height is $(\Delta p/p)_{\text{bucket height}} = 4.2 \times 10^{-3}$, which corresponds to a minimal bucket voltage of $V_{\text{bucket}} = 1 \text{ kV}$ for a proton beam with 252.7 MeV.

For pulsed PDE, the voltage can be lower, as the particles displaced by the first sweep can be extracted in the next sweep, allowing equation 5.5 not to be satisfied.

- The **range of the bucket frequency ramp** is determined by the initial and final bucket frequency offset df_{start} and df_{end} with respect to the revolution frequency of the beam and needs to be aligned with the configuration of the beam and the resonance, as illustrated in Figure 5.17.

Ideally, df_{start} should be set so that the lowest part of the bucket aligns with the highest beam momentum and can be calculated using equation 5.6.

$$df_{\text{start}} = f_{\text{rev}} \cdot \eta \cdot \frac{(\Delta p/p)_{\text{bucket height}} + (\Delta p/p)_{\text{beam spread}}}{2} \quad (5.6)$$

For MedAustron, equation 5.6 results for a proton beam with 252.7 MeV after phase jump and a bucket voltage of 1.1 kV in a starting frequency of $df_{\text{start}} = 3450 \text{ Hz}$ with respect to the revolution frequency of the beam.

In practical application, it may be advisable to start the sweep further away from the beam. While this approach would result in an increased 'dead time' at the start of the sweep, it would ensure that particles with momenta outside the FWHM momentum spread remain unaffected when the bucket is established.

The final bucket frequency offset df_{end} corresponds to the frequency where the upper part of the bucket no longer overlaps with the resonance, preventing further acceleration of the particles into resonance. This frequency offset can be calculated using equation 5.7.

$$df_{\text{end}} = f_{\text{rev}} \cdot \eta \cdot \left((\Delta p/p)_{\text{beam offset}} - \frac{(\Delta p/p)_{\text{bucket height}}}{2} \right), \quad (5.7)$$

resulting in a value of $df_{\text{end}} = 210$ Hz.

With this frequency range, the change of the bucket frequency for one sweep $\Delta f_{\text{B}} = df_{\text{end}} - df_{\text{start}}$ satisfies equation 2.55, covering the entire frequency spread of the beam.

- The **sweep time** determines the speed at which the bucket moves through the beam and, consequently, the extraction rate. If only a single sweep is performed, the sweep time is set to ten seconds. However, if the sweep is repeated multiple times for a pulsed extraction, the sweep time needs to be reduced accordingly. The bucket speed also determines the extraction efficiency for each sweep. If the bucket moves too slowly, all particles will be extracted during the first sweep, resulting in close to zero extracted intensity for the consecutive sweeps. Therefore, the sweep time needs to be reduced for pulsed extraction to ensure that enough particles remain after the first sweep. The importance of the sweep time for pulsed extraction with PDE is discussed in section 5.2.1.

The (theoretically) ideal bucket configuration for PDE at the start and the end of the sweep is shown in Figure 5.17. The frequency is given relative to the revolution frequency of the beam. The displacement and extraction of the particles at the end of the spill are not shown, as the plot is not based on simulation and serves only as a visual representation of the bucket position relative to the the beam and the resonance.

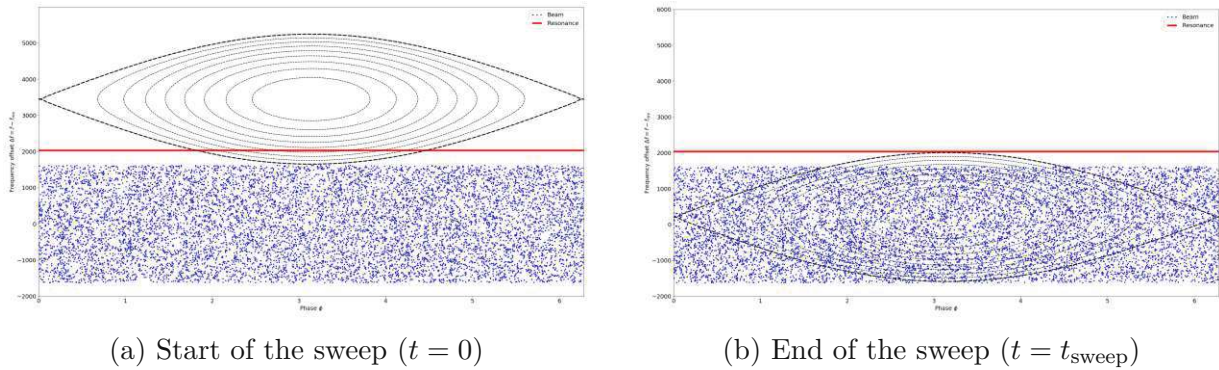


Figure 5.17.: Bucket configuration for PDE.

As the momentum offset, the bucket dimensions, the revolution frequency and the phase slip factor depend on the particle energy, the calculated parameters are only valid for a proton beam with 252.7 MeV and need to be adjusted for any other particle energy. However, a generalisation of the setup for different energies can be achieved by scaling the bucket voltage with the beam energy, maintaining a constant ratio between the bucket height and the momentum spread of the beam. Additionally, by expressing the sweep time in terms of number of turns, the speed of the sweep can also be normalised for different energies. The optimisation of PDE for various energies and particle types remains an area for future research.

The MedAustron control system allows for great flexibility in programming the frequency and voltage of the RF cavity via an SSQ file, enabling easy implementation of PDE. This extraction technique is limited to unbunched beams, as bunched beam operation requires a bucket containing the particles. Therefore, it is impossible to generate another bucket for PDE since only one cavity is installed in the synchrotron.

Figure 5.18 displays a measurement for single bucket sweep PDE with $df_{\text{start}} = 3 \text{ kHz}$, $df_{\text{end}} = -1 \text{ kHz}$, $V_{\text{bucket}} = 1 \text{ kV}$ and $t_{\text{sweep}} = 9 \text{ s}$ of a proton beam with 252.7 MeV. The chosen parameters were obtained from an optimisation scan and differ slightly from the theoretical values.

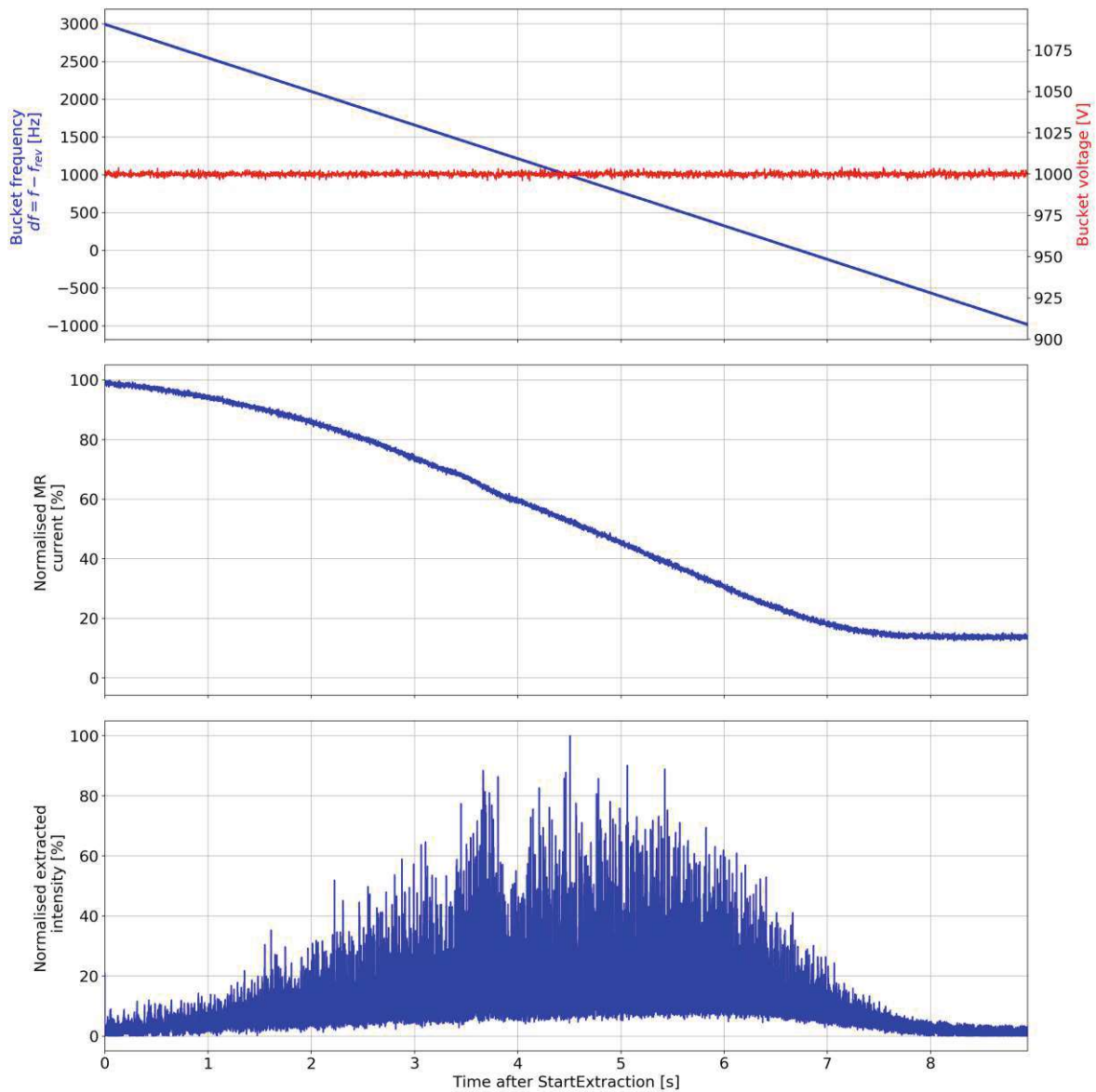


Figure 5.18.: Phase Displacement Extraction measurement with $df_{\text{start}} = 3 \text{ kHz}$, $df_{\text{end}} = -1 \text{ kHz}$, $V_{\text{bucket}} = 1 \text{ kV}$ and $t_{\text{sweep}} = 9 \text{ s}$.

The first plot presents the cavity frequency (blue) and voltage (red) measurements. The bucket voltage remains constant at 1 kV throughout the spill, while the frequency is gradually decreased to move the bucket through the beam.

The second plot displays the current circulating in the Main Ring, normalised to the flat-top value. The extraction begins abruptly, as the bucket with the selected initial frequency offset already slightly overlaps with the beam. The extraction efficiency is just above 80%, as a significant proportion of the particles remain unextracted in the ring. This can be explained by the bucket being too small and no longer overlapping with the resonance at the end of the sweep. As a result, almost no particles are extracted during the last second of the spill.

The extracted intensity (third row) forms a Gaussian curve, painting the longitudinal momentum distribution. To maintain a constant intensity throughout the spill, it is necessary to adjust the frequency ramp to a non-linear curve.

The extraction efficiency of PDE is highly dependent on the bucket voltage, as it controls the bucket height and thus the region where the bucket overlaps with both the resonance and the beam. Figure 5.19 shows the current circulating in the Main Ring for different bucket voltages with a bucket ramp from $df_{\text{start}} = 3.5$ kHz to $df_{\text{end}} = 0$ kHz in nine seconds.

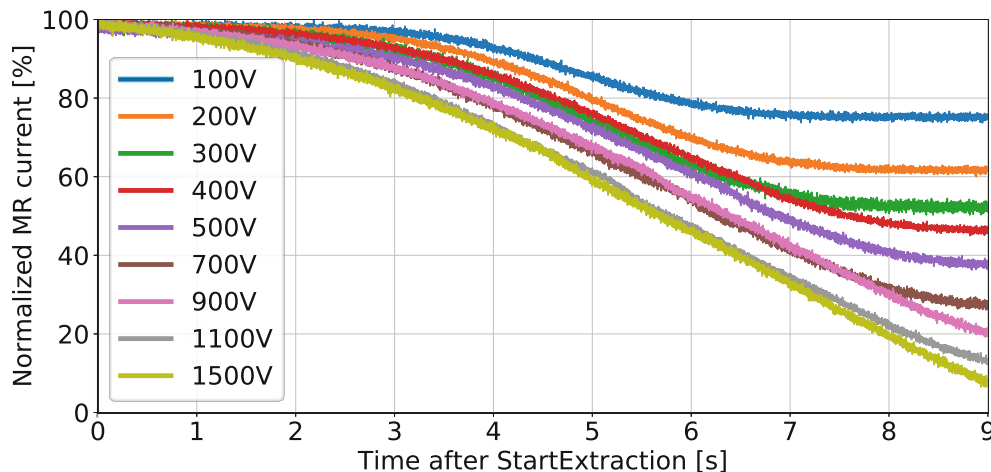


Figure 5.19.: CTS measurement for PDE with different bucket voltages.

The extraction efficiency increases monotonically with the bucket voltage. While a bucket voltage of 100 V leads to an extraction efficiency of only 25%, over 91% of the particles are extracted for a bucket voltage of 1.5 kV. A lower bucket voltage also delays the start of the extraction and increases the dead time at the end of the spill.

5.2.1. Pulsed extraction

When the bucket sweep is repeated multiple times, particles are extracted only when the bucket is aligned with the beam and the resonance. This results in an extraction that is pulsed with the repetition frequency $f_{\text{rep}} = 1/t_{\text{sweep}}$.

Once a sweep is finished at f_{end} , the bucket frequency must be ramped up again to f_{start} to continue with the next sweep. To ensure that the beam remains undisturbed during this bucket reset, the voltage is set to zero at the end of the sweep and then reset to V_{bucket} before the start of the next sweep. The resulting bucket frequency and voltage programme is shown in the top plot of Figure 5.20.

However, the quality of the pulsed extraction depends on the sweep speed. Figure 5.20 illustrates the extraction of a proton beam at 252.7 MeV for four slow sweeps of one second (2.38×10^6 turns), each with a bucket voltage of 1 kV. This corresponds to a bucket height of 4.3×10^{-3} , which is 115% of the momentum spread of the beam.

The plot of the circulating current in the Main Ring (middle) as well as the extracted intensity (bottom) shows that 80% of the particles are extracted in the first sweep, with an additional 2% reaching resonance during the second sweep. The extraction efficiency drops below 1% for all consecutive sweeps. This can be attributed to the slow sweep rate, which causes almost all particles to be immediately pushed into resonance during the first ramp of the bucket.

Ramping the voltage to zero during the bucket reset is performed to achieve a pulsed extraction with almost no particles extracted between subsequent pulses, as confirmed by the current and extracted intensity measurements. For the setup shown in Figure 5.20, the reset phase is equally long as the sweep phase. However, this is not a necessary condition, as the buckets can be reset much faster than the extraction sweep, resulting in a sawtooth-shaped frequency program. The speed of the bucket reset was constrained to $50 \mu\text{s}$ to allow sufficient time for the cavity voltage to stabilise before initiating the next sweep [50].

The intensity plot indicates that intensity spikes occur when the bucket voltage is ramped up again after the bucket reset, as particles with an unfavourable frequency are immediately extracted when the bucket is opened. To prevent this, the bucket must be moved further away from the beam before ramping up the voltage.

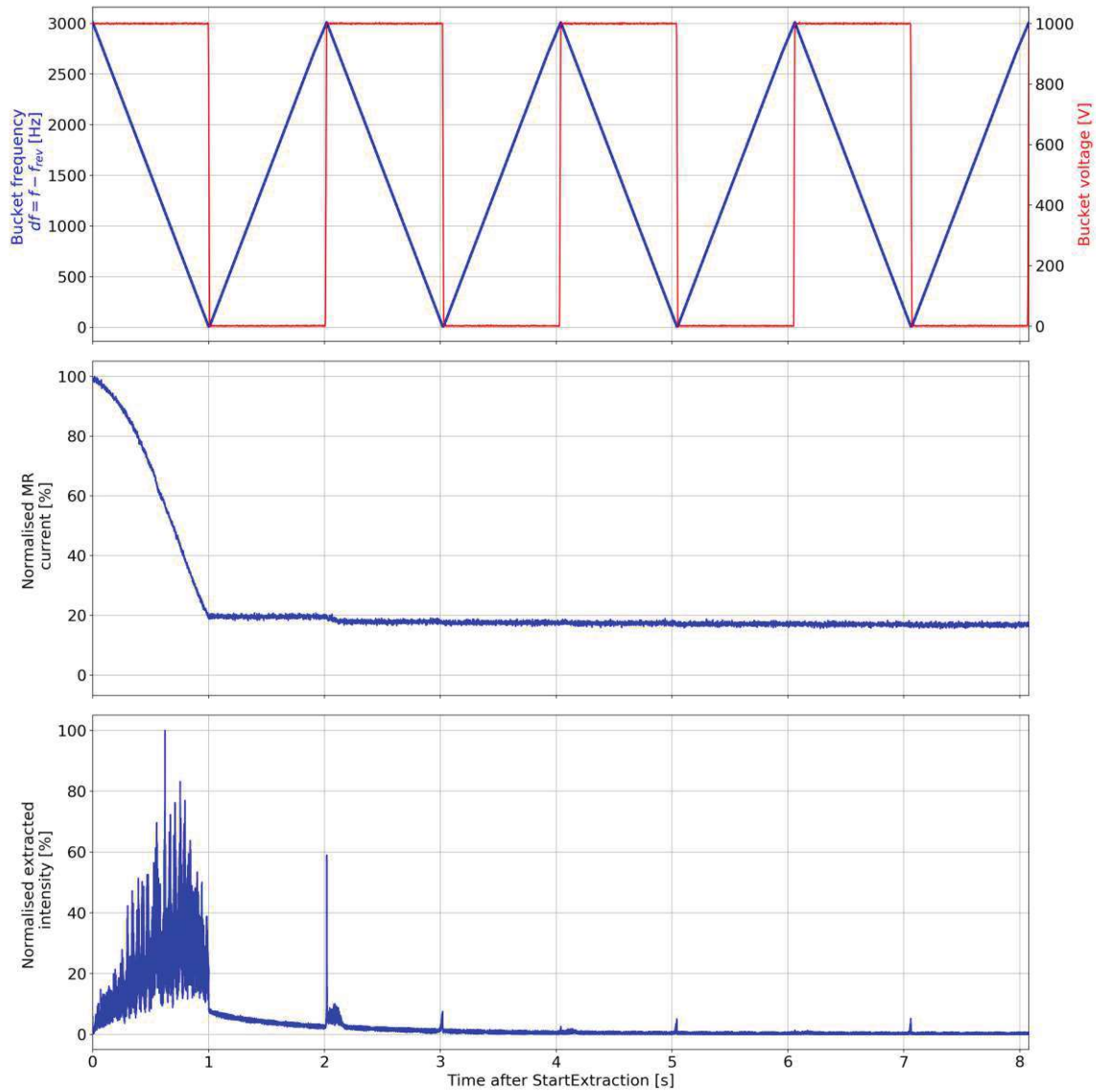


Figure 5.20.: Pulsed Phase Displacement Extraction with four sweeps ($df_{\text{start}} = 3 \text{ kHz}$, $df_{\text{end}} = 0 \text{ Hz}$, $V_{\text{bucket}} = 1 \text{ kV}$ and $t_{\text{sweep}} = 1 \text{ s}$).

To harmonise the extracted dose rate per pulse, the sweep time can be reduced. This results in a faster bucket sweep and less extraction during the first sweep. However, this method is limited by the time resolution of the frequency program of the RF cavity. Measurements for a 252.7 MeV proton beam indicate that if the sweep is faster than $t_{\text{sweep}} = 0.5 \text{ ms} \hat{=} 1,190$ turns, the extraction efficiency decreases and not all particles are extracted

from the synchrotron.

Figure 5.21 illustrates the impact of the sweep time on the dose rate per pulse. While for slow sweeps with $t_{\text{sweep}} = 40 \text{ ms} \hat{=} 95,100$ turns (Figure 5.21a) most of the particles are extracted during the first sweep and no extraction occurs after the second sweep, the uniformity of the dose rate per pulse is improved for fast sweeps with $t_{\text{sweep}} = 1 \text{ ms} \hat{=} 2,380$ turns (Figure 5.21b). Although the dose rate is still the highest for the first pulse, enough particles can still be extracted for the consecutive sweeps [50].

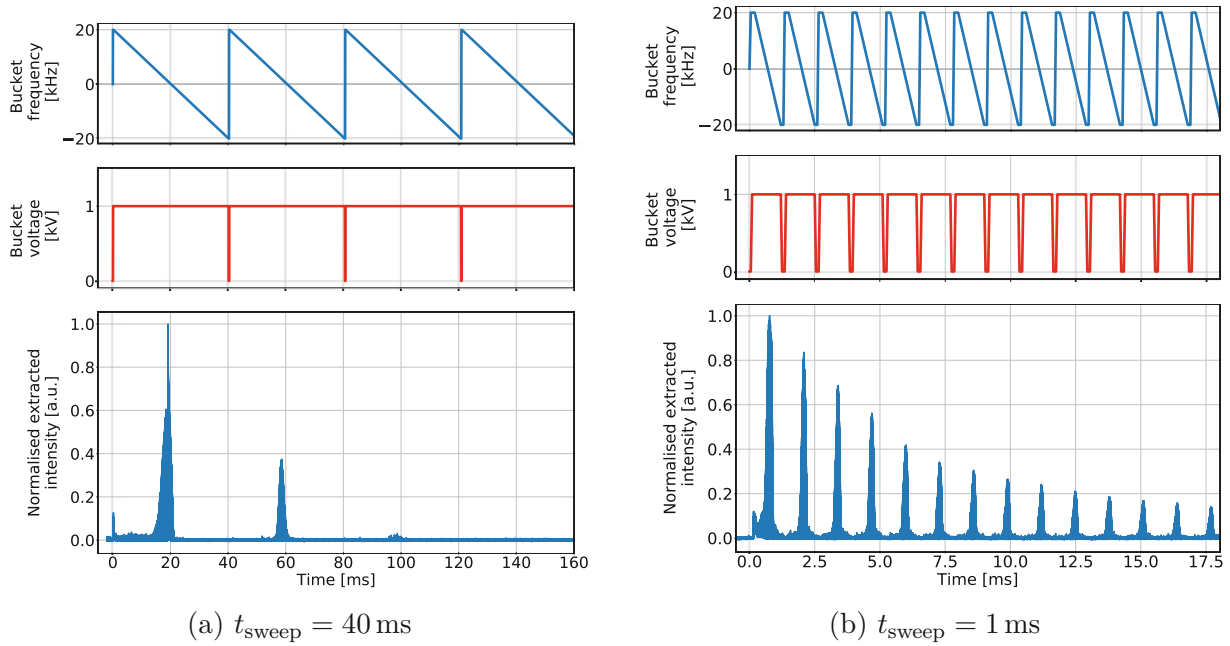


Figure 5.21.: Pulsed PDE with faster sweeps. The measurements were performed with a SiC detector developed at HEPHY [50]. (courtesy of Elisabeth Renner)

6. Intensity beam ripples

For clinical treatment with ions, it is crucial that the particle flux of the extracted beam is as constant as possible. The treatment system requires a certain dose applied to each grid point of the tumour. Fluctuations of the dose might lead to an under- or over-irradiation of the tissue, which have to be counter-measured as part of the risk mitigation by restricting the extracted dose rate. The higher the intensity ripples are, the more conservative are the safety requirements on the dose rate. By reducing the ripples, the average dose rate can be higher, extraction times can be shortened (from ten to just a few seconds) and the irradiation process can be sped up. Additionally, if the extracted dose rate is too high, it can also cause interlocks of the DDS to avoid over-irradiation. These interlocks can cause significant delays, prolonging the treatment duration and thus reducing the efficiency of the treatment.

Because of this, it is of high interest for clinical facilities to understand and mitigate the intensity ripples in order to increase treatment efficiency. The most relevant frequency regime reaches from a few tens of Hz to a few kHz, as this affects the time scale the DDS operates in and thus has a direct effect on the treatment quality. Ripples with higher frequencies above 100 kHz are only visible as a 'smearing out' of the beam intensity over time and are not relevant for safety concerns.

In reality, it is impossible to completely inhibit all intensity ripples of the extracted beam. All electrical components of the accelerator complex induce ripples with certain frequencies on the beam, due to their power supply or operating frequencies of switches and other parts of the magnets. Additionally, the movement of the circulating particles due to synchrotron motion can also cause intensity ripples in the extracted beam¹.

To better understand the impact of power supply ripples in the accelerator components on the intensity ripples of the extracted beam, a simulation of the extraction with betatron core was performed for 5,000 particles and 100,000 turns using XSuite tracking. The results were compared with the same extraction simulation, but with deliberately adding ripples on the MR quadrupole currents during extraction. These sinusoidal ripples with a period of 1,000 turns were injected with an amplitude of 0.1% of the flattop current. The high

¹Additional to the intensity ripples, also ripples in position of the beam at isocenter is of importance for the treatment efficiency. However, this study focuses on the intensity ripples only.

ripple amplitude was chosen for demonstration purposes only. The actual current ripples in the accelerator magnets have an amplitude that is two orders of magnitude smaller than those used in this simulation.

The simulation results for both scenarios are shown in Figure 6.1. To calculate the extracted intensity, the whole extraction range of 100,000 turns is divided into intervals of 50 turns each and the numbers of particles extracted in each of these intervals are counted.

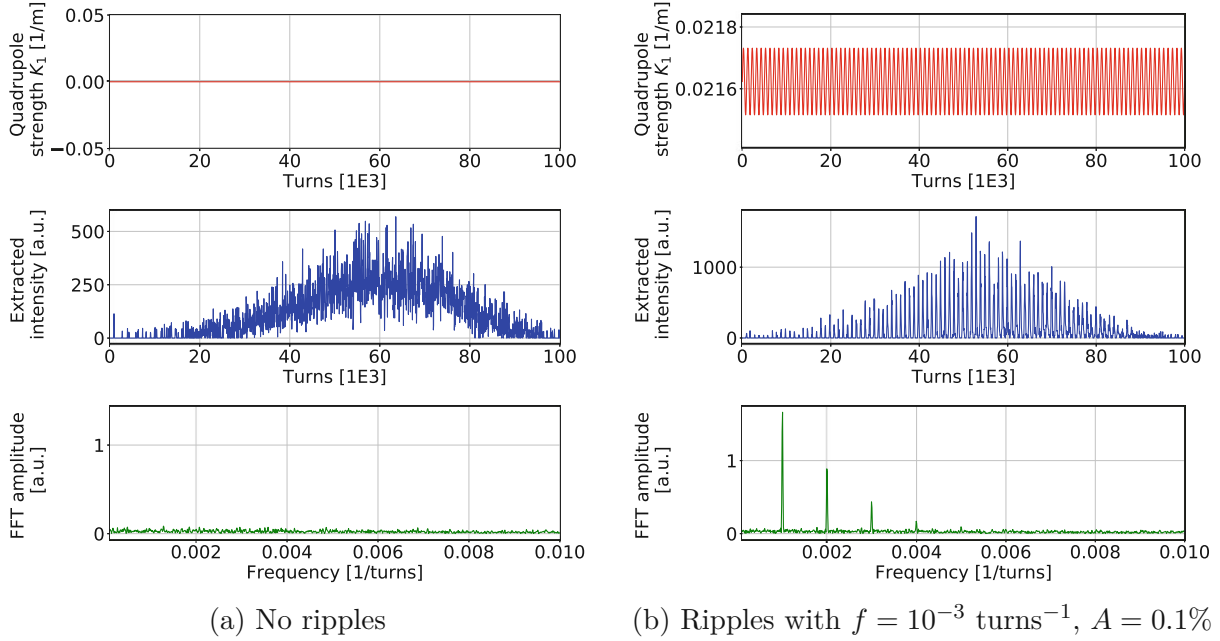


Figure 6.1.: Impact of quadrupole ripples on the extracted beam intensity.

It is clear that the ripple on the quadrupole current impacts the spill structure of the extracted beam. The difference is already visible in the plot of the intensity over time, but is even more prominent when performing a FFT of the extracted intensity over time. While the FFT shows no significant peaks for the scenario without ripples induced, the other scenario with induces ripples leads to distinct peaks in the FFT spectrum at frequencies that corresponds to the harmonics of the ripple frequency at $n \cdot 1000^{-1} \text{ turns}^{-1}$. The fact that also peaks at the harmonics of the base frequency are visible can be contributed to the high amplitude of the induced ripple, which results in non-linear effects and thus in the appearance of higher harmonics.

This exemplary simulation demonstrates the critical importance of ripple reduction to achieve a consistent dose rate. A more comprehensive analysis, including the calculation of transfer functions for various magnet families, is provided in section 6.4.

6.1. Quantification of intensity ripples

To quantify the impact of the intensity ripples on the quality of the beam, different parameters can be defined:

- The **peak to mean ratio** r is calculated by dividing the intensity by the mean intensity of the whole spill, as given in equation 6.1

$$r_i = \frac{I_i}{\langle I \rangle_{\text{spill}}} \quad (6.1)$$

The maximum of r over the entire spill is a measure for the quality of the extracted beam. For an ideal case with a perfectly constant intensity, the ripple factor is 1 for the whole spill. As the beam delivery scanning system operates at a frequency of 2 kHz, it is reasonable to downsample the acquired data to this frequency, to quantify what ripple the scanning system would 'see'. The ripple factor for the downsampled data is always smaller than for the original data, as during the downsampling process the intensity is averaged in the respective time window and therefore peaks get smoothed out.

- The **ripple factor** RF is used for a more statistical quantification of the spill quality. The whole spill is divided in windows of 10 ms each. For each of these windows, the local mean value of the intensity $\langle I \rangle_{10 \text{ ms}}$ is calculated. The ripple factor is the ratio of the local maximum and the local mean value in each of the time windows.

$$RF_{10 \text{ ms}} = \frac{\max(I)_{10 \text{ ms}}}{\langle I \rangle_{10 \text{ ms}}} \quad (6.2)$$

The quality of the whole spill can be quantified by taking the maximum (or the mean) value for all 10 ms windows. As for the peak to mean ratio, the ripple factor is 1 in an ideal case with no intensity fluctuations and is always larger than 1 in real conditions. The advantage of the ripple factor compared to the peak to mean ratio is that single intensity outliers are not taken into account as much, as calculating the ripple factor effectively corresponds to downsampling the data to 100 Hz. Additionally, slow drifts of the average intensity are compensated, as the local mean value of the intensity is used.

- The **duty factor** DF is also calculated for 10 ms windows, but takes an even more statistical approach as not the maximum intensity, but the standard deviation of the intensity σ in each of the time windows is used, as given in equation 6.3. This

approach was proposed by Singh et al. in [82] as a common standard to calculate the duty factor.

$$DF_{10\text{ms}} = \frac{\langle I \rangle_{10\text{ms}}^2}{\langle I \rangle_{10\text{ms}}^2 + \sigma_{10\text{ms}}^2} \quad (6.3)$$

To calculate the duty factor for the whole spill, either the mean or the maximum value of the duty factor for all 10 ms windows can be used. It is also possible to calculate a weighted mean value as given in equation 6.4, by weighing the duty factor of each time window with the mean intensity in this time window.

$$DF = \frac{1}{\sum \langle I \rangle_{10\text{ms}} \text{ all windows}} \sum_{\text{all windows}} DF_{10\text{ms}} \cdot \langle I \rangle_{10\text{ms}} \quad (6.4)$$

For a constant intensity without any ripples, the standard deviation is zero, so the duty factor is 1. The more ripples are present, the higher is the standard deviation and the lower is the duty factor, which is always a value between 0 and 1.

- Another parameter that can be observed is the amplitude of peaks at certain frequencies of the Fourier spectrum of the intensity over time. For this study, especially the peak at a frequency of 4 kHz is important. As shown in section 6.2, the peak at this frequency is one of the most dominant peaks in the FFT spectrum as the power converter of the dipole magnets in the Main Ring are operating at this frequency². For an extraction without any ripple mitigation methods, so the reduction of the amplitude of this peak shows how successful the suppression of the ripples in this important frequency range is.

Figure 6.2 shows the aforementioned beam quality parameters for an typical clinical spill (10s proton beam with an energy of 252.7 MeV, Empty Bucket Channelling active) for intensity data recorded with the QIM³. The peak to mean ratio r (blue, top left), the ripple factor RF (red, middle left) and the duty factor DF (green, bottom left) can be plotted over time to identify possible changes during the spill. The maximum value of the peak to mean ratio is highlighted with the dashed black line and can be used to quantify the quality of the full spill. As the ripple factor and the duty factor are more statistical parameter, it makes sense to use the median value to quantify the ripples instead of the extreme values. The FFT spectrum (blue, right) is shown for the full spill. While the position and amplitudes of all peaks are interesting and can be further analysed, to quantify

²More precisely, the dipole power converter delivers the magnet current in three phases at an operating frequency of 666.66 Hz. After a full-wave three-phase rectification of the AC signal, the resulting effective frequency of the pseudo-DC output current is $666.66 \text{ Hz} \cdot 3 \cdot 2 = 4 \text{ kHz}$.

³The QIM is used as default monitor for ripple analysis, as it is the fastest detector with the highest sampling rate.

the beam quality only the amplitude of the peak at 4 kHz is considered and marked with the dashed black line.

For the statistical parameters ripple factor and duty factor, it also makes sense to plot the values over the full spill in a histogram and a boxplot, as shown in Figure 6.3.

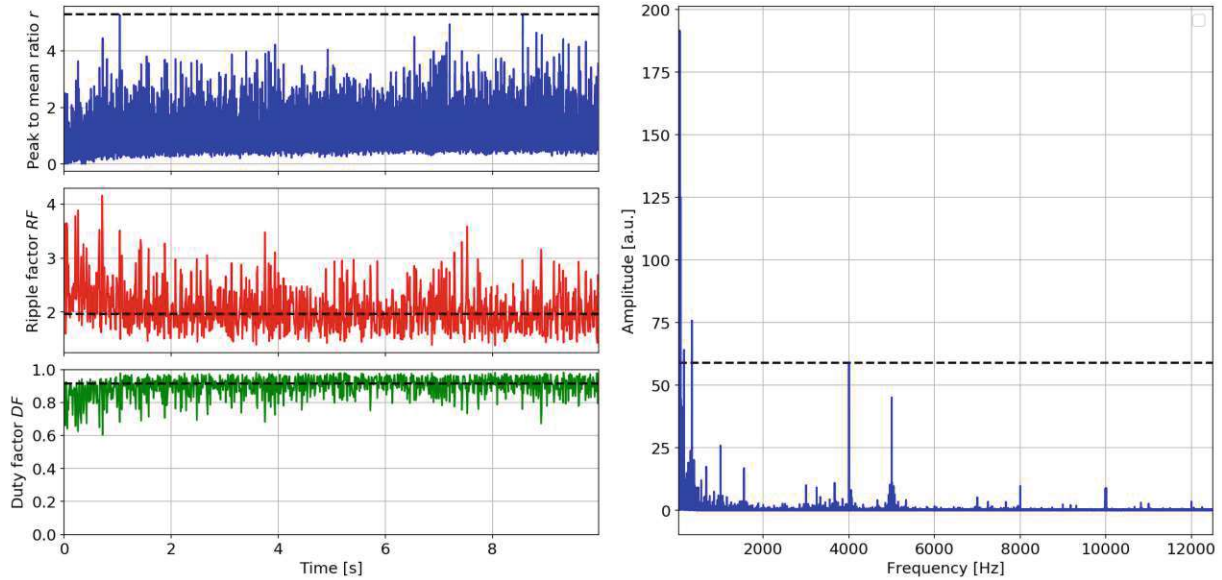


Figure 6.2.: Beam quality parameters for a 10s proton beam with an energy of 252.7 MeV (Empty Bucket Channelling active).

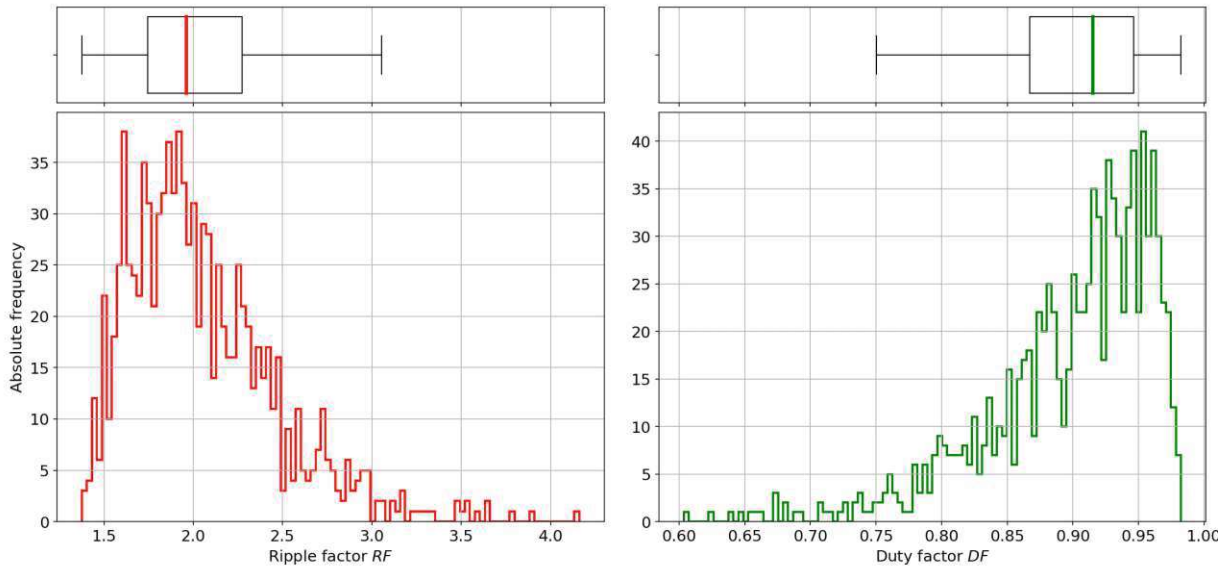


Figure 6.3.: Histogram of the beam quality parameters for a 10s proton beam with an energy of 252.7 MeV (Empty Bucket Channelling active).

The beam quality depends on the different beam parameter, such as particle type, spill length and beam energy. Table 6.1 summarises the beam quality parameters for different beam settings. Empty Bucket Channelling was active for all settings, the ripple parameters without EBC are discussed in section 6.3. The values are averaged over five spills for each setting, resulting in the mean values and standard deviations provided in Table 6.1.

Setting	r	RF	DF	4 kHz peak
proton, 10s, 252.7 MeV	5.7 ± 0.5	2.00 ± 0.05	0.91 ± 0.01	59 ± 1
proton, 10s, 62.4 MeV	5.7 ± 0.5	2.10 ± 0.03	0.92 ± 0.00	37 ± 2
proton, 1s, 252.7 MeV	2.4 ± 0.1	1.71 ± 0.05	0.94 ± 0.00	74 ± 2
carbon, 10s, 402.8 MeV/u	2.8 ± 0.2	1.66 ± 0.04	0.93 ± 0.01	409 ± 22
carbon, 10s, 120.0 MeV/u	2.9 ± 0.2	1.80 ± 0.03	0.94 ± 0.00	986 ± 16

Table 6.1.: Beam quality parameters for different beam settings (EBC active).

In general, the extraction with EBC seems to be close to optimised, with ripple factors below 2.1 and duty factors above 0.9 for all settings.

The statistical beam quality parameters (ripple factor and duty factor) are almost identical for proton and carbon ions. The peak to mean ratio seems to be significantly lower for

a carbon beam, while the amplitude of the 4 kHz peak for carbon is more than a factor 10 higher than for proton, which comes from the different implementation of EBC for the different particle types, as described in section 6.3.

The energy of the beam does not impact the ripple parameters significantly, neither for a proton nor for a carbon beam. Only the peak at 4 kHz seems to be larger (proton)/smaller (carbon) for higher energies, which can be explained by the energy-dependent effect of Empty Bucket Channelling.

A shorter spill length improves the ripples significantly, at least when judged by the peak to mean ratio, the ripple factor and the duty factor. This makes sense as for a shorter spill length, the beam is pushed faster into resonance and therefore the impact of power converter ripples is reduced. The 4 kHz peak does not follow this trend and shows a higher amplitude for the spill with one second. The worse result can be understood that while the low-frequency ripples are suppressed by the increased speed of the particles crossing the resonance, the medium-frequency ripples with frequencies of a few kHz are not affected by the different extraction speed. However, the relative impact and thus the amplitude of ripples in this frequency region is increased, as the other ripples are suppressed.

6.2. Intrinsic intensity beam ripples

As a first approach, the intrinsic intensity beam ripples can be analysed using an intensity measurement of the extracted beam in the treatment room with the CIVIDEC[®] detector, as described in section 3.2. The CIVIDEC[®] detector was used instead of the QIM due to the high bandwidth and the ability to resolve ripples with ultra-high frequencies above 1 MHz. To identify the main ripple frequencies, a FFT of the intensity over time was performed and the main peaks were detected and labelled.

The frequency spectrum can be divided in a low-frequency part for ripples with $f < 1$ kHz (shown in Figure 6.4) and a high-frequency part with $f \geq 1$ kHz (shown in Figure 6.5). All measurements were performed for a 10 s proton beam at 252.7 MeV without EBC. The main peak in the low-frequency part of the Fourier ripple spectrum is the one at 50 Hz, which is the operating frequency of the power grid in Austria. Also the harmonics of the grid frequency at 100 and 150 Hz are clearly visible. The ripple with the second-highest amplitude is at a frequency of 70 Hz. The peak at 150 Hz is also particularly prominent (and also a peak of the second harmonic at 300 Hz is present), which indicates that it is not only the third harmonic of the grid frequency, but also a base frequency of an intensity ripple in the extracted beam. Another ripple frequency seems to be at 333.3 Hz with a distinct peak at the base frequency as well as the first harmonic.

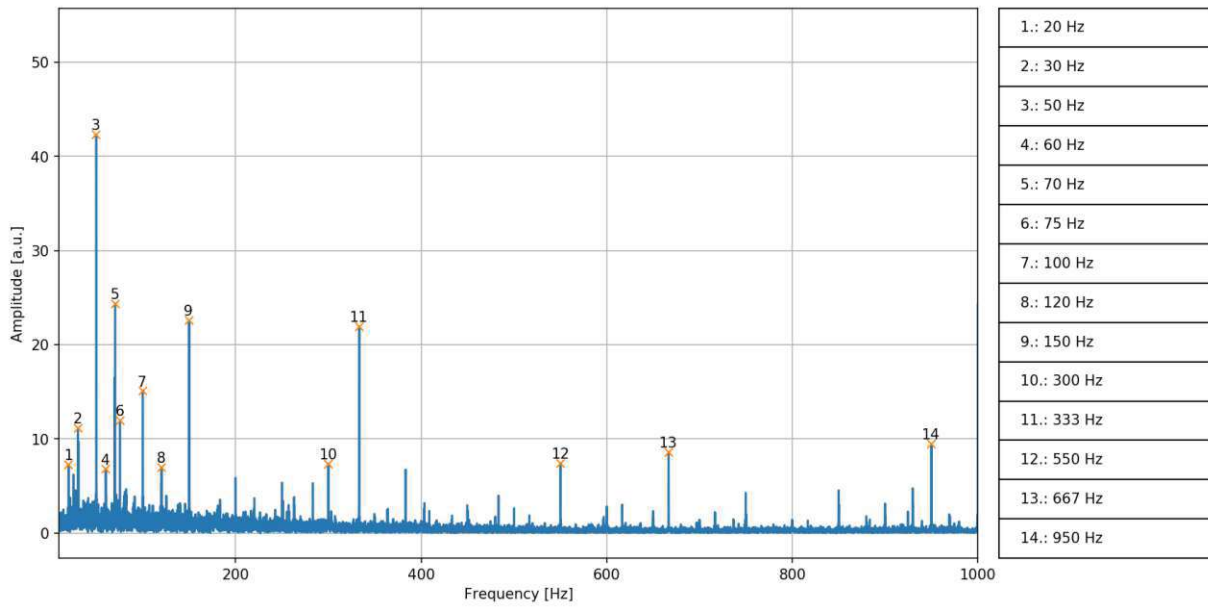


Figure 6.4.: Low-frequency intrinsic beam ripples for a 10 s proton beam with an energy of 252.7 MeV (no EBC).

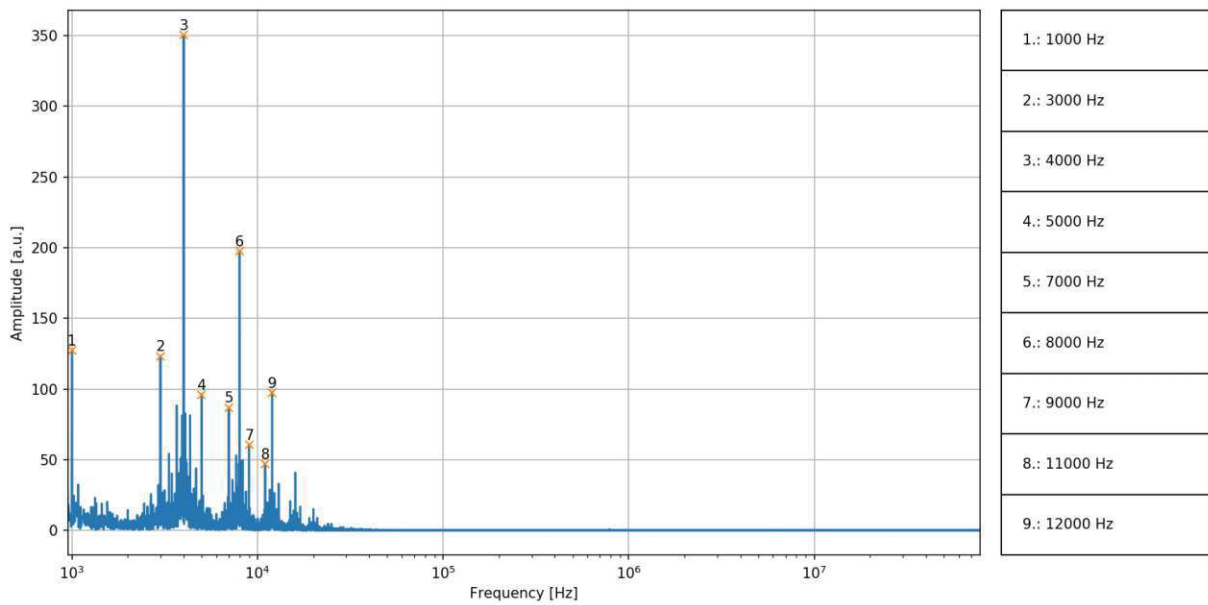


Figure 6.5.: High-frequency intrinsic beam ripples for a 10 s proton beam with an energy of 252.7 MeV (no EBC).

In the high-frequency part of the spectrum, the most dominant ripple is at a frequency of 4 kHz, which originates from the dipole switching frequency. Also the second and third harmonics of this switching frequencies are clearly visible at 8 and 12 kHz. The other peaks identified in the high-frequency spectrum are the uneven multiples at $n \cdot 1$ kHz with n in [1, 3, 5, 7, 9, 11]. It is worth mentioning that no peaks appear at the even multiples of 1 kHz (apart from the harmonics of the dipole switching frequency), it even looks like these ripples are actively suppressed, as there are significant low-amplitude 'dips' in the Fourier spectrum at 2, 6 and 10 kHz.

Note that no ripples with frequencies above approximately 40 kHz were measured. Especially in the MHz-region of the spectrum, no distinct peaks are visible and the Fourier spectrum resembles a flat line with almost zero amplitude. The accelerator effectively resembles a low-pass filter, suppressing any ripples with higher frequencies.

6.3. Empty Bucket Channelling

This thesis discusses the Empty Bucket Channelling (EBC) ripple mitigation technique. The theoretical aspects of this concept are explained in section 2.4. At MedAustron, two different EBC configurations are used, which differ in bucket placement. Long-distance EBC is used for proton beams, while short-distance EBC is implemented for carbon ions. Both configurations will be analysed and compared in this chapter using simulations and measurements.

The bucket configurations for the two EBC types are compared in Figure 6.6.

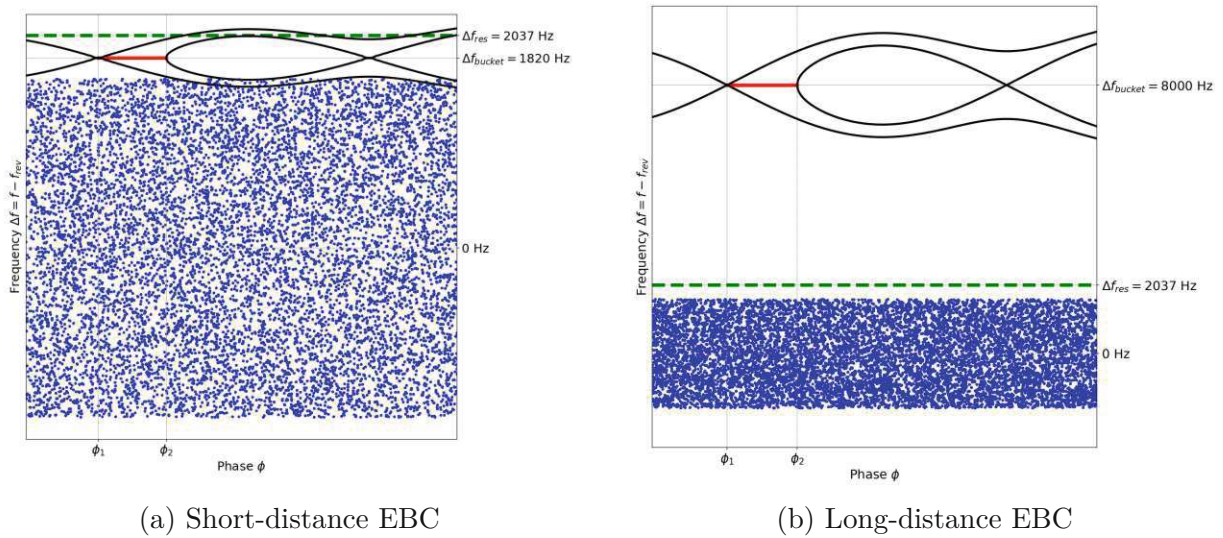


Figure 6.6.: Bucket configuration for the two EBC types implemented at MedAustron for a proton beam with 252.7 MeV.

The short-distance EBC ($\Delta f_{\text{bucket}} \sim 2 \text{ kHz}$, $V_{\text{bucket}} \sim 100 \text{ V}$) is the technique recommended in [7], where the resonance region aligns with the bucket, as visualised in 2.17. The particles are channelled through the bucket gap into the resonance for this 'proper' implementation of EBC.

For long-distance EBC ($\Delta f_{\text{bucket}} \sim 8 \text{ kHz}$, $V_{\text{bucket}} \sim 3000 \text{ V}$), the bucket is positioned with a higher frequency offset and an increased voltage. The resonance is no longer located within the bucket area and the particles are not passing through the bucket gap prior to extraction. However, this configuration still achieves significant ripple reduction, as shown in section 6.3.2. A long-distance EBC configuration is also implemented at the CERN SPS as ripple mitigation technique [62].

The long-distance setup is independent of the beam energy, as the bucket is so far away from the stack, that the energy-dependence of the bucket height and the frequency offset can be neglected. Short-distance EBC needs to be scaled with the beam energy to keep the channelling configuration identical for all energies. The bucket voltage and frequency can be scaled with equations 6.5.

$$V_{\text{bucket}} = \frac{2\pi\beta_r^2 E h |\eta| \delta_B}{4e} \quad (6.5)$$

$$\Delta f_{\text{bucket}} = f_{\text{rev}} \eta (\Delta p/p)_{\text{off}}$$

6.3.1. Simulations

Simulations of EBC were performed with BLoND for 1×10^6 particles and a spill length of 0.1 s for a carbon beam with 402.8 MeV/u. The power converter ripples were induced by adding a sinusoidal modulation of the extraction energy with a frequency of 4 kHz and a relative amplitude of 1×10^{-5} .

The extraction efficiency over time for short-distance (green) and long-distance EBC (orange) in comparison for a spill without EBC (blue) is shown in Figure 6.7.

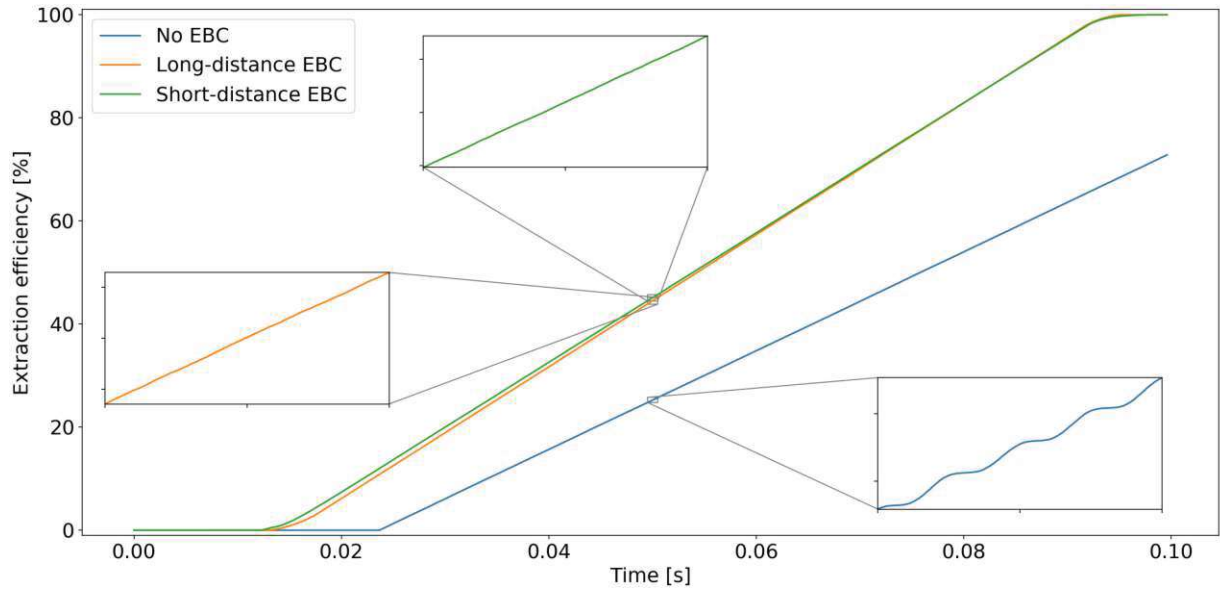


Figure 6.7.: Simulated extraction efficiency over time for a spill with and without EBC.

Figure 6.7 shows the impact of EBC on the extraction of the beam. Due to the acceleration of the particles close to the bucket, the extraction starts earlier for a spill with active

EBC. Without EBC, only 73% of the particles are extracted after 0.1 s, while all particles are extracted with EBC due to the additional acceleration of the particles.

When zooming into the efficiency plot, it becomes evident that the extraction is strongly modulated with the ripple frequency of 4 kHz for the spill without EBC, as particles are only extracted during the half-wave where the resonance approaches the beam, while extraction pauses occur when the ripple causes the resonance to move in the opposite direction. Both EBC implementations prevent this modulation, resulting in a linear extraction without any noticeable pauses. Upon closer inspection of the spill with long-distance EBC shows still a very small modulation of the extraction, whereas the modulation is completely suppressed with short-distance EBC.

The turn-by-turn extraction efficiency was used to calculate the resulting intensity of the extracted beam, using a sampling interval of 110 turns (equivalent to a sampling frequency of 25 kHz). This calculated intensity can be used to quantify the beam quality. While the mean duty factor for a spill without EBC is 0.68, the value increases to 0.88 for long-distance EBC and even 0.96 for short-distance EBC, corresponding to an increase by 29.4 and 41.2%, respectively. The close-to-ideal duty factor for short-distance EBC proves that the tune ripple is almost completely suppressed.

6.3.2. Measurements

The intensity of the extracted spill over time for a carbon beam with 402.8 MeV/u with and without EBC is shown in Figure 6.8. A long-distance EBC configuration was used for the measurement.

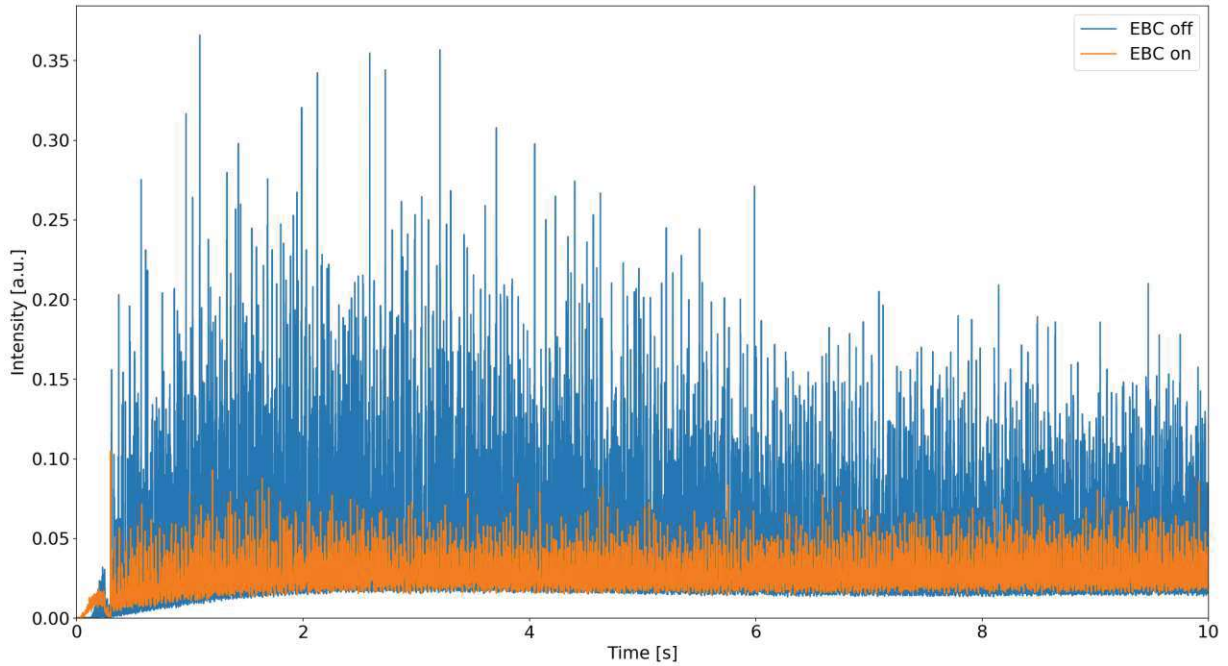


Figure 6.8.: Extracted intensity with and without EBC.

The reduction of ripples with EBC is evident, as the intensity fluctuations are significantly decreased. The beam quality parameters introduced at the beginning of this chapter were calculated for the long- and short-distance EBC configurations, based on an intensity measurement of the extracted carbon beam with 402.8 MeV/u and a spill length of ten seconds. A 2D scan of the bucket frequency and voltage was performed to find the optimised settings for both long- and short-distance implementation of EBC, resulting in the following setpoints:

- Long-distance EBC: $\Delta f_{\text{bucket}} = 8.5 \text{ kHz}$, $V_{\text{bucket}} = 2700 \text{ V}$
- Short-distance EBC: $\Delta f_{\text{bucket}} = 1.889 \text{ kHz}$, $V_{\text{bucket}} = 103 \text{ V}$

The beam quality parameters for these optimised settings are summarised in Table 6.2.

Setting	r	RF	DF	4 kHz peak
No EBC	10.6 ± 0.6	3.76 ± 0.04	0.71 ± 0.01	598 ± 18
Long-distance EBC	3.88 ± 0.33	1.69 ± 0.03	0.93 ± 0.01	16 ± 2
Short-distance EBC	2.83 ± 0.15	1.66 ± 0.04	0.93 ± 0.01	409 ± 22

Table 6.2.: Beam quality with and without EBC (Carbon, 402.8 MeV/u, 10 s).

While the short-distance implementation of EBC is more effective in reducing the overall beam quality by decreasing the peak to mean ratio and the ripple factor, the long-distance EBC is better at suppressing the 4 kHz ripple, achieving an impressive reduction of 97.3%. Both implementations significantly improve the beam quality with a duty factor increase of 31% and can be used for optimising the clinical treatment.

The impact of the EBC on the beam ripples is also evident in the FFT spectrum, as shown in Figure 6.9. The intensity measurement for a proton beam with 252.7 MeV and a spill length of ten seconds was performed with the CIVIDEC[®] detector, which allows to measure high-frequency ripples in the MHz region. The baseline for a spill without any ripple mitigation techniques is shown in red, while the spectrum with long-distance EBC active is represented with a blue line.

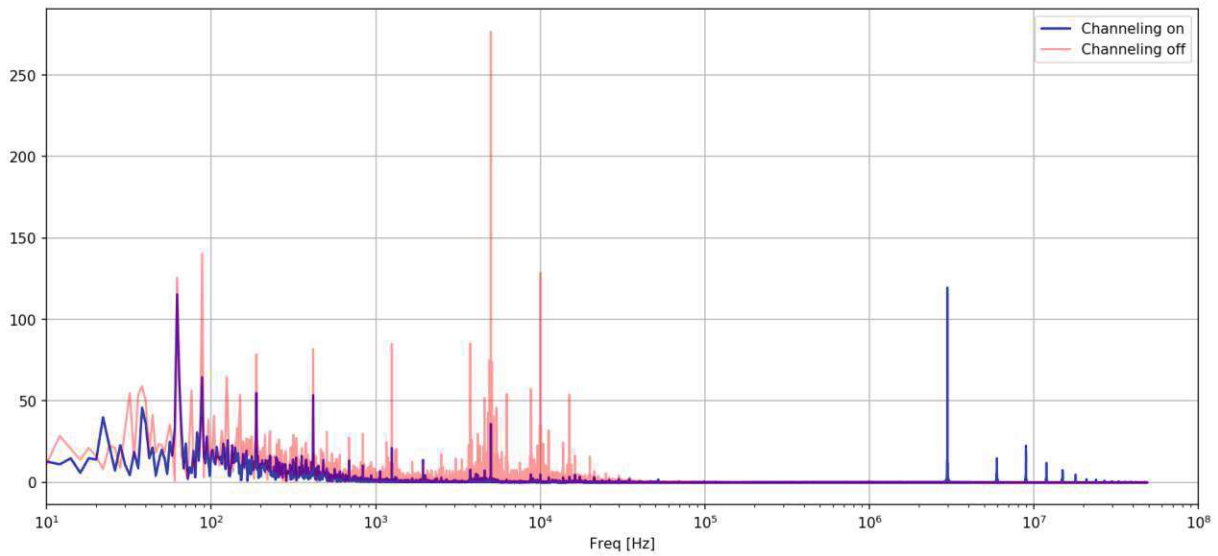


Figure 6.9.: Comparison of the beam ripples with and without EBC (Proton, 252.7 MeV, 10 s beam)

While the low-frequency ripples below 100 Hz are barely affected by EBC, the medium-frequency ripples (including the 4 kHz ripple and its harmonics) are strongly reduced. This shows the benefit of EBC, as ripples at these frequencies are most significant for clinical treatment.

However, EBC introduces a new ripple at high frequencies of a few MHz. Peaks at the harmonics of this ripple are also visible in the spectrum. The frequency of this peak corresponds to the bucket frequency $f_{\text{bucket}} = f_{\text{rev}} + \Delta f_{\text{bucket}}$. This can be understood as while the coasting beam is evenly distributed over the whole longitudinal phase space, the presence of the bucket moves the particles closer to the phase of the bucket gap, resulting in an uneven longitudinal phase distribution of the particles. This leads to a modulation of the extraction with the bucket frequency, which explains the introduction of a peak at that frequency. However, as explained before, ripples with such high frequencies are not relevant for clinical treatment, as the sampling rate of the treatment system is much lower than this frequency. As a result, these ripples are not perceived as intensity fluctuations but rather as a smearing out of the beam intensity. It is therefore acceptable for EBC to introduce new ripples in the MHz region, as long as it suppresses the ripples in the frequency region that is clinically more relevant.

6.4. Ripple transfer function

All ripples in the Fourier spectrum discussed above originate from current ripples of the Main Ring components. To quantify the impact each magnet has on the intensity ripples of the extracted beam, a ripple transfer function for each individual magnet family can be calculated.

For this, a sinusoidal ripple with known amplitude A_0 and frequency f_0 is deliberately put on the magnet current by modifying the SSQ data for the magnet. The ripple transfer function RTF for a frequency f_0 is defined in equation 6.6 as the amplitude of the peak at f_0 on the FFT of the intensity measurement, divided by the amplitude A_0^{FFT} of the injected ripple relative to the Flat-Top (FT) current I_{FT} . Particularly at higher ripple frequencies, the ripple amplitude from the output of the magnet power converter may differ from the set ripple value A_0 . Therefore, A_0^{FFT} is obtained by performing an FFT on a current measurement of the rippled magnet.

$$RTF(f_0) = \frac{A_{\text{intensity}}^{\text{FFT}}(f_0)}{\frac{A_0^{\text{FFT}}}{I_{\text{FT}}}} \quad (6.6)$$

For the intensity measurement, either the QIM or the CIVIDEC[®] detector can be used in theory. Due to availability and the low frequency of the injected ripples, the QIM was used as default measurement device. The CIVIDEC[®] detector was used to cross-check some of the obtained ripple transfer functions, which showed a good agreement between the two measurements.

The injected ripple amplitude was normalised to the flattop current of the magnet to allow a fair comparison of the different magnet. If the absolute amplitude of the injected ripple would be used to calculate the RTF , the impact would have been higher for magnets with smaller flattop currents, which would have a negative impact on the comparability for the different magnets.

The ripple transfer function was measured for a proton beam with 252.7 MeV, using the QIM detector at different base ripple frequencies and relative ripple amplitudes. The chosen frequencies were based on the intrinsic ripples discussed in the previous chapter to avoid any overlap with the injected ripple frequency. Calculating the RTF for different frequencies enables the study of frequency-dependent ripple transfer. Measurements at various amplitudes of the injected ripples can be used to detect non-linearity in the beam response to injected ripples and may indicate the presence of higher-order effects.

Figure 6.10 shows the magnet current measurement (left) and the QIM intensity measurement of the extracted beam (right) for 17 Hz ripple with an amplitude of 0.1 % of the flattop current, injected into a focusing quadrupole. The exemplary measurement was taken for a proton beam with 252.7 MeV without EBC.

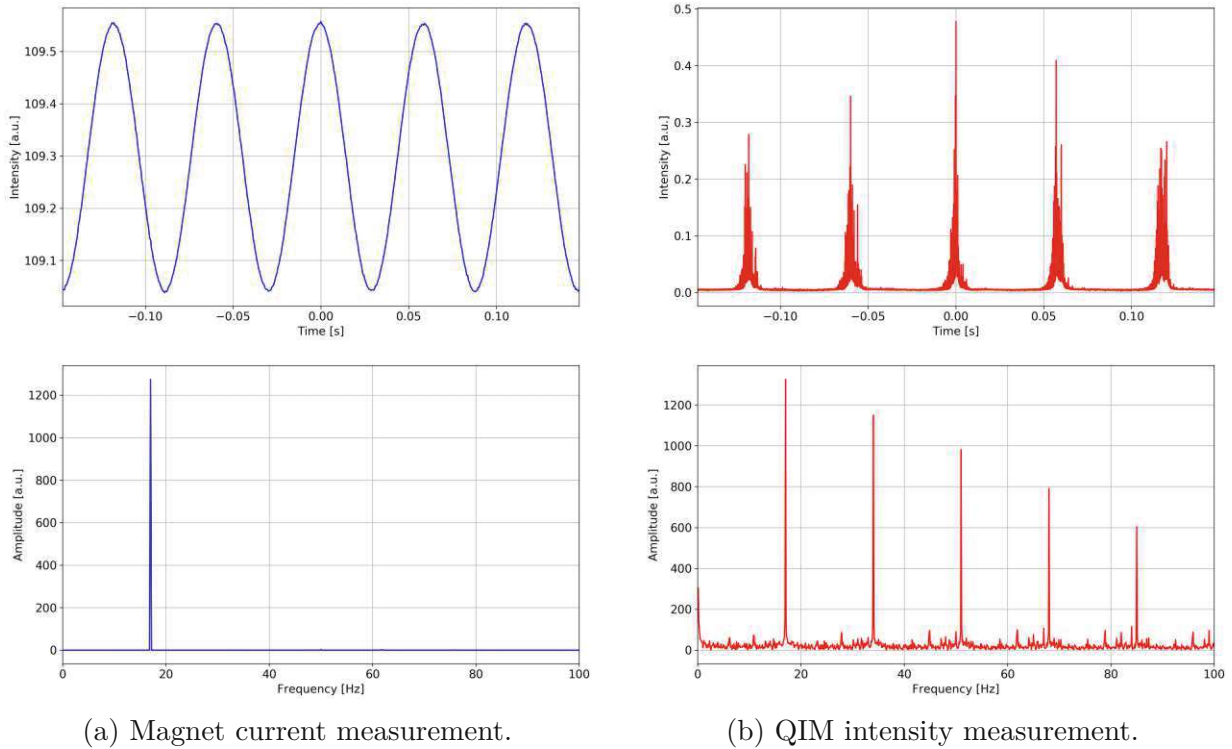


Figure 6.10.: Exemplary ripple transfer function measurement.

The measurement of the magnet current indicates that the sinusoidal ripple with a frequency of 17 Hz is correctly applied and that the power converter follows the set current. The Fourier spectrum reveals that the peak at 17 Hz is dominant, with such a high amplitude that all other peaks are no longer visible.

The intensity measurement of the extracted beam shows a pulsed extraction with a pulse frequency of 17 Hz. Particles are extracted only when the tune matches the extraction condition, which is determined by the quadrupoles and thus also modulated with a sine wave. Extraction pauses occur during the other parts of the modulation outside of that tune window. The FFT spectrum indicates that the dominant peak is the 17 Hz peak. However, the harmonics of this frequency are also clearly visible at 34, 51, 68 and 85 Hz, as well as beyond 100 Hz (not shown in Figure 6.10 (b)). The amplitudes of the harmonics $n \cdot 17$ Hz appear to decrease linearly with the harmonic number n . This presence of the harmonics of the injected ripple can be observed for all magnets of the Main Ring and indicates non-linear effects in the beam dynamics of the Main Ring.

The ripple transfer function for all Main Ring magnets (averaged over three spills each) for a 10 s proton beam (252.7 MeV) with EBC for $f_0 = 62$ Hz and $A_0 = 0.1\%$ is shown in Figure 6.11.

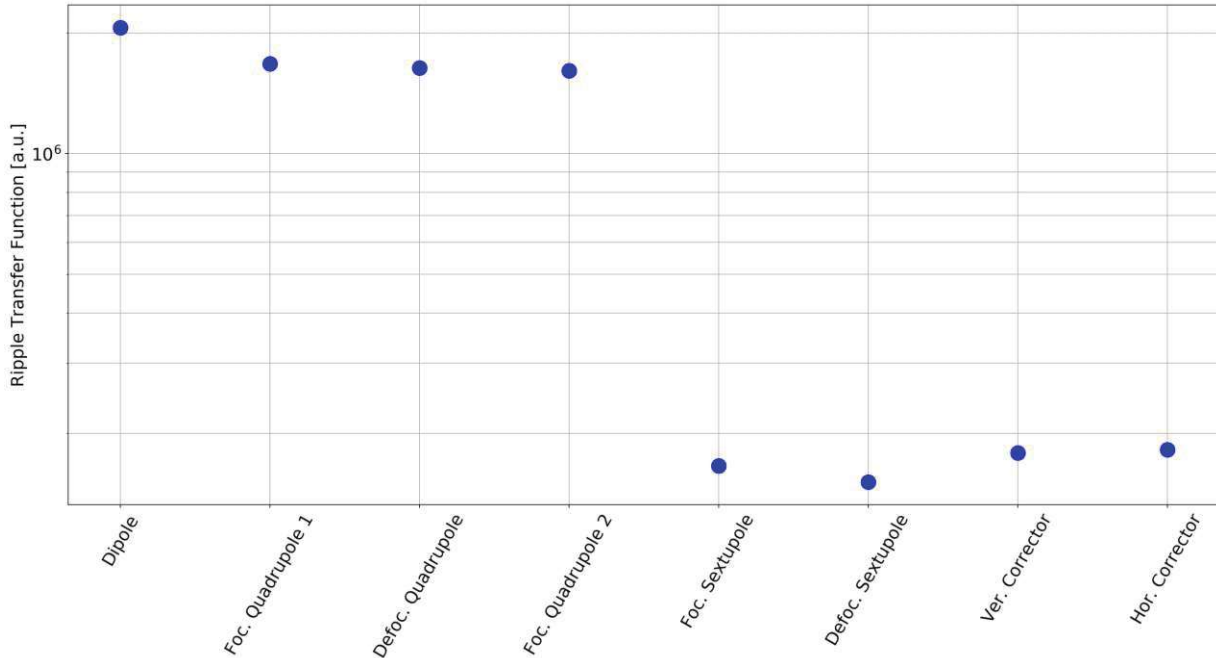


Figure 6.11.: Ripple transfer function for a 10 s proton beam (252.7 MeV) with EBC ($f_0 = 62$ Hz and $A_0 = 0.1\%$).

The measured *RTFs* indicate that the dipole ripples have got the strongest effect on the intensity ripples of the extracted beam, followed by the three quadrupole families. The two sextupole families and the horizontal and vertical corrector magnets have only a minor impact on the intensity beam ripples, with an *RTF* one order of magnitude smaller than for the dipole and quadrupole families.

This result can be attributed to the fact that intensity ripples in the extracted beam can only arise from tune or position fluctuations within the Main Ring. The dipoles affect the beam position and the quadrupoles determine the tune, resulting in a high *RTF* for these magnets. In contrast, the sextupoles in first approximation only impact the chromaticity, resulting in a low *RTF*. The corrector magnets also affect the beam position, which explains why the corresponding *RTF* is higher than that of the sextupoles. However, their impact is much smaller than that of the dipoles, resulting in a still negligible ripple transfer.

The frequency dependence of the ripple transfer function is shown in Figure 6.12. The *RTF* for different frequencies $f_0 = 62 \text{ Hz} + n \cdot 100 \text{ Hz}$ is plotted in relation to the *RTF* at 62 Hz. A value above one (red line) indicates that the *RTF* is higher for higher frequencies, while the ripple impact is decreased for values below one.

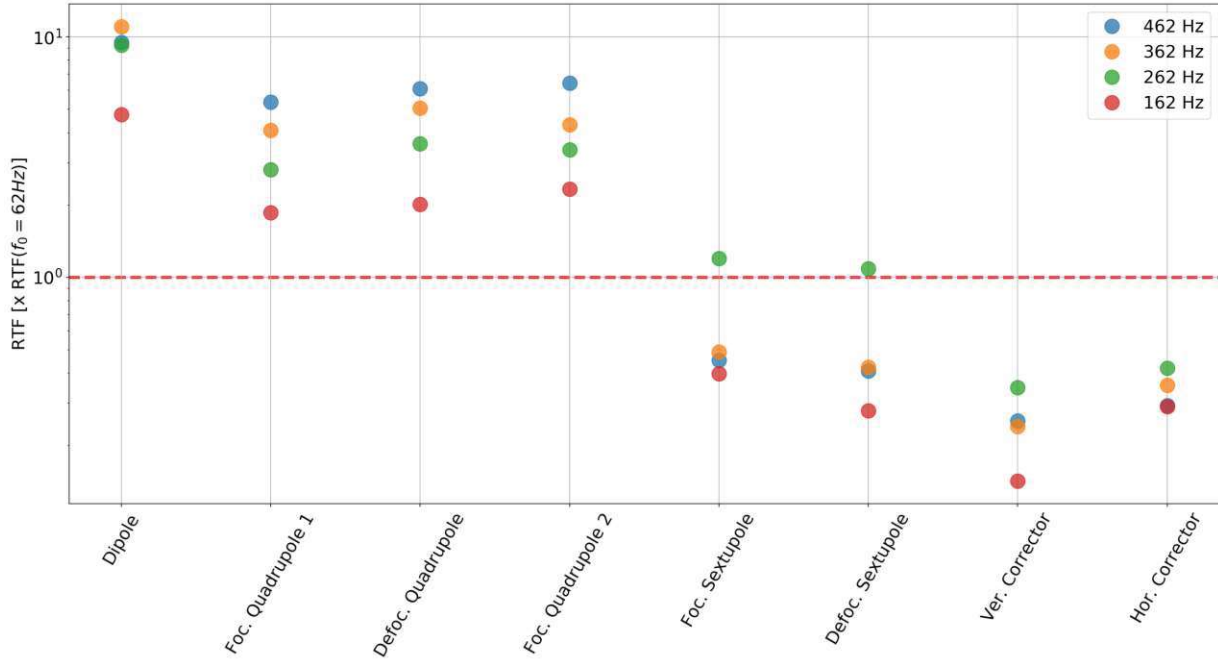


Figure 6.12.: Frequency-dependence of the ripple transfer function for a 10s proton beam (252.7 MeV) with EBC.

For the dipole and quadrupole families, ripples are transferred more at higher frequencies, resulting in an increasing *RTF* as the frequency increases. It is worth noting that for the dipoles, the *RTF* for the ripple with the highest frequency $f_0 = 462 \text{ Hz}$ does not follow the trend and is lower than the value for $f_0 = 362 \text{ Hz}$. One possible explanation is that the dipoles act as a low-pass filter and a frequency of 462 Hz is close to the cut-off frequency of the magnet. The cut-off frequency for the quadrupoles is much higher, so the effect is only visible for dipoles. To verify this explanation, it would be beneficial to measure the *RTF* for even higher ripple frequencies. However, the speed of the power converter limits the ripple frequencies that can be applied.

The *RTF* for the sextupole families and corrector magnets decreases for higher frequencies, with the differences between the measured frequencies being relatively small and within statistical fluctuations. The only exception for the sextupoles is the ripple with $f_0 = 262 \text{ Hz}$, which results in a slightly higher *RTF* than the reference ripple with 62 Hz.

This behaviour is reproducible over multiple spills and is not fully understood. Additional measurements and simulations of the RTF are required to gain a better understanding of the frequency dependence of the ripple transfer function.

To quantify the ripple reduction with EBC as long-distance setup, the ripple transfer function can be compared for a spill with and without EBC. The relative RTF reduction for the different magnet families⁴ is summarised in Table 6.3.

Magnet family	RTF reduction with EBC [%]
Dipole	65.6
Focussing quadrupole 1	45.3
Focussing quadrupole 2	49.9
Focussing sextupole	62.6
Defocussing sextupole	52.9
Vertical corrector	55.5
Horizontal corrector	52.6

Table 6.3.: Reduction of the RTF with EBC for different magnet families (10s proton beam, 252.7 MeV).

EBC significantly reduces the impact of the ripples by around 50% for all magnet families. The spill smoothing effect of EBC is thus also visible in the RTF measurement. The largest impact is observed for the dipoles with an RTF reduction of 65.6%. This is also confirmed by the fact that, as shown in section 6.3, EBC strongly reduces the amplitude of the 4 kHz ripple, which originates from the dipoles.

⁴For the defocussing quadrupole family, no measurement data for a spill without EBC is available, thus no relative RTF reduction can be calculated.

6.5. Ripples for alternative extraction methods

The intensity ripples for betatron core extraction can be compared with the ripples for the alternative extraction methods discussed in this thesis, to identify possible room for improvements. The duty factor (averaged over five spills) for different extraction techniques are summarised in Figure 6.13. The value for betatron core extraction without EBC is drawn as dashed red line for reference.

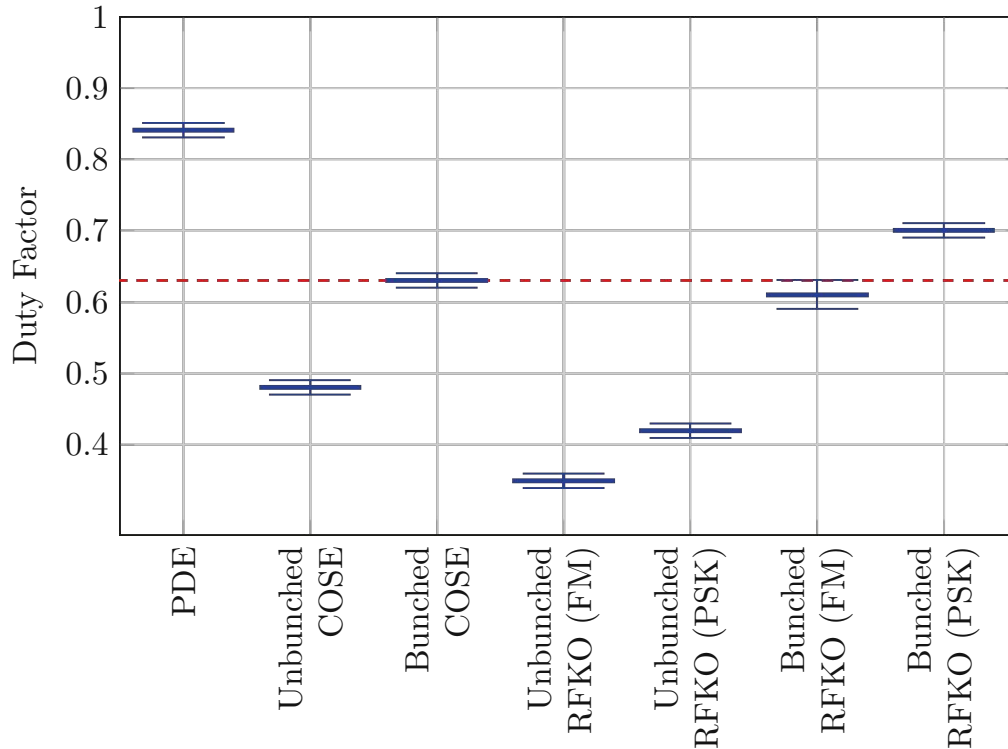


Figure 6.13.: Average duty factor for alternative extraction methods (proton, 252.7 MeV, 10 s). The red line denotes the duty factor for betatron core extraction without EBC.

Figure 6.13 demonstrates that the beam quality is best for PDE with a duty factor of 0.84. This excellent performance can be attributed to the fact that PDE can be viewed as the inverse of EBC, and the particles cross the resonance quickly when they pass through the bucket gap. Furthermore, a single sweep PDE does not introduce any additional ripples as there is no repetitive parameter change.

On the other hand, unbunched COSE extracts the beam with a very poor quality, indicated

by a low duty factor of 0.48. Further analysis shows that especially the amplitude of the 4 kHz ripple is more than 22 times higher than for betatron core extraction without EBC. This can be explained as the dipoles need to be ramped during COSE, which increases the impact of the dipole power converter.

Keeping the beam bunched during COSE improves the spill quality by 31%. This is expected as in bunched mode, the particles rotate in the bucket at the synchrotron frequency, which leads to an increased speed when crossing the resonance and therefore to an increased duty factor.

Unbunched COSE can be combined with EBC, as an empty bucket can be created in the same way as for betatron core extraction. Both long-distance and short-distance EBC was tested with COSE, resulting in the beam quality parameters summarised in Table 6.4. The beam quality was measured for five spills each and the mean value as well as the standard deviation was calculated.

Setting	r	RF	DF	4 kHz peak
COSE (No EBC)	46.9 ± 4.4	8.57 ± 0.20	0.48 ± 0.01	11180 ± 270
COSE (Long-distance EBC)	41.7 ± 2.0	8.39 ± 0.23	0.48 ± 0.01	10800 ± 500
COSE (Short-distance EBC)	18.1 ± 1.3	3.70 ± 0.05	0.76 ± 0.01	7140 ± 250

Table 6.4.: Beam quality for combining COSE with EBC (proton, 252.7 MeV, 10 s).

While the long-distance EBC does not show an improvement compared to COSE without EBC, the short-distance implementation of EBC significantly improves the spill quality. The duty factor increases by 58%, and the peak-to-mean ratio, as well as the ripple factor, are more than halved. The amplitude of the ripple at 4 kHz is reduced while still remaining relatively high.

The reason why (in contrary to betatron core extraction) only short-distance EBC improves the spill quality can be found in the details of the extraction process for COSE. The beam remains stationary while the resonance is moved away from the bucket. Therefore, the bucket needs to overlap with the resonance to allow proper channelling of the particles through the bucket gap, which is only the case for short-distance EBC. As the beam is not accelerated towards the bucket as it is the case for betatron core extraction, long-distance EBC does not have an effect on the beam ripples.

To optimise the effect of EBC with COSE, it is necessary to synchronise the movement of the empty bucket with the resonance sweeping, which ensures a constant relation between the bucket and resonance throughout the sweep. This implementation would lead to a hybrid extraction that combines both COSE and PDE. The optimisation of the bucket movement is not discussed here and will be the topic of future studies.

The beam quality for RFKO extraction depends strongly on the excitation method. For FM, the Fourier spectrum is dominated by the sweep frequency and its harmonics, as shown in Figure 6.14.

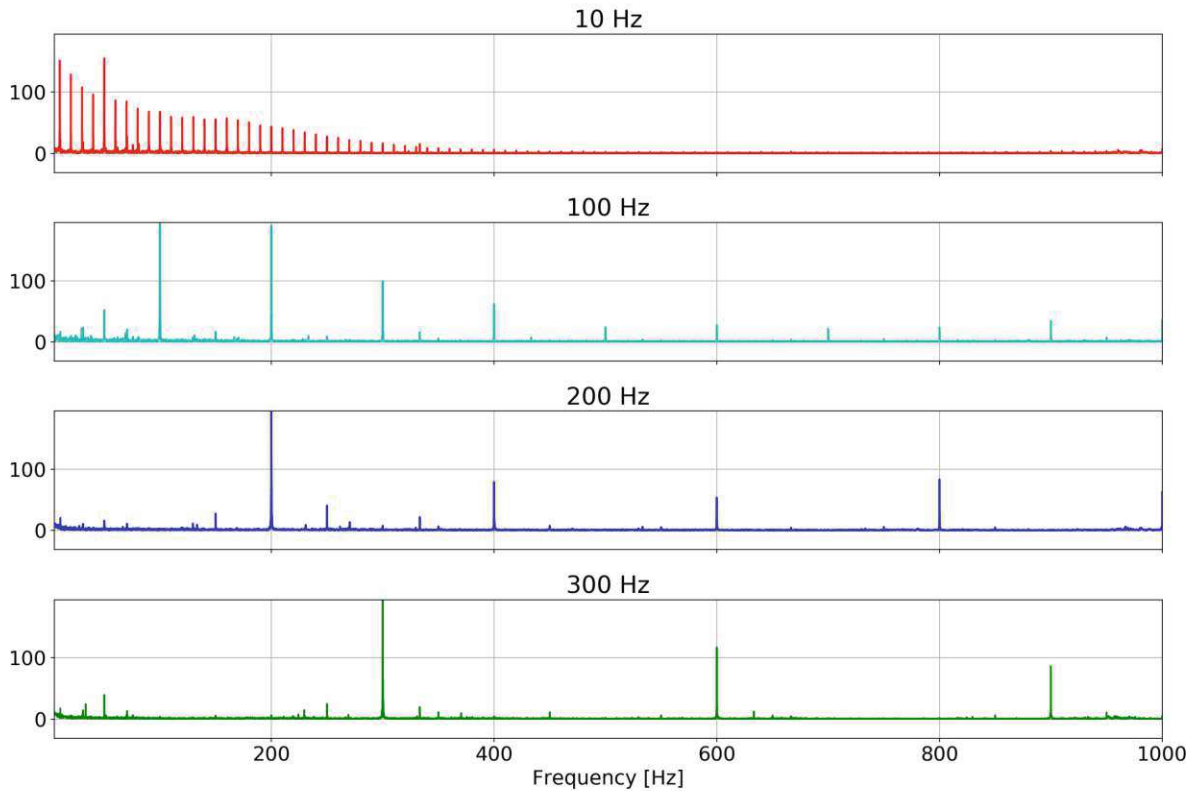


Figure 6.14.: Fourier spectrum of the extracted intensity for bunched FM with different sweep frequency values.

The higher the sweep frequency, the fewer peaks are in the clinically relevant frequency range and the smoother is the extracted beam. However, the sweep frequency cannot be set to extremely high values, as the extraction efficiency decreases for sweep frequencies above 500 Hz. This can be explained as the when the excitation frequency is changed too fast, there is not enough time for the particles to cross the resonance.

For Phase Shift Keying, ripples are introduced by the shift frequency. However, due to the randomness of the phase shift, the resulting ripples are not as prominent as for FM excitation. For unbunched beam, the duty factor for RFKO with PSK is increased by 20% compared to RFKO with FM, while the maximum peak to mean ratio is reduced by 29%. As for COSE, bunched beam operation reduces the effect of the ripples due to the smooth-

ing effect of the bucket rotation also for RFKO, leading to a 74% increase of the duty factor for FM and 67% for PSK.

Figure 6.15 illustrates the duty factor for the different excitation signals in a histogram. The duty factor distribution within one spill confirms the trend discussed above with PSK resulting in a better beam quality than FM and bunched beam operation increasing the duty factor even further.

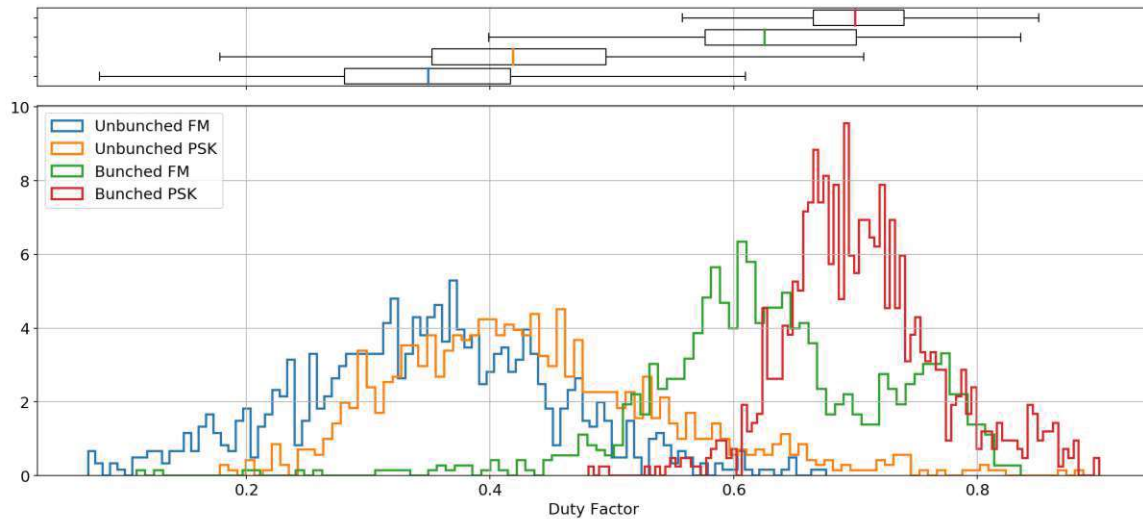


Figure 6.15.: Histogram of the duty factor for different RFKO excitation signals.

The quality of the extracted beam can be further optimised by using advanced excitation signals by combining two or more bands (dual FM, dual PSK, extended PSK, ...). Feedback and feedforward loops can be implemented to compensate for reproducible ripples. The author leaves the implementation of these advanced techniques to future studies.

7. Conclusion and outlook

As part of this thesis, alternative extraction methods were analysed, simulated and successfully tested at MedAustron. A proof of concept was delivered for RFKO, COSE and PDE, and an experimental setup was established to extract and deliver the beam to the treatment room.

RFKO benefits from the flexibility of choosing an excitation method, thanks to the tailored excitation signal generation by the SDR. While FM introduces ripples at the sweep frequency that can hardly be avoided, PSK is a promising technique for extracting the beam with a high duty factor. Four candidates were identified through multi-dimensional parameter optimisation, which exhibit promising behaviour during extraction as well as transmission to the room. $\text{KOE}\alpha+$ with an increased momentum offset ($Q_x = 1.6716$, $Q'_x = -1.5$, $(\Delta p/p)_{\text{off}} = -2.3 \times 10^{-3}$) appears to be the most favourable candidate in terms of efficiency, beam distribution at the ESE, and dispersion at the MST. The parameter may require adjustments during commissioning but provides a good starting point for further optimisation. RFKO is compatible with bunched beam operation and allows for multi energy extraction, which is beyond the scope of this thesis.

COSE is a stable and easy-to-implement alternative to betatron core extraction. Its compatibility with bunched beam operation can be used for an intuitive implementation of multi energy extraction by combining magnet and radial loop position ramps. The energy step is restricted by the energy acceptance of the HEBT, which was measured to be 2.1 MeV in case the HEBT setpoint is positioned in the middle of the energy range.

PDE extracts the beam by sweeping the frequency of the empty bucket, while both the beam and the lattice remain stationary. The sweep can be repeated multiple times for pulsed extraction. The repetition frequency determines both the extraction efficiency and the dose per pulse.

Ripple mitigation is a crucial topic for optimising treatment performance. The intensity ripple spectrum at MedAustron is dominated by ripples at 50 Hz and 4 kHz, originating from the power grid and the power converter of the dipoles, respectively. To reduce the impact of these ripples, the EBC technique can be used, which involves increasing the resonance crossing speed of the particles by a stationary empty bucket. The bucket can be implemented in either a short- or long-distance configuration. Both setups improve the beam quality significantly. Short-distance EBC reduces the overall peak to mean ratio,

while long-distance EBC remarkably suppresses the ripple at 4 kHz. EBC introduces additional ripples at the bucket frequency, which are not relevant for clinical treatment. The measurement of the ripple transfer function indicates that the dipoles and quadrupoles are the most crucial components for ripple reduction. The quality of the spill for RFKO depends on the excitation method, with PSK performing better than FM. Bunched beam operation further improves the beam quality. PDE results in a favourable beam quality that is comparable to betatron core extraction with EBC. COSE exhibits the worst beam quality, which can be improved by the implementation of short-distance EBC.

The development and implementation of advanced excitation methods are of interest to further optimise RFKO extraction. Especially identifying additional frequency bands in the beam transfer function to improve spill quality has shown great success at other facilities [44, 83]. The computation of the excitation signal can be further improved by automatically reading the revolution frequency and beam tune in the SDR. Amplitude modulation and control over the intensity profile of the beam can be achieved by triggering the extraction within the SDR. This thesis specifically addresses the extraction from the Main Ring. Subsequently, proper commissioning and parameter optimisation are also necessary for the transmission of the beam from the MST through the HEBT to the treatment room. A proper concept for MEE with RFKO was already developed in [84], which needs to be further tested and optimised with simulations and measurements.

For COSE, the focus of the development lies on implementing multi-energy extraction. The configuration discovered in this thesis can be further optimised to improve the quality of the extracted beam. Non-linear magnet ramps can be used to achieve a uniform intensity profile of the sub-spills. Scaling the setpoint of the HEBT magnets would be beneficial in increasing the energy acceptance and thus the achievable energy step. Finally, a time-resolved range measurement can be performed in the treatment room to confirm the different energies and quantify the actual energy distribution.

Optimising PDE, especially for pulsed extraction, involves similar approaches as for COSE, as the focus is on optimising the frequency ramp for a uniform extraction intensity. The voltage can be adjusted for each sweep to compensate for the different dose rates per pulse. Finally, the sweep time can be further reduced to investigate a possible application of PDE for FLASH irradiation.

Another potential area for future improvement is the development of a user-friendly simulation framework capable of accurately simulating all extraction methods and beam manipulation techniques discussed in this thesis. As demonstrated in section 3.1, XSuite is a highly flexible simulation toolkit that is well-suited for this task. One approach is for the user to simply select the extraction method and relevant parameters, allowing the simulation toolkit to automatically simulate the extraction process. This unified simulation setup would reduce the need for multiple simulation codes and simplify the simulation process.

The studies presented in this thesis combine three promising alternative extraction methods with extensive ripple analysis, laying the groundwork for improving the efficiency and treatment quality of medical facilities worldwide. The results are crucial for a deep understanding of the complex beam dynamics during extraction, which is a key aspect for addressing some of the most important challenges in slow extraction optimisation. The findings from this thesis pave the way for numerous future developments and serve as a foundation for exciting opportunities that I look forward to exploring.

A journey of a thousand miles begins with a single step.

Laozi

List of Figures

1.1.	Dose depth profile for a typical treatment with protons, photons and electrons.	1
1.2.	The MedAustron accelerator complex.	3
1.3.	The Main Ring of the MedAustron accelerator complex.	5
1.4.	Principle of the beam chopper.	8
1.5.	A typical SSQ time-current curve for a Main Ring quadrupole magnet.	11
2.1.	The Frenet-Serret coordinate system.	15
2.2.	Phase space ellipse defined by the Twiss functions.	21
2.3.	Phase oscillations without acceleration.	24
2.4.	Contour plot of the longitudinal Hamiltonian (stationary bucket).	25
2.5.	Contour plot of the longitudinal Hamiltonian (accelerating bucket).	26
2.6.	Typical phase jump process.	28
2.7.	Comparison of the momentum distribution with and without phase jump.	29
2.8.	Tune footprint with resonances up to fourth order.	31
2.9.	Contour plot of the Kobayashi Hamiltonian.	33
2.10.	Steinbach diagram near a resonance Q_{res} .	34
2.11.	Phase space at the ESE for three particles with different momentum offsets.	35
2.12.	Overview of the principal methods for slow extraction.	37
2.13.	Schematic view of betatron core extraction in the Steinbach diagram.	38
2.14.	Schematic view of tune sweep extraction in the Steinbach diagram.	39
2.15.	Schematic view of RFKO extraction in the Steinbach diagram.	41
2.16.	Configuration for ripple mitigation.	51
2.17.	Typical bucket configuration for EBC.	52
3.1.	Structure of a typical MAD-X script.	55
3.2.	Exemplary initial particle distribution for simulating RFKO.	58
3.3.	Physics modules of XSuite.	63
3.4.	Tune measurement with the vertical Schottky.	67
4.1.	View from the top and the front of the horizontal Schottky device and the simulated static electric field.	71
4.2.	Schematic RFKO setup at MedAustron.	71
4.3.	The impact of the machine parameters on the extraction setup.	73

4.4.	Tune-chromaticity scans with different momentum offsets for RFKO optimisation at the ESE.	76
4.5.	Extraction efficiency and spiral step for $KOE\alpha$ for different strengths of the resonance sextupole.	77
4.6.	Extraction efficiency for $KOE\alpha$ for different beam emittances.	78
4.7.	Tune-chromaticity scans with different momentum offsets for RFKO optimisation at the MST.	81
4.8.	Horizontal dispersion at the MST entry.	83
4.9.	Measured transmission from the ESE to the MST for different ESE kick strengths.	85
4.10.	Particle current in the Main Ring for unbunched RFKO without any excitation.	87
4.11.	Comparison of the CTS particle current in the Main Ring for bunched and unbunched RFKO.	88
4.12.	Schottky spectrum for bunched beams.	89
4.13.	Beam stability for bunched RFKO with reduced RF voltage.	90
4.14.	Beam stability for optimised settings for bunched RFKO.	91
4.15.	Maximum deflection angles for the clinical energy ranges for proton and carbon beams.	94
4.16.	Simulated spill lengths for different excitation amplitudes.	95
4.17.	Simulation of amplitude modulation for RFKO.	98
4.18.	RFKO extraction efficiency for different FM bandwidths.	101
4.19.	Exemplary FM signal.	102
4.20.	Exemplary BPSK signal.	104
4.21.	Measured circulating MR current for RFKO extraction.	105
4.22.	DDM beam intensity measurement for RFKO in IR1.	106
4.23.	Simulated energy distribution at the isocentre of a proton beam at 252.7 MeV.	108
5.1.	Beam configuration for unbunched COSE before the start of the extraction.	111
5.2.	Extracted intensity and effective spill length for different COSE magnet ramps.	112
5.3.	Unbunched COSE measurement with a magnet ramp of -0.4%	113
5.4.	Comparison of unbunched COSE with unbunched tune sweep extraction.	114
5.5.	Bunched COSE measurement with a radial position ramp from 20 to 10 mm.	116
5.6.	Extraction efficiency for different radial loop ramps for bunched COSE.	118
5.7.	Schematic configuration for MEE with bunched COSE.	119
5.8.	Extraction test for ten energy MEE with bunched COSE.	120
5.9.	Schematic configuration for MEE with the 'full jump back' approach.	121

5.10. Extraction test for ten energy MEE with bunched COSE with the 'full jump back' approach.	121
5.11. QIM intensity measurement for ten energy MEE with bunched COSE with the 'full jump back' approach.	122
5.12. Schematic configuration for MEE with the 'draw back' approach.	124
5.13. Extraction test for ten energy MEE with bunched COSE with the 'draw back' approach.	124
5.14. Intensity of the second sub-spill at the DDM for two energy MEE.	126
5.15. Energy acceptance magnification by scaling the setpoint of the HEBT magnets for ten energy MEE.	127
5.16. Comparison of the measured and set current for ultra-fast COSE.	128
5.17. Bucket configuration for PDE.	132
5.18. Phase Displacement Extraction measurement.	133
5.19. CTS measurement for PDE with different bucket voltages.	134
5.20. Pulsed Phase Displacement Extraction with four sweeps.	136
5.21. Pulsed PDE with faster sweeps.	137
6.1. Impact of quadrupole ripples on the extracted beam intensity.	139
6.2. Beam quality parameters for a 10 s proton beam with an energy of 252.7 MeV (Empty Bucket Channelling active).	142
6.3. Histogram of the beam quality parameters for a 10 s proton beam with an energy of 252.7 MeV (Empty Bucket Channelling active).	143
6.4. Low-frequency intrinsic beam ripples for a 10 s proton beam with an energy of 252.7 MeV (no EBC).	145
6.5. High-frequency intrinsic beam ripples for a 10 s proton beam with an energy of 252.7 MeV (no EBC).	145
6.6. Bucket configuration for the two EBC types implemented at MedAustron.	147
6.7. Simulated extraction efficiency over time for a spill with and without EBC.	148
6.8. Extracted intensity with and without EBC.	150
6.9. Comparison of the beam ripples with and without EBC.	151
6.10. Exemplary ripple transfer function measurement.	154
6.11. Ripple transfer function for a 10s proton beam (252.7 MeV) with EBC.	155
6.12. Frequency-dependence of the ripple transfer function.	156
6.13. Average duty factor for alternative extraction methods.	158
6.14. Fourier spectrum of the extracted intensity for bunched FM with different sweep frequency values.	160
6.15. Histogram of the duty factor for different RFKO excitation signals.	161
B.1. GnuRadio script for frequency modulation.	183

B.2. GnuRadio script for binary phase shift keying. 184

List of Tables

1.1.	Particle types and clinical energy ranges at MedAustron.	2
2.1.	Transfer matrices for special magnets.	18
2.2.	Comparison of the extraction techniques.	47
2.3.	Extraction method used by selected accelerator facilities.	49
3.1.	Parameters of the longitudinal distribution of the circulating proton beam.	59
3.2.	Capabilities of the simulation tools.	65
3.3.	Properties of detectors relevant for this thesis.	68
4.1.	Promising candidates for RFKO extraction.	79
4.2.	Horizontal distribution parameters for RFKO candidates at the ESE in comparison with betatron core extraction.	80
4.3.	Horizontal distribution parameters for RFKO candidates at the MST in comparison with betatron core extraction.	82
4.4.	Dispersion at the MST for RFKO candidates.	83
4.5.	Compensated ESE kick for RFKO candidates.	84
4.6.	Comparison of simulated and measured values for tune and chromaticity.	86
4.7.	Maximum deflection angles with the MedAustron kicker for different particle types and beam energies.	94
4.8.	Excitation strengths and kicker voltages required for a 10 s extraction.	96
4.9.	Measured number of particles and calculated transmission efficiency.	107
6.1.	Beam quality parameters for different beam settings (EBC active).	143
6.2.	Beam quality with and without EBC.	151
6.3.	Reduction of the RTF with EBC for different magnet families.	157
6.4.	Beam quality for combining COSE with EBC.	159
A.1.	A typical timing sequence for a 10 second proton beam.	181

Bibliography

- [1] J. Hughes and J. Parsons. Flash radiotherapy: Current knowledge and future insights using proton-beam therapy. *International Journal of Molecular Sciences*, 21(18), 2020.
- [2] H. Tsujii. Overview of Carbon-ion Radiotherapy. *Journal of physics. Conference series*, 777(1):12032, 2017.
- [3] D. Pignalosa and M. Durante. Overcoming resistance of cancer stem cells. *The Lancet - Oncology*, 13(5):e187–e188, 2012.
- [4] M. Durante, J. Debus, and J.S. Loeffler. Physics and biomedical challenges of cancer therapy with accelerated heavy ions. *Nature reviews physics*, 3(12):777–790, 2021.
- [5] M. Kausel. Helium Beam Commissioning at the Injector of the MedAustron Ion Cancer Treatment Facility: Source branch, LEBT and LINAC, 2023. Master Thesis at the Vienna University of Technology.
- [6] N. Gambino, M. Kausel, G. Guidoboni, L. Penescu, V. Rizzoglio, C. Schmitzer, and C. Kurfürst. First injector commissioning results with helium beam at MedAustron Ion Therapy Center. *Journal of Physics: Conference Series*, 2244(1):012109, 2022.
- [7] Accelerator Complex Study Group. *Proton-Ion Medical Machine Study (PIMMS) Part I*. CERN, 1999.
- [8] Accelerator Complex Study Group. *Proton-Ion Medical Machine Study (PIMMS) Part II*. CERN, 2000.
- [9] G. Feldbauer. Extraction methods for the MedAustron Synchrotron, 2011. Diploma Thesis at the Vienna University of Technology.
- [10] E. Sargsyan. *MedAustron Injector - Design Report*. MedAustron, 2010. Functional specifications, Version 1.0.
- [11] P.J. Bryant and U. Dorda. *MedAustron MEBT design report*. MedAustron, 2010. Engineering Note, Version 1.1.

- [12] P.J. Bryant and U. Dorda. *MedAustron Synchrotron design report*. MedAustron, 2010. Engineering Note, Version 1.1.
- [13] P.J. Bryant and U. Dorda. *MedAustron HEBT design report*. MedAustron, 2010. Engineering Note, Version 1.4.
- [14] C. Weiss, E. Griesmayer, and U. Penitz. Chopper-off latency measurement at MedAustron, 2022. CIVIDEC Instrumentation CW/174, v2.0.
- [15] M. Barnes, T. Fowler, and T. Stadlbauer. *Technical Requirement Specification MedAustron Beam Chopper Power Converter*. MedAustron, 2013. Engineering Specification, Version 1.0, ES-100701-b-MBA.
- [16] M.T.F. Pivi, L. Adler, G. Guidoboni, C. Kurfürst, C. Maderböck, D.A. Prokopovich, V. Rizzoglio, I. Strasik, M.G. Pullia, and M. Pavlovič. Gantry Beamline and Rotator Commissioning at the MedAustron Ion Therapy Center. In *Proceedings of the 13th International Particle Accelerator Conference (IPAC 2022), Bangkok, Thailand*, pages 2933–2936, 2022.
- [17] T. Haberer, W. Becher, D. Schardt, and G. Kraft. Magnetic scanning system for heavy ion therapy. *Nuclear Instruments and Methods in Physics Research Section A: Accelerators, Spectrometers, Detectors and Associated Equipment*, 330(1):296–305, 1993.
- [18] Y. Iwata, T. Kadowaki, H. Uchiyama, T. Fujimoto, E. Takada, T. Shirai, T. Furukawa, K. Mizushima, E. Takeshita, K. Katagiri, S. Sato, Y. Sano, and K. Noda. Multiple-energy operation with extended flattops at HIMAC. *Nuclear Instruments and Methods in Physics Research Section A: Accelerators, Spectrometers, Detectors and Associated Equipment*, 624(1):33–38, 2010.
- [19] S. Sato, T. Furukawa, and K. Noda. Dynamic intensity control system with RF-knockout slow-extraction in the HIMAC synchrotron. *Nuclear Instruments and Methods in Physics Research Section A: Accelerators, Spectrometers, Detectors and Associated Equipment*, 574(2):226–231, 2007.
- [20] M. Lis, W. Newhauser, M. Donetti, M. Durante, U. Weber, B. Zipfel, C. Hartmann-Sauter, M. Wolf, and C. Graeff. A facility for the research, development, and translation of advanced technologies for ion-beam therapies. *Journal of Instrumentation*, 16(03):T03004, 2021.
- [21] A. De Franco, C. Schmitzer, N. Gambino, T. Glatzl, S. Myalski, and M.T.F. Pivi. Optimization of synchrotron based ion beam therapy facilities for treatment time

- reduction, options and the MedAustron development roadmap. *Physica Medica: European Journal of Medical Physics*, 2020.
- [22] H. Wiedemann. *Particle Accelerator Physics*. Springer, 2015. Fourth Edition.
- [23] M. Conte and W.W. MacKay. *An Introduction to the Physics of Particle Accelerators*. World Scientific, 2008.
- [24] S.Y. Lee. *Accelerator Physics*. World Scientific, 2004. Second Edition.
- [25] K. Soutome and H. Tanaka. Higher-order formulas of amplitude-dependent tune shift caused by a sextupole magnetic field distribution. *Phys. Rev. Accel. Beams*, 20:064001, 2017.
- [26] F. Tecker. Longitudinal Dynamics. In *Proceedings of the CERN Accelerator School 2014 in Prague*, 2014.
- [27] R. Gouiran, K.H. Reich, I. Gumowski, and C. Bovet. A selection of formulae and data useful for the design of A.G. synchrotrons, 1970. CERN/MPS-SI/Int. DL/70/4.
- [28] Friedhelm Caspers. Schottky signals for longitudinal and transverse bunched-beam diagnostics, 2009.
- [29] E. Wanvik. Real-Time Schottky Measurements in the LHC, 2018. Bachelor Thesis at the Norwegian University of Science and Technology.
- [30] M. Betz, O.R. Jones, T. Lefevre, and M. Wendt. Bunched-beam Schottky monitoring in the LHC. *Nuclear Instruments and Methods in Physics Research Section A: Accelerators, Spectrometers, Detectors and Associated Equipment*, 874:113–126, 2017.
- [31] M.Q. Barton. Beam Extraction from Synchrotrons. *Proceedings of the 8th International Conference on High-Energy Accelerators (HEACC 1971), Geneva, Switzerland*, pages 85–88, 1971.
- [32] M.G. Pullia. Transverse aspects of the slowly extracted beam, 2000. CERN/PS 2000-06 (DR).
- [33] W. Hardt. Ultraslow extraction out of LEAR (transverse aspects), 1981. CERN Internal Note PS/DL/LEAR Note 81-6.
- [34] S. van der Meer. Stochastic extraction, a low-ripple version of resonant extraction, 1978. CERN-PS-AA-78-6.

- [35] D. Boussard, M. Gyr, K.H. Kissler, and T. Linnecar. Slow extraction at 400 GeV/c with stochastic RF noise, 1980. CERN-SPS-AOP-MG-jf, CERN-SPS-Improvement-Report-179.
- [36] F. Kühnleubl. Design study of radio frequency knockout slow extraction for the MedAustron synchrotron, 2020. Master Thesis at the Vienna University of Technology.
- [37] K. Brown, J. Cullen, J.W. Glenn, Y.Y. Lee, A. Mcnerney, J. Niederer, T. Roser, A. Soukas, J.E. Tuozzolo, and N. Tsoupas. Design of a resonant extraction system for the AGS booster. In *Proceedings of the 1999 Particle Accelerator Conference, New York*, volume 2, pages 1270 – 1272, 1999.
- [38] C.S. Park, J. Amundson, and L. Michelotti. Tracking Simulation of Third-Integer Resonant Extraction for Fermilab’s Mu2e Experiment, 2015. FERMILAB-PUB-15-042-CD.
- [39] R. Singh and P. Forck. Reducing Fluctuations in Slow-Extraction Beam Spill Using Transit-Time-Dependent Tune Modulation. *Physical Review Applied*, 13, 2020.
- [40] M. Tomizawa, Y. Arakaki, T. Kimura, S. Murasugi, R. Muto, H. Nakagawa, K. Okamura, Y. Shirakabe, H. Sato, T. Toyama, E. Yanaoka, M. Yoshii, A. Schnase, S. Shirakata, and K. Mochiki. Performance of Resonant Slow Extraction from J-PARC Main Ring. In *Proceedings of the 3rd International Particle Accelerator Conference (IPAC 2012), New Orleans, Louisiana, USA*, 2012.
- [41] P.A. Arrutia Sota. Optimisation of Slow Extraction and Beam Delivery from Synchrotrons, 2020. Master Thesis at the University of London.
- [42] P.A. Arrutia Sota, P. Burrows, A. De Franco, M.A. Fraser, B. Goddard, V. Kain, F. Kühnleubl, M.T.F. Pivi, D.A. Prokopovich, and F.M. Velotti. Implementation of a Tune Sweep Slow Extraction with Constant Optics at MedAustron. In *Proceedings of the 13th International Particle Accelerator Conference (IPAC 2022), Bangkok, Thailand*, pages 1715–1717, 2022.
- [43] V. Kain, F.M. Velotti, M.A. Fraser, B. Goddard, J. Prieto, L.S. Stoel, and M. Pari. Resonant slow extraction with constant optics for improved separatrix control at the extraction septum. *Phys. Rev. Accel. Beams*, 22(10):101001, 2019.
- [44] K. Noda, T. Furukawa, S. Shibuya, T. Uesugi, M. Muramatsu, M. Kanazawa, E. Takada, and S. Yamada. Advanced RF-KO slow-extraction method for the reduction of spill ripple. *Nuclear Instruments and Methods in Physics Research*, 492:253–263, 2002.

- [45] P. Niedermayer and R. Singh. Excitation signal optimization for minimizing fluctuations in knock out slow extraction, 2024. PREPRINT (Version 1).
- [46] T. Furukawa, K. Noda, M. Muramatsu, T. Uesugi, S. Shibuya, H. Kawai, E. Takada, and S. Yamada. Global spill control in RF-knockout slow-extraction. *Nuclear Instruments and Methods in Physics Research Section A: Accelerators, Spectrometers, Detectors and Associated Equipment*, 522:196–204, 2004.
- [47] F. Ebina, M. Umezawa, and K. Hiramoto. Improvement of extraction efficiency from a slow extraction synchrotron by applying the constant spiral step condition. *Nuclear Instruments and Methods in Physics Research Section A: Accelerators, Spectrometers, Detectors and Associated Equipment*, 685:1–6, 2012.
- [48] E. Ciapala. Stacking and Phase Displacement Acceleration. In *Proceedings of the CERN Accelerator School 1984 in Paris*, pages 195–225, 1985.
- [49] P.A. Arrutia Sota, P. Burrows, M.A. Fraser, and F.M. Velotti. Millisecond burst extractions from synchrotrons using RF phase displacement acceleration. *Nuclear Instruments and Methods in Physics Research Section A: Accelerators, Spectrometers, Detectors and Associated Equipment*, 1039:167007, 2022.
- [50] E. Renner, K. Knoll, F. Kühteubl, F. Plassard, D.A. Prokopovich, C. Schmitzer, A. Gsponer, and S. Waid. Investigating pulsed slow extraction schemes at the MedAustron synchrotron. In *Proceedings of the 15th International Particle Accelerator Conference (IPAC 2024), Nashville, USA*, pages 3595–3598, 2024.
- [51] F. Kühteubl, E. Renner, L. Adler, L. Fischl, X. German, G. Guidoboni, K. Holzfeind, C. Kurfürst, C. Maderböck, M.T.F. Pivi, F. Plassard, D.A. Prokopovich, V. Rizzoglio, I. Strasik, C. Schmitzer, A. Wastl, P.A. Arrutia Sota, and M.A. Fraser. Investigating alternative extraction methods at MedAustron. In *Proceedings of the 14th International Particle Accelerator Conference (IPAC 2023), Venice, Italy*, pages 2419–2422, 2023.
- [52] F. Kühteubl. Evaluation of the Slow Extraction Survey, 2022. Presentation at the ICFA Mini-Workshop on Slow Extraction 2022, January 25, 2022.
- [53] F. Kühteubl. Evaluation of the Slow Extraction Survey, 2022. Presentation at the iFAST-REX collaboration meeting, February 17, 2022.
- [54] M.G. Pullia, E. Bressi, L. Falbo, C. Priano, S. Rossi, C. Viviani, A. Garonna, M. Kronberger, T. Kulenkampff, C. Kurfürst, F. Osmic, L. Penescu, M.T.F. Pivi, C. Schmitzer, P. Urschütz, and A. Wastl. Betatron core driven slow extraction at

- CNAO and MedAustron. In *Proceedings of the 7th International Particle Accelerator Conference (IPAC 2016)*, Busan, Korea, 2016.
- [55] A. De Franco, L. Adler, F. Farinon, N. Gambino, G. Guidoboni, G. Kowarik, M. Kronberger, C. Kurfürst, S. Myalski, S. Nowak, M.T.F. Pivi, C. Schmitzer, I. Strasik, P. Urschütz, A. Wastl, and L. Penescu. Slow Extraction Optimization at the MedAustron Ion Therapy Center: Implementation of Front End Acceleration and RF Knock Out. In *Proceedings of the 9th International Particle Accelerator Conference (IPAC 2018)*, Vancouver, BC, Canada, 2018.
- [56] S. Savazzi, E. Bressi, G. Debernardi, L. Falbo, V. Lante, C. Priano, M.G. Pullia, P. Meliga, and G. Russo. Implementation of RF-KO extraction at CNAO. In *Proceedings of the 10th International Particle Accelerator Conference (IPAC 2019)*, Melbourne, Australia, 2019.
- [57] P. Meliga, E. Bressi, G. Debernardi, L. Falbo, and C. Priano. Design and Commissioning of the RF-KO Extraction at CNAO. In *Proceedings of the 14th International Particle Accelerator Conference (IPAC 2023)*, Venice, Italy, 2023.
- [58] S. Ivanov and O. Lebedev. A Stochastic Slow Extraction Scheme for U70 Synchrotron. In *Proceedings of RuPAC XIX*, Dubna, Russia, 2004.
- [59] K. Brown, L. Ahrens, J. Brennan, J. Glenn, T. Roser, T. Russo, N. Tsoupas, K. Smith, and K. Zeno. Status of Slow Extraction of High Intensity Protons from Brookhaven’s AGS. In *Proceedings of the 2003 Particle Accelerator Conference*, Portland, Oregon, USA, 2003.
- [60] M.G. Pullia. Status Report of the CNAO Construction and Commissioning. In *Proceedings of the 2nd International Particle Accelerator Conference (IPAC 2011)*, San Sebastián, Spain, 2011.
- [61] P.A. Arrutia Sota, P. Burrows, H. Damerau, M.A. Fraser, M. Vadai, and F.M. Velotti. Implementation of RF Channeling at PS for Spill Quality Improvements. In *Proceedings of the 13th International Particle Accelerator Conference (IPAC 2022)*, Bangkok, Thailand, pages 2114–2117, 2022.
- [62] P.A. Arrutia Sota. RF techniques for spill ripple improvement, 2024. Presentation at the 5th Slow Extraction Workshop at MedAustron in Wiener Neustadt.
- [63] P.A. Arrutia Sota, M.A. Fraser, G. Hagmann, V. Kain, G. Papotti, A. Spierer, F.M. Velotti, P.N. Burrows, and R. Piandani. Empty-bucket techniques for spill-quality

- improvement at the CERN Super Proton Synchrotron. *Phys. Rev. Accel. Beams*, 27:074001, 2024.
- [64] R. Cappi and C. Steinbach. Low Frequency Duty Factor Improvement for the CERN PS Slow Extraction using RF Phase Displacement Techniques, 1981. CERN/PS/OP 81-10.
- [65] L. Deniau, H. Grote, G. Roy, and F. Schmidt. *The MAD-X Program*. European Laboratory For Particle Physics, Geneva, Switzerland, 2022. User’s Reference Manual, Version 5.08.01, <http://mad.web.cern.ch/mad/>.
- [66] L. Adler, A. De Franco, F. Farinon, N. Gambino, G. Guidoboni, C. Kurfürst, S. Myalski, M.T.F. Pivi, C. Schmitzer, I. Strasik, and A. Wastl. Synchrotron emittance analysis procedure at MedAustron. In *Proceedings of the 7th Int. Beam Instrumentation Conf. (IBIC 2018), Shanghai, China*, 2018.
- [67] CERN. BLonD: Beam Longitudinal Dynamics simulator. <https://blond.web.cern.ch/>.
- [68] H. Timko, J.E. Müller, A. Lasheen, and D. Quartullo. Benchmarking the Beam Longitudinal Dynamics code BLonD. In *Proceedings of the 7th International Particle Accelerator Conference (IPAC 2016), Busan, Korea*, 2016.
- [69] CERN. XSuite: An Integrated Beam Physics Simulation Framework. <https://xsuite.readthedocs.io/en/latest/>.
- [70] G. Iadarola, R. De Maria, S. Łopaciuk, A. Abramov, X. Buffat, D. Demetriadou, L. Deniau, P. Hermes, P. Kicsiny, P. Kruyt, A. Latina, L. Mether, K. Paraschou, G. Sterbini, F. F. Van Der Veken, P. Belanger, P. Niedermayer, D. Di Croce, T. Pieloni, L. Van Riesen-Haupt, and M. Seidel. Xsuite: An Integrated Beam Physics Simulation Framework. In *Proceedings of the 68th ICFA Advanced Beam Dynamics Workshop on High-Intensity and High-Brightness Hadron Beams (HB 2023), Geneva, Switzerland*, pages 73–80, 2023.
- [71] C. Krantz, R. Cee, F. Faber, E. Feldmeier, T. Fischer, M. Galonska, A. Peters, B. Kröck, U. Scheeler, S. Scheloske, C. Schömers, A. Weber, M. Witt, and T. Haberer. Slow Extraction Techniques at the Marburg Ion-Beam Therapy Centre. In *Proceedings of the 9th International Particle Accelerator Conference (IPAC 2018), Vancouver, Canada*, 2018.
- [72] K. Noda, M. Kanazawa, A. Itano, E. Takada, M. Torikoshi, N. Araki, J. Yoshizawa, K. Sato, S. Yamada, H. Ogawa, H. Itoh, A. Noda, M. Tomizawa, and M. Yoshizawa.

- Slow beam extraction by a transverse RF field with AM and FM. *Nuclear Instruments and Methods in Physics Research Section A: Accelerators, Spectrometers, Detectors and Associated Equipment*, 374(2):269–277, 1996.
- [73] T. Yamaguchi, Y. Okugawa, T. Shiokawa, T. Kurita, and T. Nakanishi. Slow beam extraction from a synchrotron using a radio frequency knockout system with a broadband colored noise signal. *Nuclear Instruments and Methods in Physics Research Section B: Beam Interactions with Materials and Atoms*, 462:177–181, 2020.
- [74] G. Russo. Radio Frequency KnockOut (RFKO) extraction: hardware analysis and beam optics simulation and optimization, 2019. Master Thesis at the Politecnico di Torino.
- [75] H.J. Yao, G.R. Li, Q. Zhang, S.X. Zheng, X.L. Guan, and X.W. Wang. RF-knockout slow extraction design for XiPaf synchrotron. In *Proceedings of the 57th ICFA Advanced Beam Dynamics Workshop on High-Intensity, High Brightness and High Power Hadron Beams (HB 2016)*, Malmö, Sweden, 2016.
- [76] S. Ruan, J. Yang, J. Zhang, G. Shen, H. Ren, J. Liu, J. Shangguan, X. Zhang, J. Zhang, L. Mao, L. Sheng, D. Yin, G. Wang, B. Wu, L. Yao, M. Tang, F. Cai, and X. Chen. Design of extraction system in BRing at HIAF. *Nuclear Instruments and Methods in Physics Research Section A: Accelerators, Spectrometers, Detectors and Associated Equipment*, 892:53–58, 2018.
- [77] E. Feldmeier and E.C. Cortés García. private communication, June 2022.
- [78] R. Öfferlbauer. RFKO extraction implementation at the MedAustron medical accelerator, 2022. Unpublished Project Thesis at the Vienna University of Technology.
- [79] F. Plassard. Beam loss optimisation for slow extraction at MedAustron, 2024. Presentation at the 5th Slow Extraction Workshop at MedAustron in Wiener Neustadt.
- [80] P. Niedermayer, R. Geißler, and R. Singh. Software-Defined Radio Based Feedback System for Beam Spill Control in Particle Accelerators. *Proceedings of the GNU Radio Conference*, 8(1), 2023.
- [81] C. Schoemers, E. Feldmeier, J. Naumann, R. Panse, A. Peters, and T. Haberer. The intensity feedback system at Heidelberg Ion-Beam Therapy Centre. *Nuclear Instruments and Methods in Physics Research Section A: Accelerators, Spectrometers, Detectors and Associated Equipment*, 795:92–99, 2015.

- [82] R. Singh, P. Forck, P. Boutachkov, S. Sorge, and H. Welker. Slow Extraction Spill Characterization from Micro to Milli-Second Scale. In *Proceedings of the 9th International Particle Accelerator Conference (IPAC 2018)*, Vancouver, BC, Canada, 2018.
- [83] E.C. Cortés García, E. Feldmeier, M. Galonska, C. Schömers, M. Hun, S. Brons, R. Cee, S. Scheloske, A. Peters, and T. Haberer. Optimization of the spill quality for the hadron therapy at the Heidelberg Ion-Beam Therapy Centre. *Nuclear Instruments and Methods in Physics Research Section A: Accelerators, Spectrometers, Detectors and Associated Equipment*, 1040:167137, 2022.
- [84] F. Plassard. Simulation of multi-energy extraction with RFKO, 2024. Presentation at the 5th Slow Extraction Workshop at MedAustron in Wiener Neustadt.
- [85] F. Kühsteubl. Dynamic simulation of Main Ring ramping and extraction of the MedAustron synchrotron with MAD-X, 2017. Bachelor Thesis at the Vienna University of Technology.
- [86] F.M. Velotti, L.S. Esposito, M.A. Fraser, V. Kain, S. Gilardoni, B. Goddard, M. Pari, J. Prieto, R. Rossi, W. Scandale, L.S. Stoel, F. Galluccio, M. Garattini, and Y. Gavrikov. Septum shadowing by means of a bent crystal to reduce slow extraction beam loss. *Phys. Rev. Accel. Beams*, 22:093502, 2019.
- [87] K. Mizushima, T. Shirai, T. Furukawa, S. Sato, Y. Iwata, K. Noda, and H. Uchiyama. Reduction of uncontrollable spilled beam in RF-knockout slow extraction. *Nuclear Instruments and Methods in Physics Research Section A: Accelerators, Spectrometers, Detectors and Associated Equipment*, 606:325–329, 2009.
- [88] M.T.F. Pivi, L. Adler, A. De Franco, F. Farinon, N. Gambino, G. Guidoboni, G. Kowarik, M. Kronberger, C. Kurfürst, H.T. Lau, S. Myalski, S. Nowak, C. Schmitzer, I. Strasik, P. Urschütz, A. Wastl, and L. Penescu. Status of the Carbon Commissioning and Roadmap Projects of the MedAustron Ion Therapy Center Accelerator. In *Proceedings of the 10th International Particle Accelerator Conference (IPAC 2019)*, Melbourne, Australia, 2019.
- [89] S. Sato, T. Furukawa, and K. Noda. Development of intensity control system with RF-knockout at the HIMAC synchrotron. In *Proceedings of EPAC 2006, Edinburgh, Scotland*, 2006.
- [90] J. Li and Y. Yuan. RF Excitation Parameters in Resonant Extraction. In *Proceedings of the 13th Symposium on Accelerator Physics (SAP 2017)*, Jishou, China, 2018.

- [91] N. Carmignani, C. Biscari, M. Serio, G. Balbinot, E. Bressi, M. Caldara, M.G. Pullia, J. Bossler, and G. Venchi. RF-knockout Extraction System for the CNAO Synchrotron. In *Proceedings of the 8th International Particle Accelerator Conference (IPAC 2017), Copenhagen, Denmark,, 2010*.
- [92] C. Schömers, E. Feldmeier, M. Galonska, T. Haberer, J. Horn, and A. Peters. First Tests of a Re-accelerated Beam at Heidelberg Ion-Beam Therapy Centre (HIT). In *Proceedings of the 1st International Particle Accelerator Conference (IPAC 2010), Kyoto, Japan, 2010*.
- [93] G. Feldbauer, M. Benedikt, and U. Dorda. Simulations of Various Driving Mechanisms for the 3rd Order Resonant Extraction from the MedAustron Medical Synchrotron. In *Proceedings of the 2nd International Particle Accelerator Conference (IPAC 2011), San Sebastián, Spain, 2011*.
- [94] P.J. Bryant and K. Johnsen. *The Principles of Circular Accelerators and Storage Rings*. Cambridge University Press, 2005.
- [95] K. Noda, T. Furukawa, S. Shibuya, M. Muramatsu, T. Uesugi, M. Kanazawa, M. Torikoshi, E. Takada, and S. Yamada. Source of spill ripple in the RF-KO slow-extraction method with FM and AM. *Nuclear Instruments and Methods in Physics Research Section A: Accelerators, Spectrometers, Detectors and Associated Equipment*, 492:241–252, 2002.
- [96] P.A. Arrutia Sota and M. Pari. Slow extraction simulations at CERN. Advancements, benchmarking and next steps, 2022. Presentation at the iFAST-REX Collaboration Meeting.

Acknowledgements

This thesis wouldn't have been possible without the incredible support of many people, and I want to express my deepest thanks to each and every one.

First, I want to express my gratitude to my supervisor at TU Wien, Michael Benedikt, for supporting my academic career and giving me the freedom to explore different areas of slow extraction. I want to especially thank my supervisor at MedAustron, Dale Prokopovich. His exceptional mentorship and constructive feedback have guided me through the last years. I am incredibly grateful for the countless hours you spent discussing physics me and for always being a source of encouragement.

A big thank you goes to my colleagues at MedAustron, particularly the Accelerator and Beam Physics group led by Greta Guidoboni. It was an amazing experience being (again) part of this incredible team and benefiting from your experience in the field. A special shout-out to the RFKO core team - Alexander Wastl, Dale Prokopovich, Elisabeth Renner, Fabien Plassard, and Xavier German - for your valuable contributions to my studies, your helpful feedback on my thesis, and the amazing teamwork during countless shift hours.

I'm also thankful to the IFAST-REX collaboration, led by Peter Forck, for giving me the opportunity to conduct a parameter survey among the participating facilities, and to the whole slow extraction community for the many inspiring presentations and discussions at conferences and workshops. Thank you to my colleagues at CERN - Matthew Fraser, Pablo Arrutia Sota, and Taylor - for the fruitful collaboration and the active exchange of knowledge. I also want to acknowledge the support from HIT, particularly Christopher Cortés and Eike Feldmeier, for assisting us with your expertise in the RFKO GnuRadio code, as well as CIVIDEC[®] for allowing us to use their detector for ripple analysis.

Finally, I want to thank my family and my girlfriend. Your endless love, encouragement, and belief in me have been my foundation throughout this journey. I couldn't have done this without you.

A. Example of a typical timing sequence

Table A.1 shows a typical timing sequence for a 10 second proton beam with 252.7 MeV and active empty bucket channelling.

Timing event	Time after <i>StartCycle</i> [μ s]
<i>StartCycle</i>	0
<i>StartMultiturn</i>	100,275
<i>StopMultiturn</i>	100,305
<i>StartAcceleration</i>	148,228
<i>PrepareExtraction</i>	834,728
<i>RFJump</i>	957,728
<i>StartMXR</i>	958,728
<i>StartExtraction</i>	959,728
<i>StopMXR</i>	983,728
<i>StartChopper</i>	1,209,728
<i>StopChopper</i>	11,209,728
<i>StopExtraction</i>	11,211,728
<i>StopRFSynchrotron</i>	11,211,927
<i>StartHysteresis</i>	11,211,928
<i>EndCycle</i>	12,211,928

Table A.1.: A typical timing sequence for a 10 second proton beam with 252.7 MeV (empty bucket channelling active). Only timing events relevant for this thesis are listed.

The timing is independent of the particle energy until *StartAcceleration*. However, after this timing event, the relative times change for different energies due to the energy dependence of the length of the acceleration process.

To save time improve efficiency, the betatron core is activated at *StartExtraction* even before the resonance sextupole finishes ramping up at *StopMXR*. This is possible as the head of the beam is cut by the still-closed chopper, preventing any particles from being transmitted to the treatment room before *StartChopper*. The effective extraction length is defined by the timing of the *StartChopper* and *StopChopper* event.

For a spill with active empty bucket channelling, the sRF system is turned off at *StopRFSynchrotron* after the end of the extraction. In case of deactivated empty bucket channelling, the timing event is moved after *RFJump* to allow for the debunching of the beam.

B. Flowchart of the GnuRadio script used for RFKO

This chapter displays flowcharts of the GnuRadio scripts used for signal generation for RFKO. The scripts were thankfully provided by C. Cortés and E. Feldmeier from the Heidelberger Ionenstrahl-Therapiezentrum [77]. They were further adapted and customised for application at MedAustron.

A flowchart is provided for two excitation signals used for this thesis:

- Frequency modulation (Figure B.1)
- Binary phase shift keying (Figure B.2)

For FM, a sawtooth modulation is used. A sawtooth wave $\text{saw}(f, t)$ with frequency f can be defined by its Fourier series representation B.1.

$$\text{saw}(f, t) = \frac{1}{2} - \frac{1}{\pi} \sum_{n=1}^{\infty} \frac{\sin(2\pi n f t)}{n} \quad (\text{B.1})$$

Binary phase shift keying utilises a random number generator $\text{random}(0, 1)$, generating the integers 0 or 1 with the same probability.

For both methods, the final excitation signal is then generated via the SDR using the USRP sink for communication.

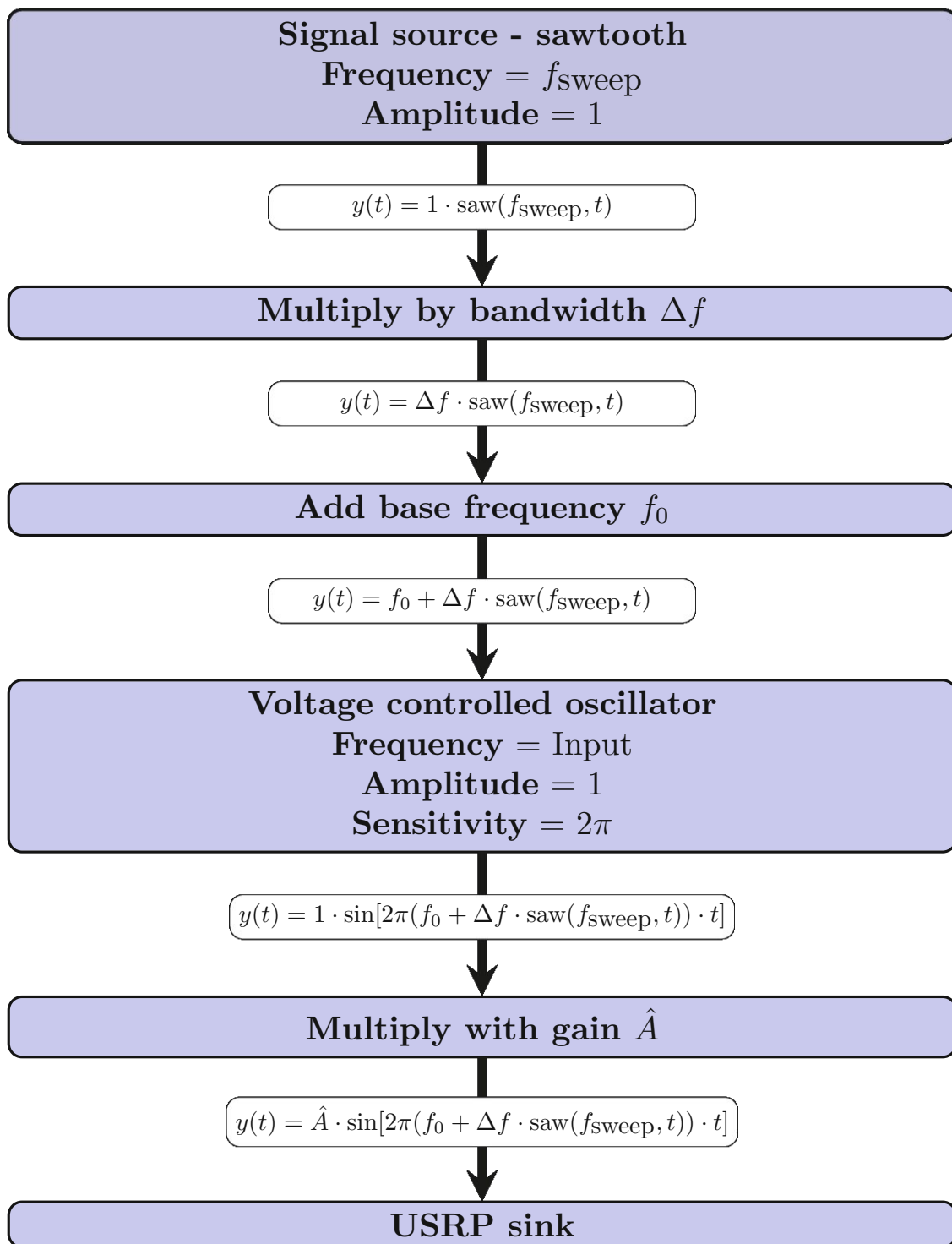


Figure B.1.: GnuRadio script for frequency modulation. (courtesy of Eike Feldmeier/HIT)

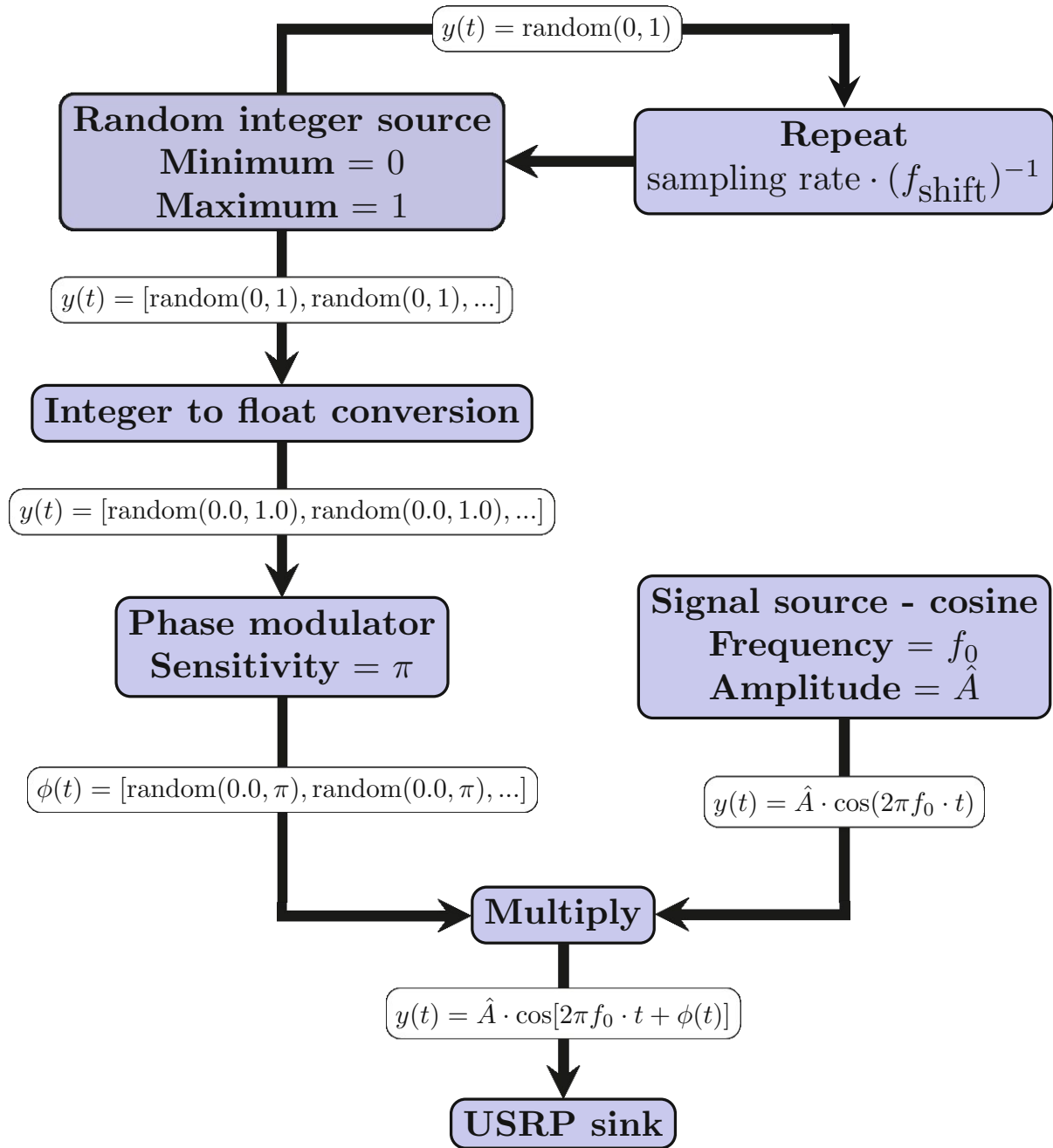


Figure B.2.: GnuRadio script for binary phase shift keying. (courtesy of Eike Feldmeier/HIT)